

# **On the Use of Potential Theory for Thermal Modeling in Metal Cutting**

Der Fakultät für Maschinenwesen der Rheinisch Westfälischen  
Technischen Hochschule Aachen vorgelegte Dissertation zur  
Erlangung des akademischen Grades eines

**Doktors der Ingenieurwissenschaften**

von

**Matthias Brockmann**





# Content

## *Inhaltsverzeichnis*

<b>1</b>	<b>Introduction.....</b>	<b>1</b>
<b>2</b>	<b>State of the Art.....</b>	<b>5</b>
2.1	Model Verification and Validation .....	5
2.2	Significance of Thermal Effects in Metal Cutting .....	8
2.3	Thermal Conceptual Models in Metal Cutting Theory .....	11
2.4	Fundamentals of Heat Transfer.....	13
2.4.1	Fourier's Law of Heat Flux .....	13
2.4.2	Partial Differential Equation for Heat Conduction .....	14
2.4.3	Thermal Boundary Conditions.....	16
2.5	Analytical Thermal Models .....	18
2.5.1	Mathematical Models .....	18
2.5.2	Overview of Analytical Computational Models .....	19
2.6	Fundamentals of Potential Theory .....	24
2.7	Use of Potential Theory in Metal Cutting.....	27
2.8	Conclusions from the State of the Art.....	28
<b>3</b>	<b>Objectives and Scientific Approach.....</b>	<b>29</b>
<b>4</b>	<b>Elementary Solutions Approach .....</b>	<b>31</b>
4.1	Complex Temperature and Heat Flow Field Function .....	31
4.2	Methodology for Derivation of Complex Functions for Cutting .....	33
4.2.1	Superposition of Elementary Functions.....	37
4.2.2	Model Parameter Study .....	46
4.2.3	Calibration of Model Parameters.....	54
4.2.4	Correlation of Model and Cutting Parameters .....	59
4.3	Model Outcomes .....	60
4.3.1	Temperature Field.....	60
4.3.2	Heat Flow Field .....	61
4.4	Conclusions from Elementary Solutions Approach .....	62
<b>5</b>	<b>Panel Method Approach.....</b>	<b>63</b>
5.1	Fundamentals of Panel Methods.....	63
5.2	Methodology for the Application of Source Panels .....	67
5.2.1	Discretization of Cutting Kinematics .....	69
5.2.2	Consideration of Thermal Boundary Conditions .....	71
5.2.3	Generating the Potential Function.....	73
5.2.4	Calibration .....	76
5.3	Model Outcomes .....	79
5.3.1	Temperature Distribution Fields .....	79
5.3.2	Consideration of Wear and Tool Geometry .....	80
5.4	Intermediate Conclusions from Panel Method.....	82

---

<b>6 Model Validation .....</b>	<b>83</b>
6.1 Description of Conducted Cutting Experiments .....	83
6.1.1 Measurement Devices and Method.....	85
6.1.2 Cutting Experiments on Fundamental Test Rig.....	89
6.1.3 Cutting Experiments on Broaching Machine .....	91
6.2 Investigation of Thermal Boundary Conditions.....	93
6.3 Validation of Presented Approaches .....	99
6.3.1 Validation of the Elementary Solutions Approach .....	100
6.3.2 Validation of Panel Method Approach .....	104
6.4 Conclusions and Comparison of Both Approaches .....	110
<b>7 Comparison to Other Modelling Approaches.....</b>	<b>111</b>
7.1 Comparison to Conventional Modelling Approaches.....	111
7.2 Comparison to the Finite Element Method .....	114
7.3 Intermediate Conclusions and Assessment .....	118
<b>8 Summary and Outlook .....</b>	<b>119</b>
<b>9 Appendix .....</b>	<b>123</b>
9.1 Definitions of Characteristic Thermal Values.....	123
9.2 Detailed Mathematical Derivations .....	125
9.3 Source Codes .....	130
9.4 Result Tables from Cutting Experiments .....	134
<b>10 References .....</b>	<b>135</b>

# Formula Symbols and Abbreviations

*Formelzeichen und Abkürzungen*

## Capital Letters

$A, dA$	$\text{m}^2$	Heat Flux Area
$A$	-	Influence Matrix
$A_{i,j}$	-	Coefficient of Influence Matrix
$E$	-	Source Strength Parameter or Electrical Field
$F(z)$	-	Complex Function
$F_C$	N	Cutting Force
$F_n(z)$	-	Complex Function Number $n$ in Superposition
$F_E$	N	Coulomb Force
$F_G$	N	Gravitational Force
$F_P$	N	Passive Force
$F_x, F_y, F_z$		Cutting Force Components
$H(x,y)$	-	Heat Flux Distribution Field
$K_i, K_j$	-	Nodes in Panel Method Approach
$K_{IR}$	-	Calibration Factor of Infrared Camera
$P_i, P_j$	-	Panel in Panel Method Approach
$Pe$	-	PÉCLET Number
$Q$	J	Heat Amount
$\dot{Q}$	W	Heat Flow
$R, dR$	$\text{m}^3$	Control Volume Function
$R_{IR}$	-	Spectral Response Function of Infrared Camera
$S, dS$	$\text{m}^2$	Surface Function of Control Volume
$S$	$\text{W}/\text{m}^3$	Spectral Radiance
$S_{black}$	$\text{W}/\text{m}^3$	Ideal Spectral Radiance of Black Body
$T$	K, °C	Temperature Value or Isotherm
$T(x,y)$	K, °C	Temperature Function or Distribution Field
$T_0$	K, °C	Temperature for DIRICHLET Condition

$T_{cal}$	K, °C	Calibrated Temperature
$T_{IR}$	K, °C	Infrared Camera Temperature
$T_{ref}$	K, °C	Reference Temperature
$T^*$	-	Dimensionless Temperature
$U$	J	Internal Energy

**Small Letters**

$a$	$\text{m}^2/\text{s}$	Temperature Diffusivity
$a_{I\max}$	-	Maximum Source Strength
$a_{n1}, a_{n2}$	-	Elementary Solution Parameters
$a_p$	m	Cutting Depth
$b$	$\text{W}/\text{m}^2 \cdot \text{s}$	Boundary Condition Vector
$b_i$	$\text{W}/\text{m}^2 \cdot \text{s}$	Boundary Condition at Panel $i$
$b_{flow}$	$\text{W}/\text{m}^2 \cdot \text{s}$	Parameter for Consideration of Cutting Speed
$c$	J/K	Heat Capacity
$d$	mm	Dislocation Parameter
$f$	m, mm/rev	Feed per Revolution or Tooth
$f(T,y)$	K, °C	Temperature Function (DIRICHLET Condition)
$k$	-	Counting Index
$l, w$	m	Width and Height of Rectangular Heat Flux Area
$l_w$	mm	Window Size for Panel Method
$m$	kg	Mass
$n$	-	Counting Index or Corner Solution Parameter
$r$	m	Radius of Complex Argument
$r_a$	-	ratio of source strengths
$r_n$	-	ratio of number of sources
$r_{i,j}$	m	Dislocation Vectors between Panel and Nodes
$r_n$	-	Ratio of Source Number
$r_\varepsilon$	°	Cutting Edge Radius
$s$	-	Source Strength Vector

$s_i, s_j$	-	Source Strength Parameter of Panels
$t$	s	Time
$t_{int}$	ms	Integration Time
$u, v$	$m^{-1}$	Derivatives of Complex Function in $x$ - and $y$ Direction
$u^*, v^*$	m/s	Normal and Tangential Induced Velocity
$v_c$	m/min	Cutting Velocity
$\dot{q}''$	$W/m^2$	Heat Flux
$\dot{q}_{Source}'''$	$W/m^3$	Volumetric Heat Source Strength
$\dot{q}_x'', \dot{q}_y'', \dot{q}_z''$	$W/m^2$	Heat Flux Components
$q_k$	-	Strength of Source $k$
$x, y, z$	m	Spatial Dimension in $x$ , $y$ and $z$ - Direction
$x', y'$	m	Relative Coordinate on Line Heat Source
$x_n, y_n$	m	Dislocation Parameters
$z$	m	Complex Argument
$z_n$	m, mm	Complex Dislocation Parameters

### Greek Letters

$\Gamma$	-	Vortex Strength Parameter
$\Phi(x,y)$	-	Real Valued Part of Complex Function
$\Psi(x,y)$	-	Imaginary Part of Complex Function
$\alpha$	-	Coefficient of Bessel Function
$\beta_{i,j}$	rad	Angle between Dislocations Vectors
$\Delta t$	s	Time Increment
$\varepsilon_i, \varepsilon_j$	rad	Global Angular Position of Relative Coordinates
$\varepsilon$	-	Emissivity
$\varepsilon_a$		Apparent Emissivity
$\varphi$	rad	Angle of Isotherms or Complex Argument
$\lambda$	$W/(m \cdot K)$	Heat Conductivity
$\lambda_{ref}$	-	Reference Value for Panel Method
$\eta_\lambda$	-	Material Calibration Coefficient

---

$\eta_v$	-	Cutting Speed Calibration Coefficient
$\rho$	kg/m <sup>3</sup>	Density

## Abbreviations

BC	Boundary Conditions
Black	Ideal Black Body
CAL	Calibrated Value
CH, Chip	Chip Region
Clear	Clearance Face of the Tool
Contact	Contact Area between Rake Face and Chip
Grey	Grey Body
InSb	Indium Antimonide
InGaAs	Indium Gallium Arsenide
IR	Infrared Camera
Panel	Panel Parameters
PCBN	Polycrystalline Boron Nitride
PDE	Partial Differential Equation
PVD	Physical Vapor Deposition
Pyro	Pyrometer
Rake	Rake Face or Contact Zone
Real	Real Body
RPT	Rise per Tooth
Shear	Shear Region of Metal Cutting
Source	Source Strength
Tool	Cutting Tool Region
Work	Work Piece Region

## Mathematical Operators

$d/dx$	m <sup>-1</sup>	Substantial Derivative of Variable $x$
$\partial/\partial x$	m <sup>-1</sup>	Partial Derivative of Variable $x$
$\nabla$	m <sup>-1</sup>	Nabla Operator, Gradient Vector

---

$K_0$	-	BESSEL Function (Order Zero, Second Kind)
$dR$	-	Infinitesimal Element of $R$
$i$	-	Imaginary Unit
$s^{-l}$	-	Inverse Source Strength Vector
$e$	-	Exponential Function



# 1 Introduction

Cutting of metal with a geometrically defined cutting edge is a complex physical process. The cutting tool penetrates the work piece material until a critical shear stress is reached and a layer of the surface is removed. The freshly produced chip is immediately pushed out over the rake face of the tool. Both processes - the plastic deformation in the shear zone and the friction between chip and rake face - induce heat flows into the chip, the tool and the work piece, causing a temperature distribution field in each of these components. The occurring temperature magnitudes can reach significantly high values.

The temperature distribution in each of the components have major influence on productivity of the cutting process, quality of the manufactured product and hence profitability. Elevated temperatures in the tool can cause excessive tool wear rate or early tool breakage leading to higher tool costs. Thermal effects on the work piece, either geometrically by thermo-elastic deformation or by metallurgical change of the work piece surface, can even result in scrap part production. In fact, the insufficient knowledge of the complex thermal interactions in metal cutting prevent industrial production to profit from the full power capability of nowadays available machine tools.

Due the importance of thermal effects, temperatures and heat in metal cutting have been topic of research since reported scientific work in this field exists. Experimental work conducted by LORD THOMPSON [THOM98] who investigated temperatures occurring during boring of copper was already published in 1789. Even though the objective of his work was to understand the nature of heat itself rather than measuring temperatures in the metal cutting process, his contribution can be considered as the first documented research in this field. TAYLOR [TAYL07] recognized the correlation of tool wear and tool temperature already in 1907. His empirical law for assessment of tool life time is still in use today. The first systematic investigations for temperature measurements can be dedicated to GOTTHEIN [GOTT25] in 1925. In his work he measured the temperatures at the tool-chip contact zone using the thermocouple method. Due to the high influence of the condition in the junction between the two thermocouple components, all thermocouple measurement methods are prone to errors, which is still valid in modern research work. To overcome this problem, SCHWERD [SCHW33] introduced the first contactless measurement method in 1933. Thereby he used a lens made of salt focusing the heat radiation on a thermocouple occurring during a turning process. His experimental setup can be considered as the first investigation using pyrometry for the metal cutting process.

As all temperature measurement methods are prone to errors and require high experimental efforts, the need for predictive models arose early in industry and academia. First model attempts were of empirical nature but due to the limited validity of empirical models, analytical and simulation models were developed. Pioneering work in this field was made from BLOK [BLOK38], JAEGER [JAEG42] and ROSENTHAL [ROSE46]. BLOK coined the term heat partition ratio, which describes the fraction of a

heat source flowing into the stationary part of a moving heat source problem. For metal cutting this fraction needs to be considered for heat flow from the shear zone into the work piece and for heat flow from the friction zone into the tool. JAEGER and ROSENTHAL first applied the moving heat source model to metal cutting. JAEGER considered a heat source with parallel movement to the stationary member, ROSENTHAL one with perpendicular movement. The approach of the moving heat source combined with a heat partition ratio function is found in the vast majority of research work until today and can be considered as a major milestone in analytical modelling of temperature fields in metal cutting.

Despite this work of merit, analytical models are still not capable to predict temperature fields to a sufficient degree. This lack of model validity is caused, amongst other reasons, by the limited mathematical approaches, i.e. only real-valued functions, taking into account of most analytical models. The present thesis deals with the development of methodologies for thermal modeling based on a class of complex functions termed potential functions. The basics of these functions are described in Chapter 2. Furthermore, Chapter 2 provides the modelling philosophy applied to this work and states the relevant state of art, structured according to this philosophy. Based on the identified deficits, the detailed modelling plan and objectives of the thesis are given in Chapter 3. Chapter 4 describes a simple approach for derivation of a complex model based on elementary solutions of potential theory. While this approach can be regarded as a feasibility study, Chapter 5 provides a systematic methodology based on a discretization approach. The systematic method explicitly considers boundary conditions and geometry, which are characteristic for the metal cutting process. This systematic is based on the so-called Panel Method. An introduction to this theory, the application for the metal cutting process and detailed discussion about the model outcomes are discussed. To validate both novel approaches, validation experiments are conducted. The experiments on a fundamental test rig and a broaching machine are presented in Chapter 6. This chapter also contains a brief description of a measurement method combining infrared camera and two-color pyrometer. The objective of this method is to decrease measurement uncertainty opposite to the single use of each measurement device. Finally, in Chapter 7 the developed methodologies are compared to conventional analytical modelling approaches and discretization methods.

## Einleitung

Das Spanen von Metall mit geometrisch bestimmter Schneide ist ein komplexer physikalischer Prozess. Dabei dringt das Werkzeug in das Werkstückmaterial ein bis eine kritische Schubspannung erreicht wird und eine Schicht von der Oberfläche abgetragen wird. Der neugebildete Span wird danach direkt über die Spanfläche des Werkzeuges ausgeschoben. Beide Prozesse - die plastische Deformation in der Scherzone und die Reibung zwischen Span und Spanfläche - induzieren Wärmeströme in den Span, das Werkzeug und das Werkstück, welche eine Temperaturverteilung in jeder dieser Komponenten verursacht. Die auftretenden Größenordnungen der Temperatur können signifikant hohe Werte erreichen.

Die Temperaturverteilung in den jeweiligen Komponenten hat maßgeblichen Einfluss auf die Produktivität des Zerspanprozesses, die Qualität des gefertigten Produktes und schlussendlich der Wirtschaftlichkeit. Erhöhte Temperaturen im Werkzeug können überhöhten Verschleißzuwachs oder vorzeitigen Werkzeugbruch verursachen der zu höheren Werkzeugkosten führt. Thermische Effekte im Werkstück, entweder geometrisch durch thermo-elastische Verformung oder Änderung des metallurgischen Zustandes der Werkstückoberfläche, können sogar in der Erzeugung von Ausschussteilen resultieren. Tatsächliche verhindert die unzureichende Kenntnis der komplexen thermischen Wechselwirkungen bei der Metallzerspanung, dass die industrielle Produktion von der vollen Leistungsfähigkeit heutzutage verfügbarer Werkzeugmaschinen profitieren kann.

Aufgrund der Bedeutung der thermischen Effekte sind Temperaturen und Wärme Forschungsthematik seit es dokumentierte wissenschaftliche Arbeiten in diesem Bereich gibt. Experimentelle Arbeiten, durchgeführt von LORD THOMPSON [THOM98] , welcher die beim Bohren von Kupfer auftretenden Temperaturen untersuchte, wurden bereits 1789 veröffentlicht. Obwohl das Ziel seiner Arbeiten vielmehr das Verständnis der Beschaffenheit der Wärme selbst als das Messen von Temperaturen im Zerspanprozess war, kann sein Beitrag als erste dokumentierte Forschungsarbeit in diesem Bereich angesehen werden. TAYLOR [TAYL07] erkannte den Zusammenhang zwischen Werkzeugverschleiß und Werkzeugtemperatur bereits 1907. Sein empirisches Gesetz für die Bewertung der Standzeit des Werkzeuges ist noch heutzutage in Gebrauch. Die ersten systematischen Untersuchungen zur Temperaturmessung im Jahre 1925 können GOTTHEIN [GOTT25] zugeschrieben werden. In seiner Arbeit maß er die Temperaturen während des Werkzeug-Span Kontaktes mit der Thermo-element Methode. Aufgrund des großen Einflusses der Bedingungen im Verbindungsbereich der beiden Thermoelementpartner sind jegliche Messungen mit Thermoelementen fehleranfällig. Um dieses Problem zu überwinden führte SCHWERD [SCHW33] 1933 die erste kontaktlose Messmethode ein. Dabei nutzte er eine Linse aus Salz welche die Wärmestrahlung, die während eines Drehprozess auftrat, auf ein Thermoelement fokussierte. Sein experimenteller Aufbau kann als erste Pyrometeruntersuchung des Zerspanprozesses angesehen werden.

Da alle Temperaturmessmethoden fehleranfällig sind und einen hohen experimentellen Aufwand benötigen, entstand die Notwendigkeit nach Vorhersagmodellen in der Industrie und der akademischen Welt früh. Wegweisende Arbeiten im Feld der analytischen Modellierung wurden von BLOK [BLOK38], JAEGER [JAEG42] and ROSENTHAL [ROSE46] durchgeführt. BLOK prägte den Begriff des Wärmeverteilungsverhältnisses, welcher den Anteil des Wärmestroms aus einer Wärmequelle der in den stationären Partner eines bewegten Wärmeleitungsfalls fließt, beschreibt. Für die Zerspanung muss dieser Anteil z. B. für den Wärmestrom aus der Scherzone in das Werkstück und für den Wärmestrom aus der Reibzone in den Span berücksichtigt werden. JAEGER und ROSENTHAL wendeten erstmals das Modell der bewegten Wärmequelle für die Zerspanung an. JAEGER berücksichtigte eine Wärmequelle mit Parallelbewegung relativ zum stationären Partner, ROSENTHAL eine mit Orthogonalbewegung. Der Ansatz der bewegten Wärmequelle in Verbindung mit der Wärmestromverteilungsfunktion findet sich im Großteil heutiger Forschungsarbeiten und stellt einen Meilenstein in der Entwicklung analytischer Modelle dar.

Trotz dieser verdienstvollen Arbeiten sind analytische Modelle immer noch nicht befähigt, Temperaturfelder zu einem zufriedenstellendem Grad vorherzusagen. Dieser Mangel an Modellvalidität wird, unter anderem, bedingt durch den eingeschränkten Einsatz von mathematischen Lösungsansätzen, d. h. nur reelle Funktionen wurden in derzeitigen analytischen Modellen genutzt. Die vorliegende Arbeit behandelt die Entwicklung von Methoden zur thermischen Modellierung basierend auf einer bestimmten Klasse komplexer Funktionen, sogenannten Potenzialfunktionen. Die Grundlagen dieser Funktionen werden in Kapitel 2 beschrieben. Weiterhin gibt Kapitel 2 einen Überblick über die angewandte Modellierungsphilosophie und gibt einen, nach dieser Philosophie strukturierten, Überblick über den relevanten Stand der Technik. Aufbauend auf den identifizierten Defiziten werden ein detaillierter Modellierungsplan und die Ziele dieser Arbeit in Kapitel 3 dargestellt. Kapitel 4 beschreibt dabei einen einfachen Ansatz zur Ableitung von komplexen Modellen, der auf den Elementarlösungen der Potenzialtheorie basiert. Während dieser Ansatz als eine Art Machbarkeitsstudie angesehen werden kann, gibt Kapitel 5 eine Übersicht über eine systematische Methode basierend auf einem Diskretisierungsansatz. Diese systematische Methode berücksichtigt die für die Zerspanung charakteristischen Randbedingungen und Geometrien explizit. Die Systematik baut auf die sogenannte Panelmethode auf. Eine Einführung dieser Methode, die Anwendung für Zerspanprozesse und eine detaillierte Diskussion der Ergebnisse wird in diesem Kapitel gegeben. Zur Validierung der beiden neuartigen Ansätze wurden Validierungsexperimente durchgeführt. Die Experimente welche auf einem Analogieprüfstand und einer Räummaschine durchgeführt wurden, werden in Kapitel 6 vorgestellt. Dieses Kapitel beinhaltet ebenfalls eine kurze Beschreibung der angewandten Messmethode, welche Infrarotkamera und Zweifarbenpyrometer kombiniert. In Kapitel 7 werden die entwickelten Methoden abschließend mit bestehenden analytischen Modellierungsansätzen und Diskretisierungsmethoden verglichen.

## 2 State of the Art

### *Stand der Technik*

Research of thermal modeling in cutting metal materials is widely spread and many researchers have been working in this field for decades. Due to the great number of contributions, only a choice is mentioned during this chapter. The choice of these contributions is structured according to a distinct verification and validation philosophy described in Subchapter 2.1. Appropriate definitions and the modelling approach relevant for this thesis are described. Model Validation can only be conducted for specific modelling objectives. Chapter 2.2 therefore briefly states empirical work describing the significance of thermal effects in metal cutting. The main purpose of this chapter is to illustrate possible use of the developed models and give an idea of the needed accuracy. An overview of relevant conceptual model can be found in Chapter 2.3. For the derivation of analytical models, the fundamentals of heat transfer are necessary. A metal cutting specific derivation of the significant fundamentals is given in Chapter 2.4. Chapter 2.5 provides an overview of current thermal models, i.e. mathematical and computational models with a focus on analytical computational models and the analysis of their deficits. The fundamentals for an approach with another class of functions, i.e. complex functions, is finally given in Chapter 2.6.

### 2.1 Model Verification and Validation

#### *Modellverifikation und -validierung*

Models are used to describe, understand and predict a part of the physical reality. Different kind of models exist dependent on their intended use. [ORTL09] categorizes models according to their transparency on a black and white scale. Black-box models in this sense are a class of models with unknown internal mechanisms. However input and output behavior can be determined. In comparison, white-box models are fully transparent, i.e. the governing mechanisms are known. In between of these two limits there are different kind of combinations called grey-box models. Another categorization can be done by the applied mathematics. Static or dynamic models refer to consideration of time. Stochastic models or deterministic models are applied if random events have to be taken into account or not. Continuous models allow model variables to attain arbitrary values within the defined model boundaries. Discrete models in contrast only allow particular values.

Regardless of the model category, the question of model credibility is of major importance for later application of the model. Model credibility is closely connected to verification and validation. [SCHL79] summarized the verification and validation process and appropriate terminology in a graphical representation called the Sargent Circle. The circle is shown in Figure 2.1 and described in the following.

The reality of interest describes the physical system or the part of the physical reality that is studied. The choice of the particular reality of interest includes the regarded

scale, which can be a unit problem, a component problem, subsystem or a complete system. Modeling of a complete system means an iterative verification and validation process according to Figure 2.1 for each scale. Defining the reality of interest for engineering applications include consideration of a particular use case. This use case especially defines the outcomes of the model activities and the demanded accuracy. Furthermore, relevant metrics and scales for sufficient model fidelity should be provided when choosing the reality of interest. Model fidelity is defined as “*the difference between simulation and experimental outcomes*” [THAC04, p. VIII].

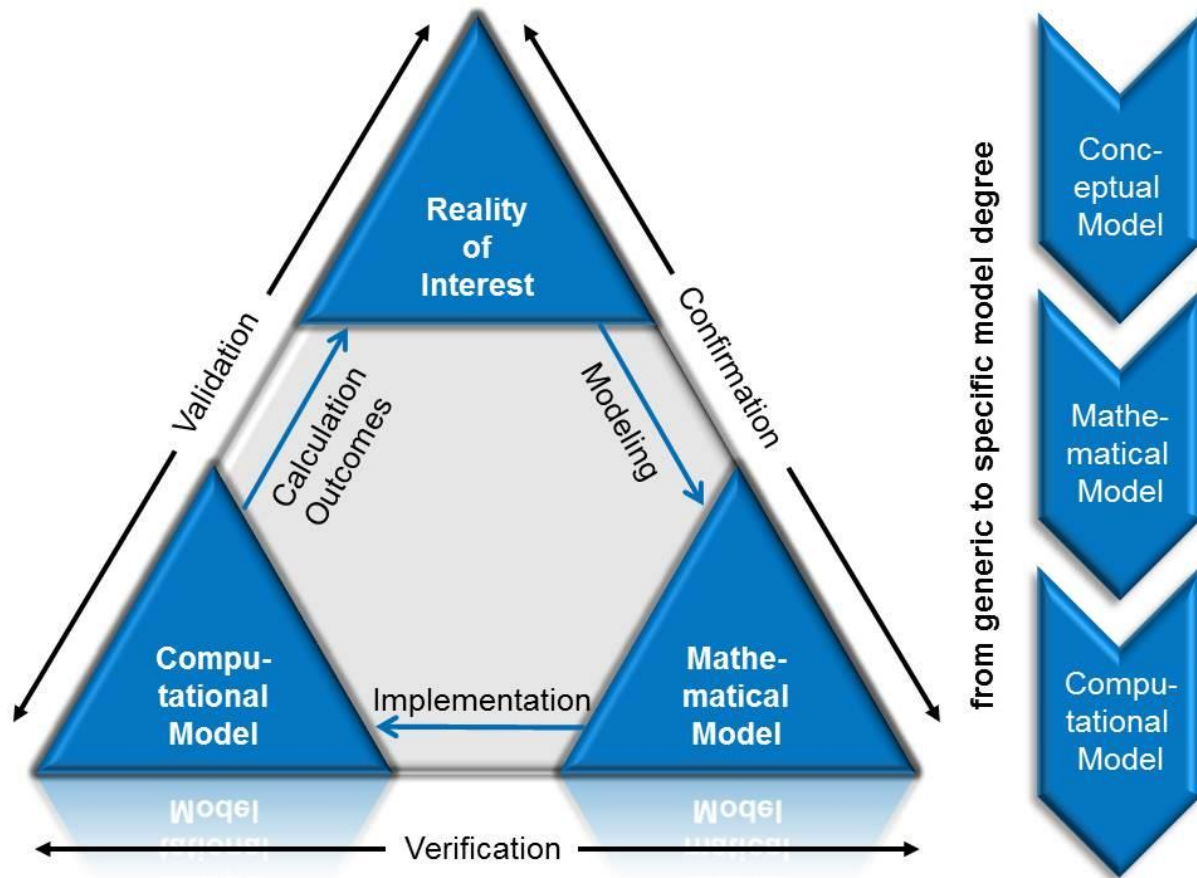


**Figure 2.1:** Modified Sargent Circle [SCHL79] and model types  
*Sargent Circle*

The process of representing the reality of interest in a mathematical model is termed modeling. The assessment of the correctness of this model is called confirmation. Mathematical models require a preceding conceptual model. Conceptual models are also used to design later validation trials. Typical conceptual models in engineering are for example the bent beam, the mass-spring system or point masses.

The mathematical model describes the conceptual model with the help of mathematical equations. For engineering problems, these equations are usually differential equations, constitutive equations, geometry, initial conditions and boundary conditions.

The process of finding solutions for the mathematical model, which is mostly connected to software implementation, leads to computational models. For one mathematical model there can be several computational models.

Computational models are “*the numerical implementation of the mathematical model, usually in the form of numerical discretization, solution algorithm and convergence criteria*” [SCHW07]. For correct parameterization, both physical parameters and discretization parameters are sufficient.

The calculation outcomes of the computational models are finally compared to the reality of interest. For the comparison, uncertainty in the computational model and the validation experiments need to be quantified. The comparison is conducted against the metrics and demanded accuracy which were defined when choosing the relevant reality of interest.

Conceptual model, mathematical model and computational model represent the deductive model approach from generic to specific. With these model types, [SCHW07] defines verification and validation as follows:

- Verification: “*The process of determining that a computational model accurately represents the underlying mathematical model and its solution.*”
- Validation: “*The process of determining the degree to which a model is in accurate representation of the real world from the perspective of the intended uses of the model.*”

These definitions were coined from the American Society of Mechanical Engineers Standards Committee on Verification and Validation in Computational Solid Mechanics [SCHW07]. Interpreting the definitions yield that verification can be regarded as a purely mathematical issue (“Do I solve the equation right?”). This includes the right mathematical solutions and the right software implementation. In contrast, validation is the domain of physics (“Do I solve the right equation?”) and is always connected to experimental comparison. The definition of validation in the stated way implies that there can only be a certain degree to which a model and the reality are in accordance. Furthermore the term intended use implies that an agreement whether a model is acceptable or not necessarily need to be connected with real engineering problems. If the model outcomes are not in favorable agreement with the reality, models can be either revised or calibrated. Revising or changing the model form applies to the conceptual and mathematical model. In most cases, assumptions made in the mathematical model need to be revised, e.g. including varying material constants, three-dimensional influences or instationary effects.

The term calibration refers to the computational model. Calibration is “*the process of adjusting physical modeling parameters in the computational model to improve agreement with the experimental data*” [SCHW07]. A change in either the mathematical model or conceptual model is a model revision, which means that the whole verification and validation process needs to be repeated. For complex modeling of whole systems, a subsystem calibration however is acceptable. Following the verification and validation philosophy stated, the following chapters provide an overview of actual conceptual models, mathematical models and computational models for temperature distribution in metal cutting. The reality of interest is described by stating the significance of temperatures for metal cutting processes.

## 2.2 Significance of Thermal Effects in Metal Cutting

*Bedeutsamkeit von thermischen Effekten in der Metallzersetzung*

Industrial manufacturing of products is always a compromise between cost, productivity and quality. Dependent on the industry branch and the company philosophy, emphasis is put on one of these directions. Following one of these directions requires an optimization of the manufacturing process with defined objectives. The key to optimization is the understanding of the nature of the manufacturing process and appropriate effects of changes. Thermal effects caused by the temperature fields in the components work piece, chip and tool have direct influence on the manufacturing process and its outcomes, a choice of application fields is summarized in Figure 2.2 and will be described in the following with the help of chosen literature.

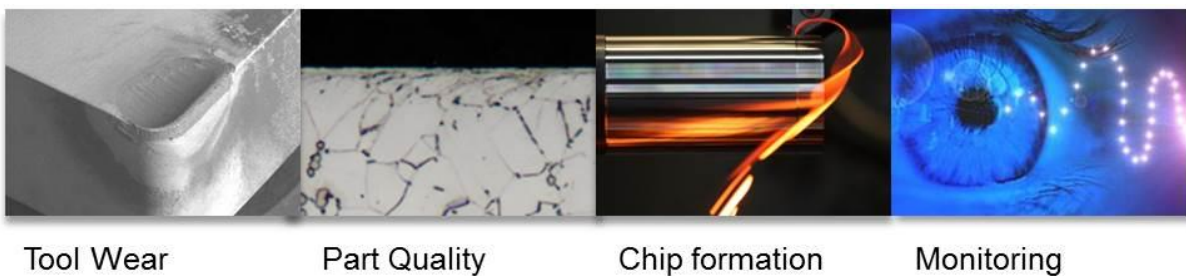


**Figure 2.2:** Significance of temperature fields for metal cutting applications

*Bedeutsamkeit von Temperaturfeldern für Zerspanungsanwendungen*

The influence of *tool temperatures* on the wear behavior was already determined by TAYLOR [TAYL07] in 1907, however little systematic research has been conducted with quantitative consideration of temperature fields. Wear mechanisms and wear behavior are associated with the costs of the manufacturing process. GRZESIK terms the lack of systematic measurement fields in the tool as a “*technical paradox*” [GRZE06, p. 651]. KLOCKE categorizes the qualitative wear mechanisms due to the cutting tool temperature [KLOC07, p. 79]. While the influence of adhesive wear decreases with increasing cutting tool temperature, diffusion wear and oxidation wear occur. Thermal overload of the cutting tool results in thermal cracks. The direction of these cracks is similar to the direction of the isotherms [KLOC07, p. 84]. SATO ET AL. investigated the influence of temperature on the tool wear during a drilling process. The pyrometer measurements yielded a rapid increase of temperature near the bottom surface of the work piece, which is responsible for an increased wear rate [SATO13, pp. 45–46]. The appropriate differences in temperature magnitudes can be assessed around 100 °C when cutting 0.5 % carbon steel. WANIGARATHNE ET AL. conducted a study for turning of AISI 1045 steel with grooved tools. The measurements with an infrared camera showed a difference of up to 60 °C difference dependent of the location on the tool [WANI05, p. 1218]. This clear difference underlines the importance of modeling temperature fields rather than average temperatures. For different wear states chosen points on the tool showed a temperature difference of around 150 °C while other points showed only a difference of 20 °C [WANI05, p. 1219]. This order of magnitude is also determined from WERSCHMÖLLER ET AL. by

measuring with PCBN Tool sensorized with thin-film thermocouples during turning of aluminum [WERS11, p. 6].

Temperatures evolving in the *work piece* can have two different kind of influence, i.e. geometrical shape deviations or alteration of the metallurgical surface and subsurface structure. The former is caused by thermo-elastic deflection of the work piece or the work piece holder. Both influences are directly related to the quality of the manufactured product. According to BRINKSMEIER, the temperatures in the work piece are one major process signature [BRIN11]. DENKENA ET AL. measured deflections and temperatures during milling of a structural aluminum part. The investigation showed significant differences in the shape error of the work piece, dependent on the temperature distribution in the part occurring during machining [DENK10, p. 1017]. The different temperature distributions were caused by different machining strategies. Local temperature differences for the two temperature fields were examined in the magnitude of 40 °C, causing a shape error up to 100 µm. FLEISCHER ET AL. investigated thermal deflections of a cast iron part during drilling operation. From the experimental temperature measurements conducted, the work piece surface heat flux was calculated and correlated to the thermal deflection with the help of a simulation. The results showed deflections up to 25 µm, and a maximum difference of surface heat flux of around 1200 W/mm<sup>2</sup> for different cutting parameters [FLEI07, pp. 120–121]. Besides geometrical deviations, temperature fields can also influence the surface and subsurface structure. SUHAIL ET AL. investigated the influence of temperature fields on the surface roughness for turning of AISI 1020 steel. The work piece temperatures were measured with a thermometer. A main effect analysis yielded higher temperatures as favorable for lower surface roughness values, within the tested cutting parameter limits [SUHA10, pp. 105–106]. Maximum temperature deviations around 40 °C were determined, maximum surface roughness average deviations were found from 0.7 µm to 3.1 µm. Investigations of the influence of temperature fields in the surface integrity, i.e. the metallurgical alteration of the subsurface, were conducted by CHOU AND SONG. In their work, the formation of White Layers occurring during hard turning of AISI 52100. The developed temperature distribution model proposes a correlation between temperature penetration depth and formation of white layer thickness, which was validated by means of experiments [CHOU05, pp. 493–494]. FERGANI ET AL. investigated the influence of the temperature field in the work piece on the grain size and hardness for turning aluminum. Again the penetration depth of the temperature field was found to have major influence on the work piece microstructure. Difference in maximum temperature ranged form around 80 °C for average grain sizes between 50 µm and 110 µm.

The *temperature field in the chip* is the most difficult to measure. This is on the one hand due to the limited accessibility of sensors, on the other hand chip dimensions in conventional cutting processes are relatively low. Chip formation and appropriate material behavior is usually connected the productivity of the manufacturing process. SUTTER AND RANC measured temperatures during orthogonal cutting of C15 and 42CrMo4 steel on a ballistic test bench by means of a pyrometer. During the test a

maximum temperature of 867 °C for the 42CrMo4 steel and 630 °C for the C15 steel was observed [SUTT07, p. 1513]. The location of the temperature maximum was found to be dependent on the cutting speed. The distance of the maximum to the contact zone was found to have a minimum corresponding to a critical cutting speed value. LIU ET AL. measured temperatures during turning of GCr15 steel with the tool-work thermocouple method. Work piece hardness and feed rate was varied during the trials. The trials yielded a temperature maximum around 580 °C, even if hardness or feed rate were further increased. This effect was explained to be caused by material softening and increasing heat taken away with the chip [LIU02, pp. 202–203]. In general, the temperatures occurring in the chip can drastically change the material behavior. NEUGEBAUER ET AL. [NEUG11] summarized the influence of cutting speeds, and hence temperatures, on the friction coefficient, the deformation behavior and the chip formation process itself. In their work it is explained that “*the temperature in the shear zone has a radical influence on chip formation*” [NEUG11, p. 630].

Taking into account the stated application fields, knowledge about temperature distribution can be used to *plan, monitor and optimize* machining processes. Measurement devices in the tool were used to develop tool condition monitoring systems. BIERMANN ET AL. [BIER13] developed an in-process monitoring system using a Nickel / Nickel-Chromium layer on the rake face of the used tool. The layer was manufactured via thin film technology by a PVD process. The system can be used for turning operations. KERRIGAN ET AL. developed a system for milling operations [KERR12]. The temperature measurement was realized by a thermocouple integrated in a solid carbide cutting tool. The system was used for milling carbon fiber reinforced polymer components. LE COZ ET AL. developed a similar system for drilling [LE C12, p. 437].

The cited research articles show the significance of temperatures for metal cutting. All investigations yielded that not only the magnitude of the temperatures, but rather the distributions within the components chip, tool and work piece are of major interest. In terms of the modeling process described in Chapter 2.1, the reality of interest can be formulated as the interacting temperature fields in the components for different materials and cutting parameters. The physical problem formulated in this way can be regarded as a unit problem, i.e. not the whole components need to be considered because the interesting physical process happen immediately close the shear and friction zone.

For the required model fidelity there is no simple way of definition as it is difficult to quantify the deviations between temperature distribution fields. Qualitative observations can help to assess the credibility of models. The required temperature magnitudes are dependent on the application case. As the model developed in this thesis is not dedicated to a certain application, a specific temperature value can not be identified. However, summarizing the findings from the stated research articles, an accuracy around 50 °C can be regarded as sufficient for most of the cited cases, taking also into account the high uncertainty in temperature measurements during metal cutting. The more important outcome for temperature modeling is the distribution of the temperature fields and the resulting heat flux distribution in the components.

## 2.3 Thermal Conceptual Models in Metal Cutting Theory

### *Thermische Konzeptmodelle in der Zerspanungstheorie*

The process of metal cutting is a complex physical process involving different kind of mechanisms that have to be taken into account for a thermal analysis. For the analysis and modeling, a conceptual model is needed, describing all relevant heat sources, geometries, kinematics and boundary conditions. Conceptual models can be regarded as descriptive models and represent the first stage of abstraction from the reality of interest. In order to derive mathematical and appropriate computational models, conceptual models as the first step of abstraction are needed. For the definition of the models, two kind of conceptual model need to be distinguished: chip formation model and thermal model. For the mathematical model only the thermal model is of interest, however, for the scope of validity a thermal conceptual model is always in connection with an appropriate chip formation model. A broad overview of conceptual models for chip formation and thermal models is given in [ARRA13]. Here, only models relevant for this thesis will be stated.

The thermal conceptual models available in metal cutting theory, assume the cause for temperature changes in sources of heat located at distinct areas of interest with a distinct heat source strength. The heat sources are caused by either plastic deformation or friction, transforming mechanical energy into heat. Locations of the plastic deformation heat sources can be found at the primary shear zone, the secondary shear zone at the chip-tool interface and at the clearance face at the work piece-tool interface. Frictional heat sources are located at the tool where the chip is pushed out over the rake face and also at the clearance face [MERC45]. While most of the conceptual models in use consider these heat sources partly or complete, a distinction can be made due to the assumed subsystems and the material flow considered.

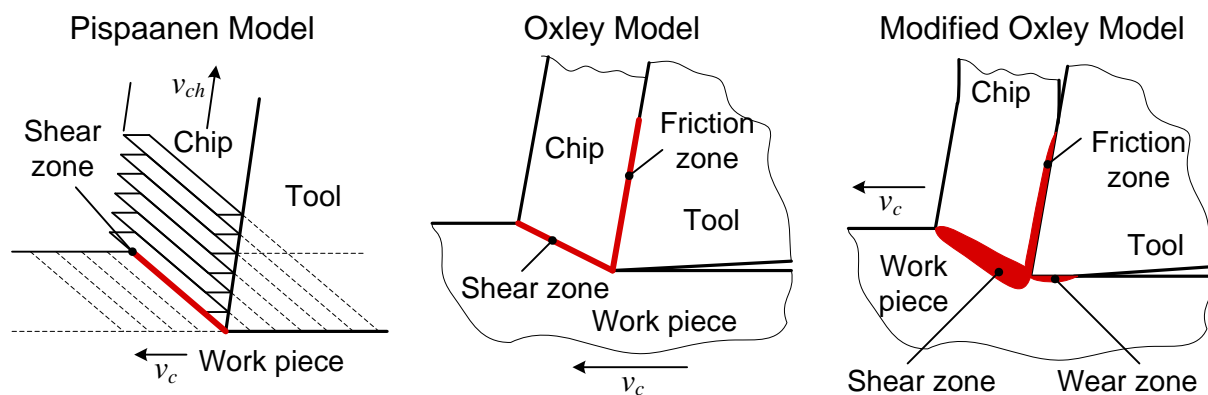


**Figure 2.3:** Conceptual Models for Heat Sources in Cutting

### *Konzeptmodelle für Wärmequellen in der Zerspanung*

One of the first approaches of a conceptual model for chip formation was the so-called card model of metal cutting. The approach was originally introduced from PIISPAANEN [PIIS48] and is shown on the left-hand side of Figure 2.3. The chip formation process in this approach is modeled similar to a deck of cards, sliding away upon each other. Material flow from work piece material into the chip is neglected, as

the cards are modelled as separate bodies. The sliding angle relative to the cutting direction can be considered and is usually chosen along the shear plane. For thermal modeling, the heat source is assumed between the two sliding bodies, i.e. not inside the material. PIIS PANEN'S model was used as conceptual model for many thermal model approaches. The appropriate thermal conceptual model was first considered from JAEGER [JAEG51] using a moving band heat source along the surface of a stationary body. This model can in principle be used for the shear zone and the rake face, however separate models are needed. While the assumption of a heat source above the surface seems sensible for the rake face, material flow is neglected when applying JAEGER'S model for the shear zone.

Another renown model was given from OXLEY [TAY80] depicted in the middle of Figure 2.3. In his model, the tool is assumed ideally sharp and the chip is modelled as a rectangular body. The thermal conceptual model assumes chip, tool and work piece as separate bodies. This separation of the subsystems requires coupling conditions after the modeling of the distinct subsystems, which is usually done in terms of equalization equations for the temperature distribution at the interface areas. Assuming the shear zone heat source inside the work piece, material flow can be considered with this model approach. CHILDS contribute a model for consideration of the friction heat source in this model [CHIL78]. The most renown mathematical model for this conceptual model was introduced from KOMANDURI AND Hou [KOMA00]. Their model is explained in detail in a later section.

A more generic form for the conceptual model based on the OXLEY approach contains material flow from the work piece into the chip and consist of only two subsystems, i.e. the tool and the work piece-chip model. The appropriate heat sources can have an arbitrary shape, a further heat source at the clearance face can be considered. For the chip a contact length at the rake face can be considered and is not modelled with an infinite length. However, in terms of chip breaking and chip form an ideal smooth chip is assumed. Even though two submodels exist geometrically, they need to be coupled for a thermal modeling. This approach requires a thermal model type which can cope with complex geometries, compare right-hand side of Figure 2.3. A consideration of e.g cutting edge radius is possible with this approach. While the difference compared to the normal Oxley approach seems not significant, another type of mathematical model is needed to cover these differences.

While the differences between the conceptual models seem marginal concerning the description of kinematical relationships and geometry, the impact for the thermal modeling is significant. Changing e.g. the geometry of the tool from a simple ideally sharp edge to a tool with cutting edge radius leads to a totally other class of mathematical equations. These equations, subsequently, can lead to totally other kind and shapes of temperature fields, in particular for the shape and location of the area of maximum temperatures. Examples for appropriate computational models of the different approaches are given in Chapter 2.5.2.

## 2.4 Fundamentals of Heat Transfer

### Grundlagen der Wärmeübertragung

In order to derive analytical models for the thermal behavior in metal cutting, a mathematical model describing a suitable conceptual model has to be chosen. The temperature field can in general be dependent on time and the spatial dimensions  $x$ ,  $y$  and  $z$ . As governing physical mechanism heat conduction is assumed, neglecting radiation and convection for the regarded system of chip, tool and work piece. For derivation of mathematical models, the law of heat flux, the partial differential equation for heat conduction and appropriate thermal boundary conditions need to be considered.

#### 2.4.1 Fourier's Law of Heat Flux

##### Fouriersches Gesetz der Wärmestromdichte

The law of heat flux was empirically derived from JOSEPH FOURIER in 1822 and states that “*the heat flux resulting from thermal conduction is proportional to the magnitude of the temperature gradient and opposite to its sign*” [FOUR22]:

$$\dot{q}''(y) = -\lambda \cdot \frac{dT(y)}{dy}. \quad (2.1)$$

The heat flux is defined as the heat amount  $Q$  per time and area, indicated by the point and the two dashes, and consequently has the unit of  $[J/s \cdot m^2]$  or respectively  $[W/m^2]$ . The proportional constant  $\lambda$  is called thermal conductivity and has the unit  $[W/m \cdot K]$ . Equation 2.1 is true, if the temperature  $T(y)$  only varies in  $y$  direction, compare left-hand side of Figure 2.4.

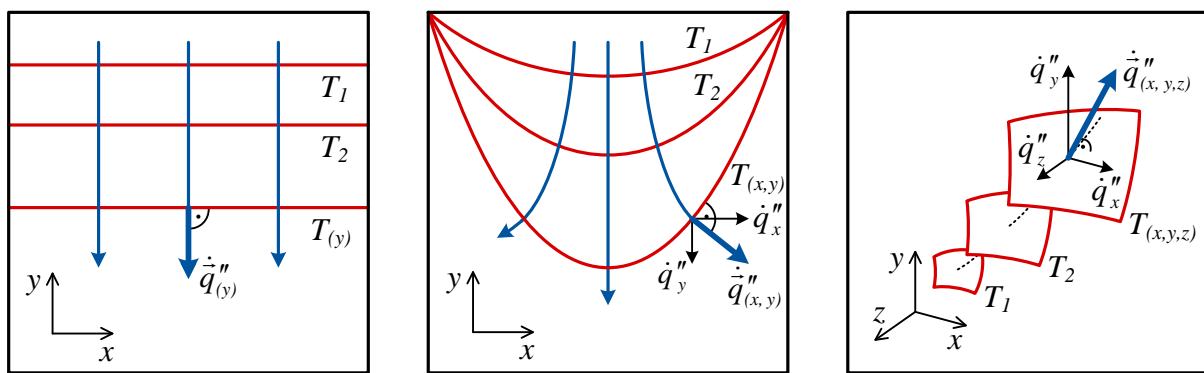


**Figure 2.4:** Fourier's Law

*Fouriersches Gesetz*

The minus sign indicates that heat always flows from higher to lower temperatures, hence in this example in negative  $y$  direction, if  $T_1 > T_2$ . A linear temperature distribution, i.e. constant gradient in  $y$  direction, would yield a constant heat flux.

In the middle of the figure, an exemplary case with a temperature distribution  $T(x,y)$  in the two dimensions  $x$  and  $y$  is sketched. It becomes obvious that the heat flux, in

general, is a vector quantity, consisting of a component of heat in each direction. In the general form, the three-dimensional Fourier's Law can be expressed as:

$$\vec{q}''(x, y, z) = -\lambda \cdot \vec{\nabla}T(x, y, z) \quad (2.2)$$

where  $\nabla$  is the gradient vector into the three spatial dimensions, The appropriate components of the heat flux vector consequently are:

$$\dot{q}_x'' = -\lambda \cdot \frac{\partial T(x, y, z)}{\partial x}, \dot{q}_y'' = -\lambda \cdot \frac{\partial T(x, y, z)}{\partial y}, \dot{q}_z'' = -\lambda \cdot \frac{\partial T(x, y, z)}{\partial z} \quad (2.3)$$

A sketch is shown on the right-hand side of Figure 2.4. The isothermal lines transfer to isothermal surfaces in the three-dimensional space. In general also the heat conductivity  $\lambda$  can be dependent on the location within the material. The amount of heat  $Q$  flowing through a freely chosen surface  $A$  within the time  $t$  can be calculated by using the expression:

$$Q = \int \int \int_A (\vec{q}'' \cdot \vec{n}) dt dA . \quad (2.4)$$

In Equation 2.4 the vector quantity  $n$  is the normal vector of the surface  $A$ . Fourier's Law yields the relationship between temperature and heat flux distribution.

## 2.4.2 Partial Differential Equation for Heat Conduction

*Partielle Differentialgleichung für Wärmeleitung*

Using the three-dimensional Fourier's Law, the partial differential equation (PDE) of heat conduction can be derived. The following derivation for metal cutting applications is based on LIENHARD [LIEN11, pp. 54–56]. An arbitrary three-dimensional control volume regarded for the analysis is shown in Figure 2.5. The coordinate system is moving with the tool at the same velocity  $v_c$  and the control volume is assumed to be stationary relative to this coordinate system. Even though in reality there can be a changing cutting speed, the equation derived is still valid and can be corrected with a coordinate transformation [CARS59, p. 14]. The control volume is denoted as  $R$ , the surface of  $R$  is referred to as  $S$ . A surface element  $dS$  is chosen and two vectors, namely the unit normal vector  $n$  with a magnitude equal to unity and the heat flux vector defined by Equation 2.2. For the derivation it is not important if the infinitesimal small control volume is taken from the chip region  $R_{Chip}$ , the tool region  $R_{Tool}$  or the work piece region  $R_{Work}$ . Applying the First Law of Thermodynamics for a closed system without work transfer yields:

$$\dot{Q} = \frac{dU}{dt} = \iiint_R (\rho c \frac{\partial T}{\partial t}) dR , \quad (2.5)$$

where  $dU/dt$  is the change of internal energy connected with the change of heat  $Q$  per time  $t$ ,  $\rho c$  is the specific heat capacity and  $\partial T/\partial t$  is the partial time derivative of the temperature  $T$ . For consideration of the heat sources in metal cutting, a volumet-

ric heat source could be located inside the control volume. Heat sources in metal cutting are denoted  $R_{Shear}$  for the shear zone region,  $R_{Contact}$  for the contact zone of tool and chip and  $R_{Clearance}$  for the contact zone between tool and work piece at the clearance face. For the general derivation it is not necessary to choose the control volume in one of these specific regions. The amount of heat released is denoted by  $q_{Source}$  and indicated with three dashes in Equation 2.6 as it refers to a volumetric quantity. Consequently, the unit is [W/m<sup>3</sup>].

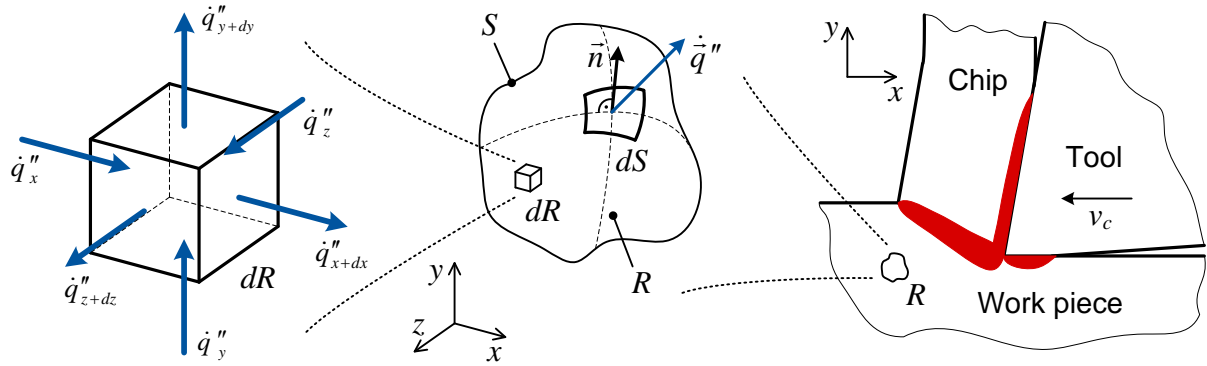


**Figure 2.5:** Control Volume and Characteristic Regions of Metal Cutting  
*Kontrollvolumen und charakteristische Regionen der Zerspanung*

The physical reasons for heat sources in metal cutting are mainly by friction and plastic deformation. Sources of heat therefore can occur at the shear zone, the rake face and on the clearance face due to clearance face wear. These characteristic regions are sketched in the right-hand side of the figure. For the following derivation the distinct zones are not of importance.

The total heat generated within the control volume  $R$  can be derived by the change of the heat flux in and out off the volume and the input from the heat sources to:

$$\dot{Q} = - \iint_S (-\lambda \vec{\nabla} T) \cdot (\vec{n} dS) + \iiint_R \dot{q}_{Source}''' dR. \quad (2.6)$$

The minus sign at the first integral indicates that energy input to the control is counted positive. As  $S$  refers to a surface and  $R$  to a volume, the appropriate integrals are surface and volume integrals, respectively. Following the conservation of energy, replacing the heat flow in Equations 2.5 and 2.6 yield:

$$\iint_S (\lambda \vec{\nabla} T) \cdot (\vec{n} dS) = \iiint_R [\rho c \frac{\partial T}{\partial t} - \dot{q}_{Source}'''] dR. \quad (2.7)$$

The left-hand side of Equation 2.7 contains the integral over the surface area of the control volume  $S$ . For convenience, the integral can be converted into a volume integral by application of Gauss's Theorem. The theorem states that any continuous function of position, in this case the term  $\lambda \nabla T$ , can be replaced by the appropriate volume integral over  $R$  [LIEN11, p. 55] by taking the gradient  $\nabla$  into account.

By replacing the integral and considering that  $R$  is a freely chosen control volume, the integrand must be equal to Zero. Equation 2.7 can be consequently rewritten as:

$$\vec{\nabla}(\lambda \vec{\nabla} T) + \dot{q}_{Source}'' = \rho c \frac{\partial T}{\partial t}. \quad (2.8)$$

Equation 2.8 is the general partial differential equation for heat conduction, with considering three dimensions, internal heat sources, non-constant heat conductivity and instationary effects. Based on further assumptions, other forms that are frequently used can be derived. For one dimension  $x$ , constant heat conductivity  $\lambda$  and without sources, the equation transforms to:

$$\lambda \frac{\partial^2 T}{\partial x^2} = \rho c \frac{\partial T}{\partial t}. \quad (2.9)$$

This form of the differential equation is applied if time effects are of interest. For modeling of temperature fields stationary forms of the PDE can be derived. Neglecting time effects but taking a second dimension  $y$  into account, the partial differential equation results to:

$$\frac{\partial^2 T}{\partial x^2} + \frac{\partial^2 T}{\partial y^2} = 0. \quad (2.10)$$

Forms of Equations 2.9 and 2.10 are the most widely used forms for heat conduction applications.

#### 2.4.3 Thermal Boundary Conditions

##### *Thermische Randbedingungen*

For the formulation of a mathematical model for metal cutting, additionally to the governing equation, the boundary conditions need to be formulated. An overview of boundary conditions relevant for thermal modeling is summarized in Figure 2.6. Here, the temperature  $T(x,y)$  was plotted into a three-dimensional plot for better visibility, as the boundary conditions can not be seen at the isothermal plot. Isothermal plots only refer to the  $x$ - $y$  space, while for the thermal boundary conditions the correlation to the temperature itself is important. The boundary conditions can be noted as either DIRICHLET or NEUMANN Boundary Condition.

DIRICHLET Boundary Conditions, also referred to as boundary conditions of first order, prescribe a temperature value or a temperature function at the boundary. If e.g. the boundary at  $x = 0$  is considered, the DIRICHLET Boundary Condition can be formulated as:

$$T(0, y) = f(T, y), \quad (2.11)$$

$$T(0, y) = T_0,$$

which means that either a function  $f(T, y)$  or a constant value  $T_0$  can be preset at the boundary. This boundary condition can be used for metal cutting e.g. at the regions

of the work piece, chip or tool far away from the cutting where room temperature is prevalent. The heat flux at the boundary, i.e. the direction of the isotherms after Equation 2.1, is unknown. The DIRICHLET Boundary Condition is depicted on the left-hand side of the figure.

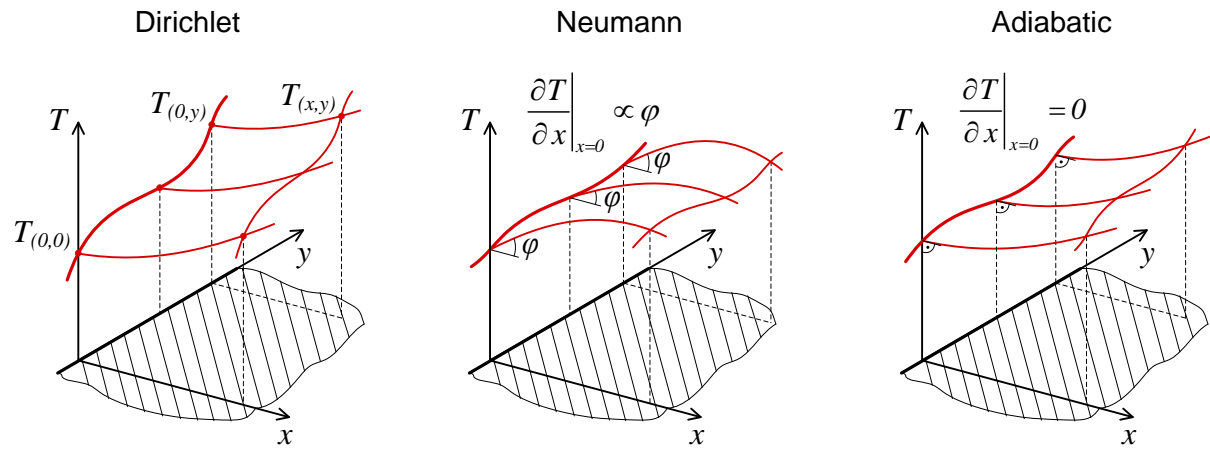


**Figure 2.6:** Boundary Conditions in Metal Cutting

*Randbedingungen bei der Zerspanung*

For NEUMANN Boundary Condition in contrast, the heat flux in normal direction on the surface is prescribed. Such boundary condition can be found, if a heat source is located at the boundary, e.g. at the tool-chip interface and a certain heat source strength is known or assumed. If again the condition at  $x = 0$  is regarded, the NEUMANN Boundary Condition can be formulated as:

$$\frac{\partial T(0, y)}{\partial x} = C. \quad (2.12)$$

The constant  $C$  is the desired value at the boundary. From FOURIER's Law it was derived that the gradient is correlated to the heat flow at the boundary. In the middle of the figure, the NEUMANN Condition can therefore be found as angle  $\varphi$  relative to the  $x$  axis. The NEUMANN Condition is often used at the shear zone and the rake face for the appropriate heat sources occurring in metal cutting.

A special case of the NEUMANN Boundary Condition is the adiabatic boundary, depicted on the right-hand side of the figure. At an adiabatic boundary there is no heat flow through the boundary to the surrounding, the temperature gradient is equal to Zero. Hence, the angle  $\varphi = 90^\circ$  and the temperature function is running orthogonal to the  $x$  axis:

$$\frac{\partial T(0, y)}{\partial x} = 0. \quad (2.13)$$

The adiabatic boundary condition is widely used in modeling of temperature fields. Dependent on the chosen subsystems, usually clearance face, chip backside and uncut work piece material are chosen as adiabatic boundaries. Also the chip-tool contact zone is often modelled as adiabatic.

## 2.5 Analytical Thermal Models

### *Analytische thermische Modelle*

The inherent difficulties of temperature measurements during the metal cutting process and the lack of simple reliable methods induce the need for modelling. Models can be either empirical, simulative or analytical. Empirical models are based on observation in terms of measurement and subsequent regression to yield a mathematical formula, often in form of a power law. For the derivation of empirical models the governing physical equations and mechanisms are not needed. Due to the lack of physical foundation of the formulas, empirical models are often only valid for the regarded case. Simulation models based e.g. on Finite Element Methods replace the partial differential equation with the appropriate difference equation and solve them on a grid of defined sampling points. This approach allows solutions for complex geometries, instationary cases and coupled approaches, however the governing physical equation is linearized at a very early modeling stage. Analytical models, however not applicable on complex problems, deliver a solution without linearization of the problem and therefore are transferable to other cases with the same governing equation. Shaw claims that “*analytical approaches, even though often more complex than we would like, must be relied on to obtain a broad insight into the all important thermal aspects of metal cutting*” [SHAW05, p. 215]. The following subchapters provide a chosen overview of available computational models used for modeling of temperature fields in metal cutting. Emphasis is laid on analytical approaches, however some simulative works are also covered.

### 2.5.1 Mathematical Models

#### *Mathematische Modelle*

As derived in detail in Chapter 2.4, the mathematical model for thermal issues in metal cutting is completely described by means of the FOURIER’s Law, the partial differential equation of heat conduction and the thermal boundary conditions. The differences in most approaches applied for metal cutting can be found in the assumptions for the categories.

The heat flux value is either computed by means of Fourier’s law. Most cases assume the difference form of the equation, i.e. the gradient are replaced by the respective differences. For the partial differential equation, mainly the simplified two-dimensional form (Laplace Equation, compare Equation 2.9) and the simplified instationary form (Equation 2.10) are used for analytical modeling. For the thermal boundary conditions all real boundaries are usually assumed adiabatic (i.e. NEUMANN Condition). Only the areas with heat input (shear zone and rake face) have a preset value for the heat flow (DIRICHLET Condition). In the following an overview of different approaches for solutions of this mathematical model is given.

### 2.5.2 Overview of Analytical Computational Models

#### *Übersicht analytische Berechnungsmodelle*

For the development of computational models, solutions for Equations 2.8, 2.9 and 2.10, namely the general partial differential equation for heat conduction, the instationary one-dimensional and the two-dimensional stationary equation, are sufficient. While the general equation can only be solved numerically, for Equations 2.9 and 2.10 closed form analytical solutions are available. Solutions for these equations can be found either with construction methods, e.g. GREEN's Function, or simply by putting the derivatives into the appropriate equation. However, not all solutions of the partial differential equation are useful for modeling of heat problems. This should be shown by means of the following example. Equation 2.10 states that the second derivative of  $x$  added to the second derivative of  $y$  equals Zero. Considering an arbitrary function  $T(x,y) = x \cdot y$ , the two derivations are yielded to:

$$\frac{\partial T}{\partial x} = \frac{\partial}{\partial x}(x \cdot y) = y \quad \text{and} \quad \frac{\partial^2 T}{\partial x^2} = \frac{\partial}{\partial x^2}(y) = 0 \quad (2.14)$$

and the same is true for the  $y$ -derivative. Adding the two derivatives shows that Equation 2.10 is fulfilled and  $T(x,y)$  is a solution. Obviously, the function however is not a suitable solution for heat conduction problems in metal cutting, as the function represents simple hyperboles in the  $x$ - $y$  space. The examples shows that solving the governing equation is an essential property, but not sufficient to be a credible computational model for temperature fields in metal cutting. In the following an overview of applied mathematical solutions for temperature fields in metal cutting is given. The focus is on the mathematical functions that were used. Emphasis is laid on solutions for Equation 2.10, however also solutions for Equation 2.9 are mentioned, as well as simulative approaches if analytical solutions are integrated in the simulation.

A more detailed overview of mathematical solutions for heat problems based on GREEN's Function can be found from [LING02, pp. 11–67]. Another detailed overview of mathematical solutions for heat conduction in solids was given by CARSLAW AND JAEGER [CARS59]. Even though the solutions were derived for generic engineering cases, various solutions derived in this work were used by different researchers for modelling of temperatures in metal cutting. Especially the idea of the *instantaneous point source of heat* and subsequent derivations from this theory had shown to be appropriate solutions. The instantaneous point source of heat is “*a finite quantity of heat liberated at a given point and time in an infinite solid*” [CARS59, p. 255]. The appropriate equation:

$$T(x, y, z, t) = \frac{Q \cdot a}{8\lambda(\pi at)^{3/2}} \exp \left\{ -[(x-x')^2 + (y-y')^2 + (z-z')^2]/4at \right\} \quad (2.15)$$

is a solution of the general partial differential equation 2.8 without heat sources. The term  $Q$  stands for the amount of heat liberated in zero time from the point source,  $\lambda$  is

the heat conductivity,  $a$  the temperature diffusivity,  $t$  the time and  $x'$ ,  $y'$  and  $z'$  the location of the point heat source, compare left-hand side of Figure 2.7.

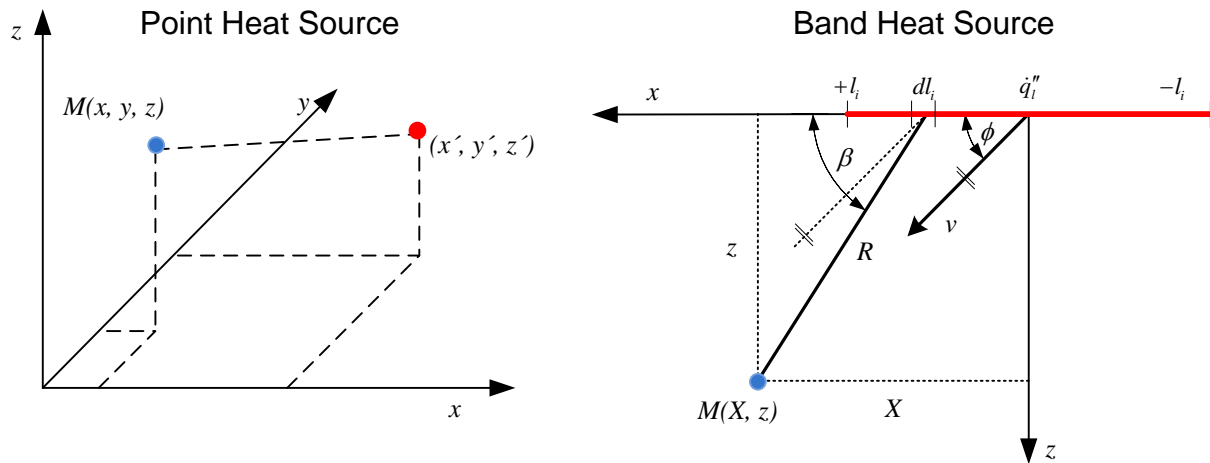


**Figure 2.7:** Point and Band Heat Source  
Punkt- und Bandwärmequelle

JAEGER followed up the idea of the instantaneous heat source and applied it to several heat conduction problems of engineering interest. His renown work about friction sliders is still in use of many analytical and simulative approaches nowadays. Overall, JAEGER provided solutions for a moving band heat source, a moving rectangular heat source, a solution for an instationary model for a finite time, a stationary heat source, a heat source of varying strength and a heat source moving with varying velocity [JAEG42]. The solutions published were already derived in [CARS59], however JAEGER used real values for sliding contacts of two bodies. Especially the solution for the band heat source moving with constant velocity  $v$  in  $x$ -direction is often referred to as *JAEGER Solution*.

The solution is derived from Equation 2.15 by means of integration, firstly in  $y$ -direction and then along the length  $2l$  of the heat source. Assuming an insulated slider, only values for  $z < 0$  are regarded. This fact is termed semi-infinite solid. The basic integral, and therefore the basic mathematical solution applied, is always of the following kind:

$$\int_0^a e^{\pm u} \cdot K_0(\alpha u) du \quad (2.16)$$

The integration limit  $a$  is usually the half-length of the heat source  $l$ , the term  $u$  contains the velocity of the heat source and the coordinates  $x$ ,  $K_0$  is the BESSEL Function of second kind and order Zero. A generalized form of this solution, namely for a band heat source moving with an inclination angle was already derived in [CARS59, p. 270]. HAHN used this solution in his work for deriving a computational model for the temperature distribution along the shear plane. His work was indeed the first one applying the equation explicitly for metal cutting applications, the solution is therefore often termed *HAHN Solution*. The basic mathematic solution is the same as Equation 2.16 but contains the angle in the expression  $u$ .

Several researchers have used the solution of the instantaneous heat source and subsequent derivatives like Equation 2.16. TRIGGER AND CHAO use Equation 2.15 to calculate the tool temperature distribution in the tool-chip contact zone and the average temperature of the tool [CHAO53, p. 60]. For the chip they calculated an average temperature rise. Experimental tests with a dynamometer and a tool-work piece thermocouple were used to parameterize the equations. In a later publication, the integral solution of kind 2.16 for the moving heat source was used [CHAO55, p. 111]. The integral was used to discuss the influence of the variable termed  $u$  in Equation 2.16. Trigger and Chao identify  $u$  as thermal number defined as  $vt/a$ , the ratio of cutting speed  $v$ , uncut chip thickness  $t$  and temperature diffusivity  $a$ . Influences of the thermal number on chip curvature and other metal cutting phenomena are discussed. LEONE uses the line heat solution to calculate the heat partition ratio for the heat flowing back into the work piece from the shear zone [LEON54, p. 121]. The experimental data from HAHN [HAHN51] and TRIGGER AND CHAO [TRIG51] were used to validate the equation. LEONE concluded that the heat fraction going into the work piece decreases with increasing thermal number. LOEWEN AND SHAW applied PIISPANEN's model and the JAEGER equation to calculate temperature in the tool [LOEW54, p. 218]. The form for  $z = 0$  as it was used from TRIGGER AND CHAO [TRIG51] was applied and validated with various examples. RAPIER investigated temperature distributions in tool, chip and work piece by means of simulation in the form of relaxations patterns. Even though he did not use Equation 2.16 in the integral form, the problem of the inclined moving heat source was solved numerically [RAPI54, p. 402]. In a further work, CHAO AND TRIGGER used equation 2.15 to develop an iterative method to calculate the temperature field at the tool-chip contact zone [CHAO55, p. 1111]. For the numerical approach, several point heat sources were located on the tool face and the influence on other sources was determined. For considering the adiabatic boundaries, image heat sources located symmetrically outside the tool were positioned. NAKAYAMA used the solution for the inclined moving heat source to evaluate the temperature rise for an orthogonal turning experiment [NAKA56, p. 2]. The analysis revealed an influence of the initial work piece temperature on the cutting process. CHAO AND TRIGGER made further contributions to the application of the Bessel Function integral [CHAO58, p. 313]. Here, explicit numerical solution values of the integral are applied. A further numerical analysis of the inclined moving heat source was provided from DAWSON AND MALKIN [DAWS84].

The most extensive and detailed analysis was provided from KOMANDURI AND Hou, compare right-hand side of Figure 2.7. In their first work they applied Equation 2.16 for the shear zone heat source [KOMA00, p. 1727] and the influence on chip and work piece. A further solution of Equation 2.15 was applied for the temperature field in the tool [KOMA01a, p. 65]. The third contribution describes the influence of combined heat sources from friction zone and shear zone [KOMA01b]. Besides the known solution, KOMANDURI AND Hou especially used the method of images to define adiabatic boundaries for chip, tool and work piece. TOUNSI ET AL. proposed a methodology for identification of material constants within practical ranges for metal cutting.

A simplified solution based on Equation 2.15 and the work of KOMANDURI AND HOU is used to study the influence on stress, strain and strain rate [TOUN02, p. 1378]. A further modified version of KOMANDURI AND HOU can be found from CHOU AND SONG. In their work, they used a modified solution of Equation 2.15 to predict white layer formation for hard turning [CHOU05, p. 485]. Further applications and modifications with different applications of the model from KOMANDURI AND HOU can be found from [MÜLL04], [HUAN05], [KARP06a], [KARP06b], [RICH06], [KUMA12], [FAHA13] [KARA13] and [ZHOU13].

While the solutions based on Equation 2.15 can be solved by means of the BESSEL Function, also the Error Function can be used as mathematical solution. WEINER used the Error Function for development of a model for solution of Equation 2.9, i.e. he solved the equation for the one-dimensional instationary case [WEIN55, p. 1333]. YOUNG AND CHOU came to a similar equation for calculating shear plane temperatures [YOUN94, p. 933]. Also SUTTER AND RANC used this type of solution for comparison of their temperature measured in the chip by means of thermography [SUTT07, p. 1516]. VENUVINOD AND LAU used an Error Function Approach for calculate rake face temperatures for oblique cutting [VENU86, p. 3]. Their approach was however based on the theory of moving rectangular heat source. STEPHENSON AND ALI also used a rectangular heat source however they did not include a movement the heat source, but rather considered the changing conditions for interrupted cutting. The solution contains the exponential function and the Error Function and was applied to an analogy experiment [STEP92, p. 114]. JIANG ET AL. [JIAN13] and LIN ET AL. [LIN13] applied this approach for real milling processes. ZHANG AND LIU used a simplified solution based on the Error Function to evaluate the influence of diffusion layers in coated tools [ZHAN08, p. 621] and [ZHAN09].

RADULESCU AND KAPOOR developed a model based on Fourier Series. The numerically solved approach is used to develop a model for consideration of heating and cooling times of the tool during interrupted cutting [RADU94, p. 116]. An approach of this kind is used due to the periodic nature of milling processes. STEPHENSON ET AL. also use a periodic approach based on the approach of RADULESCU AND KAPOOR [STEP97, p. 496]. The approach is used to predict temperatures during contour turning. MOUFKI ET AL. apply a power function to solve Equation 2.7. A solution for an orthogonal cutting process with temperature dependent friction law is considered. The power function is expanded by means of a TAYLOR Series [MOUF98, p. 2111]. In a further work, the computational model is used to calculate temperatures during oblique cutting [MOUF04, p. 979]. KIM proposes another FOURIER Series for temperature calculation for the moving heat source problem [KIM11, p. 898]. Recently, LUCHESI ET AL. proposed the use of a Kernel Function Series, resulting in a periodic expression similar to a FOURIER Series for modeling the temperature field in two-dimensional solids. The approach was numerically used to estimate heat source strengths in metal cutting [LUCH12, pp. 65–66].

Summarized, the number of different mathematical solutions for Equations 2.8, 2.9 or 2.10 used for modeling of temperature fields in metal cutting is limited to basically

four different kind of solutions, i.e. the Bessel Function, the Error Function, Fourier Series or other Series and simple mathematical functions, namely Exponential Function and Root Functions. An overview is given in Table 2.1.

**Table 2.1:** Overview of mathematical solutions used in metal cutting

*Übersicht mathematischer Lösungen angewandt in der Zerspanung*

Basic Mathematical Solution	Author
BESSEL Function	[CHAO53], [LEON54], [LOEW54], [CHAO58], [NAKA56], [KOMA00], [KOMA01a], [KOMA01b], [MÜLL04], [HUAN05], [KARP06a], [KARP06b], [RICH06], [KUMA12], [FAHA13] [KARA13], [ZHOU13]
Error Function	[WEIN55], [YOUN94], [VENU86], [STEP92] [YOUN94] [SUTT07], [ZHAN08], [ZHAN09], [JIAN13], [LIN13]
FOURIER or other Series	[RADU94], [MOUF98], [STEP97], [MOUF04], [KIM11], [LUCH12]
Simple Functions	[TRIG51], [LEON54], [LOEW54], [CHAO55], [KOMA01a], [TOUN02]

In the analysis only the mathematical solution itself is mentioned independent from the way of derivation. Furthermore the analysis only classifies the basic function used, in detail the equations are more complicated and have different kind of parameter definitions. The main conclusion is, that only a limited number of basic mathematical solutions is in use for modeling temperature fields in metal cutting. When analyzing the models based on the BESSEL Function, in particular, most of the models can be considered as enhancement or optimizations of the model of KOMANDURI AND Hou. TAY classifies only three kind of analytical model types, i.e. moving heat source method, image source methods and semi-analytical models [TAY93]. The disadvantage, which is resulting from the limited use of mathematical solutions, is the limitation of possible temperature field shapes and their appropriate area of maximum temperatures. Furthermore, the way of application for this solution, is limiting the possible geometrical shapes that can be considered. In the model of KOMANDURI AND Hou, the BESSEL Function is used for the heat source at the shear zone and the rake face. The appropriate boundary conditions at this regions, i.e. adiabatic boundaries at chip backside and rake face, is considered with the help of mirrored sources. The mathematical structure of the equation, however, allows only two sources. This fact limits the model of KOMANDURI AND Hou to simple wedge or rectangular shapes. Other shapes, e.g. the consideration of a cutting edge radius or a third heat source at the clearance face is not possible without modification.

## 2.6 Fundamentals of Potential Theory

### Grundlagen der Potenzialtheorie

The analysis of existing analytical computational models showed, that only a few mathematical solutions of the two-dimensional partial differential equation are in use for modelling of temperature fields in metal cutting. All the solutions used, have in common that they are exclusively real-valued functions. Besides solutions in the real-valued space, complex functions solving Equation 2.10 are existing. These functions are widely used for two or three dimensional cases due to their simple application. A complex function is a function of the complex argument  $z$ , where:

$$z = x + i \cdot y = r \cdot e^{i\varphi} \quad (2.17)$$

The two spatial dimensions  $x$  and  $y$  are separated by the imaginary unit  $i$ . For certain calculations also polar coordinates with radius  $r$  and angle  $\varphi$  can be used, see left-hand side of Figure 2.8. The complex function  $F(z)$  can be expressed as:

$$F(z) = \Phi(x, y) + i \cdot \Psi(x, y) \quad (2.18)$$

with the real-valued part of the function  $\Phi(x, y)$  and the imaginary part  $\Psi(x, y)$ . The functions  $\Phi(x, y)$  and  $\Psi(x, y)$  itself are both real-valued functions and can be plotted into an  $x$ - $y$  graph.

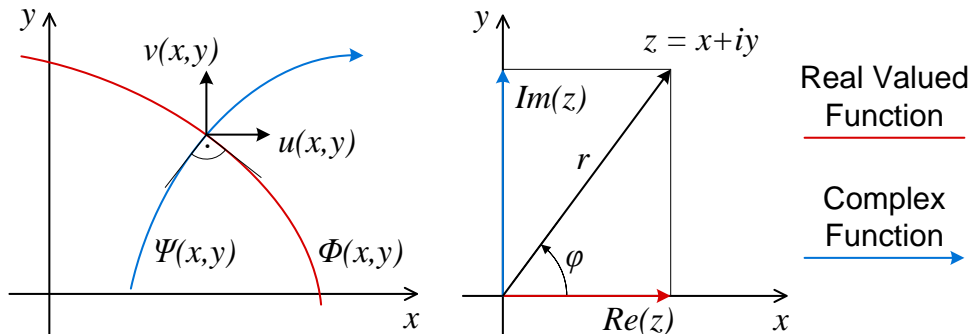


**Figure 2.8:** Plot of the Complex Argument and Potential Functions

*Grafische Darstellung des komplexen Arguments und Potenzialfunktionen*

There is a special class of complex functions existing, which is termed potential functions. For these functions the real part and the imaginary part fulfill the so-called Cauchy-Riemann Condition [TRUC08, p. 132]:

$$\frac{\partial \Phi}{\partial x} = \frac{\partial \Psi}{\partial y}, \frac{\partial \Psi}{\partial x} = -\frac{\partial \Phi}{\partial y} \quad (2.19)$$

If the Cauchy-Riemann Conditions are true, the function  $F(z)$  fulfills the partial differential equation for heat conduction. This can be shown by computing the derivatives in  $x$  and respectively  $y$  direction for Equation 2.19. Furthermore, the real part  $\Phi(x, y)$  is

running orthogonal to the imaginary part  $\Psi(x,y)$  when plotting both in an  $x$ - $y$  diagram. A generalized plot of the real and imaginary part is given on the right-hand side of Figure 2.8. In the figure also the derivatives of the imaginary function, often referred to as induced velocities  $u(x,y)$  and  $v(x,y)$ , are plotted:

$$u(x, y) = \frac{\partial \Psi(x, y)}{\partial y}, v(x, y) = -\frac{\partial \Psi(x, y)}{\partial x} \quad (2.20)$$

According to the Cauchy-Riemann Condition the functions  $u(x,y)$  and  $v(x,y)$  can also be expressed with the derivatives of the real-valued function  $\Phi(x,y)$ . A graphical overview of a choice of potential functions is given in Figure 2.9. The solutions are named after an interpretation of the two scalar fields. Both real-valued function and imaginary function are plotted.

The fact that using potential functions for modelling inherently yield two orthogonal scalar fields and appropriate relations of the derivatives makes them very interesting for application of heat problems. Real part and imaginary part of the function can be interpreted as temperature distribution and heat flow field, a fact that was already mentioned by CARLSLAW AND JAEGER [CARS59, p. 421].

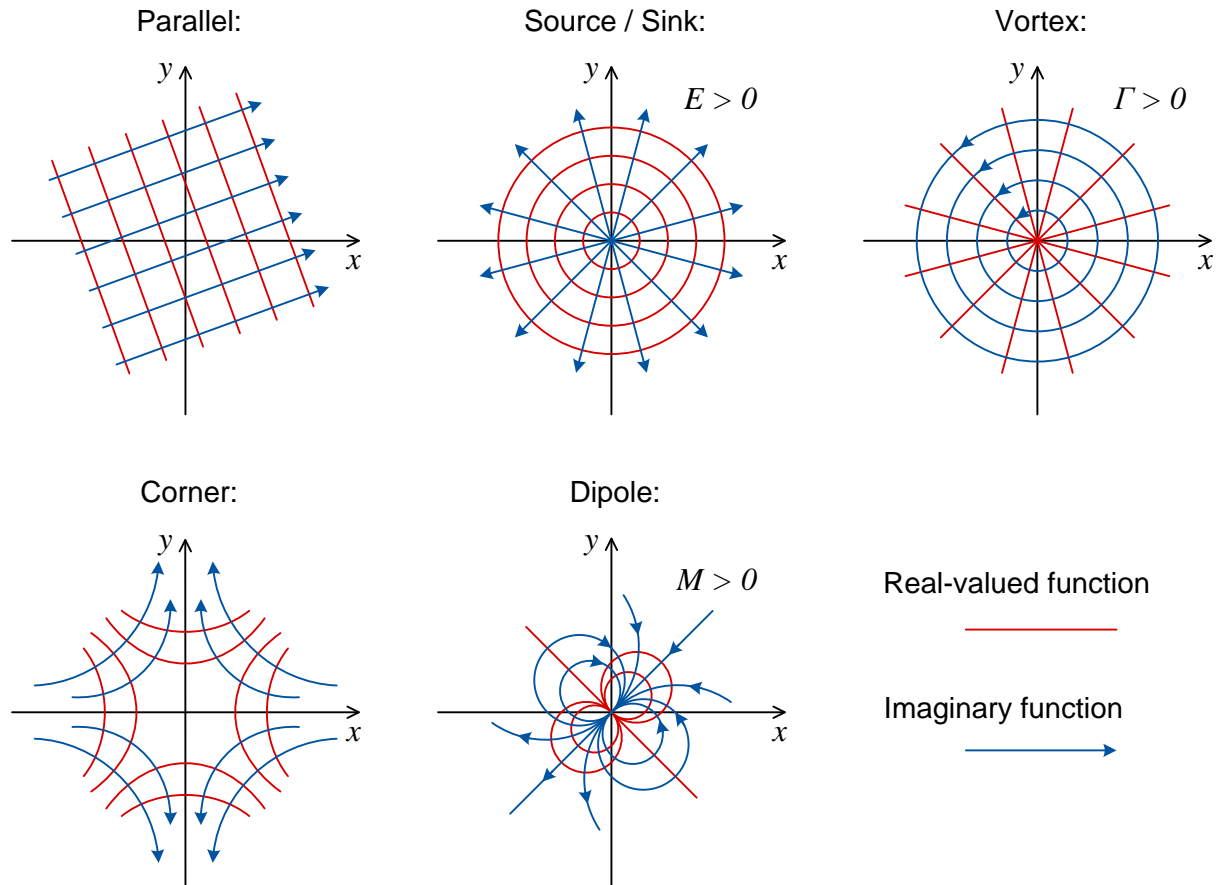


**Figure 2.9:** Plot of Chosen Potential Functions

*Grafische Darstellung ausgesuchter Potenzialfunktionen*

There are two more advantages that motivate the use of potential theory for metal cutting applications. Firstly, more complicated shapes in which the heat flow is re-

vant can be modelled compared to the presented solutions in Chapter 2.5.2. Secondly, there is a considerable number of known solutions within the theory that can be used. As the partial differential equation for heat conduction is a linear partial differential equation, the principle of superposition can be applied, i.e. the solutions can be arbitrarily added together and yield other plots. This enables a huge variety of possible solutions using the potential theory.

The potential theory was already widely applied in other engineering disciplines. Figure 2.10 presents chosen applications of the potential theory. In electrostatics, the potential theory was used to model the electrostatic field between cathode and anode. The real-valued function is interpreted as the electrostatic potential, the orthogonal scalar field resulting from the imaginary function yield the electrical field lines  $E$ . Using the derivatives of the electrical field function yields the Coulomb Force  $F_E$ . A simple approach can be conducted using the dipole solution shown in Figure 2.9. For the description of the gravitational field between two bodies  $m$  and  $M$ , the potential theory can be applied using the source solution. Real-valued and imaginary function can be interpreted as gravitational potential. The derivative can be used to compute the gravitational force  $F_G$ .

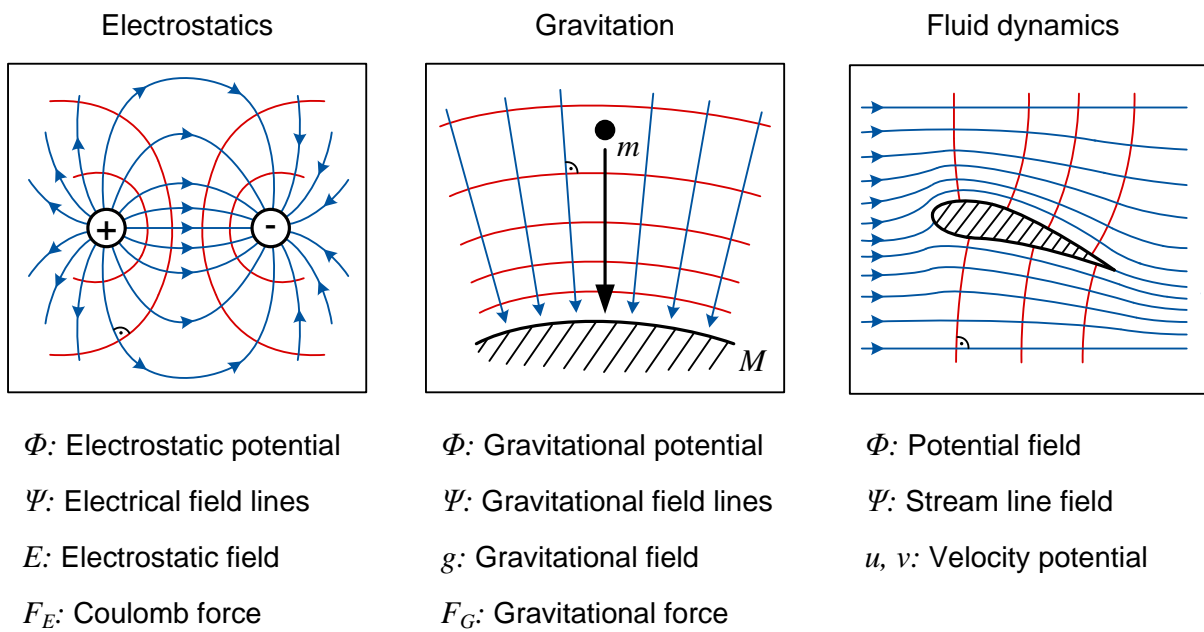


**Figure 2.10:** Use of Potential Theory in Physics and Engineering

*Anwendung der Potenzialtheorie in Physik und Ingenieurwesen*

In fluid mechanics, the theory is used to model flow fields [TRUC08, pp. 227–266]. The real part of the function is interpreted as potential field, the imaginary part as stream lines field. The induced velocities  $u$  and  $v$  yield the flow velocities at every location  $x$  and  $y$  of the field. All the presented applications show that the potential theory can be successfully applied after physical interpreting the two scalar fields and the appropriate derivatives. The reason for the optimal use and widely spread application of the potential theory in these different fields is obvious: All stated application fields require solutions of exactly the same partial differential equation.

## 2.7 Use of Potential Theory in Metal Cutting

### Gebrauch der Potenzialtheorie in der Zerspanung

Even though widely spread applications of potential theory in other engineering fields are available, the fact that solutions for the same mathematical model are needed, did not lead yet to a direct application for modeling of temperature fields in metal cutting. As described, CARSLAW derived the basic function for the vast majority of computational models in metal cutting, i.e. the instantaneous point heat source as basis for e.g. the JAEGER Model and the model of KOMANDURI AND HOU. Carlsaw furthermore mentioned potential theory in his work: *"From the theoretical point of view it has always been recognized that the point source corresponds to the fundamental solution of potential theory, and that a complete development of the theory of conduction of heat in bounded regions can be obtained by constructing Green's functions analogous to those of potential theory. [CARS59, p. 255]"* Despite this citation, he did not further evaluate the use of potential theory for metal cutting problems.

BICKEL AND WIDMER already recognized the physical analogy of temperature fields to electrical fields in 1951 [BICK51, pp. 242–243]. For the determination of the temperature field in a turning operation, they designed an electrolyte tub with the shape of a cutting tool.

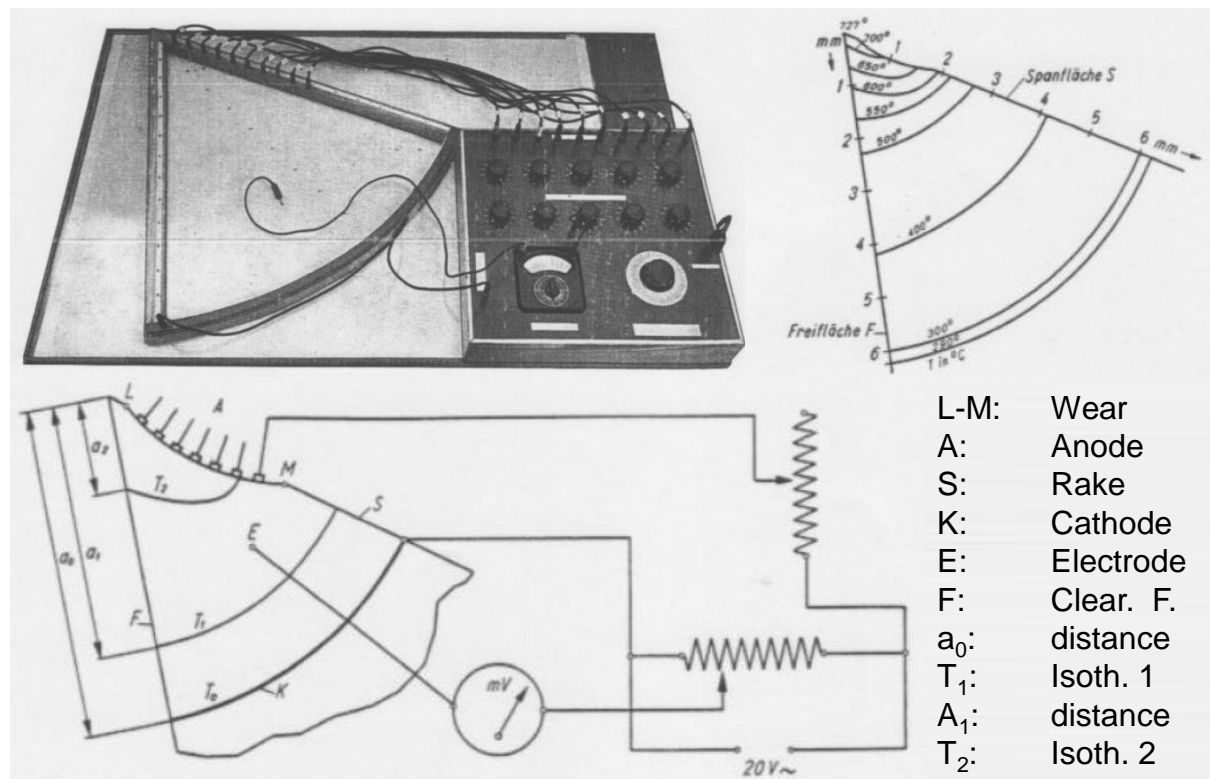


**Figure 2.11:** Analogy Experiment of Bickel and Widmer [BICK51, p. 240]

*Analogieexperiment von Bickel und Widmer [BICK51, p. 240]*

An original picture of the experimental setup is shown on the upper left-hand side of Figure 2.11. The anode was used as the electron source representing the influence of the heat source due to crater wear on the rake face. The cathode arc was placed

sufficiently far away from the interesting region. Plotting of equal voltages measured manually with an electrode (voltmeter) yielded a field shown on the upper right-hand side of Figure 2.11. The lines of same voltage represent the isotherms in the tool, which were calibrated against point measurements in the cutting tool. The work of BICKEL AND WIDMER can be considered as a first historical validation of the application of potential theory for modeling temperature fields in metal cutting.

## 2.8 Conclusions from the State of the Art

### *Fazit aus dem Stand der Technik*

Temperatures evolving in the tool, chip and work piece during metal cutting are of major significance for productivity, cost and part quality. More precise, especially the distribution of the temperatures in the distinct components are the reality of interest. The measurement of temperature fields is difficult and prone to errors, hence there is a need for modelling.

Analytical models have the advantage of being physically founded, transferable and require low computation time. However, recent computational analytical models are not sufficient and only use a limited number of real-valued functions. The potential theory provides complex solutions, these solutions were successfully applied in other engineering fields where solutions of exactly the same partial differential equation are needed. The opportunities for an application of potential theory in metal cutting can be stated as described in the following:

- The potential theory offers a variety of mathematical solutions and combinations of these functions. This yields a great variety of possible characteristics of the isotherms, e.g. location of maximum temperatures, shape of the isotherms.
- For the potential theory, no separate sub-models are needed. The cutting kinematics can be modelled directly by selecting distinct isotherms as adiabatic boundaries. In particular, the mass flow between work piece and chip and the fact that both components have no boundary against each other can be considered.
- As a consequence from this, more complex geometries beyond the OXLEY model can be considered (e.g. cutting edge radius), if suitable isotherms can be found or constructed.
- Due to the modeling of complex functions, two scalar fields are modelled at once. For thermal applications, the temperature field and the heat flow field can be modeled at once.

A first experimental evidence that this theory can be feasible for modeling temperature fields in metal cutting is available from experimental work from BICKEL AND WIDMER. Taking into account these conclusion, an application of the potential theory for thermal modeling in metal cutting seems viable.

### 3 Objectives and Scientific Approach

#### *Zielsetzung und wissenschaftliche Vorgehensweise*

The state of the art revealed that complex solutions from potential theory have not been yet applied for modeling in metal cutting. However, this theory provides suitable solutions which could be particularly advantageous for thermal modeling in metal cutting. Hence, the main research hypothesis of this work can be formulated:

- The complex solutions of the partial differential equation of heat conduction provided from potential theory are feasible to derive computational models for temperature fields and heat flux distribution in metal cutting.

“Feasibility” in this context includes, that it is indeed possible that there is not any available combination of potential functions which can represent the thermal behavior of metal cutting problems. The term “temperature fields and heat flux in metal cutting” refer to chip, tool and work piece, where not necessarily all components need to be modeled with one single model. Taking into account the research hypothesis, the objective of the thesis can be formulated as:

- The objective of the thesis is to develop methodologies which can be used for the application of potential theory for thermal modeling of metal cutting.

For the development of methodologies, two distinct model approaches will be evaluated. Formulating the main research questions associated with this objective are connected to the three main pillars of verification and validation:

1. Which combination of solutions from the potential theory need to be taken in account to solve the partial differential equation of heat conduction for metal cutting applications and how do they have to be parameterized (Verification)?
2. How can the appropriate boundary conditions, geometry and heat sources of metal cutting be integrated in the model and to which degree does this model represent the measured temperature field from experiments (Validation)?
3. How precise is the model when taking experimental data and the model sensibility into account and how can the temperature fields of different models be compared?

To address these research questions, the modeling approach of [THAC04] is applied as stated in Chapter 2.1. The approach can be considered as a deductive approach as the model degree goes from the more generic conceptual model over the mathematical mode to the specific computational model. A systematic adaption of the method and the overview of the approach is given in Figure 3.1. The approach was chosen due to explicit integration of physical testing in the modeling activities in the validation and is laid out according to [ASME06].

The modeling process starts with the selection of the reality of interest, which was described in Chapter 2.2 in this thesis. Suitable requirements for thermal models in metal cutting and sufficient temperature magnitudes were evaluated. The conceptual model for chip formation for this thesis can mainly be described with the Oxley Model.

However, this is only due to simplification reasons, also more complex geometries e.g. cutting edge radius will be considered in this thesis. In terms of thermal conceptual models, an approach using distinct line heat sources will be used.

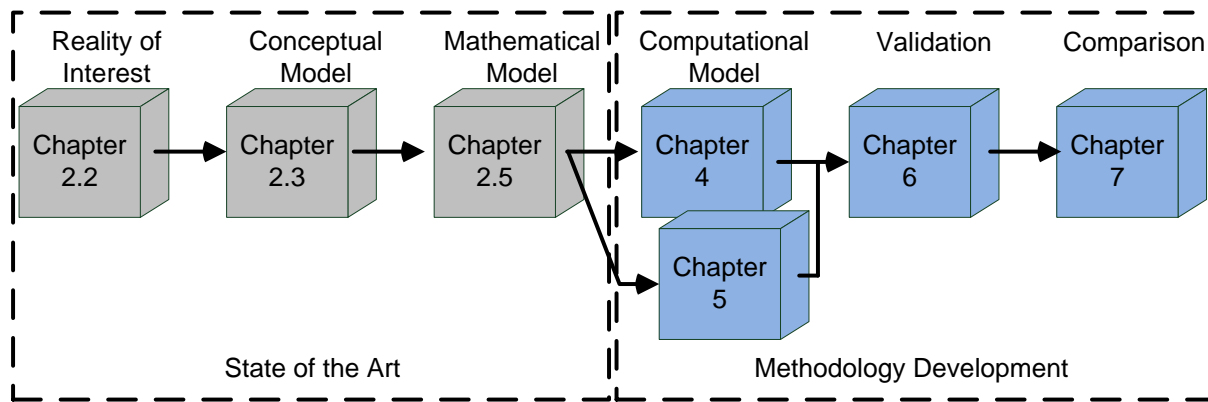


**Figure 3.1:** Structure of the Thesis

#### *Struktur der Arbeit*

After the abstraction to the conceptual model described in Chapter 2.3, a mathematical model can be formulated. The mathematical model used for this thesis was derived in Chapter 2.4 and is represented by Fourier's Law, the two-dimensional partial differential equation and the appropriate thermal boundary conditions in Chapter 2.5.1. The use of correct thermal boundary conditions is of major importance for the modeling activities.

As stated in the objective, the main focus of the work is the development of methodologies for the use of potential theory. To attain first indications on confirmation or falsification of the research hypothesis, Chapter 4 provides a simple modeling approach based on the elementary solutions of potential theory. This chapter addresses mainly the first research question. The derived model and the preliminary calculations can be regarded as what was termed feasibility in the research hypothesis.

These recommendations are subsequently considered in Chapter 5 which describes the development of a more generic model for temperature and heat distribution in metal cutting. A systematic approach called Panel Theory is applied. This theory can be considered as enhancement of the elementary solutions approach using discretization of the cutting kinematics.

Chapter 6 describes the calibration and validation experiments, which were designed on the basis of the conceptual model. The experiments are conducted on two different machine tools in order to provide sufficient empirical data to make the validation independent on distinct hardware disturbances. One vital part of the experiment is the applied measurement method which is also described in this chapter. Both, the first and the second research question are addressed by this chapter.

In Chapter 7 the derived models are compared to other modeling approaches, i. e FE simulation and existing analytical model results. Advantages and disadvantages of the two approaches developed in this work are discussed.

## 4 Elementary Solutions Approach

### *Ansatz mit Elementarfunktionen*

For the derivation of analytical computational models, solutions for the PDE of heat conduction are necessary. The potential theory provides a special class of complex functions which fulfill this criteria. This chapter describes a simple approach using the elementary solutions of potential theory. For this approach, initially, the complex heat and temperature function is introduced. Based on this definition a generic methodology for derivation of the function for thermal modeling in metal cutting is described. An application of the methodology, featured by the steps superposition, parameter study, calibration and correlation, is provided for representative metal cutting cases.

### 4.1 Complex Temperature and Heat Flow Field Function

#### *Komplexe Temperatur- und Wärmestromfeld Funktion*

Complex potential functions provide two scalar fields running orthogonal to each other. Furthermore, the partial derivatives in  $x$  and  $y$  direction yield a characteristic vector field. For the application of potential theory for thermal modeling in metal cutting, the scalar fields and the vector field need to be defined in terms of their physical meaning.

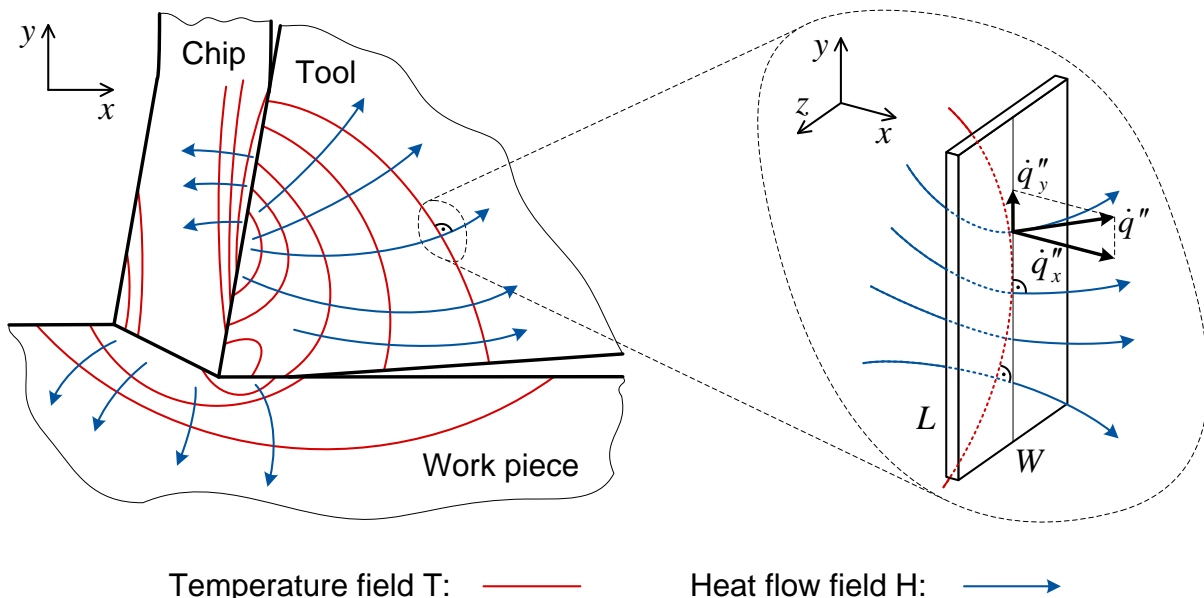


**Figure 4.1:** Heat Flow Field, Heat Flow and Temperature Field  
*Wärmestrom, Wärmestrom- und Temperaturfeld*

For thermal modeling, the two scalar fields can be defined as temperature and heat flow field. The temperature field  $T(x,y)$  yields the distribution of the temperature at each location of  $x$  and  $y$  and features isothermal lines. An orthogonal scalar field to the temperature field firstly seems to have no physical meaning. Taking into account FOURIER'S Law however shows that a gradient field according to the CAUCHY-

RIEMANN condition can be interpreted as heat flow field. This field  $H(x, y)$  shows the direction of the heat flow at each location of  $x$  and  $y$ . Based on that, the complex function for thermal modeling can be formulated as:

$$F(z) = T(x, y) + i \cdot H(x, y). \quad (4.1)$$

Both fields are sketched on the left hand side of Figure 4.1 for a simplified cutting operation. The components chip, tool and work piece are sketched as separate bodies with characteristic temperature field and an orthogonal heat flow field. The latter field is marked with an arrow. Considering the heat conductivity  $\lambda$  of the appropriate material, i.e. tool or work piece material, the heat flux can be calculated:

$$\dot{q}_x'' = -\lambda \frac{\partial T(x, y)}{\partial x} = -\lambda \frac{\partial W(x, y)}{\partial y}, \quad \dot{q}_y'' = -\lambda \frac{\partial T(x, y)}{\partial y} = \lambda \frac{\partial W(x, y)}{\partial x}, \quad (4.2)$$

where  $\dot{q}_x$  and  $\dot{q}_y$  are the respective components in  $x$  and  $y$  direction of the heat flux vector  $\dot{q}$ . The amount of heat  $Q$  flowing through a freely chosen surface  $A$  within the time  $\Delta t$  can subsequently be determined using the expression:

$$Q = \Delta t \cdot \iint_A (\vec{\dot{q}}'' \cdot \vec{n}) \cdot dA. \quad (4.3)$$

Equation 4.3 is usable for quantification of heat through complex surface shapes in general. For metal cutting applications rather simple shapes are of interest. Considering the two-dimensional approach the area can be represented by a rectangle with length  $l$  in  $y$  direction and with  $w$  in  $z$  direction. Applying Equation 4.3 for this case yields:

$$Q = \Delta t \cdot \int_{y=0}^l \int_{z=0}^w \begin{pmatrix} \dot{q}_x'' \\ \dot{q}_y'' \end{pmatrix} \cdot \begin{pmatrix} 1 \\ 0 \end{pmatrix} \cdot dA = \Delta t \cdot \int_{y=0}^l \int_{z=0}^w \dot{q}_x'' \cdot dy dz = w \cdot \Delta t \cdot \int_{y=0}^l \dot{q}_x'' \cdot dy. \quad (4.4)$$

Using Equation 4.4 can be used to calculate the heat flow and amount of heat for particular areas in metal cutting like chip-tool interface, clearance face or shear zone. For rectangular surfaces which are not parallel to the  $y$ - $z$  plane, the respective angle has to be considered.

As for all physical models using potential theory, the interpretation of the two scalar fields can be chosen freely. The assignment of the temperature field to the real-valued part of Equation 4.1 is based on the knowledge of the elementary solutions and their characteristic scalar fields. However, choosing the reverse approach, i.e. assigning the temperature field to the imaginary part of 4.1 would also be feasible. As a consequence from the CAUCHY-RIEMANN Condition, the heat flux can also be calculated with both fields, compare Equation 4.2.

The analytical computation of the heat flow field and the heat flux is one of the major advantages of the potential theory modeling, because the existence of an orthogonal field is ensured. Other modeling approaches do not necessarily yield such a field, hence the heat flux needs to be determined empirical and iterative, e.g. inverse approach for heat flux determination.

## 4.2 Methodology for Derivation of Complex Functions for Cutting

*Methodik zur Herleitung von komplexen Funktionen für die Zerspanung*

The approach using elementary functions for the derivation of complex potential function was widely used in other engineering fields. Depending on the reality of interest, different approaches for the use of the elementary functions are suitable. For thermal modeling in metal cutting, a generic method was developed and is presented in Figure 4.2.

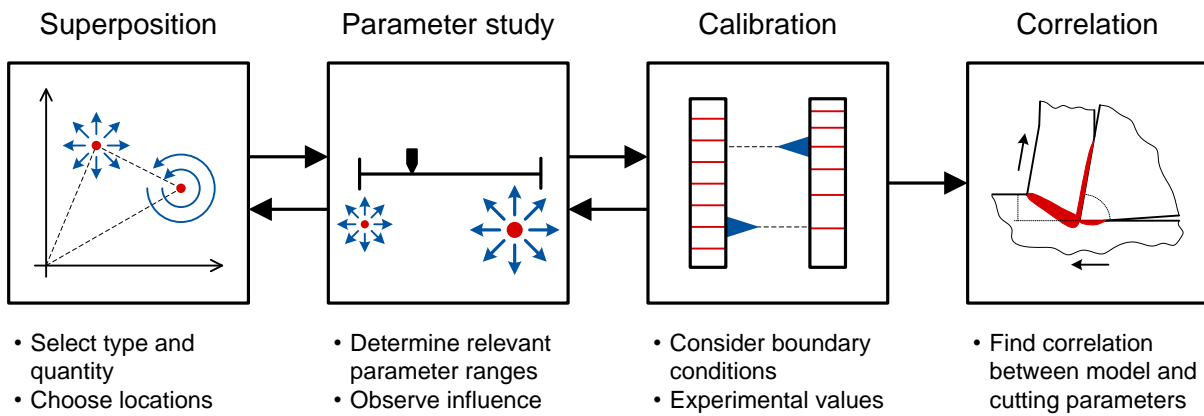


**Figure 4.2:** Methodology for Elementary Solution Approach

*Methodik für Elementarfunktionen Ansatz*

The methodology follows a step-by-step procedure with a strong iterative character, including:

- superposition of elementary functions,
- parameter study,
- calibration of model parameters,
- correlation to cutting parameters.

The fundamental of the methodology relates to the principle of superposition, i.e. if  $F_1(z)$  and  $F_2(z)$  are solutions of the PDE of heat conduction, the summation of both functions is also a solution. Concretely for the model derivation, the first step is to select the type and the quantity of the elementary solutions:

$$F(z) = F_1(z - z_1) + F_2(z - z_2) + \dots = \sum_n F_n(z - z_n). \quad (4.5)$$

In Equation 4.5 e.g.  $F_1$  could be the source solution and  $F_2$  the vortex solution as sketched in Figure 4.2. The complex temperature and heat function  $F(z)$  in general can consist of numerous elementary solutions,  $n$  indicates the quantity of these solutions. Taking into account the physical interpretations of the elementary functions gives a suggestion for the selection of the type, e.g. source solution for a simple concentric distribution of isotherms. For each solution, the location in the  $x$ - $y$  space has to be chosen subsequently. The locations are indicated by the complex dislocation parameter  $z_n$ . Mainly, the locations of each solution relative to each other have signif-

icant influence on the resulting temperature field. A particular feature of the location's choice is the generation of adiabatic boundaries in the temperature field. Adiabatic boundaries can be preset by choosing symmetrical distribution of the selected elementary functions. The symmetry axis between the elementary solutions forms the adiabatic boundary in the temperature field. This principle of symmetry was also used from KOMANDURI AND HOU, applying so-called image line heat sources to generate the adiabatic boundaries of the subsystem chip, tool and work piece.

Additionally to type, quantity and relative location, each elementary solution owns characteristic parameters. For the source solution e.g. the source strength is such a characteristic parameter. Considering the elementary solution parameters  $a$ , Equation 4.5 is extended to:

$$F(z) = F_1(z - z_1, a_{11}, a_{21}) + F_2(z - z_2, a_{12}, a_{22}) + \dots = \sum_n F_n(z - z_n, a_{1n}, a_{2n}) \quad (4.6)$$

All elementary solution have either one parameter or two parameters. For example, the indication  $a_{2i}$  means the first parameter of solution number  $i$ . There is not an elementary solution with more than two parameters.

The second step of the methodology is the study of both parameter sets: dislocation parameters and elementary solution parameters. The aim of this parameter study is the determination of physical relevant numerical value ranges of the parameters. It is well-known that numerical value ranges of the solution parameters have significant influence on the resulting scalar fields. The corner flow solution e.g. can be interpreted as fluid flow around a corner as expected. The shape of this corner is dependent on the solution parameter  $n$ . For  $n \geq 2$  the solution yields a flow around a sharp angle. For values between  $2 > n > 1$  a flow around a concave corner can be observed, values between  $1 > n > 0.5$  however yield a convex corner flow. Functions like Equation 4.6, which were generated from superposition, are dependent on a larger number of solution parameters, hence the parameter study becomes more complex. Only limited predictions about the influence of the well-known parameter ranges from the elementary solution without superposition are possible, e.g. the parallel solution is always connected to the cause of the scalar field like inflow velocity in fluid mechanics. For application in metal cutting, parameter ranges have to be determined with the help of the temperature field function.

At this step of the methodology, there is not a need for detailed measurement of temperature fields in metal cutting. Instead, the process for the parameter study is elimination of parameter ranges yielding temperature fields which are not relevant for metal cutting. Further evaluation is possible from experience and the State of the Art. The parameter study is similar to an experiment. Different combinations of parameter values have to be evaluated. While testing the parameter values, initial conclusions for influences on the temperature field can be observed. This gives valuable indications for the next step of calibration. The steps superposition and parameters study have iterative character. If the parameter study yields not any relevant temperature

field, another combination of types of the elementary functions or another relative dislocation of the functions needs to be chosen.

After studying the solution parameters, suitable numerical value ranges are available. However, the distinct values for the parameters can still be in a wide valid range. The third step of the modeling approach therefore, is the calibration of the model parameters. In the following, the expression model parameters is meant as the combination of both, dislocation parameters and elementary solution parameters. An overview of the nomenclature of parameters used for the modeling method is given in Table 4.1.

**Table 4.1:** Overview of Parameters

*Übersicht Parameter*

model parameters		cutting conditions	
dislocation parameters	elementary solution parameters	cutting parameters	material parameters
$z_n = x_n + i \cdot y_n$	$a_{1n}, a_{2n}$	$v_c, f, a_p, \dots$	$\lambda, \dots$

The calibration of the model parameters has to be conducted individually for each set of cutting conditions, i.e. set of cutting speed, feed, and further influences like work piece material and tool material. Initially, adiabatic boundaries in the resulting temperature field need to be selected. In general, any arbitrary isothermal line fulfills the requirements of an adiabatic boundary. This is due to the definition of the two scalar fields resulting from the complex potential function: temperature and heat flow field run orthogonal to each other. Consequently, the temperature gradient in normal direction on the isotherms vanishes, which yields the definition of an adiabatic boundary.

Important adiabatic boundaries for metal cutting are rake face clearance face of the tool, chip backside, as well as uncut and cut work piece surface. It is not ensured that suitable isothermal lines exist in the resulting temperature field, unless adiabatic boundaries were not preset by the principle of symmetry. In case not any suitable adiabatic boundary can be identified or generated by calibration of the model parameters, another combination of elementary function or localization need to be considered. Again the iterative character of the elementary solution approach becomes obvious.

When suitable adiabatic boundaries are identified, the temperature field is calibrated against absolute temperature values and behavior of the isotherms. Therefore, measured temperature fields or temperature values at certain locations in chip, tool or work piece are necessary. In general, the model parameters have a combined and interacting influence on the resulting temperature field. However, it can be assumed that the dislocation parameters have a stronger effect on the shape of the isotherms and that the solution parameters are responsible for the temperature magnitudes.

As the final step of the methodology, a correlation between model parameters and cutting parameters has to be conducted. This step is the actual objective of the modeling activity and requires the most experimental efforts. Purpose of the correlation is to replace the model parameters by the respective cutting conditions parameter for the temperature function  $T$ :

$$T(x_n, y_n, a_{1n}, a_{2n}) \rightarrow T(v_c, f, a_p, \lambda, \dots) \quad (4.7)$$

For the replacement, the calibration of the model parameters has to be conducted for different set of cutting parameters and hence different measured temperature fields. A systematic study of the influence of the model parameters can be conducted if experimental test with variation of only one cutting parameter are chosen, e.g. influence of cutting speed on the temperature field. The calibration for each set of cutting conditions yield a set of numerical values for the model parameters.

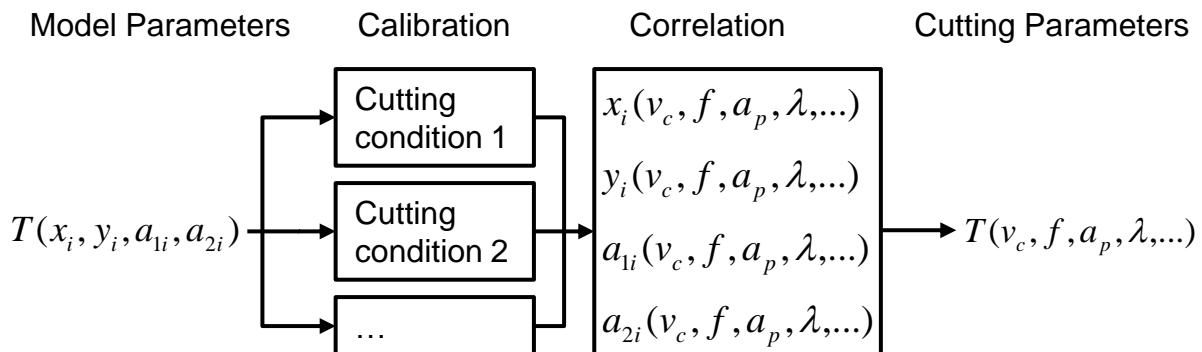


**Figure 4.3:** Correlation of model parameters and cutting parameters

*Korrelation von Modell- und Schnittparametern*

These sets can be used to find correlations for each model parameter. Replacing the model parameters by the cutting parameters in the complex potential function leads to the final computational model ready for later validation. The principal correlation procedure is summarized in Figure 4.3. In terms of complexity, the correlation of model parameters and cutting parameters for complete temperature fields in  $x$  and  $y$  direction can reach a significant number of sufficient correlations. If only characteristic values for the description of the thermal behavior are sufficient, the correlation task can be simplified. Distinct values for  $x$  and  $y$  or predefined lines or areas, e.g. in the tool or at the clearance face, can be chosen and a specific correlation with minor effort can be conducted. If a complete correlation is needed, also a full factorial parameters study needs to be conducted. This would significantly increase the modeling efforts.

The developed methodology for the elementary solutions approach was presented for general use in metal cutting applications. In the following, the steps superposition, parameter study, calibration and correlation are presented for an exemplary case. In this case, the derivation of a complex potential model for the temperature field of an orthogonal cutting operation is described.

### 4.2.1 Superposition of Elementary Functions

#### *Superposition der Elementarfunktionen*

The characteristic scalar fields of the elementary solutions allow a physical interpretation and hence suggest an estimation for the influence in superposition. An overview is given in Table 4.2.

The parallel solution e.g. yields straight lines of the scalar field, directed in a defined direction. A distortion of an existing field in this direction can be caused by using this solution. For applications with movement, this solution is connected to a relative motion in the field. In metal cutting, the relative motion can be interpreted as cutting velocity. The source solution yields concentric circular lines. As the specific name of this solution implies, a correlation to the relevant heat sources in metal cutting can be suggested.

**Table 4.2:** Influence of Elementary Solutions on the Temperature Field

*Einfluss der Elementarfunktionen auf das Temperaturfeld*

elementary solution	complex function $F(z)$	solution parameters $a$	geometrical influence	suggestion for cutting
parallel	$A \cdot z \cdot e^{i\alpha}$	$a_1 = A$ $a_2 = \alpha$	straight lines in defined direction	influence of cutting velocity
source/sink	$\frac{E}{2\pi} \cdot \ln(z)$	$a_1 = E$	circular, concentric lines	heat sources
vortex	$-i \frac{\Gamma}{2\pi} \cdot \ln(z)$	$a_1 = \Gamma$	radial lines	-
corner	$\frac{c}{n} \cdot z^n$	$a_1 = c$ $a_2 = n$	curved lines	cutting edge
dipole	$\frac{M}{2\pi} \cdot \frac{(1+i)}{z}$	$a_1 = M$	circular lines	-

Regarding the vortex solution yields a similar field to the source solution, however the real-valued function and the imaginary function are oppositely changed. The vortex solution plays a major role for modeling of fluid flow, connected to a physical correlation to occurring forces. i.e. lift and drag forces. In metal cutting, such an interpretation is not possible a priori. However, the vortex solution yields radial lines origination in one point, which could be of interest for metal cutting applications.

A way for generating curved lines in the scalar field is given by the corner solution. Again, the specific name implies the original physical interpretation, this solution can be used to model fluid flow in a corner. For metal cutting obviously the cutting edge

represents such a corner in the scalar field, hence the application of the corner solution seems viable.

Similar to the source solution, the dipole solution yields circular lines in the scalar field. This circular lines, however, are not concentric but can be rather interpreted as circles with different radii with one common tangential line. There is not an a priori suggestion for the dipole solution applied for metal cutting. In general, the suggested influences can not be easily distinguished in the resulting temperature function. Depending on the parameterization of the solutions, certain influences are stronger than others or can be neglected. The suggestions, however, allow a more systematic approach for the superposition of the elementary solutions.

From the suggestions, summarized in Table 4.2, the parallel solution, the source solution and the corner solution seem to have most significance for metal cutting applications. When combining the functions in terms of superposition, however, the influence of each single function need not necessarily be visible. The significance of the influence is also dependent from the choice of the solution parameters.

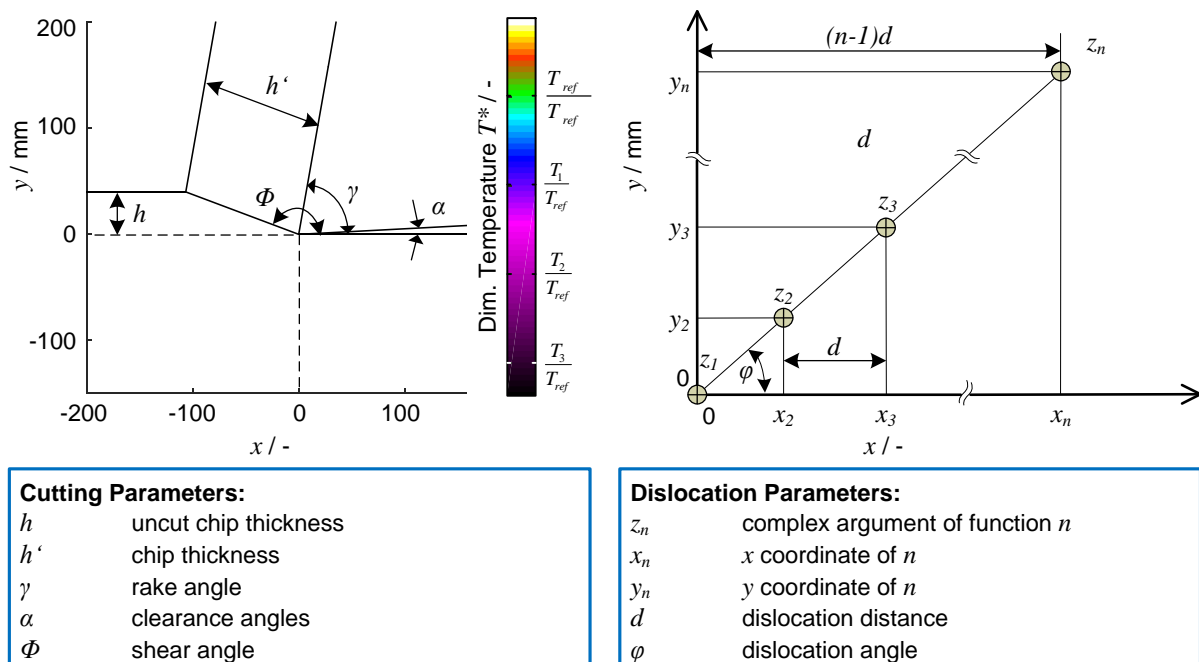


**Figure 4.4:** Cutting Kinematics and Dislocation Parameters

*Kinematische Eingriffsbedingung und Verschiebungsparameter*

For the selection of suitable elementary solutions for metal cutting, a freely chosen, simple shape of the cutting kinematics is drawn into the  $x$ - $y$  space, compare left-hand side of Figure 4.4. Referring to the earlier presented OXLEY Model, the shape represents an ideal assumption of the chip, tool, cut and uncut work piece and shear zone area. An ideal sharp cutting edge and ideal chip formation is assumed. However, the area between cut work piece and tool (clearance face) and the area between uncut work piece and tool (chip backside) are not relevant for the temperature distribution and can be neglected, even though isotherms will be predicted in this area by the modeling approach. The origin of the coordinate system is chosen at the root point

between chip, tool and work piece. For the definition of the cutting kinematics, the following parameters need to be defined:

- Cutting depth  $a_p$ ,
- Chip thickness  $t_c$ ,
- Rake angle  $\gamma$ ,
- Clearance angle  $\alpha$ , and
- Shear angle  $\Phi$ .

More accurate shapes for different cutting parameters can be applied. For the superposition and choice of suitable elementary solutions, the idealized shape is sufficient, as only the principle feasibility of the method should be investigated in this chapter. With the defined coordinate system and the cutting kinematics shape, the elementary solutions can be positioned in the  $x$ - $y$  space. For the positioning the characteristic boundaries given by the cutting kinematics shape can be considered.

For the scalar field, numeric values of the solution parameters have to be chosen. As the temperature values are defined by later calibration, the absolute values of the temperature scale for the parameter study is not relevant. Most significant is the relative values of the distinct parameters. For the analysis therefore, the dimensionless temperature  $T^*$  is defined as:

$$T^* = 100 - \frac{T}{T_{ref}} \cdot 100, \quad (4.8)$$

Where  $T$  is the value which is given from the real valued function and  $T_{ref}$  is a freely chosen relative value. For the analysis during the parameter study,  $T_{ref}$  was chosen equal to the maximum value occurring, i. e. all fields have a maximum value of 100. The negative sign in Equation 4.8 is considered due to the normally increasing values of the real-valued function. In principle, the sign does not change the shape or relative slope of the isotherms, however was chosen because of a more comprehensive presentation of the temperature plots.

For the location of the solutions, distributions in the  $x$ - $y$  space need to be chosen. For equally distributed positioning of the elementary solutions, as shown on the right-hand side of Figure 4.4, the dislocation parameters  $z_n$  can be formulated with the expression:

$$z_n = x_n + i \cdot y_n = x_n[1 + i \cdot \tan(\varphi)] = d(n-1)[1 + i \cdot \tan(\varphi)] . \quad (4.9)$$

In equation 4.9, the equal positioning of the  $n$  solutions is characterized by the distance  $d$  and the angle  $\varphi$ . The line on which the solutions are positioned can be a characteristic zone of metal cutting, i.e. contact zone, shear zone or clearance face. However, the dislocations of the solutions need not necessarily be chosen equal. In this thesis only equal distributions are chosen due to simplification reasons.

Different choices for positioning of source solutions are shown in Figure 4.5. Only the real-valued scalar function, i.e. the isothermal field is shown for each configuration. On the upper left-hand side, the simple positioning of one source solution in the origin is shown.

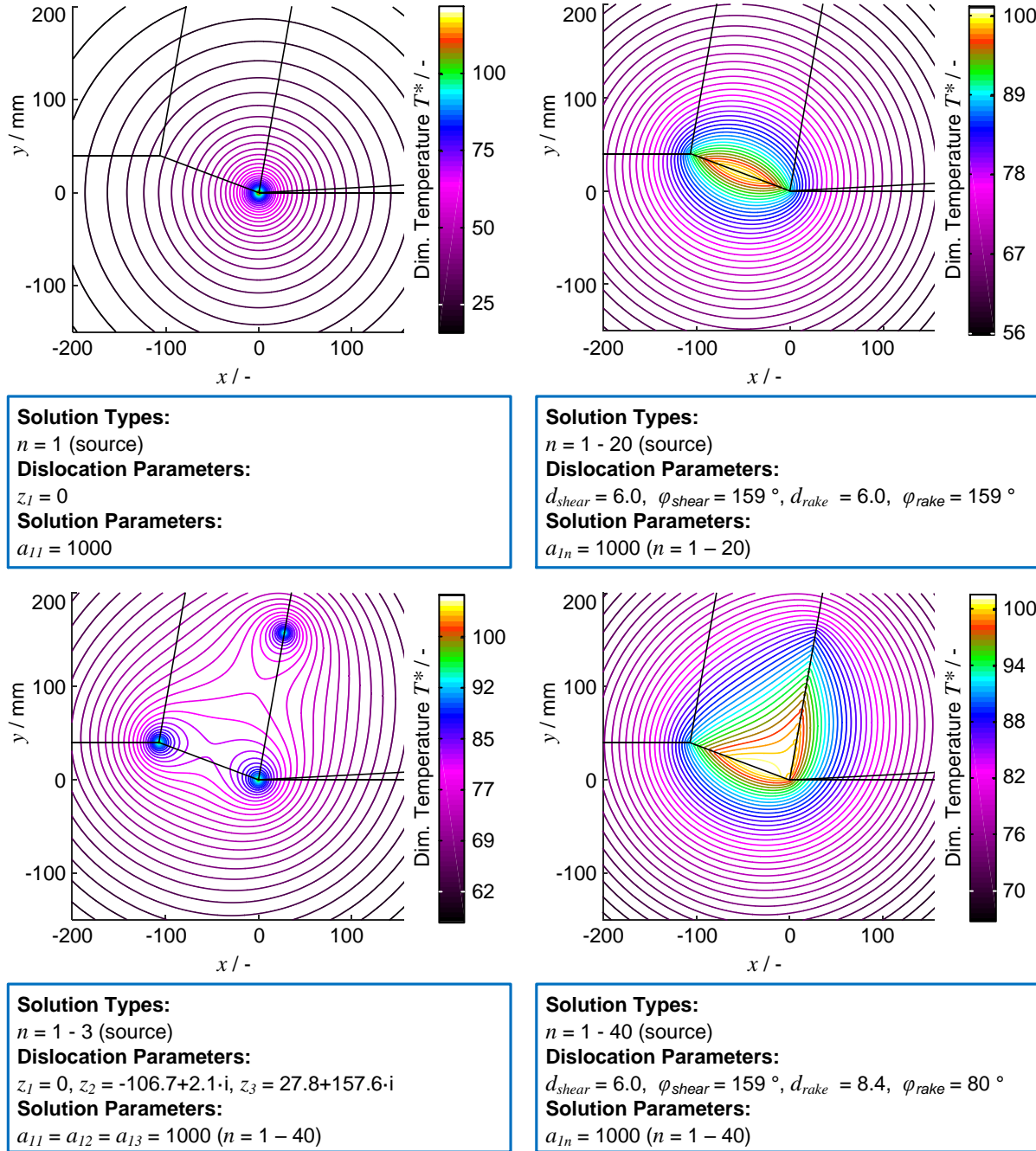


**Figure 4.5:** Superposition of Source Solutions

*Superpositionierung von Quellenlösungen*

For the only solution parameter a value of  $a_{11} = 1000$  was chosen freely. The characteristic concentric circular lines can be observed in the isothermal field. Both, dislocation and solution parameters are chosen without units. Choosing units has not any relevance yet for the resulting scalar field distribution, however the relative numerical values have significant influence. For ease of discussion, the numerical values of the

isothermal fields are not provided in the figure, as they are also not relevant for the superposition task.

On the upper right-hand side of the figure, the influence of equally distributed source solutions along the shear zone is shown. As shown in the figure, the further positioning of source solutions resulted in an elliptic distribution of the isotherms in the vicinity of the sources. In the regions with a greater distance to the sources, the influence vanishes. The complex function is given by the expression:

$$\begin{aligned} F(z) &= \sum_{n=1}^{20} F_n(z, z_n) = \sum_{n=1}^{20} \frac{a_{1n}}{2\pi} \ln(z - z_n) \\ &= 159.2 \cdot \sum_{n=1}^{20} \ln[z - 6.0 \cdot (n-1) \cdot (1 - 0.38 \cdot i)]. \end{aligned} \quad (4.10)$$

The numerical values result from Equation 4.9 using  $d = 6.0$  and  $\varphi = 159^\circ$ . A case where the sources are not placed on a line is shown on the lower left-hand side of the figure. One source was placed at the root point, one source was placed at chip backside on the shear zone and one on the contact zone between chip and tool. For all sources the same value for the solution parameter  $a_{11} = a_{12} = a_{13} = 1000$  was chosen. Regarding the scalar field, isotherms which connect the distinct sources occur. These isotherms and those in the vicinity of the sources show a complex shape. Similar to the case of two sources, this effect vanishes to the outer regions of the field. The complex function of this superposition case is given by:

$$\begin{aligned} F(z) &= \sum_{n=1}^4 F_n(z, z_n) = \sum_{n=1}^4 \frac{a_{1n}}{2\pi} \ln(z - z_n) \\ &= 159.2 \cdot [\ln(z) + \ln(z - z_3) + \ln(z - z_4)]. \end{aligned} \quad (4.11)$$

The dislocation parameters were chosen  $z_2 = -106.7 + 2.1 \cdot i$  and  $z_3 = 27.8 + 157.6 \cdot i$ , the dislocation parameters vanish for the source located at the origin. A generalized case for this approach is shown in the lower right-hand side of the figure. Therefore, twenty sources were placed on the shear zone and on the contact zone between chip and tool. For all sources independent from their location the solution parameter was chosen  $a_{1n} = 1000$  ( $n = 1 \dots 40$ ). The greater number of sources yielded again distinct isotherms connecting each two sources on both lines, however the effect of complicated shapes did not occur. The complex function of this superposition case is:

$$\begin{aligned} F(z) &= \sum_{n=1}^{40} F_n(z, z_n) = \sum_{n=1}^{40} \frac{a_{1n}}{2\pi} \ln(z - z_n) \\ &= 159.2 \cdot \left\{ \sum_{n=1}^{20} \ln[z - 6.0(n-1)(1 - 0.38 \cdot i)] + \sum_{n=1}^{20} \ln[z - 8.4(n-20)(1 + 0.7 \cdot i)] \right\} \end{aligned} \quad (4.12)$$

The first summation sign locates the sources on the shear zone and the second summation those on the contact zone. For the numerical values again Equation 4.9 was applied, where for the shear zone  $d_{shear} = 6.0$ ,  $\varphi_{shear} = 159^\circ$  and for the contact zone (rake face of the tool)  $d_{rake} = 8.4$ ,  $\varphi_{rake} = 35^\circ$  were used. The approach using only sources on the characteristic regions already yields suitable fields for thermal modeling in metal cutting.

In Figure 4.6, further elementary solutions were taking into account additionally, i.e. the parallel solution, the corner solution, the dipole solution and the vortex solution. For the sources, the same configuration of dislocation parameters, stated in Equation 4.12, was applied.

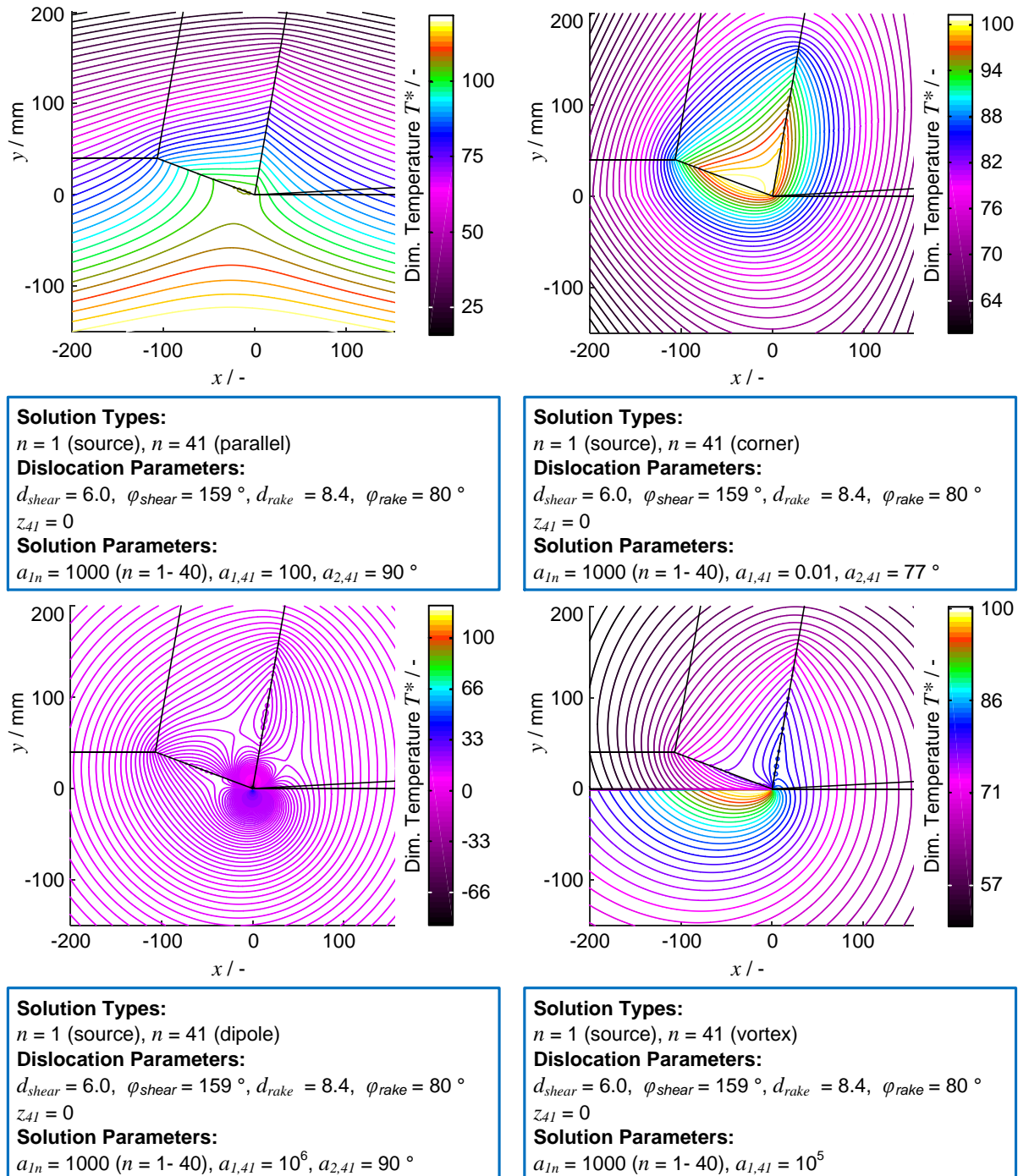


**Figure 4.6:** Superposition of Sources and further Elementary Solutions

*Superpositionierung von Quellen und weiteren Elementarfunktionen*

On the upper left-hand side of the figure, the parallel solution was used in vertical direction, i.e. the solution parameter  $a_{2,41} = 90^\circ$ . This solution parameter is connected to the angle of the isotherms. The second solution parameter was freely chosen to a value of  $a_{1,41} = 100$  and is suggested to be connected to the cutting velocity. As

shown in the figure, the parallel solution yielded a strong influence on the field. The connecting isotherms between distinct sources are still occurring, however the whole field is bended into the direction of the parallel solution. Furthermore, the concentric characteristic of the source solutions is vanishing also in the regions far away from the sources. The complex function can be expressed as:

$$\begin{aligned} F(z) &= \sum_{n=1}^{41} F_n(z, z_n) = a_{1,41} \cdot z \cdot e^{ia_{2,41}} + \sum_{n=1}^{40} \frac{a_{1n}}{2\pi} \ln(z - z_n) \\ &= 100 \cdot z \cdot e^{1.57i} + \sum_{n=1}^{40} \frac{a_{1n}}{2\pi} \ln(z - z_n). \end{aligned} \quad (4.13)$$

For the summation the expression in Equation 4.12 can be used. A superposition of source solutions and the corner solution is shown on the upper right-hand side of the figure. The corner solution is suggested to be connected to the cutting edge, as mentioned before. For this solution, the parameter  $a_{2,41} = 77^\circ$  is significant. Depending on the numerical value of the parameter, a convex or concave corner is defined. In this case, a convex corner was chosen. As shown in the figure, the effect on the temperature field by superposition with the source solutions was not as significant as the superposition of the parallel solution. However, the regions in a greater distance to the sources yielded a different characteristic, i.e. the concentric isotherms were becoming more elliptic. Using the corner solution in the origin, i.e.  $z_{41} = 0$  and choosing  $a_{1,41} = 0.01$  the appropriate complex function is given by:

$$\begin{aligned} F(z) &= \sum_{n=1}^{41} F_n(z, z_n) = \frac{a_{1,41}}{a_{2,41}} \cdot z^{a_{2,41}} + \sum_{n=1}^{40} \frac{a_{1n}}{2\pi} \ln(z - z_n) \\ &= 7.5 \cdot 10^{-3} \cdot z^{1.34} + \sum_{n=1}^{40} \frac{a_{1n}}{2\pi} \ln(z - z_n). \end{aligned} \quad (4.14)$$

The expression for the summation can be again used from Equation 4.12 using  $a_{1n} = 1000$  for  $n = 1 \dots 40$ . Considering the suggestions given in Table 4.2 the dipole and vortex solution did not allow any a priori suggestion for their use in thermal modeling of metal cutting. This assessment was due to the scalar fields of the single solutions, which originally were used in other engineering fields.. The complex function is given by the expression:

$$\begin{aligned} F(z) &= \sum_{n=1}^{41} F_n(z, z_n) = \frac{a_{1,41}}{2\pi} \cdot \frac{(1+i)}{z} + \sum_{n=1}^{40} \frac{a_{1n}}{2\pi} \ln(z - z_n) \\ &= 159.2 \cdot 10^3 \frac{(1+i)}{z} + \sum_{n=1}^{40} \frac{a_{1n}}{2\pi} \ln(z - z_n). \end{aligned} \quad (4.15)$$

On the lower left-hand side of the figure, the superposition of the source solutions and a dipole solution is shown. Thereby, dipole solution was placed in the origin  $z_{41} = 0$  and the solution parameter  $a_{1,41} = 10^6$ . The expression for the summation sign is given in Equation 4.12. As expected, the dipole solution yielded isotherms with shapes which do not seem to be relevant for metal cutting applications. Particularly the isotherms near the root point yielded a complicated shape. However, the isotherms at the contact zone between chip and tool revealed an interesting characteris-

tic, i.e. a local extremal region is formed in tool and chip. A similar characteristic was observed for turning processes [THAK15] and in general correlates to the wear lands found on cutting inserts [FANG02]. The superposition of the dipole showed, that even if no a priori suggestion for metal cutting can be made, all elementary solution could yield relevant complex functions when used in superposition with other elementary functions. The use of the vortex solution, shown in the lower right-hand side of the figure, yields a characteristic which also leads to suitable fields in metal cutting. The complex function of this superposition is given by:

$$\begin{aligned} F(z) &= \sum_{n=1}^{41} F_n(z, z_n) = -i \cdot \frac{a_{1,41}}{2\pi} \ln(z) + \sum_{n=1}^{40} \frac{a_{1n}}{2\pi} \ln(z - z_n) \\ &= -i \cdot \frac{a_{1,41}}{2\pi} \ln(z) + \sum_{n=1}^{40} \frac{a_{1n}}{2\pi} \ln(z - z_n). \end{aligned} \quad (4.16)$$

The vortex solution was placed in the origin ( $z_{41} = 0$ ) and the parameter was chosen  $a_{1,41} = 10^5$ . The positive sign indicates a vortex directed in mathematical positive direction, i.e. left turning in the figure. As shown in the figure, the effect on the temperature field by superposition with the source solutions yields a distortion of the isotherms, particularly in the chip and in the work piece region near the root point.

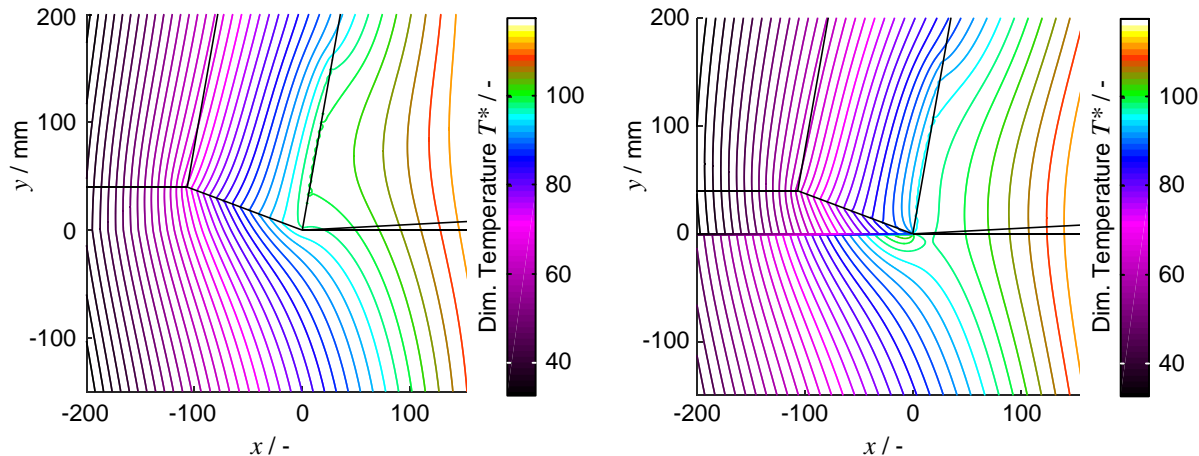
From the superposition of two types of elementary functions the described effects on the temperature distribution field were determined. The distinct functions can be used to modify the field in terms of location of extremal regions, shape of the isotherms and suggested influence of cutting edge and cutting velocity. For general cases it seems viable to take more combinations of solution types into account. On the left-hand side Figure 4.7 the superposition of the source solutions, the parallel and the corner solution is shown. For the complex function the dislocation and solution parameters were defined similar as in Equations 4.12, 4.13 and 4.14:

$$\begin{aligned} F(z) &= \sum_{n=1}^{42} F_n(z, z_n) = a_{1,41} \cdot z \cdot e^{ia_{2,41}} + \frac{a_{1,42}}{a_{2,42}} z^{a_{2,42}} + \sum_{n=1}^{40} \frac{a_{1n}}{2\pi} \ln(z - z_n) \\ &= 100 \cdot z \cdot e^{1.57i} + 75 \cdot z + \sum_{n=1}^{40} \frac{a_{1n}}{2\pi} \ln(z - z_n). \end{aligned} \quad (4.17)$$

The sources were again placed on the shear zone and the rake face. For the parallel solution the parameters were chosen to  $a_{1,41} = 100$  and  $a_{2,41} = 90^\circ$ , for the corner solution to  $a_{1,42} = 0.01$  and  $a_{2,42} = 77^\circ$ . Both solutions were placed in the origin ( $z_{41} = z_{42} = 0$ ).

Plotting of the temperature field yielded the strong influence of the parallel solution. The connections between the sources vanished, however distinct isotherms at the cutting tool region occurred. In regions of a greater distance to the contact zone, the isotherms run almost vertical. The strong influence of the parallel solution becomes even more significant when regarding the relative strength of the solutions. For the parallel solution, the strength parameter was chosen significantly lower than the strengths of the sources.

On the right-hand side of the figure, the superposition of the source solutions, the parallel solutions and the vortex solution is shown. As already seen in the superposition with only the source solutions, the field features distorted shapes, especially in the regions near the chip and the root point.


**Solution Types:**

$n = 1$  (source),  $n = 41$  (parallel),  $n = 42$  (corner)

**Dislocation Parameters:**

$d_{shear} = 6.0$ ,  $\varphi_{shear} = 159^\circ$ ,  $d_{rake} = 8.4$ ,  $\varphi_{rake} = 80^\circ$   
 $z_{41} = 0$ ,  $z_{42} = 0$

**Solution Parameters:**

$a_{1n} = 1000$  ( $n = 1-40$ ),  $a_{1,41} = 100$ ,  $a_{2,41} = 90^\circ$   
 $a_{1,42} = 0.01$ ,  $a_{2,42} = 77^\circ$

**Solution Types:**

$n = 1$  (source),  $n = 41$  (parallel),  $n = 42$  (vortex)

**Dislocation Parameters:**

$d_{shear} = 6.0$ ,  $\varphi_{shear} = 159^\circ$ ,  $d_{rake} = 8.4$ ,  $\varphi_{rake} = 80^\circ$   
 $z_{41} = 0$ ,  $z_{42} = 0$

**Solution Parameters:**

$a_{1n} = 1000$  ( $n = 1-40$ ),  $a_{1,41} = 100$ ,  $a_{2,41} = 90^\circ$   
 $a_{1,42} = 8000$

**Figure 4.7:** Sources and Parallel Solution with Vortex and Corner

*Quellen- und Parallellösung mit Wirbel und Ecke*

Using the same source positions and parameters for the parallel solution the parameters were chosen to  $a_{1,41} = 100$  and  $a_{2,41} = 180^\circ$ , for the vortex solution to  $a_{1,42} = 8000$ .

$$\begin{aligned} F(z) &= \sum_{n=1}^{42} F_n(z, z_n) = a_{1,41} \cdot z \cdot e^{ia_{2,41}} - i \cdot \frac{a_{1,42}}{2\pi} \ln(z) + \sum_{n=1}^{40} \frac{a_{1n}}{2\pi} \ln(z - z_n) \\ &= 100 \cdot z \cdot e^{1.57i} - 1273.3 \cdot i \cdot \ln(z) + \sum_{n=1}^{40} \frac{a_{1n}}{2\pi} \ln(z - z_n). \end{aligned} \quad (4.18)$$

Both solutions were placed in the origin ( $z_{41} = z_{42} = 0$ ). The isotherms run similar to the solution with the corner, the direct connections between the sources vanished again. However, the vortex solution influenced the isothermal field in a different way than the corner solution. For the strength of the vortex influence, the distinct choice of numerical values of the parameters is significant, the value was chosen eight times the strength of the source strengths. In general, further combinations of the elementary solutions are viable. The complexity for the subsequent parameter study and calibration increases with higher number of solution types. The choice of suitable solutions should be adapted to the application. In most cases a application oriented study seems viable. The findings of this subchapter provide a more detailed recommendation for the influence of the distinct elementary functions.

### 4.2.2 Model Parameter Study

#### *Modellparameterstudie*

From the superposition of the elementary functions, a first indication of suitable functions was evident. Solutions like the dipole solution seem to be not suitable. From the physical interpretation of the scalar fields, the source solution in combination with the parallel and corner solution seemed to be favorable. For the following parameter study, the following combinations of elementary solutions were chosen:

- combinations of source solutions on shear zone and rake face,
- additional superposition of corner solution,
- additional superposition of corner and parallel solution.

Other solutions, e.g. the combination of source and vortex solution also yielded sufficient results. However, this thesis focuses on the approach based on source solutions, also for the later described panel methodology. The complexity of possible parameter combinations increases with number of different solutions applied. In order to maintain a feasible and sensible parameter study, a step-by-step procedure was conducted. A summary of the conducted parameters study is shown in Table 4.3.

**Table 4.3:** Overview of the Conducted Parameter Study

*Übersicht der durchgeführten Parameterstudie*

Elementary Solutions	Investigated Parameters
source solutions	<ul style="list-style-type: none"> <li>• Influence of number of source solutions on shear zone and rake face in terms of absolute value and unequal distribution.</li> <li>• Influence of source strengths in terms of absolute values, uniform but unequal distribution on shear zone and rake face and non-uniform distribution.</li> </ul>
sources and corner solution	<ul style="list-style-type: none"> <li>• Influence of the three cases of corner angles in combination with sources on shear zone and rake face.</li> <li>• Influence of the corner strength value.</li> </ul>
sources, corner and parallel solution	<ul style="list-style-type: none"> <li>• Influence of direction of parallel solution in combination with sources and corner.</li> <li>• Influence of strength of parallel solution in combination with sources and corner.</li> </ul>

The study for the parameters mentioned in the table was not conducted full factorial but rather studied isolated, respectively varied with representative values. The main objective of the parameter study was to identify suitable numerical values of the solution and dislocation parameters. Furthermore the study yields initial recommendations for the phenomenological influence of the parameters on the temperature fields.

Based on the initial positioning of sources on the shear zone and rake face, the influence of the number of sources was investigated. The number of sources on rake face and shear zone was equal, furthermore equal strengths were chosen. Exemplary temperature fields are shown in Figure 4.8. On the left-hand side of the figure, two sources were placed on each line, one source was placed on the root point. The resulting temperature field shows the characteristic isotherms connecting the sources in complex shapes. For modeling of temperature fields in metal cutting the chosen number of sources seemed too low.

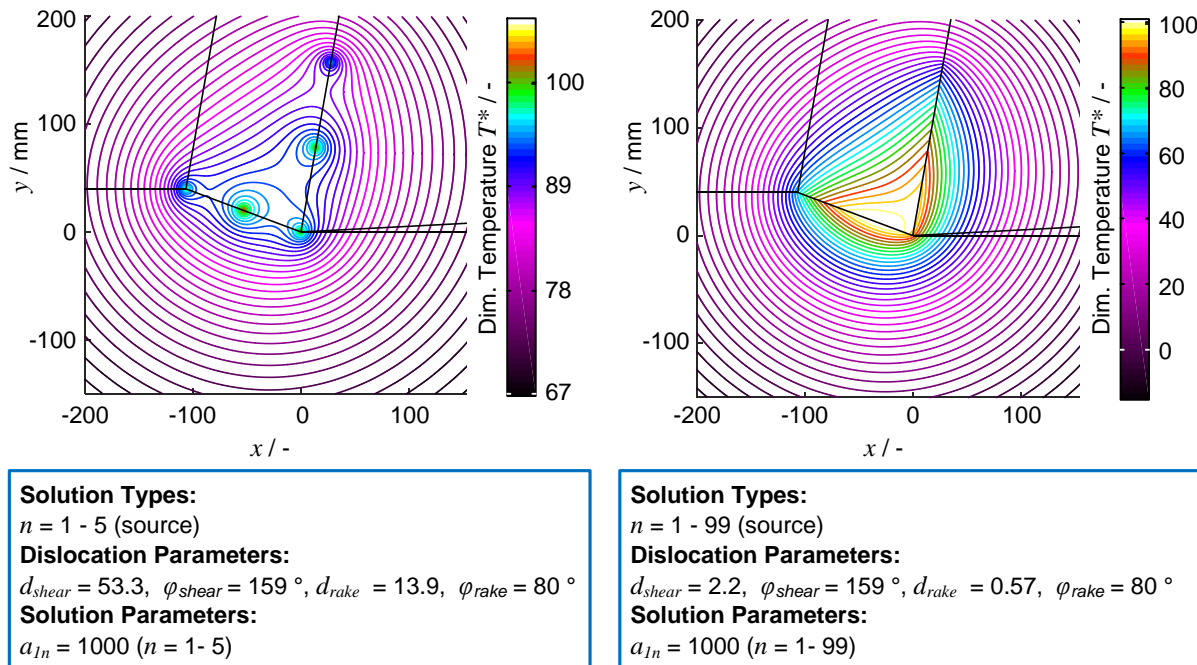


**Figure 4.8:** Influence of the Overall Number of Sources

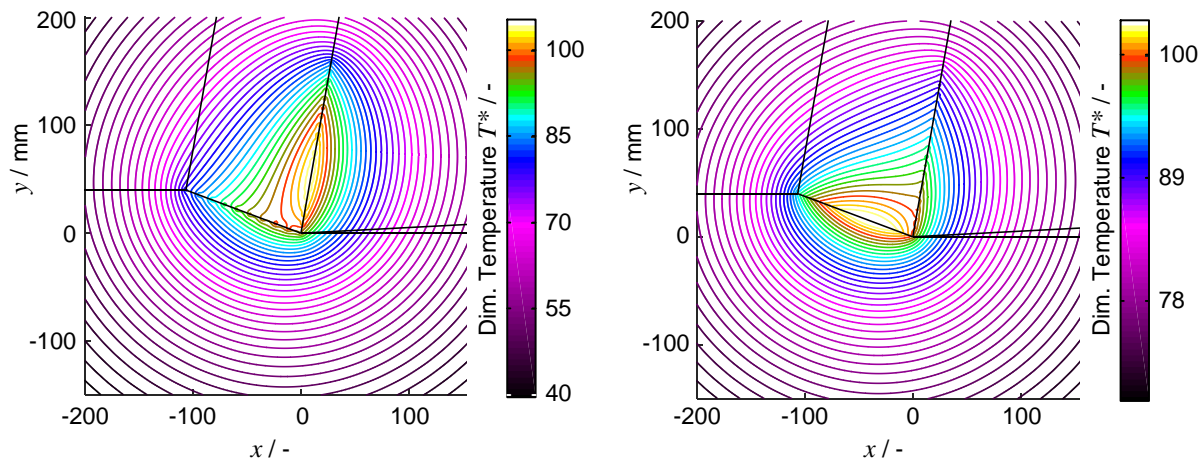
*Einfluss der gesamten Quellenanzahl*

On the right-hand side of the figure, the same equal distribution with overall 99 sources is shown. When comparing these plot against the field resulting from overall 40 sources from the last chapter (compare Figure 4.5), no significant difference was determined. The detailed analysis yielded that a numerical range from  $n = 10$  to 30 is suitable for the generation of thermal fields similar to Figure 4.5. Hence, a number of  $n = 20$  was selected as reference for all parameter studies in the following analysis.

As a next step, the influence of unequally distributed sources on rake face and shear zone was investigated. The source strengths were again chosen equal. The results for two cases are shown in Figure 4.9. On the left-hand side of the figure, the number of sources on the rake face was chosen higher than the number on the shear zone. Overall, 29 sources were place, where 9 source were located on the shear zone and 19 on the rake face. Taking into account the source at the root point, which influences both shear zone and rake face, the ratio of  $r_n$ , defined as number of sources on the rake face  $n_{rake}$  over the number of sources on the shear zone  $n_{shear}$  for the shown case is  $r_n = 2$ .

As can be seen, the higher number of source leads to a shift of the area of maximum temperatures in shape and location, i.e. the area becomes more elliptic and is shifted on the rake face. This effect increases with higher values of  $r_n$ , for values  $r_n > 4$  the maximum area is exclusively on the rake face.

A similar effect can be observed when placing more sources on the shear zone than on the rake face. On the right-hand side of the figure, the plot for a ratio  $r_n = 0.67$ , with 29 sources on the shear zone and 19 sources on the rake face is shown. Again, a shift of the maximum area, in this case to the shear zone, is resulting. For values  $r_n < 0.5$  the maximum area shifted exclusively to the shear zone. Hence, for the ratio of numbers of sources on rake face and shear zone values for  $r_n = 0.5$  to 4 are sufficient to shift the maximum area from shear zone to rake face or vice versa.


**Solution Types:**
 $n = 1 - 29$  (source)

**Dislocation Parameters:**
 $d_{\text{shear}} = 11.9, \varphi_{\text{shear}} = 159^\circ, d_{\text{rake}} = 1.5, \varphi_{\text{rake}} = 80^\circ$ 
**Solution Parameters:**
 $a_{In} = 1000$  ( $n = 1 - 29$ )

**Solution Types:**
 $n = 1 - 49$  (source)

**Dislocation Parameters:**
 $d_{\text{shear}} = 3.7, \varphi_{\text{shear}} = 159^\circ, d_{\text{rake}} = 1.5, \varphi_{\text{rake}} = 80^\circ$ 
**Solution Parameters:**
 $a_{In} = 1000$  ( $n = 1 - 49$ )

**Figure 4.9:** Influence of Unequal Source Distribution on Shear Zone and Rake Face

*Einfluss von ungleicher Quellenverteilung auf Scherzone und Spanfläche*

Additionally to the number of sources, the source strengths can be varied. In Figure 4.10 the influence of unequal source strengths on the temperature plots is summarized. Both plots in the upper half of the figure refer to unequal source strengths referring to rake face and shear zone, but equal strengths for the sources along the rake face and shear zone. The two plots on the lower half show the influence of unequal distribution along the rake face respectively the shear zone. For the analysis, the reference case with 20 sources on the shear zone and 20 sources on the rake face was chosen again.

On the upper left-hand side of the figure, the strengths for the sources on the rake face were chosen twice the value of the sources on the shear zone. The upper right-hand side shows the plot for the opposite case, i.e. twice the value of source strengths on the shear zone. Comparing the influence of the shown cases with the influence of the unequal distribution in Figure 4.9 yields an almost similar effect on

the temperature field and the shapes and location of the maximum temperature area. For the later correlation the parameterization with the source strength is favorable. Using a lower number of sources means lower overall number of parameters and low computational effort.

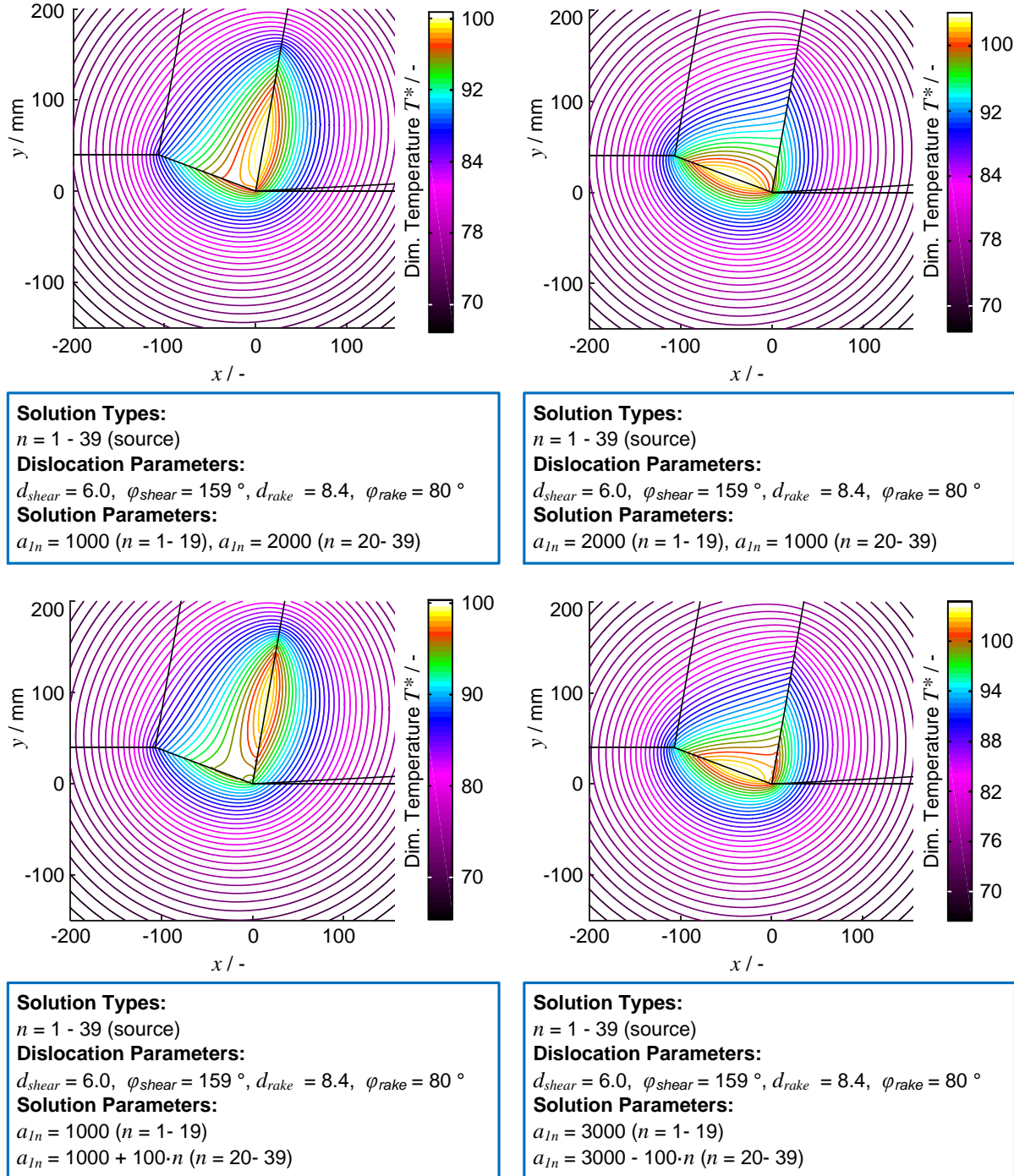


**Figure 4.10:** Influence of Unequal Source Strengths

*Einfluss ungleicher Quellenstärken*

Suitable value ranges for the difference between the source strengths on either shear zone or rake face were found up to 10 times higher. For higher values no significant changes were observed, i.e. similar to the limiting values of unequal number of

sources, the maximum temperature area is either completely on the rake face or the shear zone.

On the lower left-hand side of the figure, a case for unequal strength distribution on the rake face is shown. The values of the strengths thereby are increasing linearly from the root point along the rake face. For the strengths on the shear zone an equal value was chosen. The linear increase of the strengths again resulted in a shift of the maximum temperature area along the rake face, however, in this case the elliptic area shifts along the rake face as a whole. For the cases discussed before, the lower boundary of the elliptic shape maintained in near root point. The distribution of strengths therefore can be used to locate the temperature maximum along the rake face. Suitable values for the linear distribution were found for a difference of three times higher values between the source on the root point and the last source on the rake face. On the lower right-hand side of the figure, the temperature field for decreasing values of the source strengths, again along the rake face is shown. The source at the root point therefore was the one with lowest strength, the distribution was chosen similar to the case with increasing strengths along the rake face. A shift of the temperature maximum area to the shear zone was observed again. However, the shift as a whole was not observed.

Summarized, the superposition using only source solutions can be parameterized by the number of sources, the distribution of the sources on shear zone and rake face and unequal distribution of the source strengths. Similar influences of all these parameters changes were observed. The influence on the temperature field of a corner solution at the root point additionally to the source solutions is summarized in Figure 4.11. In this investigation only the corner parameters were varied, the reference source solution was maintained.

For the corner angle (i.e. solution parameter  $a_2$ , compare Table 4.2) the influence of three distinct cases was investigated. On the upper left-hand side an angle below  $90^\circ$  was chosen. The influence of the corner solution in comparison to the source solutions approach was relatively low. On the upper right-hand side a case for an angle large than  $90^\circ$  was freely chosen.

A choice of such a value for the angle influences the temperature field more significantly. The whole area of maximum temperature were rotated and shifted more to the shear zone, however all parameters were chosen besides the angle were chosen to equal values. Particularly the isotherms in the chip were influenced significantly, i.e. the isotherms run more orthogonal to the rake face. Overall the whole maximum area of temperature yielded a different shape compared to the case where only source solutions were used. On the lower left-hand side an angle above  $180^\circ$  was chosen. The effect on the temperature field in terms of the maximum temperature area seems similar, however, the isotherms in the work piece are influenced more significantly when choosing this case of angle values. The influence of the corner strength (parameter  $a_1$ ) is shown on the lower right-hand side of the figure. Here, the corner strength was chosen higher than in the cases before. Even though the source

strengths are still 1000 times higher than the corner strength, only the characteristics of the corner could be observed in the figure. This shows the sensitivity of the corner strength parameter.

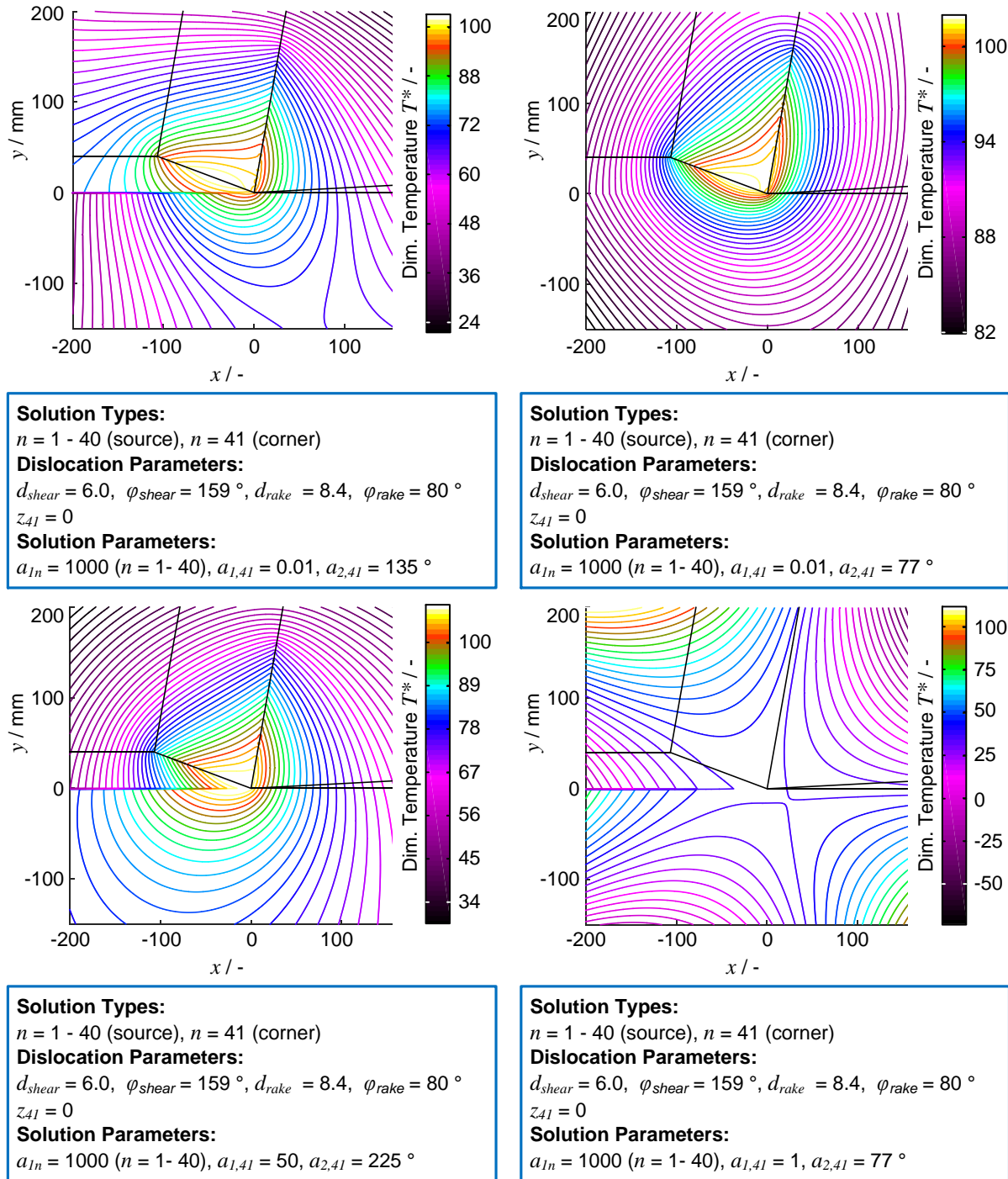


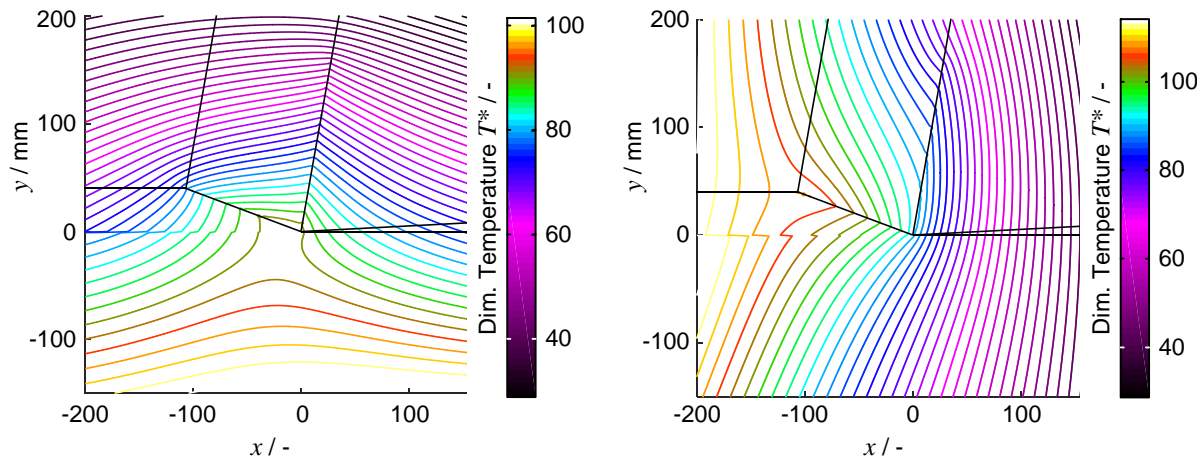
**Figure 4.11:** Influence of Corner Solution Parameters

*Einfluss der Eckenlösungsparameter*

Further analysis of the corner strength parameter showed that only a small range of values yielded suitable temperature plots for metal cutting applications. As a conclusion from the parameters study for the use of the corner solution in addition to the source solutions, the strength of the corner should be not used as a parameter but a

constant low value relative to the source solutions should be used. The angle parameter can be used to influence the isotherms in chip and tool.

As the final step of the parameters study, the influence of a parallel solution additionally to sources and corner solution investigated. For the sources again the reference solution was applied, for the corner solution a case with an angle below  $90^\circ$  was chosen, i.e. the influence of the corner was assumed to be negligible. Representative results of a study from the angle parameter of the parallel flow (i.e.  $a_2$ , compare Table 4.2) are shown in Figure 4.12.



**Solution Types:**

$n = 1 - 40$  (source),  $n = 41$  (parallel),  $n = 42$  (corner)

**Dislocation Parameters:**

$d_{shear} = 6.0$ ,  $\varphi_{shear} = 159^\circ$ ,  $d_{rake} = 8.4$ ,  $\varphi_{rake} = 80^\circ$

$z_{41} = 0$ ,  $z_{42} = 0$

**Solution Parameters:**

$a_{1n} = 1000$  ( $n = 1 - 40$ ),

$a_{1,41} = 100$ ,  $a_{2,41} = 0^\circ$ ,  $a_{1,42} = 0.01$ ,  $a_{2,42} = 77^\circ$

**Solution Types:**

$n = 1 - 40$  (source),  $n = 41$  (parallel),  $n = 42$  (corner)

**Dislocation Parameters:**

$d_{shear} = 6.0$ ,  $\varphi_{shear} = 159^\circ$ ,  $d_{rake} = 8.4$ ,  $\varphi_{rake} = 80^\circ$

$z_{41} = 0$ ,  $z_{42} = 0$

**Solution Parameters:**

$a_{1n} = 1000$  ( $n = 1 - 40$ ),

$a_{1,41} = 100$ ,  $a_{2,41} = 90^\circ$ ,  $a_{1,42} = 0.01$ ,  $a_{2,42} = 77^\circ$

**Figure 4.12:** Influence of Parallel Solution Angle

*Einfluss des Winkels der Parallelösung*

On the left-hand side of the figure, an angle of  $0^\circ$  was chosen, i.e. the parallel solution is aligned parallel to the  $x$ -axis. As can be seen, the influence of the parallel solution in general is significant within the chosen combination of elementary solutions. The characteristic maximum temperature area is shifted into the work piece, which is not suitable for application in metal cutting at all. A similar significant influence for an angle of  $90^\circ$ , i.e. parallel to the  $y$ -axis is shown on the right-hand side of the figure. Again the maximum temperature area is shifted, in this case parallel to the chip. Again the plot in the present form is not suitable for metal cutting applications.

A further parameter study on the parallel strength also did not yield suitable results, the influence of the parallel strength was too significant in the chosen combination. As a conclusion the use of the parallel solution in combination with the sources and the corner solution should not be applied for metal cutting applications.

A summary of the findings from the parameters study conducted for the combination of source, corner and parallel solution is provided in Table 4.4. These findings are

only valid for the chosen combination and on the basis of the conducted step-by-step methodology, i.e. further cross influences by choosing different combinations of the parameters can not be excluded. However, exemplary further studies of this kind were conducted without observing these cross influences.

**Table 4.4:** Summary of Parameter Influences and Relevant Value Ranges

*Zusammenfassung der Parametereinflüsse und relevante Wertebereiche*

Elementary Solutions Parameter	Parameter Influence	Value Range
overall number of source solutions	relevant distribution of isotherms for metal cutting	$n = 10 \dots 30$
unequal source distribution on rake face and shear zone	shifting of maximum temperature area and shape of the area	$r_n = 0.5 \dots 4.0$
source strengths ratio of rake face and shear zone	shifting of maximum temperature area and shape of the area	$a_{1rake}/a_{1shear} = 1 \dots 10$
source strength distribution on rake face	shifting of maximum temperature area along the rake face	$a_{1,max}/a_{1,min} < 3$
corner angle	influence of isotherms in chip or work piece	$a_2 = 0^\circ - 180^\circ$
corner strength	significant influence, constant value assumed	$a_1 = 0.1 - 0.2$

The results from the parameter study are the basis for the subsequent calibration of the model temperature plots to measured temperature fields from experiments. From the observed influences and numerical value ranges, conclusions for the influence on the characteristic regions in the temperature field can be derived. Further parameter studies for other superposition combinations can be conducted with the same approach presented in this subchapter.

As the influence of the parallel solution was determined to be significantly strong, the approach of superposition with more than the source solutions will not be considered in the following. However, the parallel solution can be interpreted as influence of cutting speed, which seems significantly necessary for an application in metal cutting. As shown later, the choice of the parallel solution is not necessary to model the influence of the material flow in metal cutting. Using a suitable parameterization of the sources yields temperature field with sufficient agreement of the reality.

### 4.2.3 Calibration of Model Parameters

#### *Kalibration der Modellparameter*

After the parameter study, suitable ranges of the dislocation and the solution parameters, as well as first recommendations for their influence on the temperature field are available. However, these parameter study is valid only as for relative numerical values. As a next step, the absolute numerical scale of the parameters need to be identified. This step needs experimental results for calibration. In the following, infrared images from experiments on a fundamental test rig were investigated for the calibration. The experiments and the measurement method are described in detail in Chapter 6. For the moment, these details might not be of interest for the process of modeling. The following calibration was conducted for different cutting parameters and work piece materials.

As shown in the two previous subchapters, a huge variety of possible combinations of elementary solutions is possible. A systematic study of all parameters requires high modelling efforts. This is in particular true for the calibration of the distinct parameters. For the following study only the combinations of sources was studied due to simplification. The positioning of sources of rake face and shear zone yielded suitable temperature fields which were considered to find application for metal cutting cases. In the parameter study, the influence of distribution, number and strength of the sources was determined. While in the study, sources were only placed on shear zone and rake face, the principal influence on the resulting temperature field is also true for positioning of sources along other lines. In the following analysis, additional sources were placed along the clearance face in order to distort the temperature field in the direction of the cut work piece surface.

For providing suitable absolute temperatures, the real valued function needs to be scaled. In the former analysis, a dimensionless temperature without any physical relevance was used as only qualitative conclusions were made. For the calibration, the temperature functions were scaled according to:

$$T_{cal}(x, y) = C \cdot T(x, y) + T_{ref} . \quad (4.19)$$

Both calibration coefficients,  $C$  and  $T_{ref}$ , were thereby chosen according to the absolute temperature scale in the infrared camera image and do not consider any measurements. The coefficient  $C$  furthermore influences the shape of the temperature field, while  $T_{ref}$  is only an offset calibration.

The calibration was conducted for three materials and different cutting speeds. While in this chapter, a purely phenomenological calibration was conducted, the numerical values are subsequently used for correlation and later calibration. For the phenomenological calibration, the recommendation from Table 4.4 were applied. In the following representative results of the investigation are presented.

On the left-hand side of Figure 4.13 the resulting temperature field from the model calibration for cutting of C 45 E steel is shown. The appropriate infrared camera image is provided on the right-hand side. As cutting parameters, a cutting speed  $v_c = 70$  m/min and a uncut chip thickness  $h = 30 \mu\text{m}$  was chosen. From the image, a triangular temperature influence zone in the tool near the root point can be observed. The chip appears with a bulk temperature distribution with parallel isotherms to the rake face.

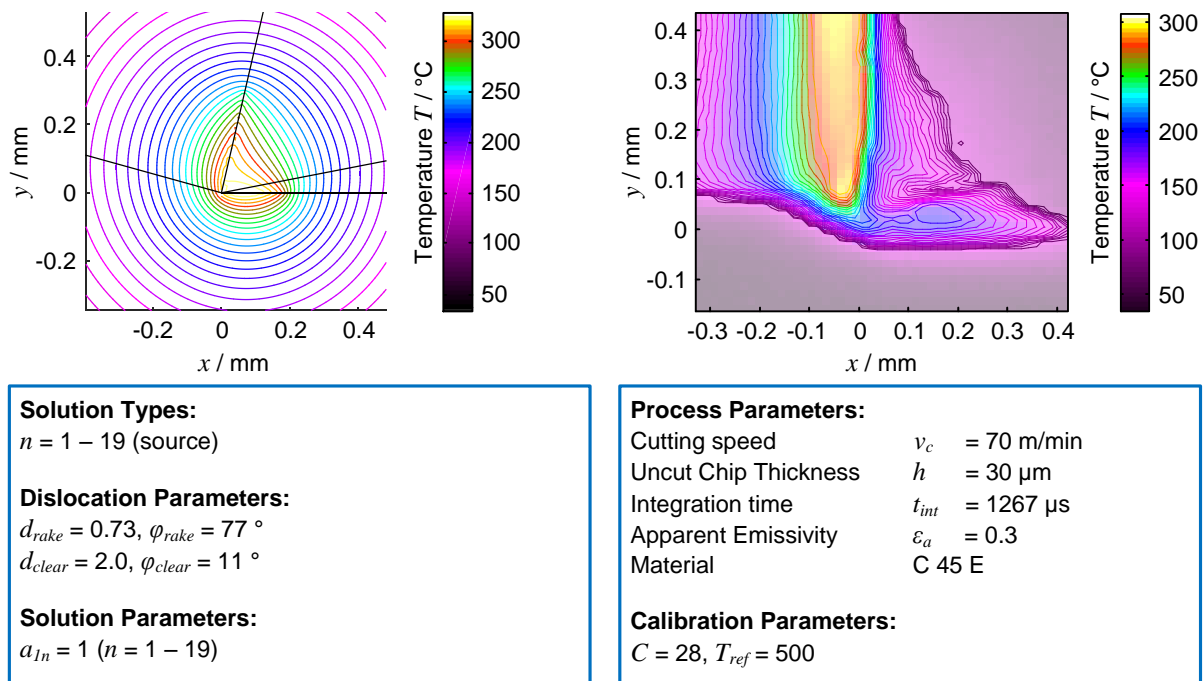


**Figure 4.13:** Calibration of Model Parameters for C 45 E

*Kalibrierung der Modellparameter für C 45 E*

However, the calibration was conducted according to the area in work piece and tool, as the temperature measurement in the chip could not be fully resolved with the infrared camera. For a full resolution at least three pixels of the camera need to be positioned on a measurement object. The minimum possible pixel pitch however was 15  $\mu\text{m}$ , while the chip thickness is around 30  $\mu\text{m}$ . However, the information can be used as maximum temperature occurring in the infrared camera image.

For the elementary function, ten sources were placed on the rake face and ten on the clearance face (including one source at the root point, counted for both lines each). The source strengths were chosen equal with value of  $a_{In} = 1$ . The calibration parameters were chosen to  $C = 28$  and  $T_{ref} = 500$ . For the resulting plot a hyperbolic shape of the isotherms in the tool can be observed. The shape was calibrated according to the shapes of the infrared camera image. While the qualitative run of the isotherms are in good agreement, the absolute values were chosen according to the temperatures evolving near the root point. The choice of only source solutions does not allow a calibration according to the absolute values of the tool. However, these values seem to be disturbed on the infrared camera image and could in reality be higher than measured.

Another investigation was conducted with Inconel 718 as work piece material. For the cutting speed a value of  $v_c = 35$  m/min was chosen while the uncut chip thickness of  $h = 30$   $\mu\text{m}$  was maintained. The appropriate infrared camera image and model plot is shown in Figure 4.14. While the absolute temperatures are in the same order of magnitude, the shape of the isotherms appear different. The maximum area of temperatures seems to be shifted from the clearance face to the rake face. In the work piece only a very slight temperature influence can be observed. Most of the significant temperature influence can be found in chip and tool in the vicinity of the rake face.

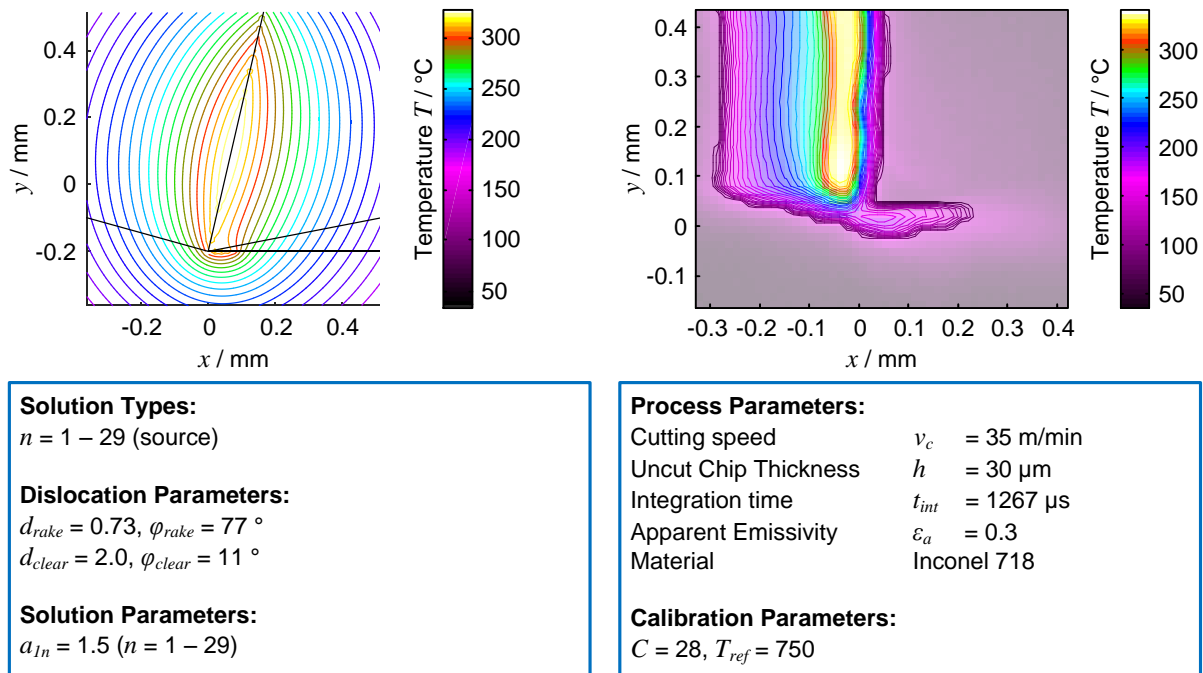


**Figure 4.14:** Calibration of Model Parameters for Inconel 718

*Kalibrierung der Modellparameter für Inconel 718*

In the potential function model, this behavior was modelled by using less sources distributed on the clearance face. Similar to the influence observed in the parameter study, the maximum temperatures are shifted along the rake face, as desired. In the shown case, 24 sources were placed on the rake face and 5 on the clearance face, for both distributions again the source in the root point was counted for each. The source strengths were maintained equal with a value of  $a_{In} = 1.5$ . For the calibration parameters, the coefficient  $C = 28$  was maintained and the reference temperature was chosen to  $T_{ref} = 750$ .

While the temperature distribution in the work piece seems in good agreement with the infrared image, the temperatures in the chip are modelled as an elliptic shape rather than parallel isotherms. Again, the not fully resolved temperature field in the chip is considered by doing so. The most significant difference of the cases investigated so far seem to be the shift of the maximum area of temperatures from the cut work piece to the rake face. This could be either caused by the different material or the lower cutting speed.

For further investigation of this phenomenon, another cutting speed of the tests with Inconel 718 is provided in Figure 4.15. The tests were conducted with cutting speed  $v_c = 70 \text{ m/min}$ . Taking the appropriate infrared camera image into account yields the characteristic triangular shape in the tool and cut work piece. Hence the effect of the shift of the maximum area of temperatures seems to be caused more from the cutting speed than from the work piece material. The absolute temperature values are comparable with the results from the lower cutting speed. Compared to the case of C 45 E, however, the temperature influence seems to go deeper inside the tool and the work piece material.

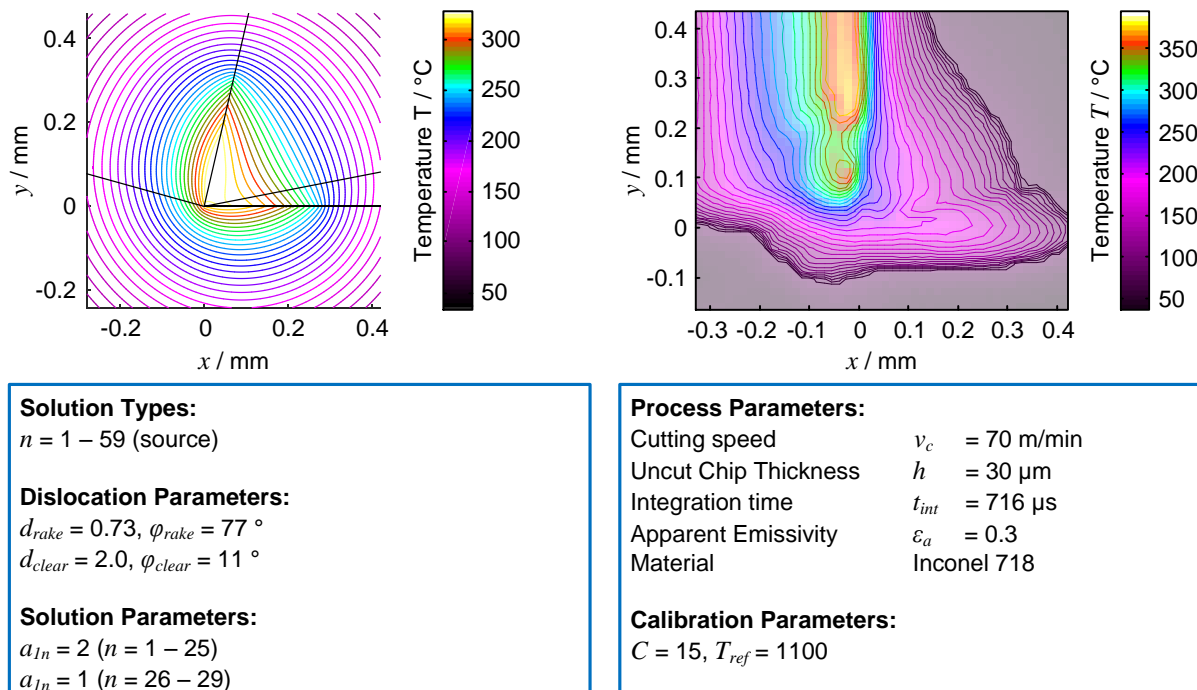


**Figure 4.15:** Calibration for Inconel 718 at Higher Cutting Speed

*Kalibrierung für Inconel 718 bei höherer Schnittgeschwindigkeit*

For consideration of these effects, further sources were placed on the clearance face. For the presented case, 25 sources were placed on the rake face and 35 sources were placed on the clearance face. The appropriate source strengths  $a_{In} = 2$  for the rake face and  $a_{In} = 1$  for the clearance face. As the absolute temperature values are comparable to the case of cutting Inconel 718 with the lower cutting speed, the calibration parameters were chosen equivalent, i.e.  $C = 15$  and  $T_{ref} = 1100$ .

With the chosen parameters, the effect of the cutting speed is in good agreement with the infrared camera image. The shape of the triangular field in the tool and the influence in the work piece can be correlated with the placement of the additional sources on the clearance face. The distribution in the chip is again different due to the explained reason. In general, the influence of the cutting speed seems to be suitably modelled by the distribution and ratio of the sources on rake face and clearance face. For consideration of the material, the calibration parameters, in particular the reference temperature  $T_{ref}$  can be used with consideration of the scaled source strength values.

As a last case presented for calibration, results from the investigation of the cutting experiments with X6NiCrTi26-15 are shown in Figure 4.16. The presented case was conducted with a cutting speed of  $v_c = 35$  m/min and an uncut chip thickness of  $h = 30 \mu\text{m}$ . As observed in the cases of Inconel 718 and C 45 E before, the maximum area of temperatures is shifted towards the rake face as can be seen on the right-hand side of the figure. Again the influence on the work piece and the tool in the area of the root point seems to completely diminish. The absolute temperatures are comparable to the order of magnitudes observed for the experiment with Inconel 718.

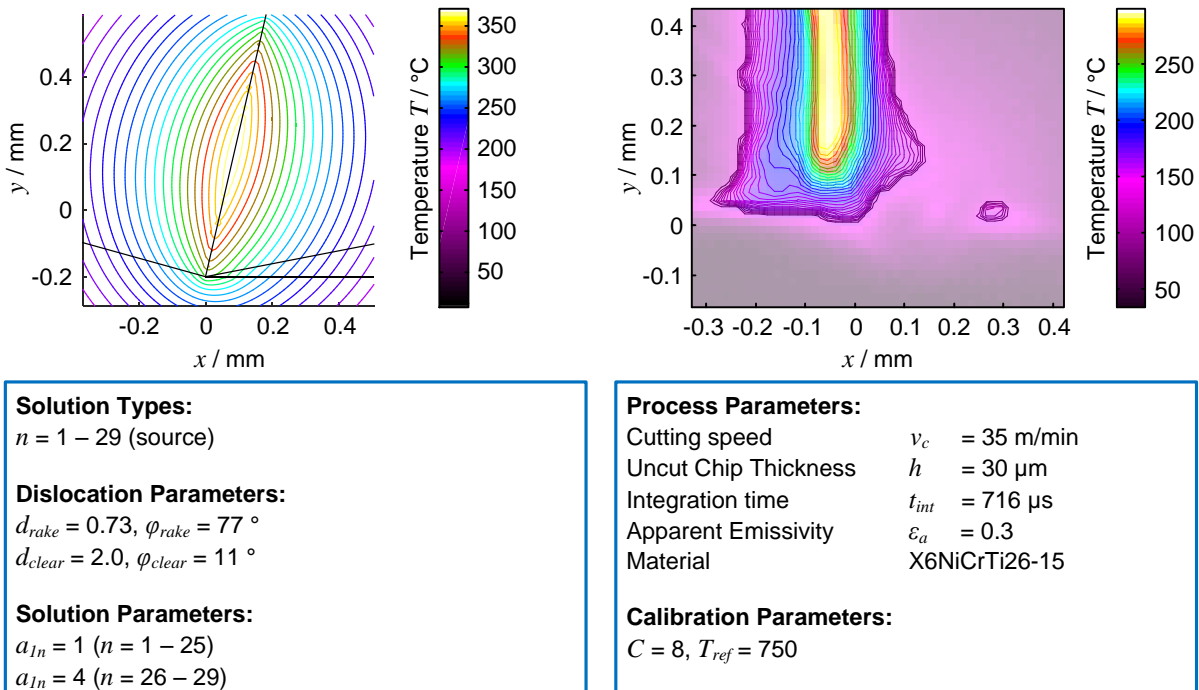


**Figure 4.16:** Calibration of Model Parameters for X6NiCrTi26-15

*Kalibrierung der Modellparameter für X6NiCrTi26-15*

In the potential theory model, again the distribution of sources on the rake face and clearance face was adapted. For the shown case again 20 sources were placed on the rake face and 5 sources were placed on the clearance face. The strength of the sources on the rake face was chosen to  $a_{In} = 1$ , while the sources on the clearance face were featured a strength of  $a_{In} = 4$ . For the calibration parameters, the coefficients were chosen to  $C = 8$  and  $T_{ref} = 750$ . The resulting model plot yields a similar shape as the one for the cases before. For the tool and chip elliptic isotherms in both directions are resulting. The influence on work piece at the root point is almost not occurring, as observed from the infrared camera images.

Further calibration experiments with other parameters sets yielded similar results as the one presented. Suitable results could not be gained for the full range of tested parameters as some infrared images had significant disturbances. As a matter of fact, the prediction quality and confidence of the elementary solution approach, is significantly dependent on the quality of the calibration. On the other hand, there are no more inputs needed for the method and a great variety of thermal fields can be considered.

#### 4.2.4 Correlation of Model and Cutting Parameters

##### *Korrelation von Modell- und Zerspanparametern*

The calibration results yielded suitable congruence between the modelled and measured temperature fields. In the following step, the distinct parameters of the calibration are correlated to the appropriate cutting parameters. This correlation yields the final model for computing relevant temperature fields and heat flows. The correlation should be understood more qualitative than as an empirical law, as the investigation conducted during calibration had a more phenomenological character. However, certain conclusion can be drawn.

Considering the calibration investigations, different cutting speeds and work piece materials were investigated. A summary of the presented experimental parameters and the model parameters is given in Table 4.5.

**Table 4.5:** Correlation Table of Model and Experimental Parameters

##### *Korrelationstabelle von Modell- und Versuchsparametern*

Material	$v_c$ [m/min]	$\lambda$ [W/mK]	$r_n$ [-]	$r_a$ [-]	$C$ [-]	$T_{ref}$ [°C]
C 45 E	70	45.1	1	1	28	500
IN 718	35	11.4	5	1	28	750
IN 718	70	11.4	1.4	0.5	15	1100
X6Ti26	35	18.7	5	0.25	8	750

In the table, the cutting speed  $v_c$  and the heat conductivity  $\lambda$  are the representative experimental parameters. Further values for the heat conductivity are provided in the later validation chapter. The distribution and strength of the sources are described by the ratio  $r_n$  (ratio of number of sources on rake face over number on clearance face) and the appropriate strength ratio  $r_a$ .

When correlating the experimental and model parameters, no clear empirical law can be determined. Further analysis with parameters not presented in the table yield similar results. However, a general correlation for the heat conductivity can is given by:

$$\lambda \sim \eta_\lambda \cdot r_a \cdot C \quad . \quad (4.20)$$

The appropriate correlation for the cutting speed influence is given by the expression:

$$v_c \sim \eta_v \cdot r_n \cdot T_{ref} \quad . \quad (4.21)$$

Both correlation coefficients  $\eta_\lambda$  and  $\eta_v$  however were found in a wide range of numerical values, hence a suitable empirical law can not be given. The elementary solution is hence strongly dependent on the calibration, especially when considering the influence of the material.

## 4.3 Model Outcomes

### *Modellergebnisse*

After conducting the steps superposition, parameters study, calibration and correlation, the computational model, i.e. the complex temperature function can be formulated. As described, one advantage of the use of potential theory is the simultaneous modelling of the heat flow field. Exemplary expressions for the model with distributed sources are described in the following. Even though the expressions seem long, both are closed analytical functions and can in principle be computed manually. Both functions are solutions of the partial differential equation of heat conduction.

#### 4.3.1 Temperature Field

##### *Temperaturfeld*

Regarding the complex temperature function for the equal distribution of the sources on shear zone and rake face yielded:

$$F(z) = \sum_{n=1}^{40} F_n(z, z_n) = \sum_{n=1}^{40} \frac{a_{1n}}{2\pi} \ln(z - z_n). \quad (4.12)$$

For the temperature function  $T(x, y)$  the real valued part of this complex function needs to be isolated. For the distinction of real valued part and imaginary part, in some cases the radial function for the complex argument  $z$  is more suitable (compare Equation 4.17). Using this expression and separating all expressions without the imaginary unit yields:

$$T(x, y) = \sum_{n=1}^{40} \frac{a_{1n}}{2\pi} \ln \left[ \sqrt{(x - x_n)^2 + (y - y_n)^2} \right]. \quad (4.22)$$

As can be seen, in the case of only using source solutions, the temperature function is consisting of the natural logarithm and the square function. Even though this functions were used for modelling of temperature fields before, Equation 4.22 should be understood as one representative result for the method of elementary solutions. Taking into account the dislocation parameters, the temperature function can be given to:

$$T(x, y) = \sum_{n=1}^{40} \frac{a_{1n}}{2\pi} \ln \left[ \sqrt{[x - (n-1)d]^2 + [y - d(n-1)\tan(\phi)]^2} \right]. \quad (4.23)$$

The appropriate values and correlations of the dislocation and solution parameters correlated to the cutting speed and the material were given in the previous chapter. Putting these values in Equation 4.23 yields the temperature function dependent on the cutting parameters.

For the other elementary solutions, similar expressions can be given for the real-valued part in a similar manner. The functions for the cutting parameter correlations can be used to replace the appropriate elementary solution parameters. By doing so a greater variety of mathematical solutions is yielded by the potential theory, allowing a great variation for the shape and maximum area of the isotherms.

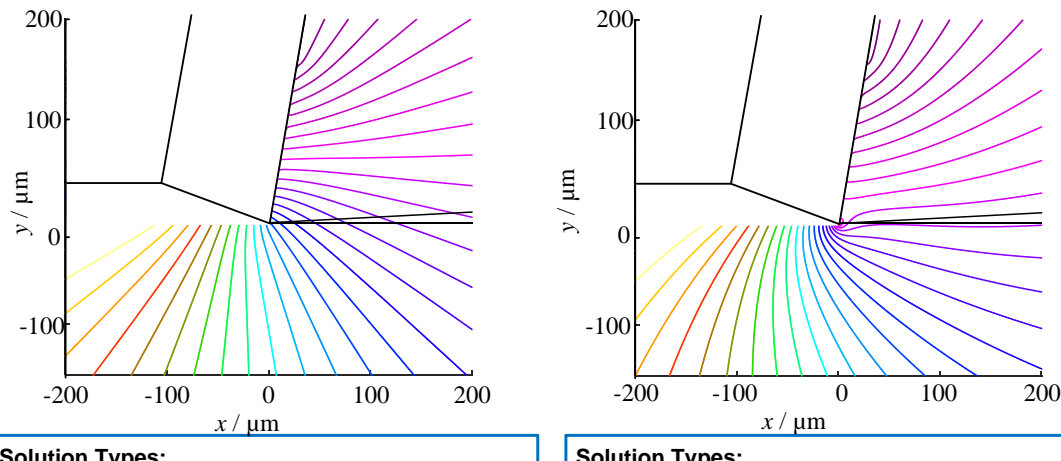
### 4.3.2 Heat Flow Field

#### *Wärmestromfeld*

When separating the imaginary part of Equation 4.12, the function for the heat flow field can be determined. As described, this function can be used to describe the direction of the two-dimensional heat flow in chip, tool and work piece. For the use of only source solutions on the shear zone and rake face, the heat flow function can be determined to:

$$H(x, y) = \sum_{n=1}^{40} \frac{a_{ln}}{2\pi} \arctan\left(\frac{y - y_n}{x - x_n}\right). \quad (4.24)$$

The absolute values of this field do not have a direct physical meaning, however the gradient describes the absolute heat flow value. In Figure 4.17 two exemplary plots of heat flow fields for the sources and the source and vortex solution is shown. Due to numerical errors only the fields in tool and work piece below the shear zone are plotted.


**Solution Types:**

$n = 1 - 40$  (source)

**Dislocation Parameters:**

$d_{shear} = 6.0$ ,  $\varphi_{shear} = 159^\circ$ ,  $d_{rake} = 8.4$ ,  $\varphi_{rake} = 80^\circ$

**Solution Parameters:**

$a_{ln} = 1000$  ( $n = 1 - 40$ )

**Solution Types:**

$n = 1 - 40$  (source),  $n = 41$  (vortex)

**Dislocation Parameters:**

$d_{shear} = 6.0$ ,  $\varphi_{shear} = 159^\circ$ ,  $d_{rake} = 8.4$ ,  $\varphi_{rake} = 80^\circ$

$z_{4I} = 0$

**Solution Parameters:**

$a_{ln} = 1000$  ( $n = 1 - 49$ ),  $a_{l,4I} = 1000$

**Figure 4.17:** Exemplary Heat Flow Fields

*Exemplarische Wärmestromfelder*

As expected for both solution approaches, a radial heat flow direction is resulting. For the solution using corner and vortex, the heat flow lines appear distorted. The value for the heat flux in  $x$  at a distinct location in the field is given by:

$$\dot{q}_x'' = -\frac{\partial H(x, y)}{\partial x} = -\lambda \cdot \sum_{n=1}^{40} \frac{a_{ln}}{2\pi} \frac{\partial}{\partial x} \arctan\left(\frac{y - y_n}{x - x_n}\right) = +\lambda \cdot \sum_{n=1}^{40} \frac{a_{ln}}{2\pi} \frac{(y - y_n)}{(x - x_n)^2 + (y - y_n)^2}. \quad (4.25)$$

The appropriate component in  $y$  direction can be found with the gradient in  $y$  direction with a positive sign. With the help of this equation, heat amount values through freely chosen areas can be calculated according to Equation 4.3.

## 4.4 Conclusions from Elementary Solutions Approach

### *Zwischenfazit aus Elementarfunktionenansatz*

As a first step for the application of potential theory for thermal modeling in metal cutting, the elementary solutions approach was investigated. This approach is based on the elementary solutions of potential theory and can be conducted following a step-by-step methodology:

- As a first step, a superposition of elementary functions with the help of a pre-defined shape of cutting kinematics need to be conducted. The analysis showed that a positioning of sources on the shear zone and rake face yielded suitable temperature field for metal cutting. Also combinations in terms of superposition with the corner solution and the vortex solution showed interesting results. The dipole solution did not yield suitable results in combination with the sources and was subsequently neglected.
- In the parameter study the influence of the dislocation and the elementary solution parameters was investigated. For the study the superposition of sources, sources and corner and sources, corner and parallel flow were investigated. The results showed that the number of sources, unequal distribution and unequal strengths of the sources have similar influence on the temperature field. The corner solution can be used to influence the field in the chip and the work piece. The parallel solution was found to have too much influence in the combination.
- The calibration with the help of infrared images recorded for experiments on a fundamental test rig showed that the chosen solution combinations based on source solutions are in principle capable to predict temperature field in metal cutting. Modelled and measured temperature fields were in good agreement.
- However, for the later correlation not all parameters could be clearly correlated to each other. Cross correlations between model parameters and cutting parameters exist. Furthermore the correlation takes a lot modeling effort, in particular for a higher number of chosen solutions.

As an intermediate conclusion, the elementary solution approach can be considered as a feasibility study for the use of potential theory for thermal modeling in metal cutting. The general approach seems sensible and yields sufficient results. However, the presented method requires huge efforts in terms of calibration and correlation. The iterative character of the method furthermore prevents a straight forward modelling method.

For the chosen source solution approach, it was derived that a positioning of the sources on the characteristic regions of the cutting kinematics was the key for suitable temperature fields. However, the number, location and distribution of the sources were chosen freely without any physical or mathematical background. A more systematic approach based on the findings from this chapter is needed.

# 5 Panel Method Approach

## *Ansatz Panelmethode*

In the previous chapter, a simple approach for the application of potential theory for thermal modeling was presented. Although the methodology can be used for the derivation of new analytical computational models, the strong iterative characteristic of the methodology implies optimal use only for certain cases. In the present chapter, the application of a more systematic approach, commonly termed as panel method, is described. After an introduction to the fundamentals of this method, the methodology for use in metal cutting is presented. Similar to the previous chapter, the distinct steps of the methodology are explained with a practical example. For the panel method, the steps are: discretization of cutting geometry, consideration of thermal boundary conditions, solution of linear equation system, and calibration.

## 5.1 Fundamentals of Panel Methods

### *Grundlagen der Panelmethoden*

A first approach based on the panel methodology for derivation of models was presented from HESS AND SMITH [HESS67]. The method was used for prediction of fluid flow around freely chosen contours. In principal, the panel method is the spatial discretization of potential functions. Put simply, a great number of elementary solutions is positioned in the complex space, in a way that a preset contour in one of the scalar fields is produced. In this context, the panel method can be regarded as a systematic advancement of the elementary solutions approach, similar to the positioning of vortex solutions along the characteristic regions of metal cutting, described in the previous chapter. There are two general elementary solutions applied for the panel method, i.e. the source solution and the vortex solution [KATZ10, pp. 206–229]. In the present thesis the source panel method is applied and hence described in the following.

Panels are linear sections of a line, which are used to approximate the desired contour within predefined area sections. The connection of two panels is termed a node. As shown on the upper left-hand side of Figure 5.1, panel  $P_j$  is positioned between the nodes  $K_j$  and  $K_{j+1}$ , nodes  $K_{j+1}$  and  $K_{j+2}$  again form panel  $P_{j+1}$ . The nodes uniquely define spatial and angular position of the panel. If  $(x_j, y_j)$  define the spatial position of node  $K_j$ , the absolute angular panel position  $\varepsilon_j$  can be computed using the equation:

$$\varepsilon_j = \arctan\left(\frac{y_{j+1} - y_j}{x_{j+1} - x_j}\right). \quad (5.1)$$

The panel geometries are shown in the upper right-hand side of the figure. For each panel a constant source strength  $s_j$ , condensed in the middle of the panel, is assumed. Different panels, however, can have different source strengths. The source

strengths are unknown for the moment and will be calculated according to the specification of the boundary conditions. The boundary conditions need to be defined in terms of the induced velocities  $u^*$  and  $v^*$ . These are the velocities in normal and tangential direction of the panel, respectively in  $x^*$  and  $y^*$  direction of the local coordinate system (indicated by the asterisk). As before, the velocities can be interpreted as heat fluxes in case of thermal modeling.

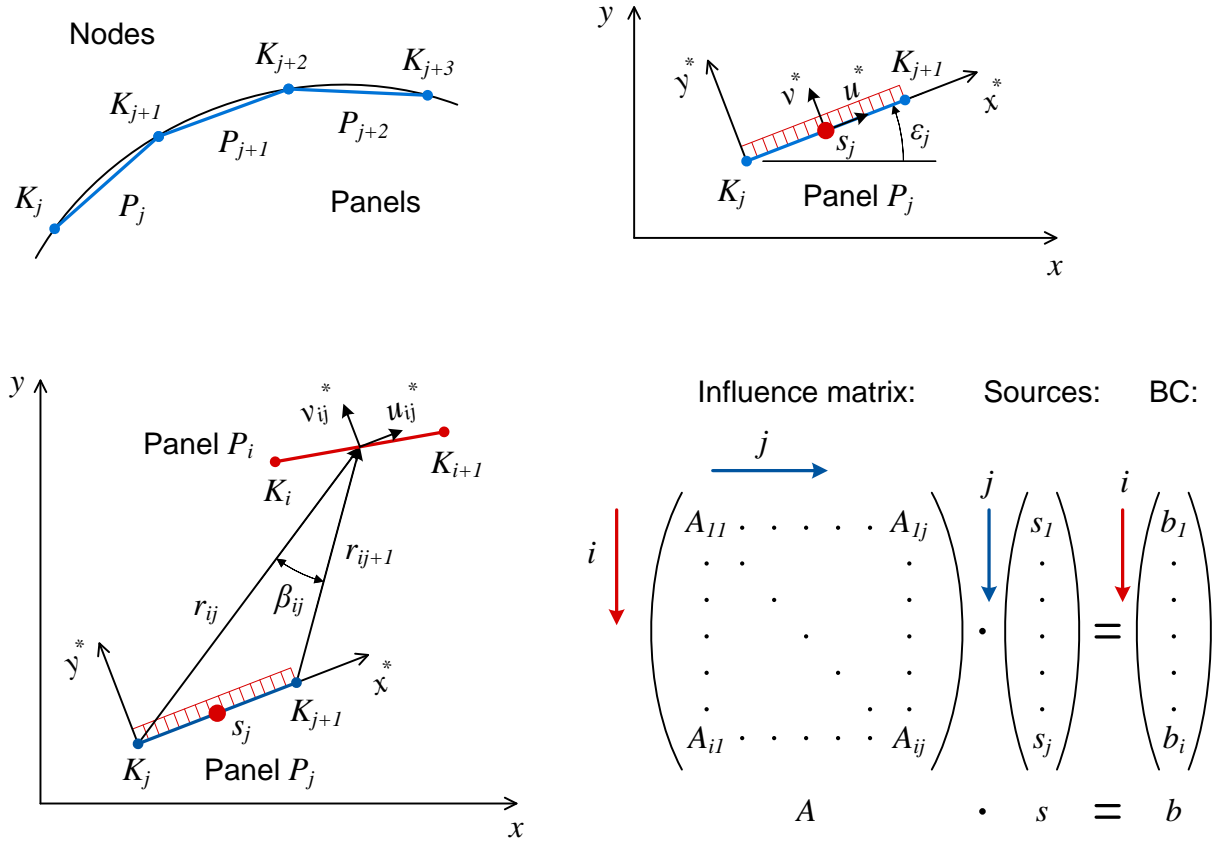


**Figure 5.1:** Panel Geometry and Influence Matrix

*Panelgeometrie und Beeinflussungsmatrix*

For the determination of the source strengths it has to be considered that each panel influences each other panel. In the lower left-hand side of Figure 5.1 a arbitrary chosen second panel  $P_i$  is sketched additionally to panel  $P_j$ . The induced velocities at the center of panel  $P_i$  caused by panel  $P_j$  can be determined using [MORA03]:

$$u_{i,j}^* = -\frac{s_j}{2\pi} \ln\left(\frac{r_{i,j+1}}{r_{i,j}}\right) \text{ and} \quad (5.2)$$

$$v_{i,j}^* = s_j \frac{\beta_{i,j}}{2\pi}. \quad (5.3)$$

Both induced velocities are stated in the local coordinate system of Panel  $P_j$ . In Equations 5.2 and 5.3, the first index is related to the panel where the influence is caused, the second index refers to the causing panel. Hence, the expression  $u_{i,j}^*$  means: induced tangential velocity at panel  $P_i$  caused by the source  $s_j$  at panel  $P_j$  in

the local coordinate system of  $P_j$ . Consequently, The magnitudes of the displacement vectors  $r_{i,j}$  and  $r_{i,j+1}$  are the connections from the center of panel  $P_i$  to node  $K_j$  respectively to node  $K_{j+1}$ . The including angle between these displacement vectors is termed  $\beta_{i,j}$ . Taking into account all induced velocities from all panels  $P_j$  on the panel  $P_i$  yields:

$$u_i^* = \sum_j u_{i,j}^*, v_i^* = \sum_j v_{i,j}^*. \quad (5.4)$$

In case of a very large distance between the panels  $P_j$  and  $P_i$ , the ratio of the distances approximates unity and the including angle vanishes. Both velocities subsequently vanish, i.e. there is no interaction between panels located far away from each other. The tangential velocity  $u_{i,j}^*$  also vanishes for all cases of  $r_{i,j}=r_{i,j+1}$ , which can be interpreted as a line from the center of panel  $P_j$ . For the influence of a panel on itself, a case differentiation is sufficient. An angle of  $\beta_{i,i}=180^\circ$  implies a normal velocity on the left-hand side of the panel, an angle of  $\beta_{i,i}=-180^\circ$  a right hand sided velocity. Hence, the choice of the angle defines if the panel is a source or a sink for the area on the right-hand side or the left-hand side of the panel. The tangential velocity on the panel vanishes.

Taking into account the global angular positions  $\varepsilon_i$  and  $\varepsilon_j$  of the respective local coordinate systems and Equations 5.2 and 5.3 yields an expression  $A_{i,j}$  for calculating the resulting normal velocity at Panel  $P_i$ :

$$A_{i,j} = \frac{1}{2\pi} \cdot \left[ \ln\left(\frac{r_{i,j+1}}{r_{i,j}}\right) \cdot \sin(\varepsilon_i - \varepsilon_j) + \beta_{i,j} \cdot \cos(\varepsilon_i - \varepsilon_j) \right]. \quad (5.5)$$

Equation 5.5 is the dimensionless normal velocity at Panel  $P_i$ . A similar expression with the respective components can be given for the tangential velocity. For consideration of the thermal boundary conditions, however, the normal component is relevant. Putting Equation 5.5 into 5.4 yields:

$$\sum_j A_{i,j} \cdot s_i = b_i. \quad (5.6)$$

The desired resulting velocity  $b_i$  at panel  $P_i$  needs to be preset and represents the boundary condition at Panel  $P_i$ . Equation 5.6 is a linear equation system with unknown source strengths  $s_i$ . In matrix notation, the matrix  $A$  is termed influence matrix, the vector  $s$  (consisting of the unknown source strengths) source vector and the vector  $b$  (consisting of the desired boundary conditions) boundary condition vector in the following. A detailed visualization of the matrix equation is given on the lower right-hand side of Figure 5.1. The normal velocity of Panel  $P_i$  can subsequently be found in line  $i$  of the matrix equation, the influence of Panel  $P_j$  on all other panels can be found in row  $j$  of the influence matrix. Solving Equation 5.5 after isolating the source vector  $s$  yields the unknown source strengths for each panel.

It is important to notice that the influence matrix  $A$  can be determined solely by setting the geometrical positions of the nodes. For the heat source strengths not any assumptions or correlations are needed. The numerical values for the strengths are rather determined systematically. Only for setting the boundary conditions vector  $b$ , i.e. the resulting induced normal velocity for each panel, the physical reality has to be considered. In terms of the flow field model from HESS AND SMITH, for each panel of the contour the resulting normal velocity vanishes, as not any fluid flow inside a rigid body is physical meaningful. The final linear equation system in form of Equation 5.6 is linear concerning the unknown source strengths. However, this may not be confused with a linearization of the physical model itself. Regarding the coefficients of the influence matrix in Equation 5.5 shows that nonlinear functionalities are considered. The panel method can therefore be considered as a discretization method of the geometric boundaries, not as a discretization of the partial differential equation. Furthermore, the space in between the characteristic boundaries is not discretized. Solving the equation system yields the unknown source strengths that can be subsequently put into Equation 5.2 or respectively 5.3. For plotting the scalar fields, the values can also be put into the complex function, which was derived during the development of the elementary solutions approach.

For consideration of movement, in principal a further parallel solution could be considered in the panel method approach. Another option is given by additional panels which do not belong to a boundary in reality. The additional panels can be used to consider a constant additional value for the boundary condition vector. In this way it can be used similar to a constant offset of the temperature field at regions where material flow need to be considered. For an application in metal cutting, further panels could be considered in the chip an the work piece area, as a relative movement of heat sources and material is occurring. The movement can be expressed in terms of suitable characteristic parameters including the cutting speed.

As described, the source panel method assumes constant source strengths at the center of each panel. However, linear distributions or functions of higher order are possible and have been realized [MORA03, pp. 273–275]. The analysis of the use of such source strengths distributions yielded a trade-off against the chosen number of panels. For flow fields around a contour, not any significant advantages were observed [KATZ10, p. 323]. As for thermal modeling enhanced boundary conditions are necessary, this conclusion is not simply transferable. First studies for more complex boundary conditions (i.e. general DIRICHLET and NEUMANN boundary conditions) can be found. Furthermore, panel methods using elementary vortex or dipole solution can be found in literature [MORA03, pp. 282–284]. As seen in the elementary solutions approach, the vortex solution is in principle suitable for metal cutting applications. An overview of the different approaches is provided from KATZ AND PLOTKIN [KATZ10, p. 262]. In their work also the extension of the method for three-dimensional applications is provided. A principle transfer to the metal cutting application could be possible. In the following, a methodology for using the simple source panel for thermal modeling in metal cutting is proposed.

## 5.2 Methodology for the Application of Source Panels

### *Methodik für die Anwendung von Quellenpanels*

As described, panel methods provide a more systematic approach for the use of potential theory. The parameters that were defined by a calibration in the elementary solutions approach are systematically determined due to their physical meaning. For the specific use of the panel method in metal cutting, a step-by-step procedure similar to the elementary solutions approach was developed. The distinct steps are:

- discretization of geometrical cutting kinematics,
- consideration of thermal boundary conditions,
- generation of potential field, and
- calibration.

The methodology can be characterized to be rather sequential than iterative as the elementary solutions approach, suggested by the missing backward arrows in Figure 5.2. This straight forward modelling approach has both advantages and disadvantages that will be discussed later. In this thesis exclusively source panels with constant source strengths are applied. However, the presented methodology can in general also be applied for vortex or dipole panels.

The first step of the methodology is the discretization of the geometrical cutting kinematics. A distinction between direct input parameters and implicit input parameters can be made. Direct input parameters are e.g. given by the tool geometry and the cutting depth. Implicit input parameters that are resulting from the chip formation need to be assumed, measured or calculated by appropriate models. After defining the cutting kinematics, a discretization of the geometry in nodes respectively panels can be conducted. There is an influence of the chosen numerical number of panels on the resulting temperature field, i.e. more panels should yield better results. Obviously, there is a need for optimization between a sufficient number of panels and computational time needed. This trade-off has to be assessed against the modeling objectives. If the model is intended to yield high resolution temperature fields for research objectives, the number of panels will be selected higher than for an industrial use of the model e.g. in an online process monitoring system. The number of panels directly correlates to number of order of the influence matrix and hence the order of the equation system.

After defining the influence matrix and the number of order, the boundary conditions have to be defined for each panel. For thermal modeling in metal cutting, these boundary conditions can be either formulated as DIRICHLET or NEUMANN conditions. Using the panel method, only NEUMANN conditions can be defined. More precise, either an adiabatic boundary or a distinct heat flux value has to be preset for each panel. Again, a distinction for setting these values can be made. Adiabatic boundaries are given by the real physical boundaries, i.e. material boundaries to the surrounding air or material to material boundaries. For setting heat flux values e.g. in the shear zone, again assumptions, measurements or appropriate models are needed. A

categorization of panels into the characteristic regions of metal cutting can help to structure the heat flux values. The outcome of this step of the methodology is the boundary conditions vector.

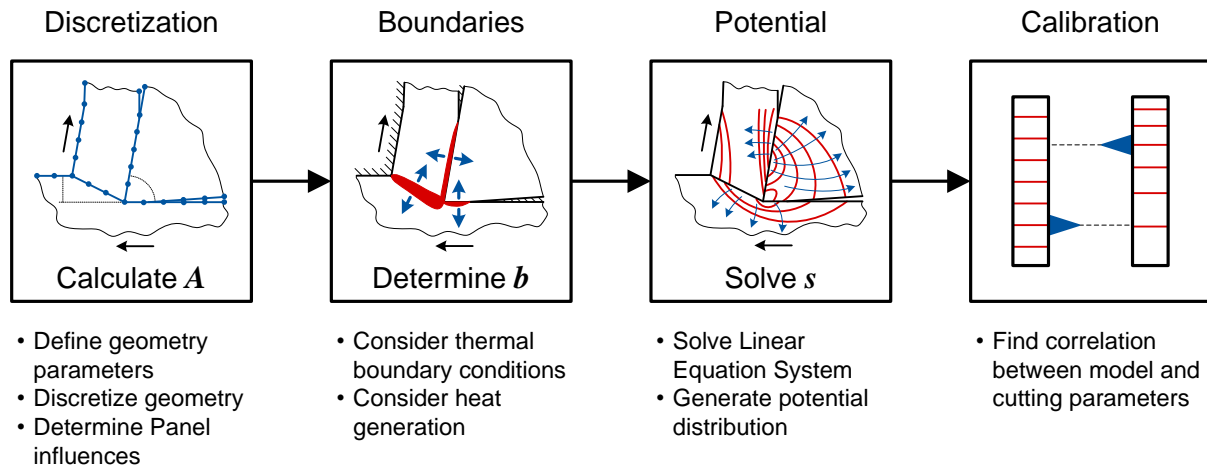


**Figure 5.2:** Methodology for Panel Method Approach

#### *Methodik zur Anwendung der Panelmethode*

With the boundary condition vector, the linear equation system with unknown source strengths can be formulated. As the number of unknown variables is equal to the number of equations, the resulting equation system is uniquely solvable. The system can be solved using conventional solving algorithms e.g. GAUß or CHOLESKY algorithm [DAHM08, pp. 51–90]. For higher numbers of panels, it can also be considered that in the boundary conditions vector many zeros can be found. This is due to the definition of adiabatic boundaries for thermal modeling. However, the influence matrix does not contain significant numbers of zeros. Using the source strength vector yields distinct values for the complex temperature function. Hence temperature and heat field can be plotted. The fields are again the real valued respectively the complex part of the function.

As the last step of the methodology, the temperature field needs to be calibrated with the help of experimental measurements. In contrast to the calibration of the elementary solutions approach, only the absolute temperature magnitude can be calibrated if necessary. The distribution of the isotherms or the parameters (i.e. source strengths) are determined by the methodology and may not be varied afterwards. The consideration of different cutting parameters was already done in the first step. For modeling of different work piece materials, the influence of the material on the implicit input parameters, e.g. chip formation or heat source strengths, needs to be evaluated. Hence a simple scaling of the temperature field in the calibration step is not possible, which is meeting the requirements of the model approach for complex temperature fields in metal cutting reality.

In the following, the method is demonstrated for exemplary metal cutting conditions. The modified model of OXLEY serves as basis. Additionally to the elementary solutions approach, effects like cutting edge radius or clearance face wear can be directly considered.

### 5.2.1 Discretization of Cutting Kinematics

#### *Diskretisierung der Schnittkinematik*

For the discretization of the cutting kinematics, panels and the appropriate nodes have to be defined. In contrast to other discretization methods, only the significant thermal boundaries are discretized but not the field within these boundaries. As a first step of the discretization, the geometry parameters have to be defined with the help of characteristic nodes. On the left-hand side of Figure 5.3, an idealized situation with shear zone (AO), friction zone (BE), cutting edge radius (ED) and clearance face (DC) is approximated. Furthermore, uncut chip thickness, chip thickness, and rake angle are considered. In general, more complex geometries, e.g. rake face geometries or chip forms, as well as non-ideal thin heat source regions could be considered with the discretization.

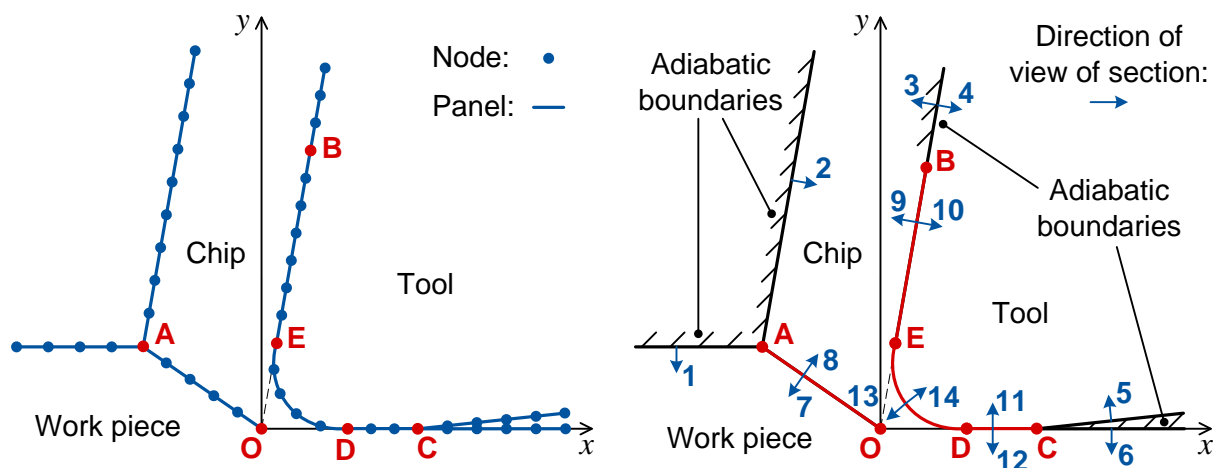


**Figure 5.3:** Discretization of Cutting Kinematics

#### *Diskretisierung der Schnittkinematik*

On the right-hand side of the figure, the distribution of the panels in distinct sections is shown. As the panels only influence a semi-infinite field above the panels, a direction of each panel needs to be defined. At boundaries where both directions are of interest, therefore, two panels need to be positioned upon each other. This is not applicable if only one direction is of interest, i.e. at the uncut work piece surface (1), the chip backside (2), the clearance face of the tool (5) and the cut work piece surface (6). However, by placing panels on these boundaries a consideration of convective heat transfer to the surrounding is viable. For the shear zone section (7,8), friction zone section (9,10), the clearance face section (11,12) and the cutting edge radius (13,14) the strengths of the panels can be chosen differently dependent on the direction. Heat partition ratios, which are common in analytical thermal models, can be considered this way. The clearance face section can be used to model the influence of a heat source due to clearance face wear. For a fresh tool without wear, the appropriate boundary condition can be assumed as adiabatic in both directions. Further boundaries, which can be considered adiabatic for both directions need also be defined with two panels, e.g. rake face of the tool (3,4).

For the different sections, the number and length of the panels can be chosen individually. In the following analysis, however, a unique length for all panels was chosen. This length was thereby defined in a way that for a given section length a whole number of nodes is generated. The numerical values for the lengths are furthermore dependent on the chosen window size. In Figure 5.3 e.g. not the whole tool is visible, but only the region close to the root point. With the defined distance between the nodes (i.e. the panel length) and the position of each node in the  $x$ - $y$  space, the influence matrix  $A$  is defined. Figure 5.4 shows a representative plot of the influence matrix for a simplified discretization without consideration of the cutting edge radius.

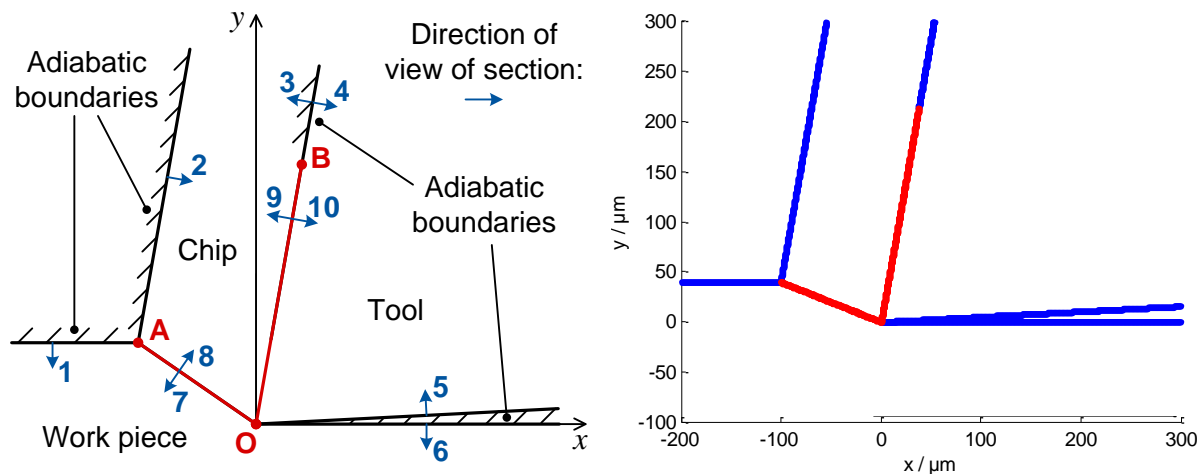


**Figure 5.4:** Implementation of Panel Discretization

*Implementierung der Paneldiskretisierung*

For this simplified case, the number of sufficient sections and hence number of panels is reduced. The definitions of the sections is shown on the left-hand side of the figure. A summary of needed parameter is given in Table 5.1.

**Table 5.1:** Overview of Discretization Parameters

*Übersicht der Diskretisierungsparameter*

Panel Parameters	Direct Geometry Parameters	Indirect Parameters
panel number $n$ (window size $l_w$ ) (panel length $l_{panel}$ )	uncut chip thickness $h$ rake angle $\gamma$ clearance angle $\alpha$ (cutting edge radius $r_e$ )	shear angle $\Phi$ contact length $l_{rake}$ (clearance face wear $l_{clear}$ )

The cutting edge radius  $r_e$  and the length of the clearance face  $l_{clear}$  wear do not need necessarily to be considered. In the table, only a set of non redundant discretization parameters is given without brackets. For a given length e.g. with a given panel length, the number panels is defined. The window size is not a direct discretization parameter, however is an important definition for the discretization, as described.

### 5.2.2 Consideration of Thermal Boundary Conditions

*Berücksichtigung der thermische Randbedingungen*

After the definition of the nodes and panels, the discretization is defined in form of the influence matrix  $A$ . The number of lines of this matrix corresponds to the number of panels, each line corresponds to the combined influence of all panels on the chosen panel. For the consideration of the thermal boundary conditions, for each panel this combined influence needs to be defined. In order to choose this values systematically, the sections were introduced during the discretization.

In Figure 5.5 an arbitrary section  $k$  is chosen, the panel  $P_k$  may be the first panel of the section. For the chosen section, there is a corresponding submatrix in the influence matrix  $A$ , defined by the section length and the subsequent number of panels in the section. As described, for some sections the influence in both directions has to be defined. The appropriate section therefore appear twice in the influence matrix.

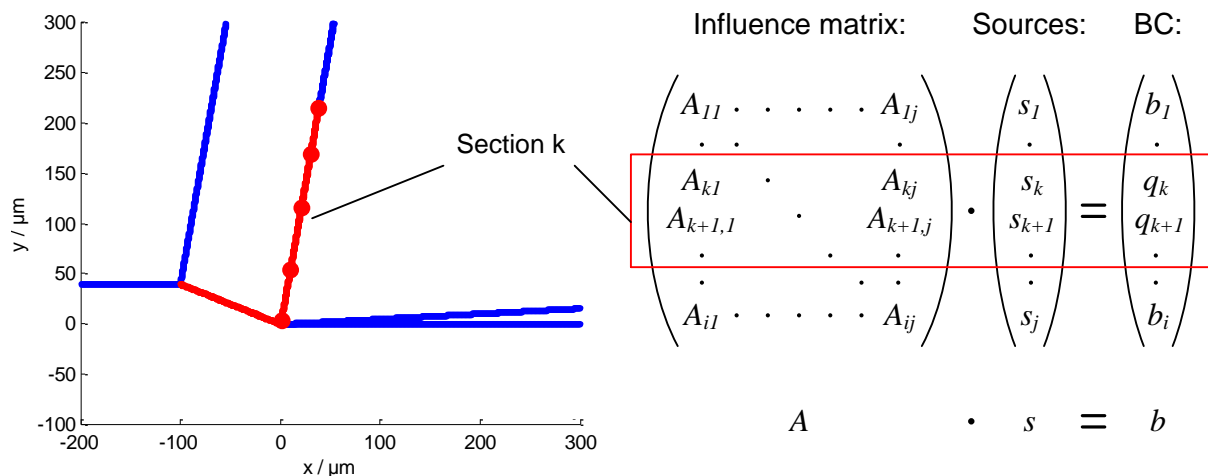


**Figure 5.5:** Boundary Condition Vector  
*Vektor mit Randbedingungen*

For the definition of the boundary condition vector  $b$ , in general three kinds of boundary conditions can be defined:

- adiabatic panel,
- transparent panels, and
- panels with defined heat source strength.

For the adiabatic panel, all combined induced heat flows from the other panels need to compensate each other. The appropriate value in the boundary condition vector is Zero. Transparent panels are panels which do not influence other panels and let all induced heat flows pass. For transparent panels the appropriate heat source strength in the source vector is set to Zero. Transparent panels are needed on boundaries where two panels are placed on each other. They always appear together with either adiabatic or panels with defined heat source strength. The reason for this is the fact that the Laplace equation do not consider heat sources within the area of interest. The sources are mathematically singularities which are put on the boundaries of the

interesting area. In principle, therefore, the areas of chip, tool and work piece are separated from each other. The resulting temperature field, however is dependent from the influence of all panels. By separating the areas from each other, the consideration of different materials is possible.

For the definition of the heat source strengths on the sections at the contact zone, the shear zone and where appropriate at the clearance face, suitable assumptions, models or measurement need to be considered. For a known function for the heat source strength  $q_{source}$  the values in the boundary condition vector can be chosen to:

$$q_k = \dot{q}_{source}''(k \cdot l_{panel}) . \quad (5.7)$$

The respective counting index  $k$  is thereby considered in a relative coordinate system, i.e.  $k$  starts from Zero to the number of panels within the appropriate section. In most cases, functions for the heat source distribution are not available. For this cases, values from suitable measurements, e.g. cutting force measurements can be taken into account. Considering the appropriate speeds a value for the overall heat source strength  $q_{source}$  can be given. When assuming an equal distribution over the section length, the values for  $q_k$  in the boundary condition vector can be given to:

$$q_k = \frac{\dot{q}_{source}''}{k} . \quad (5.8)$$

In this thesis, equal distributions for the heat source strengths were considered using force measurements, as described later. The needed parameters for the boundary condition vector are summarized in Table.

**Table 5.2:** Overview of Boundary Condition Parameters  
*Übersicht der Randbedingungsparameter*

adiabatic boundaries	transparent boundaries	heat source strengths
$b_k = 0$ (e.g. uncut work piece)	$s_k = 0$ (only in combination with other panel)	shear zone $q_{shear}$ contact zone $q_{rake}$ (clearance face $q_{clearance}$ )

For the panel method itself, it is notable that the boundary condition vector contains the source strengths in shear zone and contact zone, which in reality are dependent on cutting parameters and work piece material. After defining the influence matrix and the boundary condition vector, the derivation of the temperature fields is only mathematical, i.e. there is not any more information about cutting parameters needed. Hence, the boundary condition vector significantly influences the quality of the later modeling results. For consideration of the cutting conditions, mainly the boundary condition vector with consideration of contact length at the rake face and length and angle of the shear zone heat source should be considered from the beginning. A calibration as conducted in the elementary solutions approach is not possible.

### 5.2.3 Generating the Potential Function

#### *Generieren der Potenzialfunktion*

The discretization and the definition of nodes and panels was used for a systematic positioning of the source solution in the  $x$ - $y$  space. For this, only the induced heat flows from each panel were considered. For plotting the temperature fields, the original source solutions need to be identified. While the position and therefore the dislocation parameters are defined, for the unknown source strengths have to be determined. With the influence matrix  $A$  and the boundary conditions vector  $b$  the linear equation system is defined and can be solved:

$$A \cdot s = b \Rightarrow s = A^{-1} \cdot b. \quad (5.9)$$

The vector  $s$  contains all source strengths for each panel,  $A^{-1}$  is the inverse matrix of  $A$ . By solving the linear equation system, the unknown source strengths can be determined and put into the appropriate elementary source function. Considering this complex function for the source solutions yields:

$$\sum_i \frac{s_i}{2\pi} \cdot \ln(z - z_i). \quad (5.10)$$

In Equation 5.10 adiabatic panels and panels from the sections with heat sources are included. Transparent panels disappear from the equation, i.e. no source solution is placed at the respective location. The dislocation parameter  $z_i$  can be determined with the appropriate nodes defining the panel  $P_i$ :

$$z_i = [x_i + \frac{x_{i+1} - x_i}{2}] + i \cdot [y_i + \frac{y_{i+1} - y_i}{2}]. \quad (5.11)$$

The nodes are thereby defined by the positions  $(x_i, y_i)$  and  $(x_{i+1}, y_{i+1})$ . Equation 5.11 means that the sources are assumed to be in the middle of each panel, as it was defined in the fundamentals of the panel method.

It should be noted that Equation 5.11 is not different to the method conducted in the elementary solutions approach. The appropriate parameter study yielded that the number of source solutions, distribution of source solutions and unequal source strengths influence the temperature field. All these parameters are now systematically considered with the help of the panel method. This result shows the limited transferability of the parameter study from the elementary solution approach. For the studied cases a number  $n = 30$  was found to be sufficient, respectively there was no more influence observable on the resulting temperature field.

When setting up the linear equation system for the panel method, a number  $i = 2000$  of panels was chosen. A representative plot is shown in Figure 5.6. This choice is dependent on the chosen panel length  $l_{panel} = 2 \mu\text{m}$ . Obviously, there will be an influence on condition and stability for the solution of the linear equation system. Further studies on code verification were not conducted in the frame of this thesis as all results yielded were suitable.

In the figure, an unscaled plot corresponding to the discretization shown in Figure 5.4 before presented. The distinct choice of discretization and boundary condition parameters may not be of interest at this point. The discretization of the cutting kinematics is also sketched in the figure for easier discussion. Sections considered adiabatic are marked in blue, those with heat input are marked red.

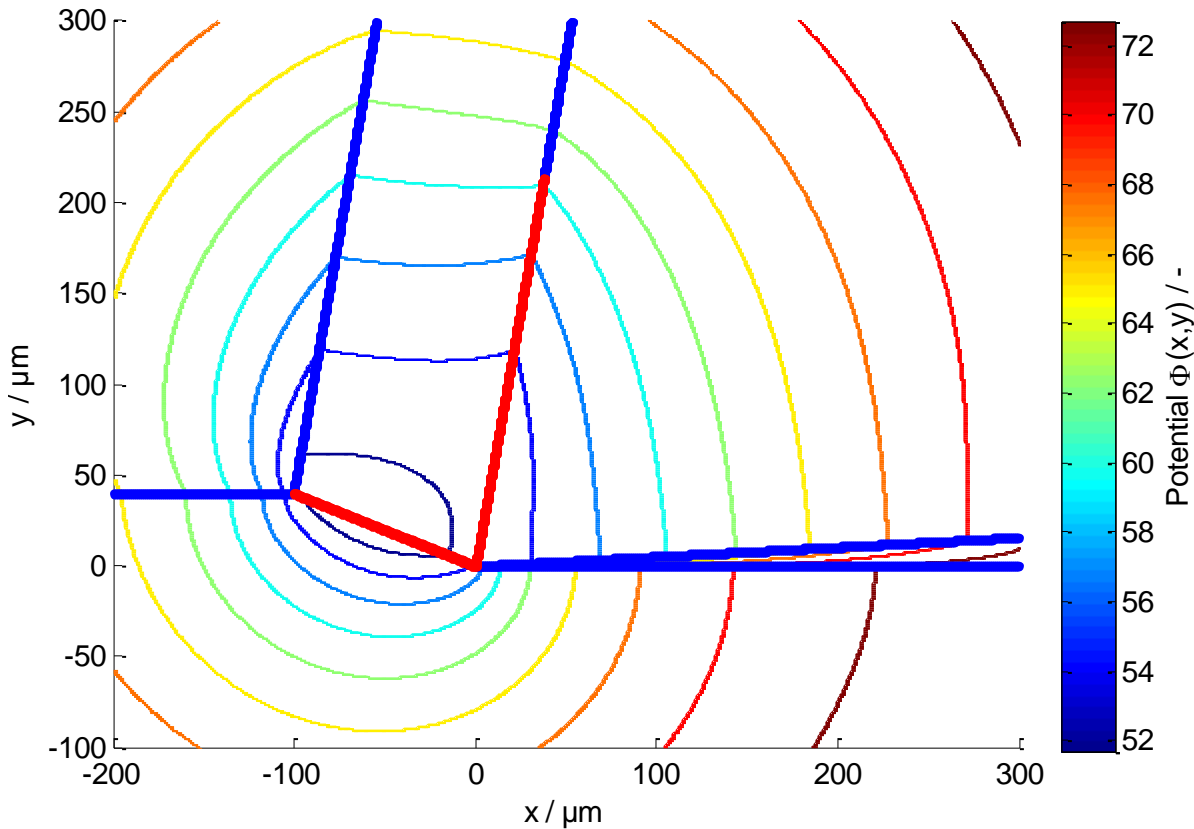


**Figure 5.6:** Plot of Unscaled Potential Function

*Darstellung der unskalierten Potenzialfunktion*

As in the elementary solution plots before, the unscaled function yields an increasing value of the potential lines away from the heat sources, i.e. the scale is flipped. When using the potential plot for later temperature fields this fact will be considered during calibration.

The shown approach using source panels does not include additional influences resulting from parallel solutions or other influences which could be correlated to the cutting velocity. This is also visible because of the parallel isotherms in the chip. As validated later, this approach is in good agreement for low cutting speeds, however is not suitable for higher cutting speeds. Event though no parallel function is included, the influence of movement can be considered by changing distinct source strengths. A possible discretization is shown on the left-hand side of Figure 5.7.

Section 3 is thereby placed at the upper boarder of the chip. The position could e.g. the location where the chip leaves the contact to the rake face in reality. A possible adiabatic area above the main friction zone is considered with section 4. Panel 3 is consisting of transparent panels, i.e. no heat source or adiabatic boundary is considered. Additionally to section 3, sources on section 8 (shear zone) are placed. These

boundaries simulate the material flow in the chip by additional heat sources. The corresponding strength are chosen freely and need to be determined by means of calibration. All other sections and their appropriate values in the boundary condition vector are maintained.

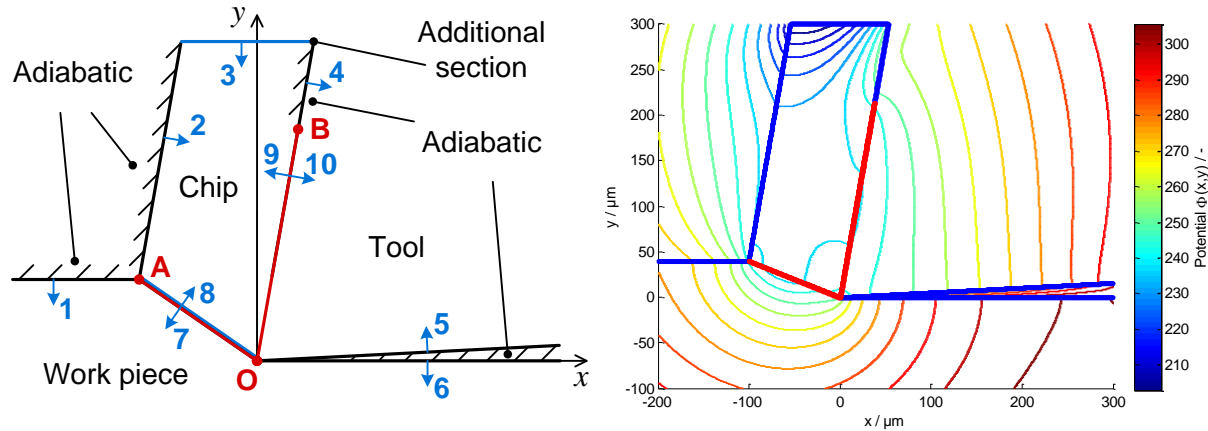


**Figure 5.7:** Consideration of Material Flow

*Berücksichtigung des Materialfluss*

The panels considered in the chip can be expressed by an additional boundary condition vector  $b_{flow}$ . This vector contains the additional constant superposition due to material flow. Equation 5.9 subsequently can be expressed as:

$$A \cdot s = b + b_{flow} \Rightarrow s = A^{-1} \cdot (b + b_{flow}). \quad (5.12)$$

On the right-hand side of the figure, the influence on the unscaled potential field is shown. As intended, the isotherms in the chip feature a shape which includes material flow from work piece into the chip. As physical sound value the PÉCLET Number or thermal number can be used. The PÉCLET Number of the chip is defined as:

$$Pe_{ch} = \frac{h \cdot v_{ch}}{a} = \frac{t \cdot v_c}{a}. \quad (5.13)$$

The product of chip thickness  $h$  and chip velocity  $v_{ch}$  can thereby be replaced by the cutting speed  $v_c$  and the uncut chip thickness  $t$  due to mass conservation,  $a$  is the temperature diffusivity. The plot shown is not perfectly matching with real temperature fields and may be understood as visualization for the influence of the additional section. The use of PÉCLET Number or thermal number is in common in many temperature models. According to the chosen characteristic length, the number can be considered as the ratio of local velocity and a characteristic "heat velocity".

In general, the use of additional sections can be used to consider more realistic boundary conditions for the modeling. Further sections can be placed at the work piece region or in the tool to consider the influence of the cutting speed. Additional sections can be furthermore applied to include shapes of the heat sources which are more complicated than the ideal thin heat source. However, it has to be considered that only closed areas can be modelled, i.e. the panels have only influence on one side.

### 5.2.4 Calibration

#### *Kalibration*

While the calibration was one of the most significant steps within the elementary solutions approach, for the panel method the calibration is the last step. Experimental measurements were necessary at an early step of the modelling process. Contrary to the latter approach, the values of the parameters within the temperature function, i.e. the real-valued function of  $F(z)$ , are not changed.

At the current modelling state, the temperature function was generated without the consideration of any material parameters. The potential function  $T(x,y)$  needs to be calibrated by means of a calibration function:

$$T_{cal} = \frac{\lambda}{\lambda_{ref}} \cdot T(x, y) + T_{ref}. \quad (5.14)$$

For this calibration the heat conductivity  $\lambda$  and two reference values  $\lambda_{ref}$  and  $T_{ref}$  are needed. For the heat conductivity the real value of the work piece material can be considered. In Figure 5.8 a possible distribution of heat conductivities is shown. The distribution is plotted into the discretization plot for visibility. For the chip and the work piece area thereby the same values are assumed.

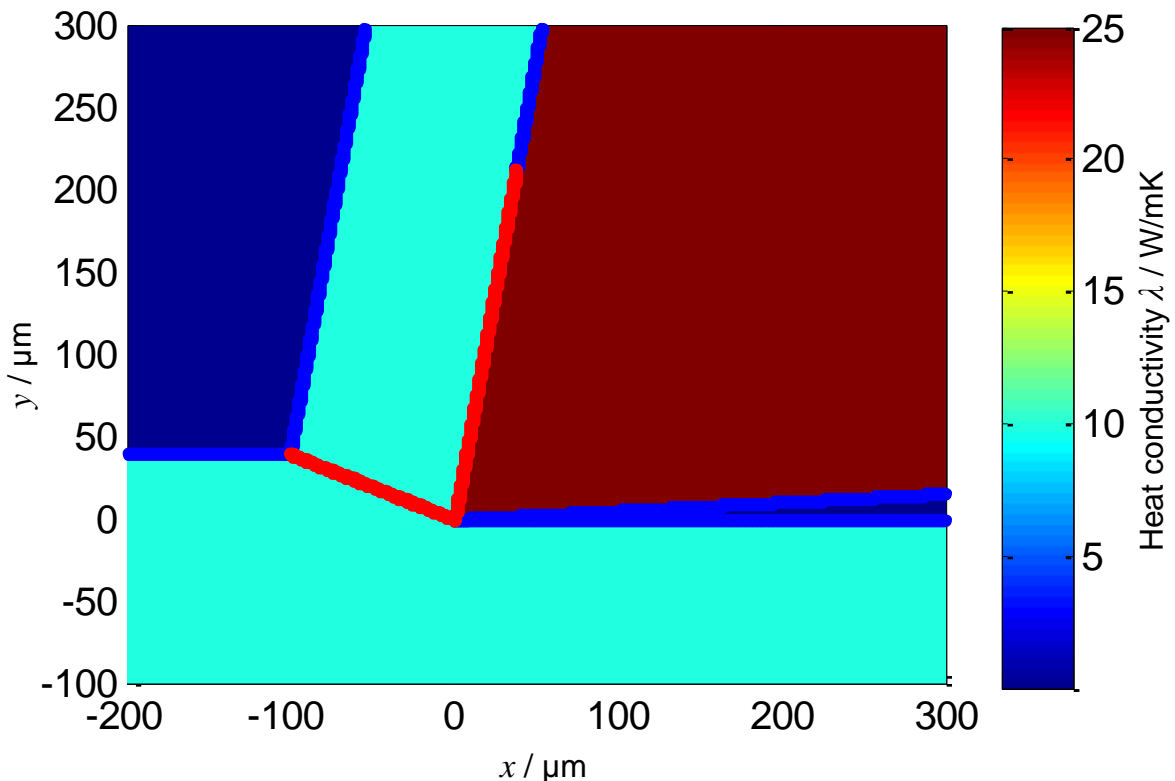


**Figure 5.8:** Consideration of Different Heat Conductivity Areas

*Berücksichtigung verschiedener Wärmeleitfähigkeitsgebiete*

In principal, general distribution of heat conductivity can be considered. For this work only the heat conductivities of the work piece material and the tool material were tak-

en into account. For the calibration, the appropriate panels are scaled with the heat conductivity and multiplied with the respective induced velocity.

For the determination of the temperature distribution, two methods were investigated, namely the inverse method and the integral method. A sketch of both methods is shown in Figure 5.9. With the inverse method shown on the upper left-hand side of the figure, the temperature distribution is calibrated from with the initial temperature  $T_0$  at the root point. However, the reference temperature can in general be chosen freely. The temperature is subsequently computed along both axes with the help of the heat conductivity and the heat flux values  $q$  from the boundary conditions vector.

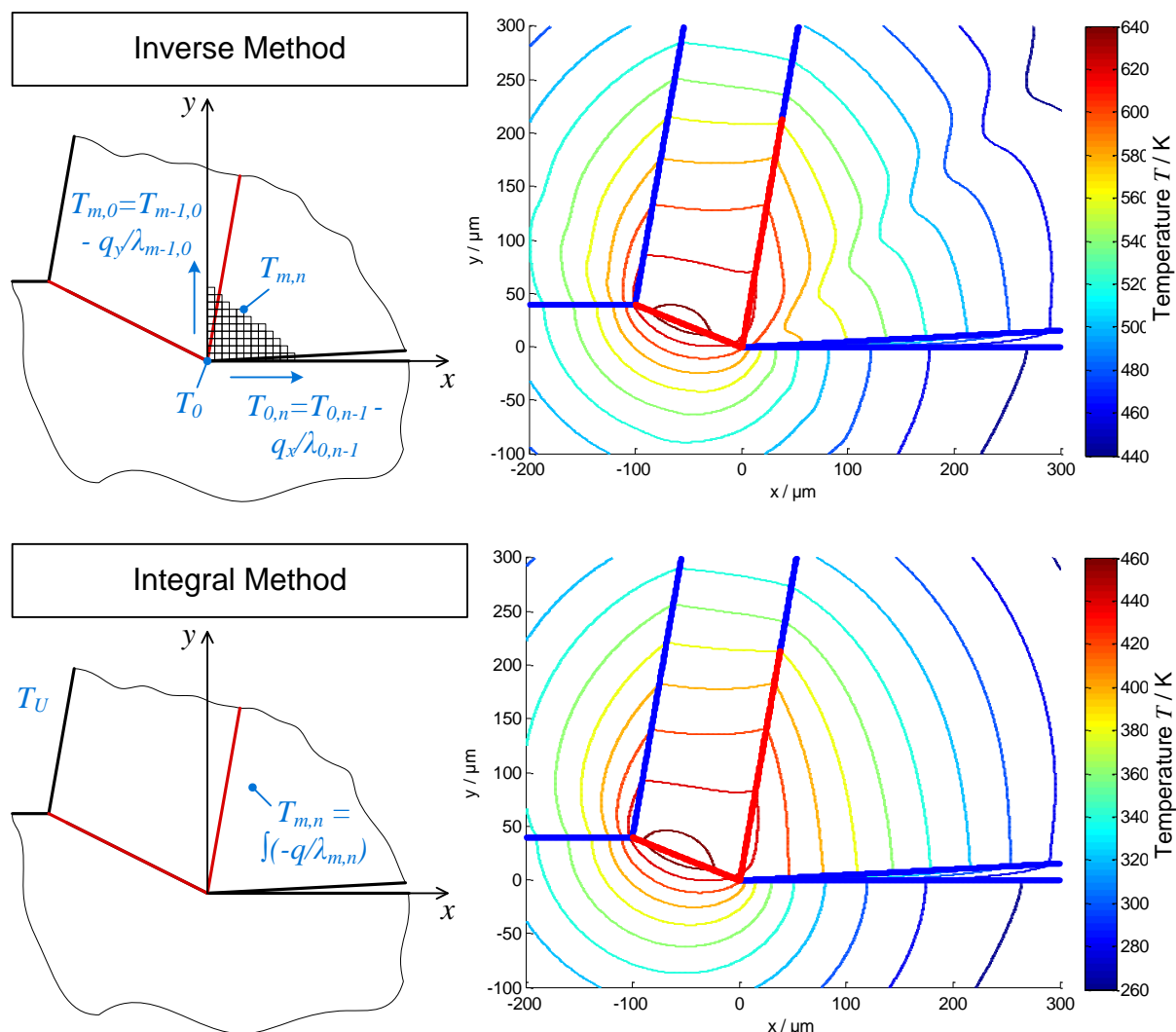


**Figure 5.9:** Inverse and Integral Calibration Method

*Inverse und Integrale Kalibrierungsmethode*

For temperatures on the  $x$ -axis e.g. by using the expression:

$$T_{0,n} = T_{0,n-1} - \frac{q_x}{\lambda_{0,n-1}} . \quad (5.15)$$

After calibration of the temperatures on the axis, the quadrants can be calibrated by means of averaging of nodes next to each other.

A plot of a temperature distribution determined with this method is shown on the upper right-hand side of the figure. As initial temperature  $T_0 = 600$  K and the heat conductivity distribution from Figure 5.8 was chosen. The curves from the resulting temperature plot are similar to the potential plots, however irregularities can be found, especially in the tool. These irregularities are presumably caused by rounding errors which are resulting from the averaging.

A second possibility to determine the temperature values can be done by using an integration function. The principle is the same then with the discrete inverse method, however optimal integration functions can be considered. For the integral method the temperature is derived by using:

$$T_{m,n} = -\int \frac{q}{\lambda_{m,n}} . \quad (5.16)$$

Again a reference value for the temperature needs to be defined. For the plot shown on the lower right hand side of Figure 5.9, for the reference temperature  $T_U = 295$  K was chosen. The resulting temperature distribution did not yield equivalent irregularities, however the temperature values were lower. The shape of the isotherms is furthermore not influenced as significantly as with the inverse method. While the run of the isotherms is more realistic with the integral method, in the temperature plot temperatures below the reference temperature occur, which is not sensible. These values occurred often when using the integral methods. For an optimal use a combination of the integral method additionally to the use of Equation seems sensible. A similar approach as the integral method for calibration of an FE Model was conducted from AL JOURDI [AL J12, p. 65].

For the calibration in this thesis, mainly the second method was used in combination with a reference value for the heat conductivity according to  $\lambda_{ref}$  Equation 5.14. In practice, initial recommendations for the reference parameters of Equation 4.15 were investigated by using the integral method. The concrete values for the parameters were however calibrated against real experimental values, as the deviation in the most cases were significant or physically not suitable (negative temperatures). Despite the method for deriving the calibration parameters, the values should in principle correlate to the distinct material and cutting condition applied. When analyzing the parameters, the term  $\lambda_{ref}$  influences both shape and absolute temperature value, while the reference temperature  $T_{ref}$  can be considered as static offset value.

Further investigations with more complicated distributions of the heat conductivity (temperature dependent values) were tested. In most cases however the results yielded irregularities similar to the one shown when using the inverse method. The reason might again be average errors. A further numerical study in terms of code verification was not conducted during this thesis. Furthermore, a calibration without considering varying heat conductivities is assessed to be sufficient, as the objective is the development of the principal use of potential theory, respectively the panel method.

## 5.3 Model Outcomes

### *Modellergebnisse*

After conducting the discretization of the cutting geometry, the definition of the boundary conditions, the generating of the potential function and subsequent calibration, the temperature fields can be plotted. As described, the panel method applied in this thesis is solely based on source panels. The analytical function describing the temperature therefore is equivalent to the one yielded with the elementary solutions approach. However, the number of used sources is much greater with and the parameters are determined in the described systematic way. Even though the functions could be determined manually in principle, the higher number of solutions and the necessary solving of the linear equation system make the panel method more a numerical method. The solution itself is still a solution of the partial differential equation of heat conduction.

One major advantage of potential theory in principle is the possible consideration of complex geometries and wear. This is viable in particular with the panel method, where geometries can be defined freely. As for each panel the appropriate boundary condition has to be defined, the influence of additional geometrical features can be either real or imaginary (as it was shown for the imaginary panel at the chip for consideration of the cutting speed influence). In the following representative temperature fields from the panel method are presented.

### 5.3.1 Temperature Distribution Fields

#### *Temperaturverteilungsfelder*

After the calibration of the potential function, the absolute values for the temperature fields can be plotted. As shown, furthermore the shape of the isotherms is influenced by the calibration. In Figure 5.10 two representative temperature plots are shown. The plots show predictions for two different uncut chip thicknesses ( $h = 40 \mu\text{m}$  on the left-hand side and  $h = 60 \mu\text{m}$  on the right-hand side). The appropriate discretization and boundary condition parameters are provided in the figure. For the number of panels a value of  $n = 2500$  was chosen. As described, the real number of panels varies slightly dependent on the lengths of the characteristic sections and the chosen panel length. A calibration as described in the previous chapter was conducted, the detailed parameters are not of interest at the moment and will be provided in the validation of Chapter 6.

Comparing the two plots yields that the temperature fields a similar behavior for both cases. This behavior is in line with the expected result, as only minor changes of the model parameters were made. The fields show the typical behavior which was already determined during the elementary solutions approach, i.e. the isotherms in tool and work piece feature a concentric behavior, while the temperature distribution in the chip shows parallel isotherms. The area of maximum temperatures is found at the

shear zone. Regarding the boundary conditions, the location of the maximum area is caused by the higher value for the source strength for the panels at the shear zone.

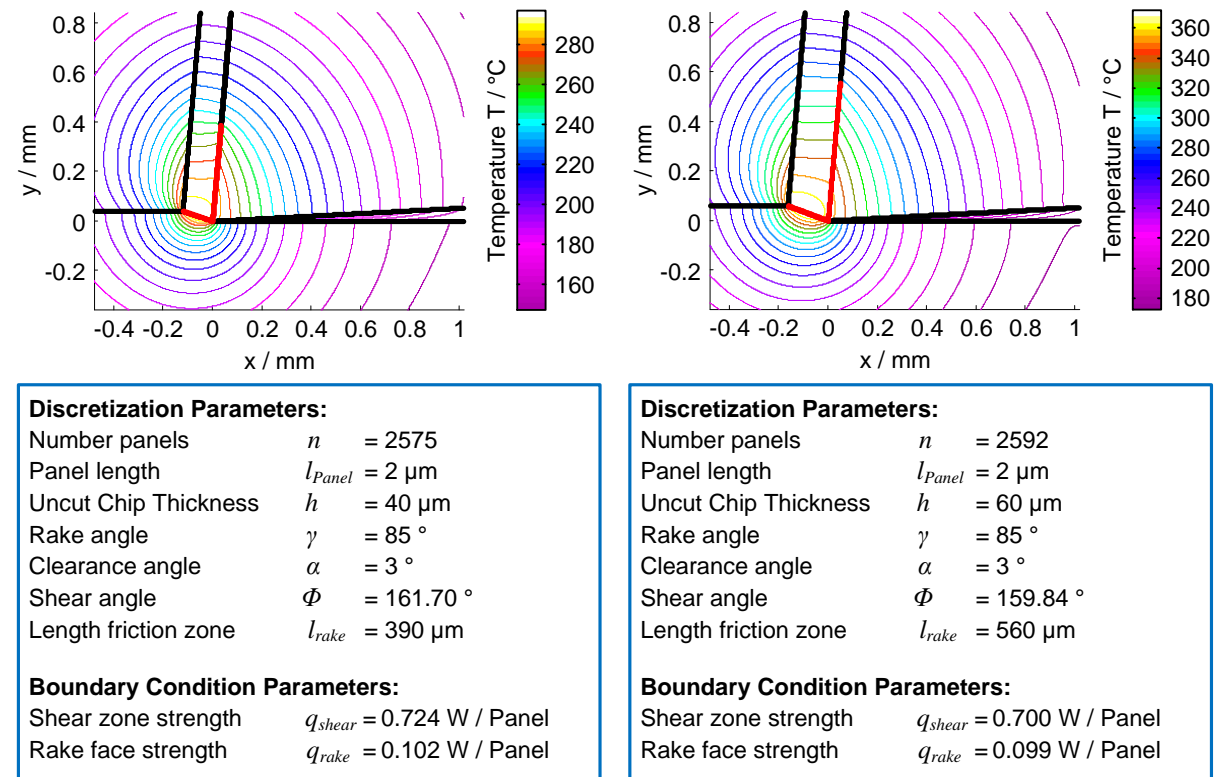


**Figure 5.10:** Exemplary Temperature Fields from the Panel Method

*Exemplarische Temperaturfelder der Panelmethode*

While the temperature fields in work piece and tool seem sensible, the distribution in the chip might be valid only for low cutting speeds. As will be shown in the validation section of this thesis, the predicted distribution is in good agreement with the reality for the broaching experiments.

### 5.3.2 Consideration of Wear and Tool Geometry

*Berücksichtigung von Verschleiß und Werkzeuggeometrie*

While the temperature fields presented in Figure 5.10 assumed an ideal sharp cutting edge, i.e. no consideration of cutting edge radius and no contact of the clearance face and the work piece surface. The latter is true for all real cutting processes, either due to the non ideal sharp cutting edge or due to clearance face wear. Both phenomena influence the resulting temperature field and will consequently be considered with the panel method within the scope of this thesis. More complex geometries, e.g. displacement of the cutting edge, crater wear on the rake face or chip breaker geometries could in principle be considered with the panel method.

In Figure 5.11 two representative temperature fields with consideration of cutting edge radius and contact at the clearance face are shown. The presented cases are equal to those before in terms of geometry and uncut chip thickness. In the figure, the appropriate section is indicated for better visibility, the cutting edge radius is con-

sidered, however not significantly visible in the discretization plot. A cutting edge radius of  $r_\beta = 10 \mu\text{m}$  was considered for both cases.

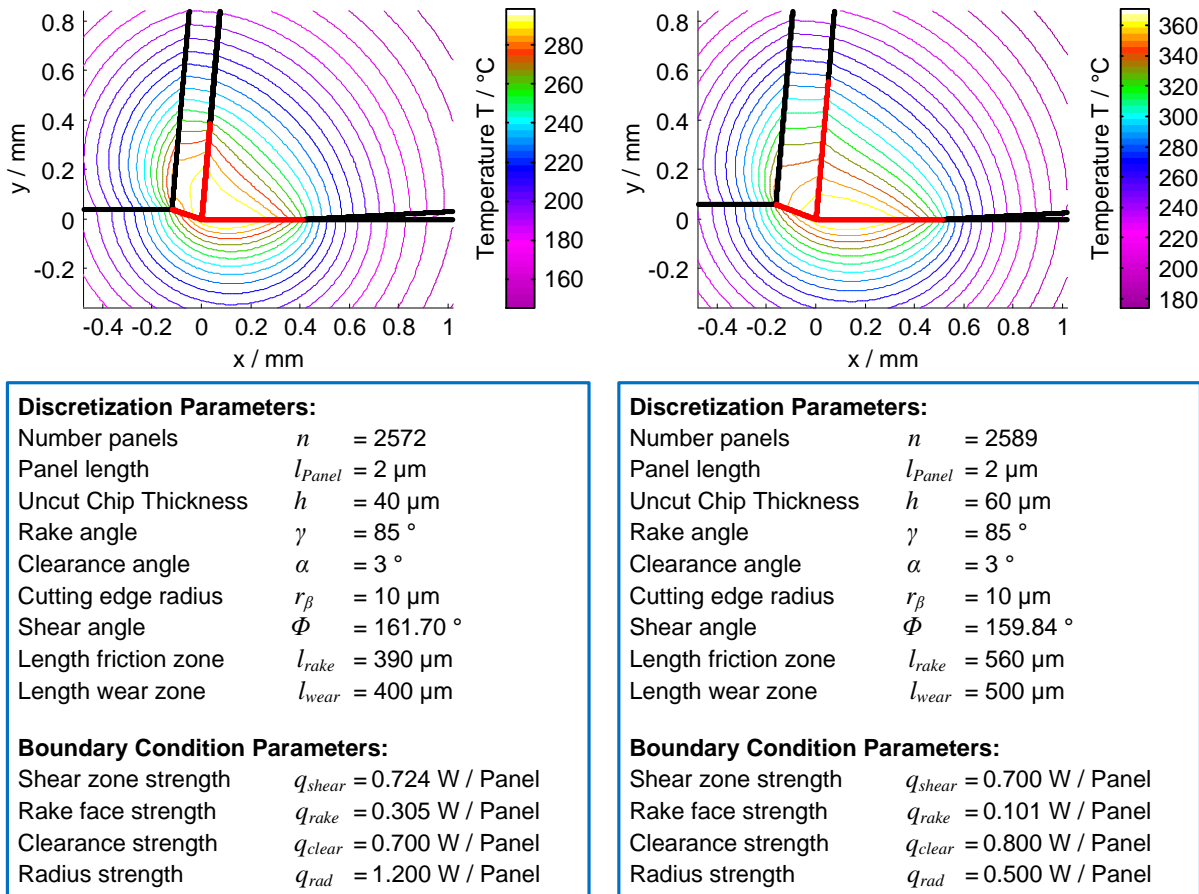


**Figure 5.11:** Consideration of Clearance Face Contact and Cutting Edge Radius  
*Berücksichtigung von Freiflächenkontakt und Schneidkantenradius*

For each additional section, which is not considered to be adiabatic, additional boundary conditions need to be defined. These additional values for the appropriate panels on the cutting edge radius and the clearance face are given in the figure (clearance face source strength  $q_{\text{clear}}$  and strength of the panels on the radius  $q_{\text{rad}}$ ).

Regarding the influence of the consideration of clearance face contact and cutting edge radius, the most significant changes to the temperature field can be found in the tool and the cut work piece region. The area of maximum temperatures is shifted from the shear zone to the clearance face along the cut work piece area. The isotherms in the work piece are distorted and become rather elliptical. For the tool a widening of the isotherms can be observed, enhancing the area of maximum temperatures to the clearance face. The isotherms in the chip, however are only slightly influenced.

Comparing the two cases of uncut chip thicknesses, the influence seems more significant relative to the ideal case before. Both temperature field result in a more unique characteristic, also the specific run of the isotherms differs from each other. The consideration of cutting edge radius and clearance face contact seems a sensible choice for the validation against experimental results.

## 5.4 Intermediate Conclusions from Panel Method

### *Zwischenfazit der Panelmethode*

The panel method provides a more systematic approach for the use of the potential theory for thermal modelling of metal cutting. For the positioning and the choice of the distinct solution parameters there is no need for parameter studies or calibration, the parameters are furthermore defined by physical and geometrical conditions. In this chapter, the use of source panels was investigated. For the use of the panel method the following steps need to be conducted:

- The first step of the panel method is the discretization of the cutting kinematics. For the discretization, nodes and panels are used to discretize the characteristic cutting kinematics and thermal boundaries of metal cutting. This can be most efficiently done by definition of sections. Panels are equivalent to source solutions. The discretization is summarized in the influence matrix. For this matrix, only geometrical input parameters are needed. However, some parameters need to be assumed, modelled or measured as they are not known *a priori* (e.g. chip thickness or shear angle).
- After defining the sections and appropriate nodes and panels, the boundary conditions for each sections need to be defined. In general, either adiabatic boundaries or those with a preset heat flux value are possible. For setting the latter, again suitable assumptions, models or measurements are needed. After choosing the boundary condition for each panel, the values are summarized in the boundary condition vector. The influence of cutting speed and material flow can in principle be considered.
- With the defined influence matrix and the boundary condition vector a linear equation system can be formulated. The source strengths of the panels are hereby the unknown variables. These sources are chosen by solving the linear equation system in a way that the combined influence of all panel on each other is equal to the predefined values in the boundary condition vector. By solving the system, the source strength are known and can be put into the elementary source solution. Hence, the temperature field can be plotted.
- The calibration needed for the method can be considered a global calibration, i.e. the distinct solution parameters are not changed after solving the linear equation system. The only calibration needed for the method is a relative heat conduction value and an offset temperature (i.e. the initial work piece temperature).

Summarized, the panel method showed good results without the need for calibration of the distinct parameters. The cutting parameters and the material parameters need to be defined implicitly by the definition of the influence matrix and the boundary condition vector. A later consideration is not possible and not allowed in terms of the methodology, however a global calibration is necessary. For the final conclusion, both models need to be validated by means measured temperature fields from cutting experiments.

# 6 Model Validation

## Modellvalidierung

This chapter describes the process of validation for the developed models using the two modeling approaches. Validation can only be realized by means of real cutting experiments. The cutting experiment setups are described in Chapter 6.1 as well as the applied thermal measurement method. Due to the significance of the thermal boundary conditions, particularly for the panel method approach, an investigation of the experimental results using infrared camera images is provided in Chapter 6.2. The validation of the developed models and a comparison of both approaches is finally presented in Chapter 6.3.

### 6.1 Description of Conducted Cutting Experiments

#### Beschreibung der durchgeführten Zerspanversuche

One of the significant features of the developed methodologies is the modular application of complex potential functions yielding a variety of possible temperature and heat flow field characteristics. These characteristics are e.g. the location of maximum temperatures, shape of the isotherms or different cutting geometries.

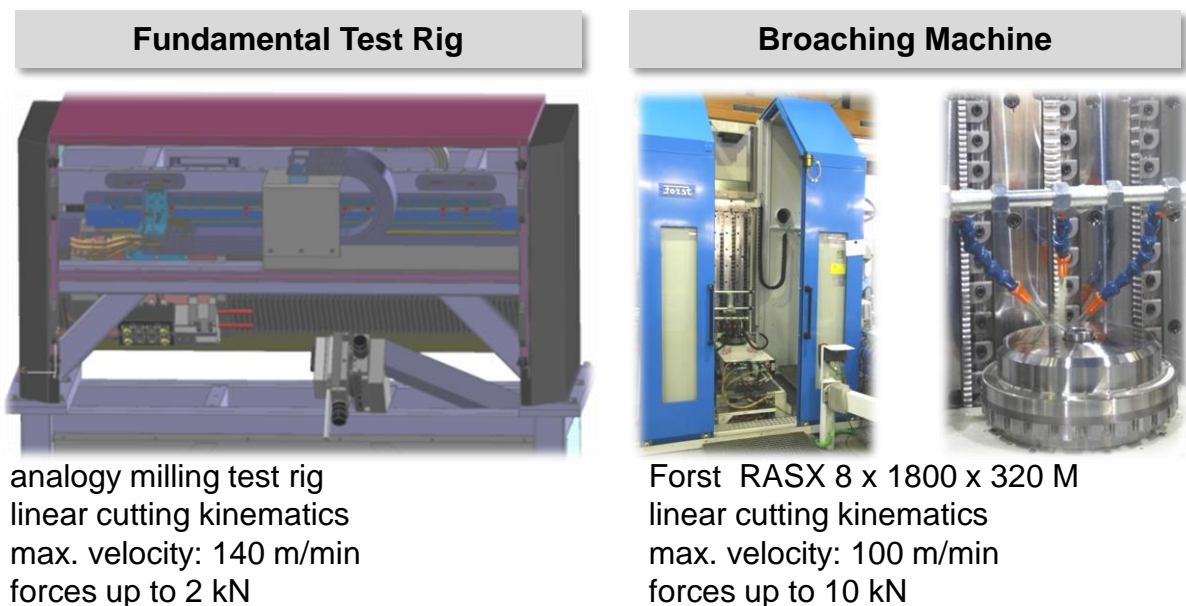


**Figure 6.1:** Test Machines Used for Cutting Experiments

*Testmaschinen zur Durchführung der Zerspanexperimente*

Due to the model assumptions, two-dimensional cutting experiments were chosen, i.e. the temperature fields were assumed to be equal in planes parallel to the cutting plane. The machines chosen for the experiments are shown in Figure 6.1. For validation of the elementary solutions approach, a fundamental test rig, developed for analogy milling trials was chosen. The panel method approach was mainly validated

on a broaching machine. Both machines feature a linear cutting kinematic, which is advantageous for the accessibility of the measurement devices.

Both methods are assumed to be valid independently from the work piece and tool material, when parameterized correctly. For validation of the material influence, five different work piece materials and two tool materials were chosen. An overview with the abbreviations used in this thesis is given in Table 6.1.

**Table 6.1:** Work Piece and Tool Materials

*Werkstück- und Werkzeugwerkstoffe*

Abbreviation	Classification	Treatment	Description	Heat Conductivity $\lambda$ [W/mK]
Work Piece Materials				
C45	C 45 E	normalized annealed	steel alloy	45.1 (300 °C)
IN718	NiCr19NbMo	forged, solution annealed, hot aged	nickel-based alloy	11.4 (20 °C)
X6Ti26	X6NiCrTi26-15	forged, solution annealed, hot aged	creep resisting steel	18.7 (300 °C)
X20Cr13	X20Cr13	forged, solution annealed, hot aged	steel alloy	30.0 (20 °C)
Tool Materials				
HSS	HS-12-1-5	powder metallurgical, annealed, hardened	high speed steel	20.0 (20 °C)
WC	WC-8Co	sintered	solid carbide	88.4 (300 °C)

The work piece materials were chosen due to their different machinability and thermal behavior during cutting. A more detailed characterization can be found in [BUSC14, pp. 34–39]. The heat conductivities of the materials C45, HSS and WC were measured with the laser flash method, the values for the other materials were taken from the supplier's data sheet. Where available the value at 300 °C was taken into account, as the region around can be considered as average magnitude.

### 6.1.1 Measurement Devices and Method

#### Messgeräte und -methode

Measuring of temperatures in metal cutting requires high experimental effort and is often prone to errors. In general, measurements requiring contact between sensor and measuring object and contactless measurements can be distinguished. For the latter, heat radiation thermometers, measuring the thermal emission of a body, are suitable for metal cutting applications [DAVI07, p. 597]. The heat radiation thermometers can be furthermore distinguished into spectral band thermometers and ratio thermometers. Spectral band thermometers hereby collect radiation over a distinct wavelength range, while ratio thermometers measure at two or more distinct wavelengths. For the cutting experiments both devices were applied. As spectral band thermometer an infrared camera (FLIR SC7500 MB) was used. The ratio radiation measurement was conducted with a two-color pyrometer (FIRE 2). A schematic view of the different principles with their characteristic wavelengths and typical spectral radiance curves are shown in Figure 6.2.

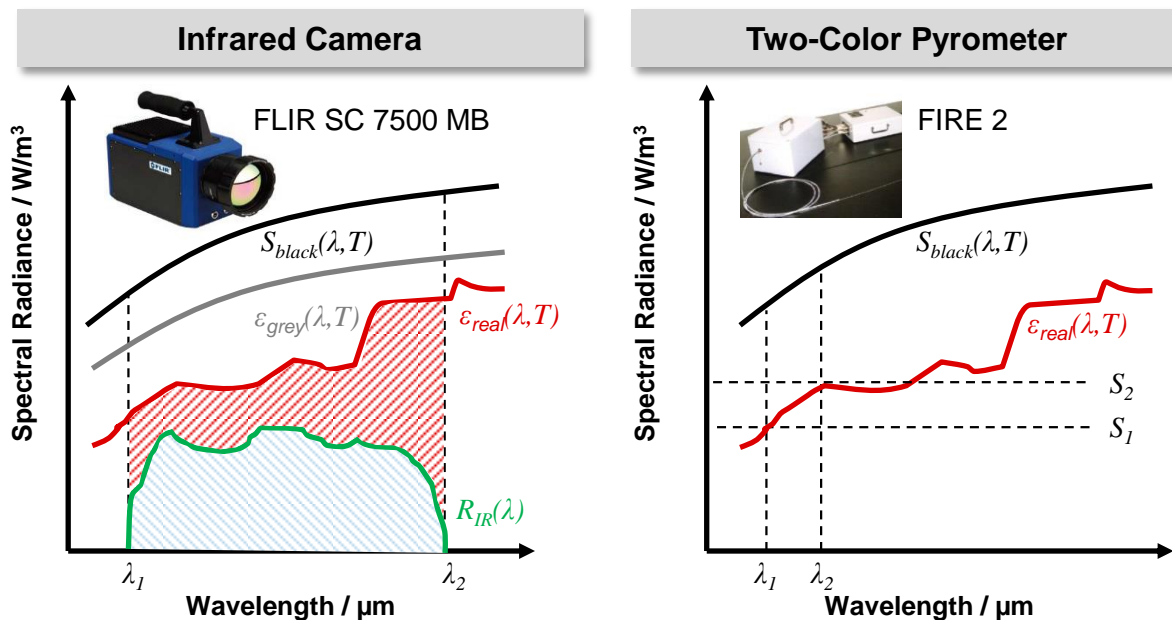


**Figure 6.2:** Characteristic Parameters of Radiation Thermometers

*Charakteristische Werte von Strahlungsthermometern*

According to PLANCK's LAW, the spectral radiance of an ideal black body  $S_{black}$  (i.e. a body which absorbs and emits all radiance) with Temperature  $T$  at wavelength  $\lambda$  can be calculated using the expression:

$$S_{black}(\lambda, T) = \frac{c_1 \cdot \lambda^{-5}}{\exp\left(\frac{c_2}{\lambda T}\right) - 1}. \quad (6.1)$$

In Equation 6.1,  $c_1$  and  $c_2$  are constants. The digital signal provided by the sensors of both measurement devices is correlated to this ideal spectral radiance, however real bodies do not show this ideal behavior. A sketch of an ideal spectral radiance curve

and that of a so called grey body (i.e. a body where the reduced spectral radiance can still be computed with Equation 6.1 using a scaling factor independent of the wavelength) is given on the left-hand side of Figure 6.2. For a real body, the spectral radiance  $\varepsilon_{real}(T, \lambda)$  owns a complex behavior dependent on the wavelength.

Temperature values provided from an infrared camera are mainly influenced by the applied optics, the sensor material and the signal processing. The incoming heat radiation is focused on a focal plane array with the help of a lens. A focal plane array is a structured sensor (pixel array) made from infrared sensitive material. This material generates a voltage proportional to the incoming radiance:

$$T_{IR} \sim K_{IR} \cdot \int_{\lambda_1}^{\lambda_2} R_{IR} \cdot \varepsilon_{real} \cdot S_{black} d\lambda. \quad (6.2)$$

In Equation 6.2, the radiance of the real body  $\varepsilon_{real} \cdot S_{black}$  is multiplied with the response function of the sensor. This function quantifies the response of the sensor material dependent on the wavelength. The temperature shown from the infrared camera TIR is correlated to the total radiance between within the spectral band of the wavelengths  $\lambda_1$  and  $\lambda_2$ . Further influences e.g. influence of the lens, camera housing temperature, or influence of signal processing are summarized in the calibration factor  $K_{IR}$ . From Equation 6.2 the strong influence of the emissivity of the real body becomes obvious. Considering the wavelength dependent response function yields, that temperatures provided from infrared camera images can not be simply calibrated in terms of a single scaling factor. The significant characteristics for the used camera are shown in Table 6.2.

**Table 6.2:** Comparison of Thermometer Properties

*Vergleich der Thermometereigenschaften*

	SC 7500 MB	FIRE 2
sensor material	InSb	InGaAs
min. resolution	15 µm (640 x 512 Pixel)	120 - 320 µm (fiber dependent)
charact. wavelengths	$\lambda_1 = 3,7 \mu\text{m}, \lambda_2 = 5,1 \mu\text{m}$ (for lens used)	$\lambda_1 = 1,7 \mu\text{m}, \lambda_2 = 2,0 \mu\text{m}$

The characteristic wavelengths are given for the far field lens used in the experiments, featuring the resolution of 15 µm at a working distance 30 cm. In the table, the properties of both, infrared camera and two color pyrometer are shown.

Different to the infrared camera, the two color pyrometer acquires no spatial resolved signal. The incoming radiance is received with a fiber, the resolution therefore can be minimally the fiber diameter. The radiance beam is divided by a beam splitter, which transmits only radiance with the two characteristic wavelengths. (For the experiments two different fibers were used, one with a diameter of 120 µm and one with

$320 \mu\text{m}$ .) Both beams are focused on a sensor each and are processed individually. The temperature  $T_{\text{Pyro}}$  provided by the pyrometer is proportional to the ratio of the spectral radiance values  $S_1$  and  $S_2$  at the characteristic wavelengths  $\lambda_1$  and  $\lambda_2$ :

$$T_{\text{Pyro}} \sim K_{\text{Pyro}} \cdot \frac{\varepsilon_{\text{real}}(\lambda_2)}{\varepsilon_{\text{real}}(\lambda_1)} \cdot \frac{S_2}{S_1}. \quad (6.3)$$

If the wavelengths are chosen close to each other, the influence of the emissivity  $\varepsilon_{\text{real}}$  vanishes. In this case, the temperature provided from the pyrometer is directly dependent on the ratio of the radiances and a calibration factor  $K_{\text{Pyro}}$ . Hence, the pyrometer yields a relative accurate absolute temperature value compared with the infrared camera. However, the temperature value is only available at one measurement location.

For the experiments conducted in this thesis, both measurement devices were used simultaneously, in order to combine the advantages of each measurement principle. The approach is described in Figure 6.3.

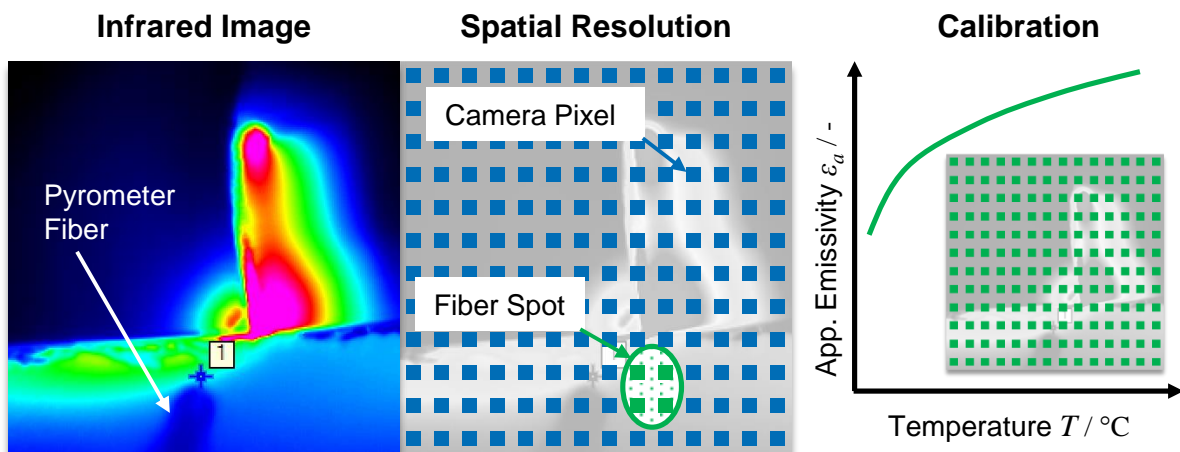


**Figure 6.3:** Emissivity Calibration using Infrared Camera and Pyrometer

*Emissionsgrad Kalibrierung mittels Infrarotkamera und Pyrometer*

In principle, the pyrometer measurement spot was pointed into the field of view of the infrared camera, in a way that a distinct area of the measurement scene is common for both devices. The shape of the pyrometer can be seen on the left-hand side of the figure. Due to the inclination, an elliptic measurement spot of the fiber is generated. By locating the pixels of the focal plane array of the camera inside the measurement spot, the apparent emissivity of the measurement object can be calculated:

$$T_{\text{Pyro}}(t) = T_{IR,spot}(t) \rightarrow \varepsilon_a(T). \quad (6.4)$$

The temperature of the pyrometer  $T_{\text{Pyro}}$  is set equal to the average temperature of the pixels  $T_{IR,spot}$  in the measurement spot. When assuming a correct temperature value of the pyrometer according to Equation 6.3, the apparent emissivity  $\varepsilon_a(T)$  can be iteratively calculated, eliminating the time  $t$ . By assuming the same emissivity behavior

for regions outside the measurement spot, the whole infrared image can be calibrated. The term apparent emissivities refers to the calibration constants in Equations 6.2 and 6.3, meaning that numerical values of emissivities need to be determined for the measurement devices used during the experiment (e.g. each infrared camera owns a unique response function of the sensor). Details of the method, i.e. enhancement to regions with other material in the measurement scene and synchronization of the devices were published in [KLOC13].

An a priori calibration for all work piece and tool material used conducted with this method. A test piece from the same charge used in the experiments was therefore heated in a furnace and measured stepwise when reaching certain temperature levels. The results for the apparent emissivities are summarized in Figure 6.4.

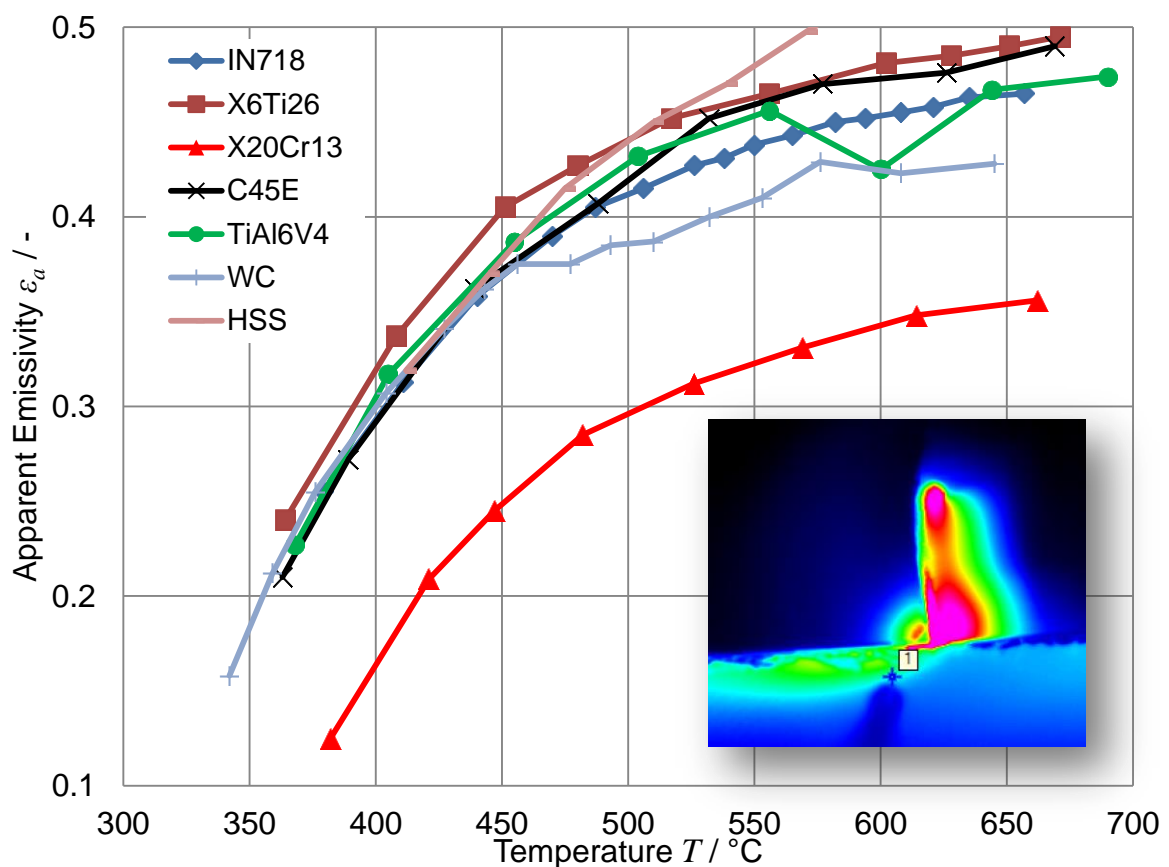


**Figure 6.4:** Apparent Emissivities of Used Materials

*Scheinbare Emissionsgrade der eingesetzten Materialien*

The measurement spot of the pyrometer was identified in the experiments by coupling a laser light through the infrared fiber. Analyzing the results yielded increasing emissivity with increasing temperature for all materials. Between 350 °C and 650 °C an increase of around 40 % was determined. Within the temperature range around 400 °C all materials, had an apparent emissivity value around 0.3. This value was assumed during the experiments for all materials besides X20Cr13 where a value of 0.2 was assumed. Additionally to the a priori determination, the pyrometer was used with the same method during the cutting experiments. The aim of this additional use of the pyrometer was the validation of the assumed emissivity.

### 6.1.2 Cutting Experiments on Fundamental Test Rig

#### *Zerspanversuche auf Analogieprüfstand*

For the model calibration and validation, a test series on the fundamental test rig was conducted. The test rig was designed for analogy milling experiments (details are given in [B USC14, pp. 45–54]). Due to the linear cutting kinematics, the accessibility of the measurement devices was ensured. The experimental setup is shown in Figure 6.5.

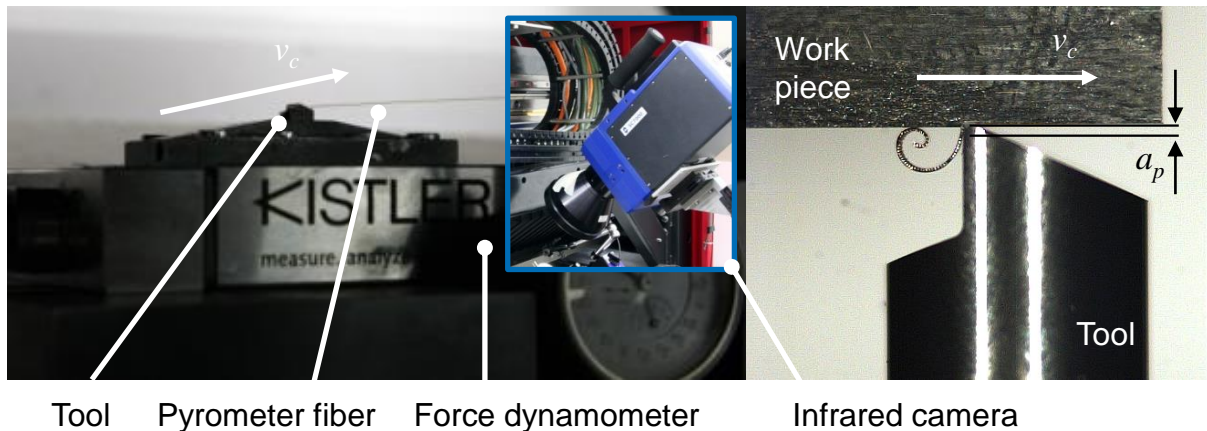


**Figure 6.5:** Experimental Setup on the Fundamental Test Rig

*Experimenteller Aufbau auf dem Grundlagenprüfstand*

During the experiments, the tool remains fixed in a clamping device and the work piece is mounted in a moving carriage. For each cut, the work piece needs to be aligned to set the cutting depth  $a_p$ . For the experiments, the cutting depth was chosen to  $a_p = 30 \mu\text{m}$  for all tests. The clamping device for the tool again is mounted on a force dynamometer (Kistler Type 9256 C2), acquiring three-dimensional force data. Both, infrared camera and pyrometer fiber are positioned in order to measure in an orthogonal plane to the cutting direction.

For the experiments on the test rig, specialized solid carbide cutting tools were used. These tools were designed according to the geometry of a milling tool, featuring a rake angle  $\gamma = 11^\circ$ , a clearance angle  $\alpha = 13^\circ$  and a measured cutting edge radius  $r_\beta = 5 \mu\text{m}$ . During the experiments, the geometry of the tools was not changed. Due to the small cutting edge radius an ideal sharp cutting edge is approximated. The tools were furthermore equipped with a reference plane orthogonal to the cutting direction for the infrared camera and the pyrometer. The work piece was positioned in the same distance to the camera as the reference plane of the tool to ensure suitable measurement of the temperature field.

An overview of the experimental plan on the fundamental test rig is given in Figure 6.6. The only cutting parameter varied during the experiments was the cutting speed  $v_c$ . Overall, four cutting speeds were tested ( $v_c = 10, 35, 70$  and  $140 \text{ m/min}$ ) for four different work piece materials (IN718, X6Ti26, X20Cr13, C45). For each material test, the highest cutting speed was chosen for validation, i.e. the model was calibrated

with the three lower cutting speeds and the result for the highest cutting speed was predicted with the model and evaluated. Furthermore, one complete cutting speed test for one material (X20Cr13) was used to validate the material's influence on the model. The experiments on the fundamental test rig were primarily used for validation of the elementary solutions approach.

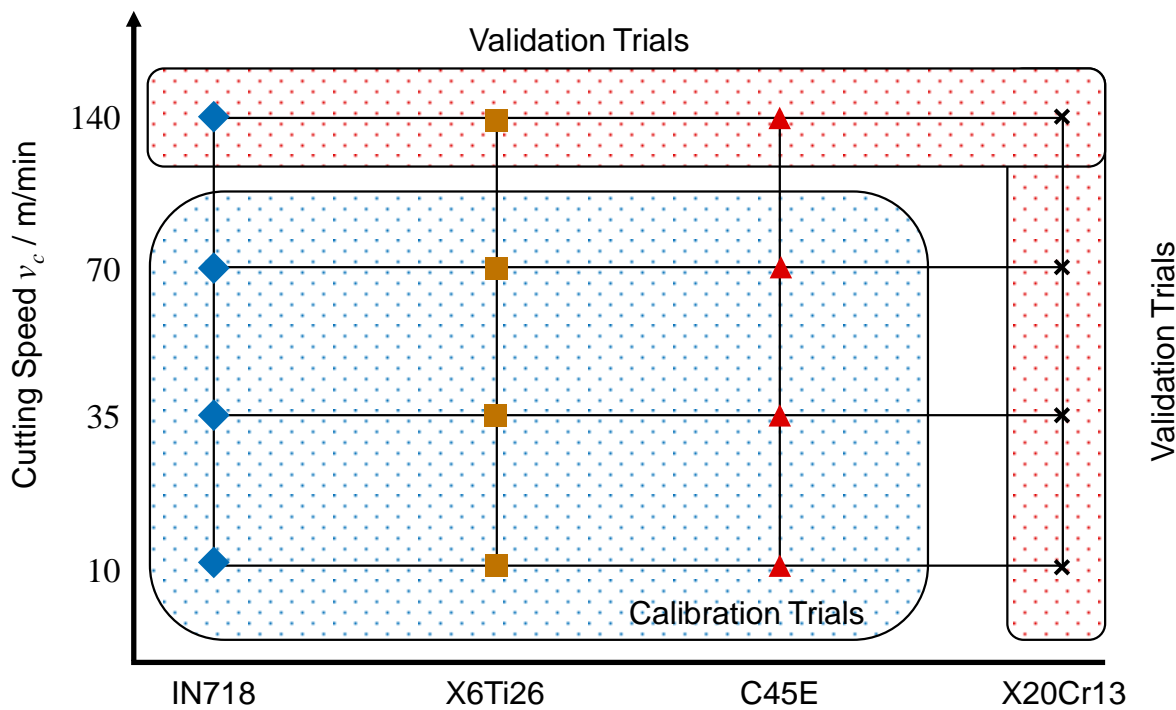


**Figure 6.6:** Experimental Plan for Calibration and Validation on the Fundamental Test Rig  
*Versuchsplan für Kalibrierung und Validierung auf dem Grundlagenprüfstand*

The forces and temperatures were measured with dynamometer, pyrometer and infrared camera as shown in the experimental setup of Figure 6.5. For the force measurement, the dynamometer used is optimized for low measurement times. When measuring the force during the experiment at the beginning and end of the cut a small vibration due to the tool entrance and exits occurs. These vibration was neglected for the data analysis. A characteristic force signal without these vibrations can be regarded as a constant force value of the time of cut. The arithmetic average value was taken into account, mainly for assessing the calibration parameters for the model. By multiplying the appropriate speed values, the order of magnitude for the heat source strengths can be computed.

The pyrometer values measured were used for the described measurement method. As described pyrometer and infrared camera were positioned in way that one spot of the measurement location was common for both devices. This spot was chosen at the stationary tool in case of the experiment on the fundamental test rig. Using the experimental setup online during the cutting experiments yields more realistic values for the apparent emissivity. In most cases the assumed value of 0.3 was however found in good agreement with the reality. Hence, for the validation this value was used to calibrate the infrared camera images.

### 6.1.3 Cutting Experiments on Broaching Machine

#### *Zerspanversuche auf Räummaschine*

A further test series was conducted on the broaching machine. Again, the linear cutting kinematics featured by this machine ensured accessibility of the measurement devices. Unlike the kinematics on the fundamental test rig, the tool moves and the work piece is fixed. The experimental setup is shown in Figure 6.7.

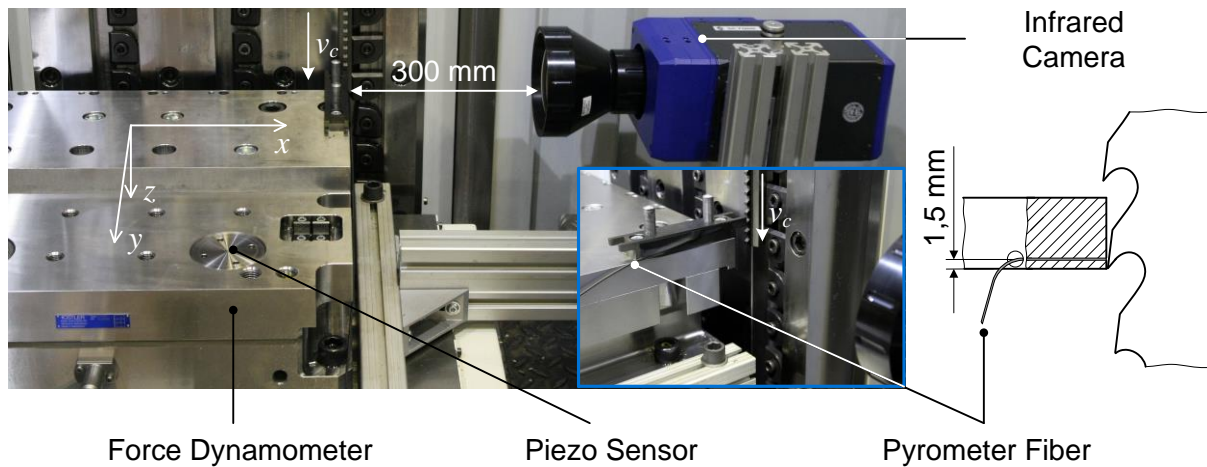


**Figure 6.7:** Experimental Setup on the Broaching Machine

*Experimenteller Aufbau auf der Räummaschine*

For measurement of the forces, the work piece was mounted on a custom made dynamometer (Kistler Z21289), replacing the original clamping device of the machine, i.e. the work piece is directly mounted on the dynamometer. The infrared camera was positioned parallel to the cutting plane in the required distance of 300 mm. For the broaching experiments, the pyrometer fiber was fed through hole (diameter  $d = 1,5$  mm), aligned on the clearance face of the tool for each cut.

A characteristic feature of the broaching process is that the uncut chip thickness  $h$  is defined by the tool geometry, i.e. the rise per tooth, compare sketch on the right-hand side of Figure 6.7. For variation of the cutting depth, therefore, different tools were applied ( $h = 20 \mu\text{m}, 40 \mu\text{m}, 60 \mu\text{m}, 80 \mu\text{m}$ ) Furthermore, different rake angles ( $\alpha = 5^\circ, 10^\circ, 15^\circ$ ) and cutting speeds  $v_c$  were tested ( $v_c = 4 \text{ m/min}, 6 \text{ m/min}, 8 \text{ m/min}, 10 \text{ m/min}$ ). The experimental plan concerning the influence of cutting speed  $v_c$  and uncut chip thickness  $h$  is shown in Figure 6.8. This plan was conducted for each rake angle and for two work piece materials (IN178 and TiAl6V4). As for the panel method, no specific calibration of the parameters is needed respectively allowed, there is not a distinct differentiation between calibration and validation parameters. In principle, all tested cutting conditions can be used as validation. For the determination of further parameters needed, the contact length between rake face and chip was read out from the infrared camera image. Furthermore, the chip thickness  $h'$  was measured after the experiments. With the help of MERCHANT's Law subsequently the idealized shear zone angle was computed.

The temperature value was used for validation of the emissivity calibration with the described method. In most cases an apparent emissivity value of 0.3 was assumed as described.

Force and temperature signals were measured with dynamometer and pyrometer as shown in the experimental setup of Figure 6.7. The force thereby measured during the cutting of each tooth of the broaching tool. For the consideration of the force values for determination of suitable values for the heat source strengths, an average value of the stationary part of the force signal during one cut was computed.

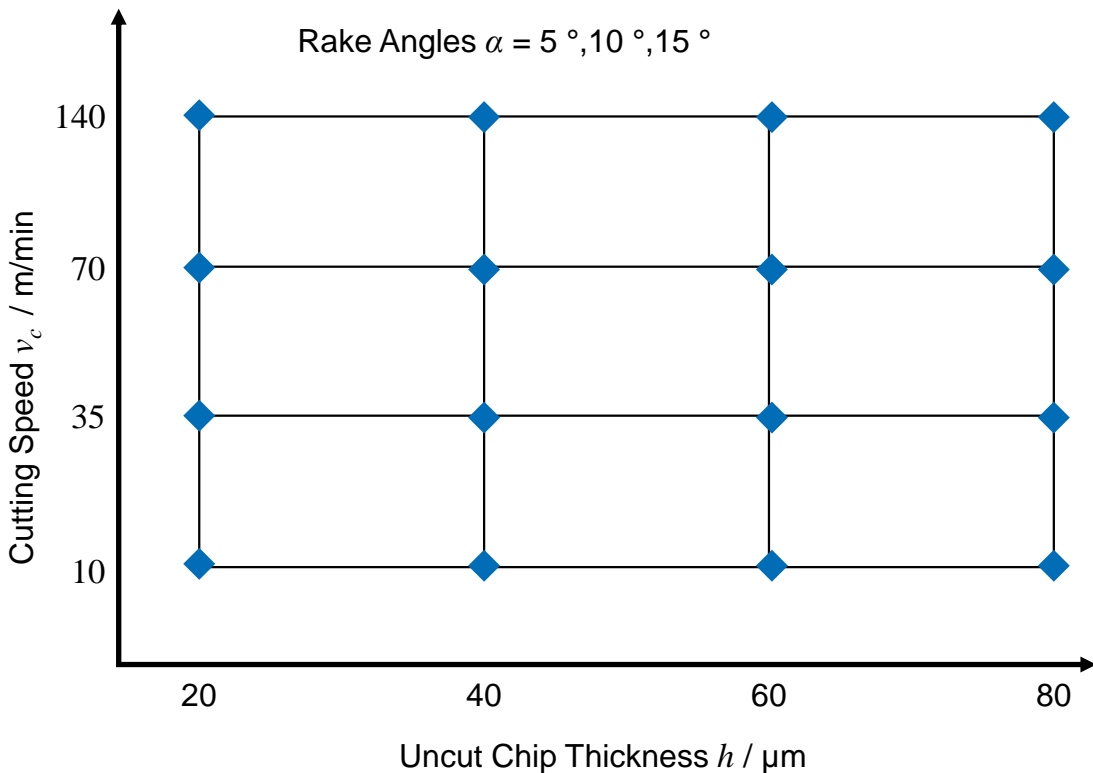


**Figure 6.8:** Experimental Plan for Calibration and Validation on the Broaching Machine  
*Versuchsplan für Kalibrierung und Validierung auf der Räummaschine*

The pyrometer measured values for the temperature when the tool is passing the small hole inside the work piece. During the passing, the force values drop slightly. With the force drop, the entrance of the tool at the hole was defined. When passing the hole, the temperatures for the pyrometer are initially too low. The pyrometer yields suitable values for temperatures above 150 °C, lower temperatures can not be measured due to the chosen wavelengths. When a suitable value is reached, the pyrometer signal was cut out and the respective values were averaged during the cut. The investigations yielded good temperature values after the entrance of each tooth. As the signals of the temperature with this method are measured in a short time after the cutting had taken place, the values are considered to be lower than during the cut, as the tool cools down after the cutting. The values of the pyrometer were therefore taken as basis for the calibration and the assessment of the infrared camera images. These values were in particular important for the determination of the value  $T_{ref}$ .

## 6.2 Investigation of Thermal Boundary Conditions

### *Untersuchung der thermischen Randbedingungen*

With the described experimental setups and the measurement method based on infrared camera and two-color pyrometer, suitable infrared images can be determined orthogonal to the cutting direction. On the upper left-hand side of Figure 6.9, a typical infrared camera image in form a contour plot from the broaching process is shown (rake angle  $\gamma = 10^\circ$ , cutting depth  $a_p = 40 \mu\text{m}$ , cutting speed  $v_c = 4 \text{ m/min}$ ). This image features the recorded digital levels for each pixel of the focal plane array of the camera. The image is presented with the help of colors indicating regions with similar values of the digital levels. For the conversion of digital levels in temperature values, the emissivities determined need to be selected. The characteristic regions of metal cutting, i.e., chip, tool, work piece, shear zone, friction zone, can be determined.

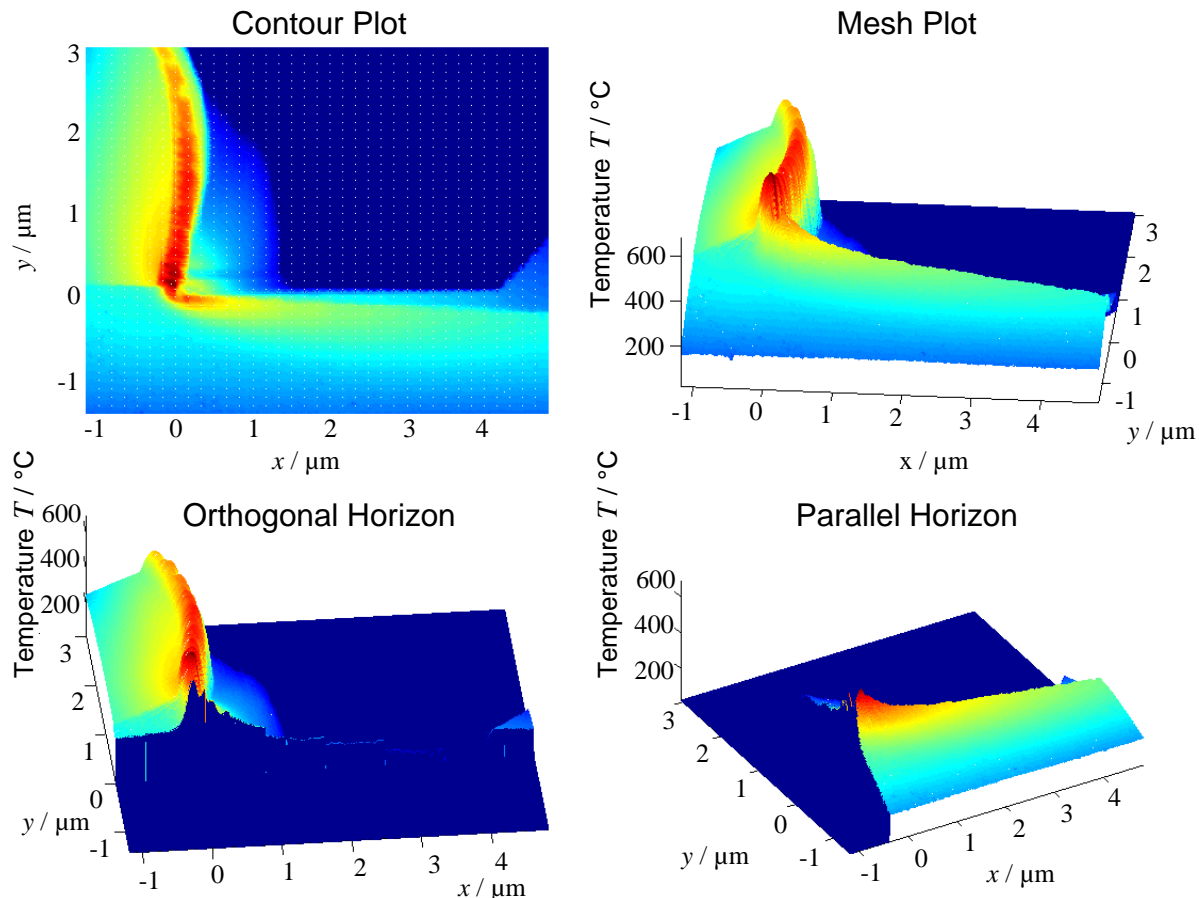


**Figure 6.9:** Infrared Image and Contour Plot

*Infrarotbild und Konturenplot*

For both modeling approaches, the thermal boundary conditions are of major significance. Besides the information about the temperature distribution in terms of the isotherms, the infrared camera images can be used to validate the assumed boundary conditions. In order to analyze the boundary conditions, the contour plot can be depicted as a mesh plot, providing as three-dimensional diagram with the temperature  $T(x,y)$  as third axis. From such a plot, compare upper right-hand side of the figure,

the gradients of the temperature in  $x$  and  $y$  direction can be determined directly. For the analysis, the mesh plot can be used to analyze the temperature behavior in distinct regions. A plane is therefore cut out of the plot and the appropriate temperature behavior on this plane can be plotted in a so called horizon plot. Two kinds of horizon plot are relevant for the thermal analysis, i.e. the orthogonal and the parallel horizon plot. On the lower left-hand side of the figure an orthogonal horizon plot is shown. This kind of plot can be used to investigate the thermal boundary condition at the appropriate surface. The plane is chosen orthogonal to the chip. On the lower right-hand side, a plot parallel to the chip is provided. This kind of plot can be used to investigate the temperature distribution along a characteristic area, e.g. along a heat source. The resulting line describing the shape of the cut mesh plot is the horizon plot.

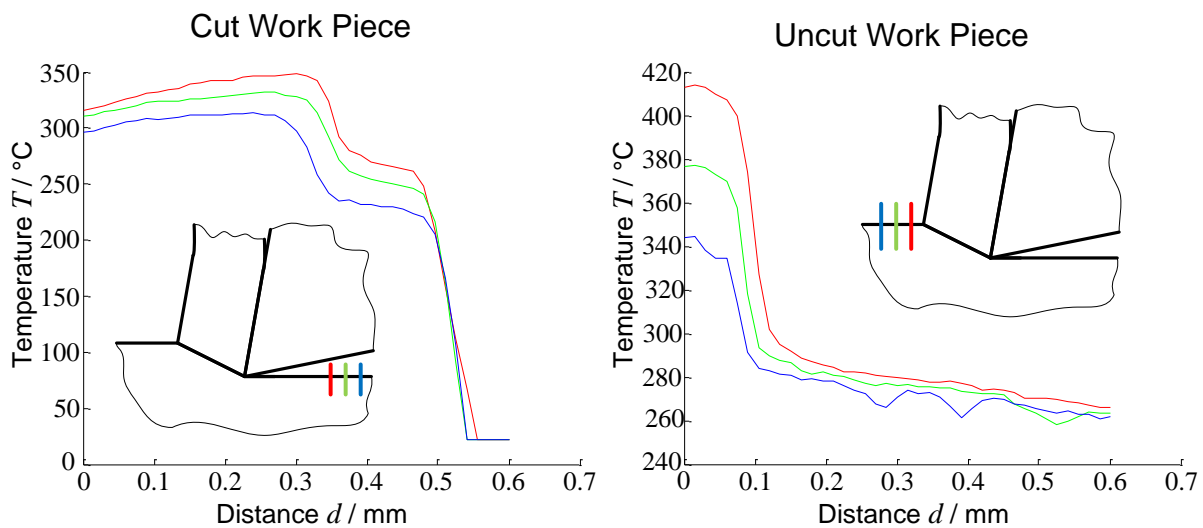


**Figure 6.10:** Adiabatic Boundaries at Work Piece Surface

*Adiabate Grenzen an Werkstückoberfläche*

In terms of boundary conditions, either NEUMANN condition (i.e. prescribing the temperature gradient) or DIRICHLET condition (i.e. prescribing the temperature value) need to be selected for each boundary. In the following, the characteristic boundaries at the work piece surface, the clearance face, the rake face and the shear zone were investigated.

For boundaries in a greater distance to the root point, the assumption of an adiabatic boundary, as special case of the NEUMANN condition was found to be suitable for all investigated cases. In Figure 6.10 the boundaries at the cut and the uncut work piece are shown for the described broaching case. To show the sensitivity of the plots, three horizon plots are provided for each analysis. For the analysis of the cut work piece a shift of 0.6 mm was chosen, compare left-hand side of the figure. As can be seen, the plots are similar to each other. In the region of the work piece, the gradient of the temperature vanishes, i.e. the boundary can be considered adiabatic. The same characteristic behavior was observed at the uncut work piece surface. For this analysis a shift of 0.225 mm was chosen. Both boundaries are in good agreement with the assumption an ideal adiabatic boundary.

In Figure 6.11 the analysis of the thermal boundary conditions at the clearance face is shown. Regarding the parallel horizon plot on the left-hand side of the figure yielded a decreasing temperature behavior when going away from the root point. The shift of the horizon plots was thereby chosen to 0.03 mm. For the analyzed distance  $d$  a temperature decrease of around 400 °C was observed. The local variable is thereby chosen along the clearance face with the origin in the root point. Having its maximum value at the root point, the behavior of the temperature can be considered as almost linear decreasing. The plots showed a slight noise compared to the analysis of the adiabatic boundaries at the work piece. All parallel horizon plots are however similar, i.e. the sensitivity in this regions is relatively low. In general, the quality of the parallel horizon plots is by nature more disturbed and it is difficult to identify the correct plane in the infrared mesh plot.

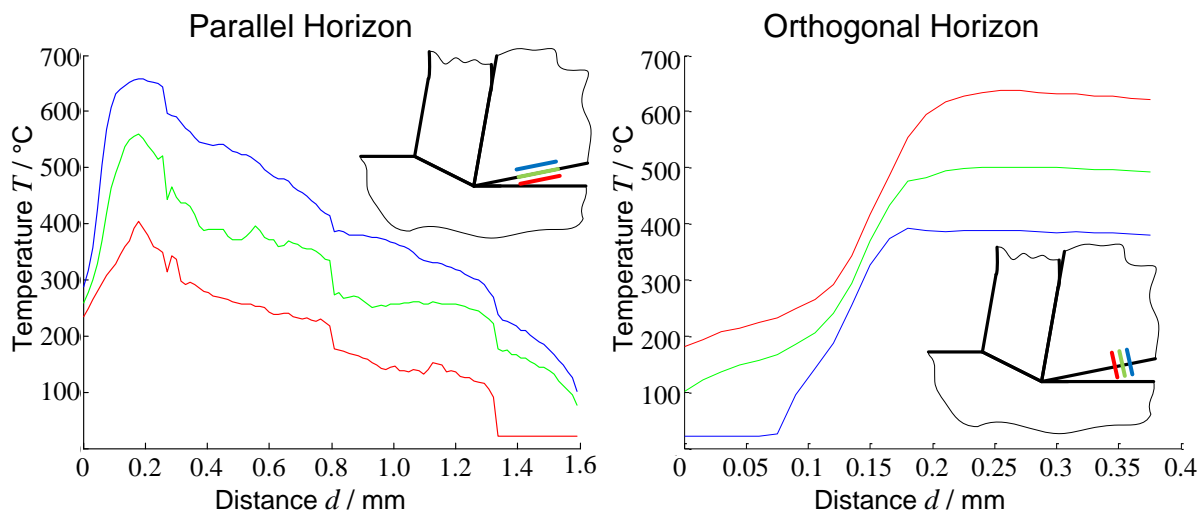


**Figure 6.11:** Thermal Boundary Condition at the Clearance Face

*Thermische Randbedingungen an der Freifläche*

Quantitative conclusions are therefore limited, qualitative conclusion, e.g. the observed linear decrease of the temperature at the clearance are possible and meaningful. On the right-hand side of the figure, the analysis of the thermal boundary condition with help of the orthogonal horizon plot is shown. The shift of the plots was chosen to 0.3 mm, the local coordinate is running defined positive in direction inside the tool. In the interesting region inside of the tool, the temperature gradient vanishes and the boundary can be considered as adiabatic. Again the orthogonal horizon plots are in agreement with each other, yielding meaningful results in terms of the thermal boundary conditions.

Figure 6.12 shows the analysis of the rake face. For the parallel horizon plot on the left-hand side of the figure a shift of 0.045 mm was chosen. As observed before, the plots itself yield disturbances in form of a noise in the temperature signal. The rake face was hereby detected with an algorithm comparing several subsequent infrared images with each other, the appropriate temperature curve is indicated with the green color in the figure. Further plots were taken parallel inside the tool (indicated by the blue color) and inside the chip (indicated with the red color). The temperature on

the rake face itself yielded an almost constant value. A characteristic behavior could not be observed. The same observation is true for the behavior of the temperature curve inside the chip. Both show temperatures around 550 °C respectively 600 °C. However, both curves are inside the measurement range of the infrared camera, otherwise the values would be cut to higher temperatures. A more characteristic behavior can be observed for the temperature curve inside the tool. The appropriate horizon plot showed a clear decrease when moving away from the root point. Temperature values decrease from around 650 °C to 300 °C. The behavior showed also an almost constant value.

For the behavior of the temperature at the rake face, different assumptions were made by several researchers. KOMANDURI AND HOU assumed a concave slope of the distribution along the rake face [KOMA00]. Further analysis were conducted and published in [KLOC15]. In this work a convex slope was identified. For the investigated cases in this thesis only convex or linear slopes were observed. Meaningful conclusions are however difficult due the strong disturbance of the parallel horizon plots.

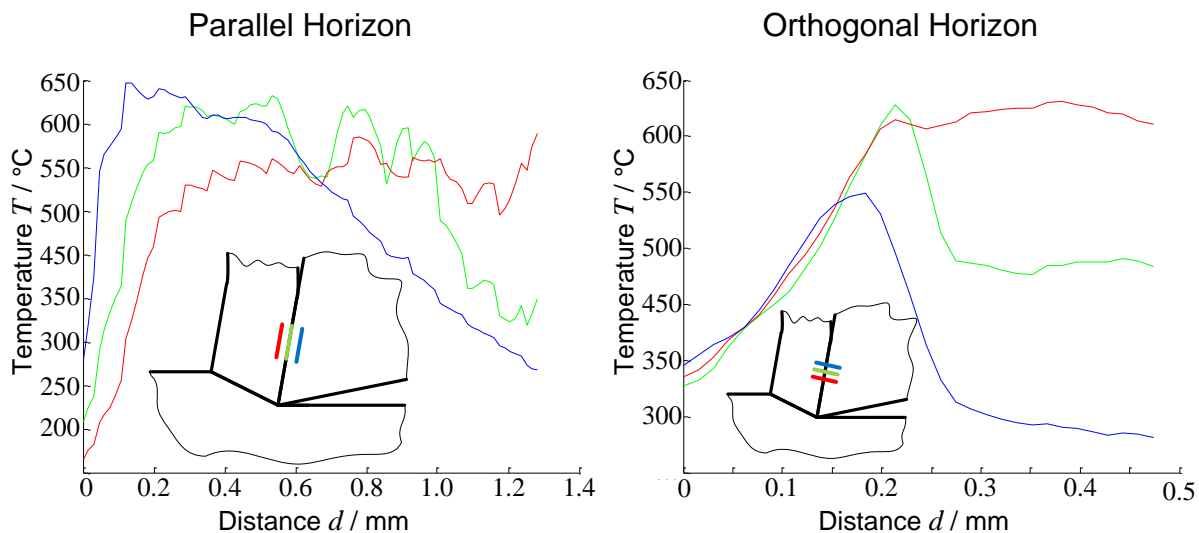


**Figure 6.12:** Thermal Boundary Conditions at the Rake Face  
*Thermische Randbedingungen an der Spanfläche*

The orthogonal horizon plots shown on the right-hand side of the figure showed again a clearer characteristic of the temperature signal. For the three plots a shift of 0.375 mm was chosen. Besides the curve chosen closer to the root point, indicated with the red color, the horizon plot yielded a similar behavior in terms of the temperature gradients. The two curves are shifted in terms of there absolute value, however they show similar gradients of the temperature before and after a distinct temperature maximum value. For the local coordinate, an increasing value was defined when moving from the chip inside the tool. The maximum point which could be observed from the curves indicates the transition from the tool to the chip region, i.e. at the maximum point the contact zone of chip and tool is assumed.

From the gradients of the orthogonal plot, the heat flux values from the rake face in chip and tool can be calculated with the help of the heat conductivities. According to FOURIER'S LAW, the heat fluxes can be computed using:

$$\dot{q}'' \approx \lambda \cdot \frac{\Delta T}{\Delta d}. \quad (6.5)$$

From the figure, the heat flux in the chip can be computed to a value of  $q_{chip} = 45 \text{ kW/m}^2$  with a heat conductivity of  $\lambda_{C45} = 45 \text{ W/mK}$  and respectively for the heat flux into the tool  $q_{tool} = 350 \text{ kW/m}^2$  with a heat conductivity of  $\lambda_{WC} = 88.4 \text{ W/mK}$  according to Table 6.1. The heat partition ratio defined as ratio of these two values becomes subsequently 0.13, i.e. only around 10 % of the heat flow into the chip. It should be noted that the conducted computation can only give a rough value and is only true for the shown analyzed temperature curves.

A similar analysis for the thermal boundary conditions at the shear zone is shown in Figure 6.13.

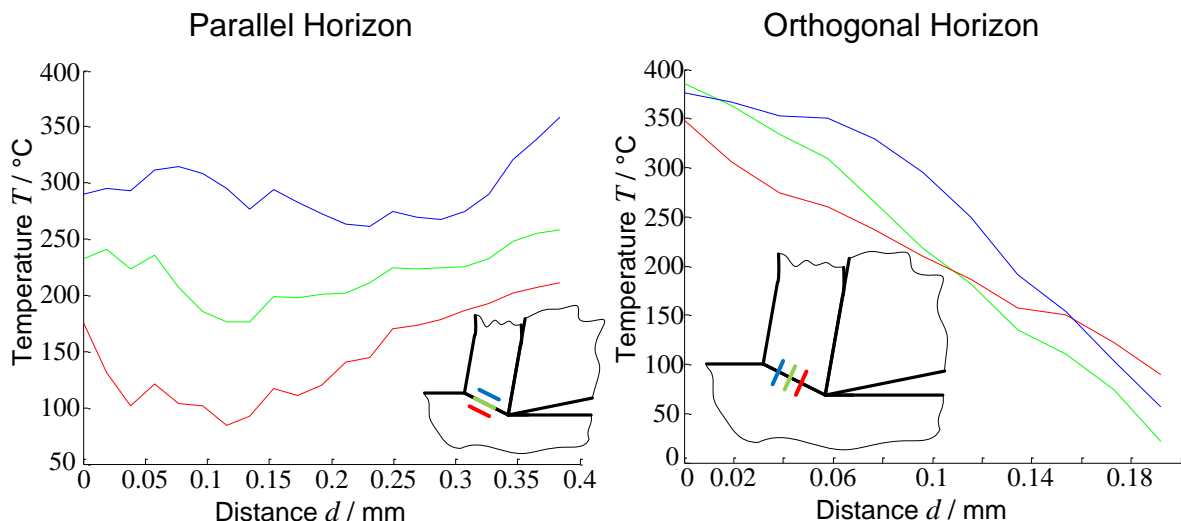


**Figure 6.13:** Thermal Boundary Conditions at the Shear Zone

*Thermische Randbedingungen an der Scherzone*

For the parallel horizon plots shown on the left-hand side of the figure, a shift of 0.03 mm was chosen. The plot on the assumed shear zone is indicated in green, the plot inside the chip in blue and the respective plot in the work piece in red. As can be seen, the temperature curves were found to be similar to each other.

For the curves at the shear zone itself and the one on the work piece, a convex behavior with a temperature minimum along the shear zone, where the local coordinate is defined positive when moving towards the root point. The temperatures in the shear zone are between 200 °C and 250 °C with increasing values near to the root point.

The orthogonal horizon plot is shown on the right-hand side of the figure. Unlike to the analysis of the rake face, not a distinct maximum value can be observed, i.e. a clear shear zone heat source could not be observed. For the plots a shift of

0.075 mm was chosen. The local coordinate is chosen positive when moving from work piece to chip area. For the shown case a heat flux value of  $q_{chip} = 100 \text{ kW/m}^2$  can be computed, where again a value of  $\lambda_{C45} = 45 \text{ W/mK}$  was used for the chip area. Compared to the heat flux value from the rake face into the tool, it can be considered that the shear zone heat source is around 30 % of the heat source at the tool. The heat flow from the shear zone into the work piece could not be observed with the analysis, which could mean that the value is negligible compared to the other source strengths.

Table 6.3 shows an overview of the investigation of the thermal boundary conditions at the characteristic regions. The recommendations for the choice of the boundary conditions are based on the analysis of the gradients of the orthogonal horizon plots. For the temperature behavior the parallel horizon plots were investigated.

**Table 6.3:** Investigation of Boundary Conditions at the Characteristic Regions

*Untersuchung der Randbedingungen an den charakteristischen Regionen*

Characteristic Region	Temperature Behavior	Boundary Condition
work piece	constant, near to initial work piece temperature	adiabatic
clearance face	linear decreasing values away from the root point	adiabatic
rake face	constant or convex decreasing values	NEUMANN (heat source strengths value)
shear zone	convex increasing values approaching root point	NEUMANN (heat source strengths value)

The analysis presented in this chapter was conducted for representative cases of the investigation. Not all parameter sets yielded clear results, especially the investigation of the shear zone was difficult. In some cases no clear distinction between the heat sources was possible but rather appeared as a bulk heat source combining shear zone and rake face heat source.

Further measurements yielded temperature values which were outside the range of the chosen temperature range of the infrared camera. Such measurements appear as adiabatic boundaries as the slope is Zero due to the cut signal. These values may not be confused with the real adiabatic boundaries occurring at the work piece and the clearance face of the tool. Further difficulties arise with the ever occurring reflections. In the presented case shown in Figure 6.9 the regions at the chip backside is obviously disturbed by such a reflection. However, when analyzing the mesh plot the reflections are not easy to identify and need to be detected in the contour plot before. These regions may not be considered for the analysis. Besides the difficulties for quantitative analysis, the investigation of the mesh plots and the appropriate horizon plots yielded a vital tool for the investigation of the thermal boundary conditions.

### 6.3 Validation of Presented Approaches

#### *Validierung der vorgestellten Ansätze*

With the presented measurement method and the methodology for investigation of the thermal boundaries the modeling approaches can be validated with the two experimental setups. For the elementary solution approach the experiments on the fundamental test rig were used for validation. The experiments on the broaching machine were used for validation of the panel method approach. As both methods are different from their scientific approach also the way for validation differs from each other. While for the elementary solutions approach simply the calibrated functions need to be evaluated, the panel method approach uses several inputs based on other physical parameters, e.g. cutting forces. In the following section representative results from the validation of both approaches are summarized.

For the validation, the appropriate temperature fields measured by means of infrared camera images are of major significance. A typical image from the broaching trials is given in Figure 6.14 in grey color scale. The images were taken with the shown window frame, covering tool, chip and work piece area. As described, the cutting edge geometry was automatically detected with an appropriate algorithm.

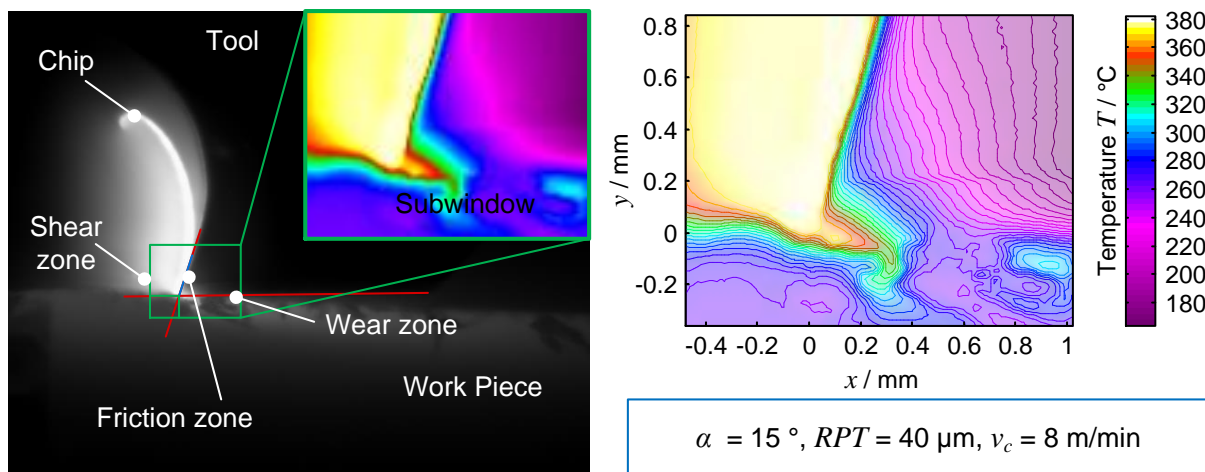


**Figure 6.14:** Chosen Window Used for Validation

*Gewählter Bildausschnitt für die Validierung*

For the validation of both approaches, a window was chosen from the infrared image, according to the chosen window of the model. The relevant dimensions are depicted on the left-hand side of the figure. Both models thereby mainly consider an area in the vicinity of the root point. In the infrared camera image, the characteristic regions of metal cutting can be identified. Distinct parameter, e.g. length of the contact zone between chip and rake face can be read out of the image.

In order to compare isotherms and their specific behavior, the colored temperature scale was chosen in line to the model plots. For a better visibility, a hybrid image with additional isotherms was generated, an exemplary image is shown on the upper right-hand side of the figure. The modelled temperature fields were plotted in similar way to ensure a simple comparison of both temperature fields.

### 6.3.1 Validation of the Elementary Solutions Approach

#### *Validierung des Elementarfunktionen Ansatz*

As a general validation of the use of potential theory, the results from the elementary solution approach are compared to the experimental results. As described in the correlation chapter, not a clear correlation of the distinct model parameters were determined. However, a rough correlation can be given with the correlation coefficients  $\eta_\lambda$  and  $\eta_v$ , describing the influence of work piece material and cutting speed. In this sense, the following comparison should be understood as qualitative validation rather than a quantitative one.

An investigation for X6Ti26 at a cutting speed of  $v_c = 140$  m/min is provided in Figure 6.15. As expected from the calibration experiments, the infrared image shown on the right-hand side of the figure, yields the characteristic triangular influence zone.

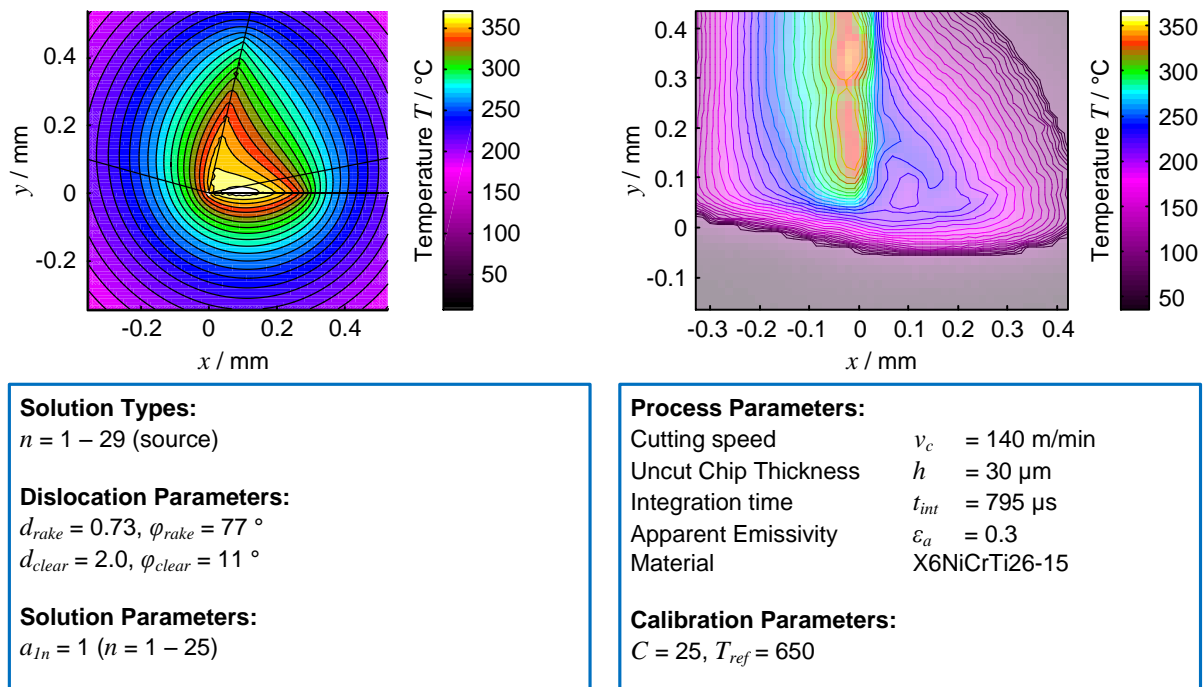


**Figure 6.15:** Comparison for X6NiCrTi26-15 at High Cutting Speed

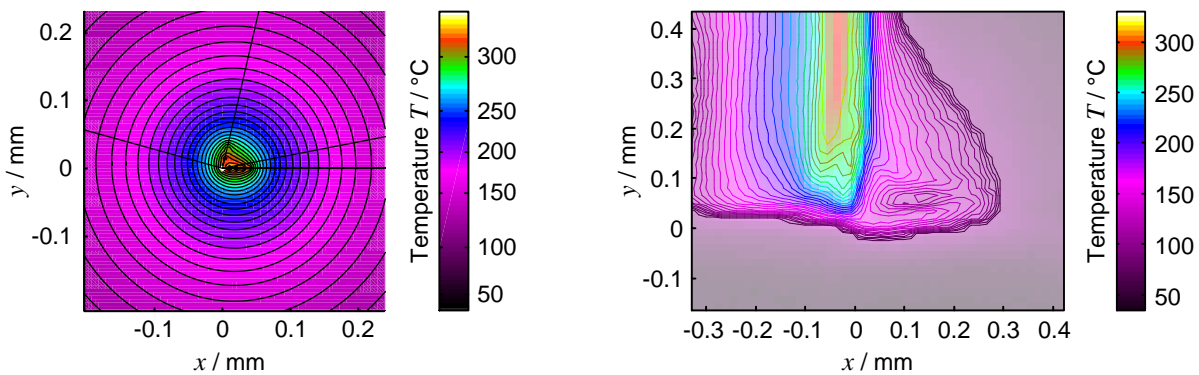
*Vergleich für X6NiCrTi26-15 bei hoher Schnittgeschwindigkeit*

The penetration depth is considerably high as well as the absolute temperature values. Temperatures in the chip are again difficult to interpret due to the resolution of the infrared camera system.

For the parameterization, a distribution of 15 sources on the rake face and 15 on the clearance face was determined. All sources were parameterized with the strength of  $a_{In} = 1$ . The calibration coefficients were set to  $C = 25$  and  $T_{ref} = 650$ . The correlation coefficient for the cutting speed is given by  $\eta_v = 0.22$ . Comparing the model plot with the infrared camera yields a good comparison of both, the temperature distribution and the absolute temperature values. In particular the area in the vicinity of the root point was found in good agreement.

During the calibration experiments, the material X20Cr13 was deliberately not considered as the results were intended for the validation of the material influence. In Figure 6.16, the results from the infrared camera measurement and the appropriate predicted model plot are presented. The shown case was tested with a cutting speed of  $v_c = 70$  m/min, the uncut chip thickness was chosen to  $h = 30 \mu\text{m}$  according to the other experiments. It may be noted that the experiment with X20Cr13 were conducted with an apparent emissivity of  $\varepsilon_a = 0.2$ , which was the lowest from all cases.

When observing the infrared camera image, the characteristic triangular influence zone in the tool can be observed similar to the results from the other materials. The penetration depth, however appears lower than in all other cases. Also, the absolute temperature values are considerably low. Furthermore, the influence zone can be found rather in the tool than on the work piece or in the area around the shear zone, as observed in some other cases.


**Solution Types:**

$n = 1 - 7$  (source)

**Dislocation Parameters:**

$d_{rake} = 0.73$ ,  $\varphi_{rake} = 77^\circ$   
 $d_{clear} = 2.0$ ,  $\varphi_{clear} = 11^\circ$

**Solution Parameters:**

$a_{In} = 1$  ( $n = 1 - 25$ )

**Process Parameters:**

Cutting speed	$v_c = 70$ m/min
Uncut Chip Thickness	$h = 30 \mu\text{m}$
Integration time	$t_{int} = 1267 \mu\text{s}$
Apparent Emissivity	$\varepsilon_a = 0.2$
Material	X20Cr13

**Calibration Parameters:**

$C = 60$ ,  $T_{ref} = 400$

**Figure 6.16:** Comparison for Material Influence with X20Cr13

*Vergleich für Werkstoffeinfluss mit X20Cr13*

In the potential theory model, the low penetration depth was considered with a lower number of sources. Overall, 4 sources were positioned on rake face and clearance face each. The strengths of the sources was determined equal. For the calibration coefficients values of  $C = 60$  and  $T_{ref} = 400$  were resulting. The correlation factor for the material is given by  $\eta_\lambda = 0.5$ .

When using these values, the influence zones of the sources on the clearance face and the rake face decrease, as desired. However, the influence zones predicted from the model are too low compared with the reality (also the different scale of the coordinate system should be noted). The influence zone in the work piece can be considered in good agreement with the experimentally determined one.

Another validation experiment with the same material at higher cutting speed is shown in Figure 6.17. The shown case was conducted with a cutting speed of  $v_c = 140. This case can be considered as the most critical as both, cutting speed and material were not considered in the calibration experiments. The measured temperature field by means of the infrared camera image yields the characteristic triangular shape for the high cutting speeds. As expected, the absolute temperature values are relatively high, the penetration depth inside the tool and the cut work piece, however can be considered in a medium range. It may be note that the isotherms between rake face and work piece surface do not belong to the material (compare with sketched cutting edge geometry in the model plot).$

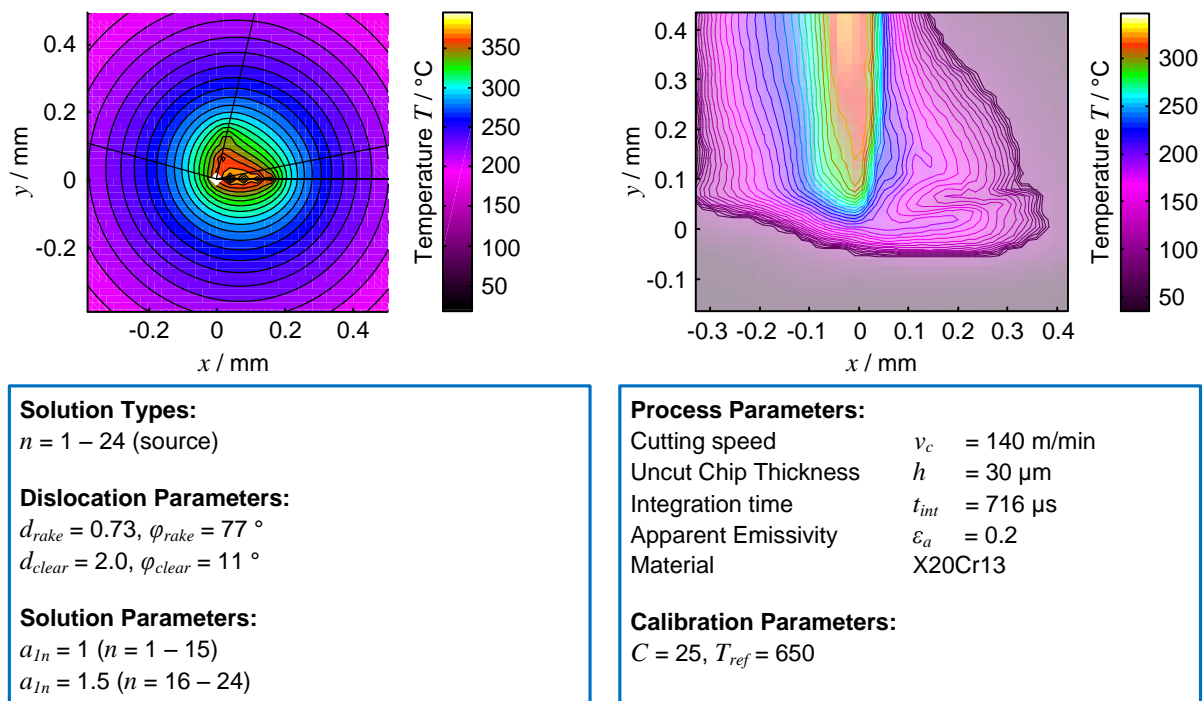


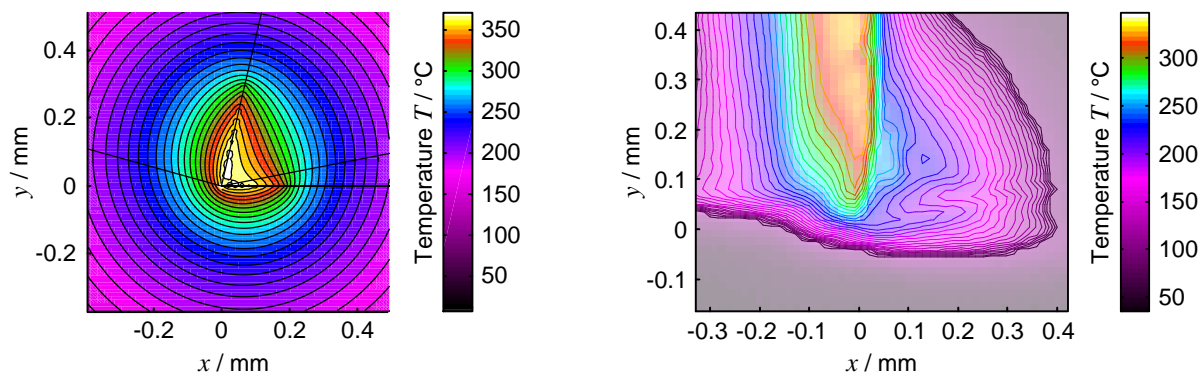
**Figure 6.17:** Comparison for Cutting Speed and Material Influence

*Vergleich des Schnittgeschwindigkeits- und Werkstoffeinflusses*

While the prediction for the lower cutting speed in the X20Cr13 material was considered with deviations to the real case, the quality of the model plot for the higher cutting speed yielded more suitable results. Despite the still to low penetration depth, the shape and the absolute temperature values are in sufficient agreement. For the shown model plot, 15 sources were placed on the rake face and 10 sources on the clearance face. The strength were determined to  $a_{In} = 1$  on the rake face and  $a_{In} = 1.5$  on the clearance face. For the calibration coefficients, values of  $C = 25$  and  $T_{ref} = 650$  were determined. The correlation factors for material and cutting speed influence are given by  $\eta_\lambda = 0.8$  and  $\eta_v = 0.14$ .

Comparing the correlation coefficients, a higher value of  $\eta_\lambda$  was determined for the present case, while the cutting speed coefficient stays in a range around 0.2. The influence of the cutting speed can therefore be considered as more stable than the material influence, which is in line with the included material's influence.

The stability of the cutting speed influence is also valid on other materials. As a representative case, the higher cutting speed for the C 45 E material is presented in Figure 6.18. Again a cutting speed value of  $v_c = 140$  m/min was tested. Again the expected influence zone in tool and work piece was observed. The absolute temperature values were considerably high as well as the penetration depth of the maximum temperature zone. Comparing the results to the model plot shown on the left-hand side of the figure yields good agreement of the two fields in shape and absolute temperature values. For the model plot, 10 sources were placed on rake face and clearance face each. The strength were determined as  $a_{In} = 1.5$  on the rake face and  $a_{In} = 1$  on the clearance face.


**Solution Types:**
 $n = 1 - 19$  (source)

**Dislocation Parameters:**
 $d_{rake} = 0.73, \varphi_{rake} = 77^\circ$   
 $d_{clear} = 2.0, \varphi_{clear} = 11^\circ$ 
**Solution Parameters:**
 $a_{In} = 1.5$  ( $n = 1 - 10$ )  
 $a_{In} = 1$  ( $n = 11 - 19$ )

**Process Parameters:**

Cutting speed	$v_c = 140$ m/min
Uncut Chip Thickness	$h = 30$ $\mu\text{m}$
Integration time	$t_{int} = 1267$ $\mu\text{s}$
Apparent Emissivity	$\varepsilon_a = 0.3$
Material	C 45 E

**Calibration Parameters:**
 $C = 28, T_{ref} = 600$ 

**Figure 6.18:** Validation of Higher Cutting Speed for C 45 E

*Vergleich für höhere Schnittgeschwindigkeiten bei C 45 E*

For the calibration coefficients, values of  $C = 28$  and  $T_{ref} = 600$  were determined. The correlation coefficient resulting is  $\eta_v = 0.23$ . Similar parameterizations were determined for other cases due to the cutting speed influence.

While the conducted experiments may be understood only as representative results, the use of the potential theory seems viable for the regarded metal cutting cases. Considering the still significantly disturbed infrared camera images, the predicted results can be assessed as suitable, in particular concerning absolute temperature values. The validation of the shapes is difficult and a clear correlation is difficult due to the strong dependence on the calibration. During the experiments, only the combination of sources was investigated due to simplification. The investigations for the elementary solutions approach should be understood as a kind of feasibility study of the potential theory in general. The more systematic panel method is validated in the following section.

### 6.3.2 Validation of Panel Method Approach

#### Validierung des Panelmethoden Ansatz

For the validation of the panel method approach, the experiments on the broaching machine were used. As described, the influence of different cutting speeds, uncut chip thicknesses and rake angles on the temperature field were investigated. In order to yield sensible temperature fields, the outcomes from the panel method were calibrated with the described method.

In Figure 6.19, a comparison of the temperature field from the panel method (left-hand side) and the appropriate infrared camera image is shown for a rake angle  $\gamma = 5^\circ$ , a rise per tooth  $RPT = 40 \mu\text{m}$  and a cutting speed  $v_c = 4 \text{ m/min}$ . It may be noted that the rake angle of the panel method is counted from the  $x$ -axis.

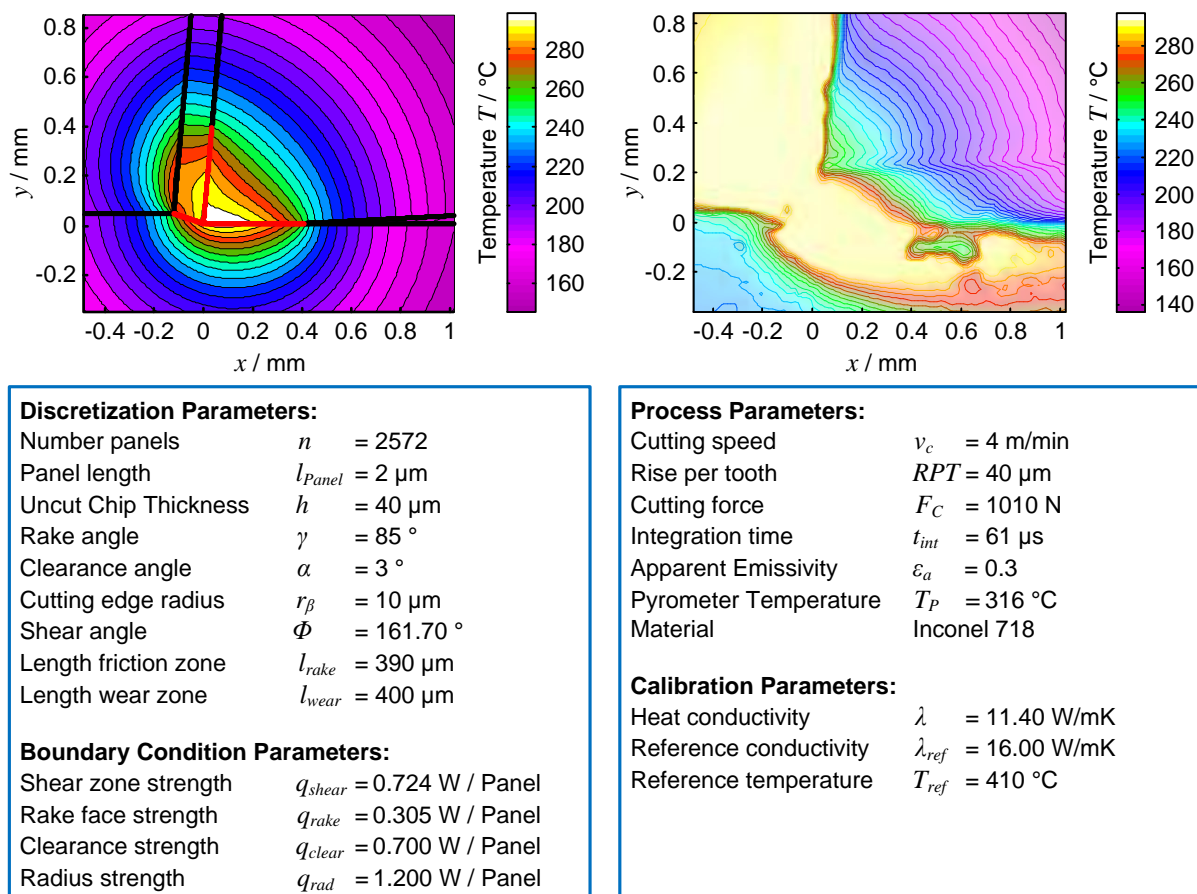


**Figure 6.19:** Comparison of Model Plot and Infrared Camera Image

*Vergleich von Modellplot und Infrarotkamerabild*

For the panel method, the cutting edge radius and the contact between clearance face and work piece surface was considered by the third section at the clearance face. For the heat conductivity a value of  $\lambda = 11.4 \text{ W / mK}$  according to Table 6.1 was chosen. Comparing the calibrated model outcomes with the infrared camera image yields a good agreement in the area of the tool and the cut work piece surface. The slight knee in the isotherms of the tool in the infrared camera image are resulting from a chamfer at the clearance face and may be neglected for the analysis. The temperature field in the chip can not be fully resolved from the infrared camera as the

chip thickness is too low, however, the measured temperatures can be considered as maximum temperatures evolving in the chip.

In Figure 6.20 an investigation of a case with a different rise per tooth  $RPT = 60 \mu\text{m}$  is shown. The appropriate infrared camera image yields a temperature field with a maximum area of temperatures shifted along the clearance face. The same effect can be observed in the tool. With the consideration of the changed uncut chip thickness in the panel model, similar results can be achieved by an increase of the contact length of chip and tool at the rake face and an increase of the section at the clearance face. The source strengths remain almost constant, despite the values considered at the panels on the cutting edge radius. For the absolute temperature values slightly higher values were observed, which is in agreement with the increased cutting force values measured.

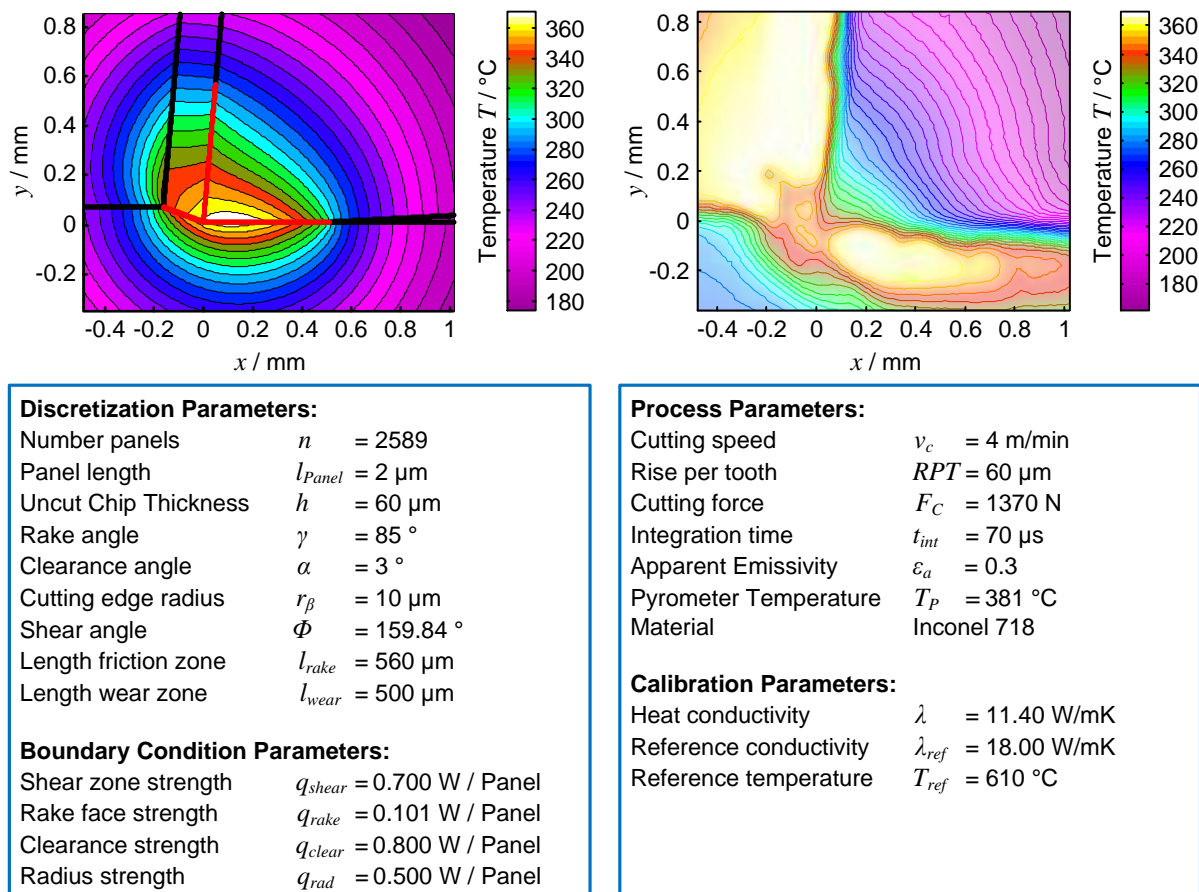


**Figure 6.20:** Comparison of the Influence of Uncut Chip Thickness

*Vergleich des Einflusses der Spanungsdicke*

For the panel method this observation can be considered with the calibration. The reference temperature was chosen to  $T_{\text{ref}} = 610^\circ\text{C}$ , which corresponds to the difference of maximum temperatures occurring in the measured temperature fields. For this case, the infrared camera image is clearer without the disturbances which were resulting at the lower  $RPT$  value. In particular, the temperature distribution in the work piece at the vicinity of the root point is in good resolution. The appropriate prediction of the panel plot matches well in this area.

In Figure 6.21, the influence of the cutting speed for the same tool parameters of rake angle and rise per tooth is shown. A cutting speed of  $v_c = 10 \text{ m/min}$  was investigated. As expected, the absolute temperature values increase significantly due to the higher cutting speed. In particular for the pyrometer value, a significantly higher value was measured. The temperature distribution in the tool and the cut work piece area is comparable to the one before, however the influence in terms of the depth inside the work piece seems to decrease. This may be caused by the decreased time for the heat to travel into the work piece at higher cutting speeds.

The influence on the absolute temperature of the higher cutting speed can be considered with the panel method by the calibration. A lower value for the reference heat conductivity and a higher value for the reference temperature were chosen. Furthermore, the measured contact length at the rake face was found significantly higher.

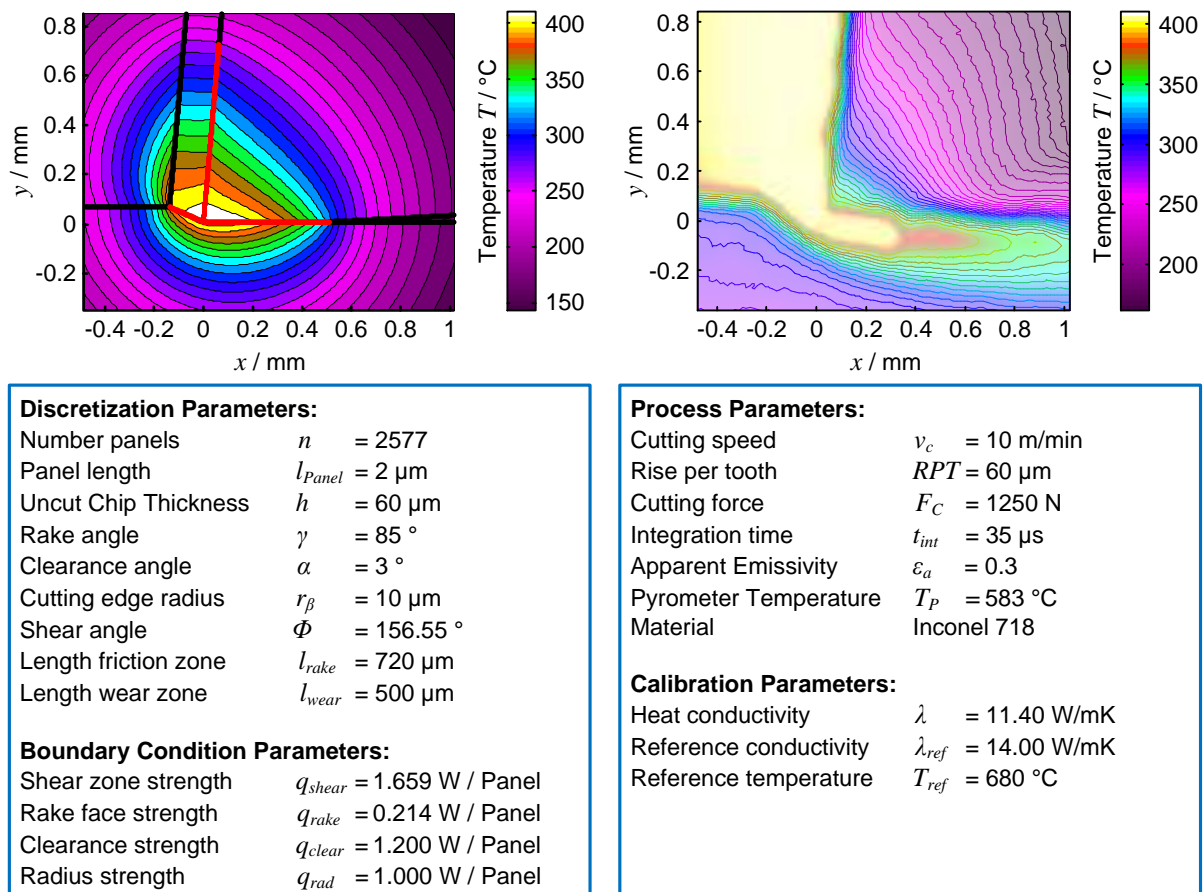


**Figure 6.21:** Comparison of the Influence of Cutting Speed

*Vergleich des Einflusses der Schnittgeschwindigkeit*

This finding was also considered in the parameterization by a higher value of  $l_{\text{rake}} = 720 \mu\text{m}$ . The length of the contact zone at the clearance face, however, was chosen similar to the one before. Due to the increase of the cutting forces, the source strengths at all sections with heat input were chosen higher than in the cases before. In particular the strength of the shear zone heat sources yielded a value which is almost double the value of the cases before.

Figure 6.22 shows a case for a tool with another rake angle  $\gamma = 10^\circ$ , a rise per tooth  $RPT = 40 \mu\text{m}$ . The cutting speed was again the lower value of  $v_c = 4 \text{ m/min}$ . The absolute temperature values are comparable to the case with the lower rake angle, as expected. Hence, the chosen reference temperature  $T_{ref}$  for the calibration of the panel method is in the same magnitude. The temperature field in the tool shows a slight tilting of the isotherms to higher angles against the  $x$  – axis. At the work piece, again, the depth of the influence is higher because of the lower cutting speed. Shape and absolute temperature values are very similar to the case with the lower rake angle.

The chosen contact lengths at the rake face and the clearance face were hence determined to be also similar. For the boundary condition parameters, equivalent values were determined, despite the value for the rake face strength.

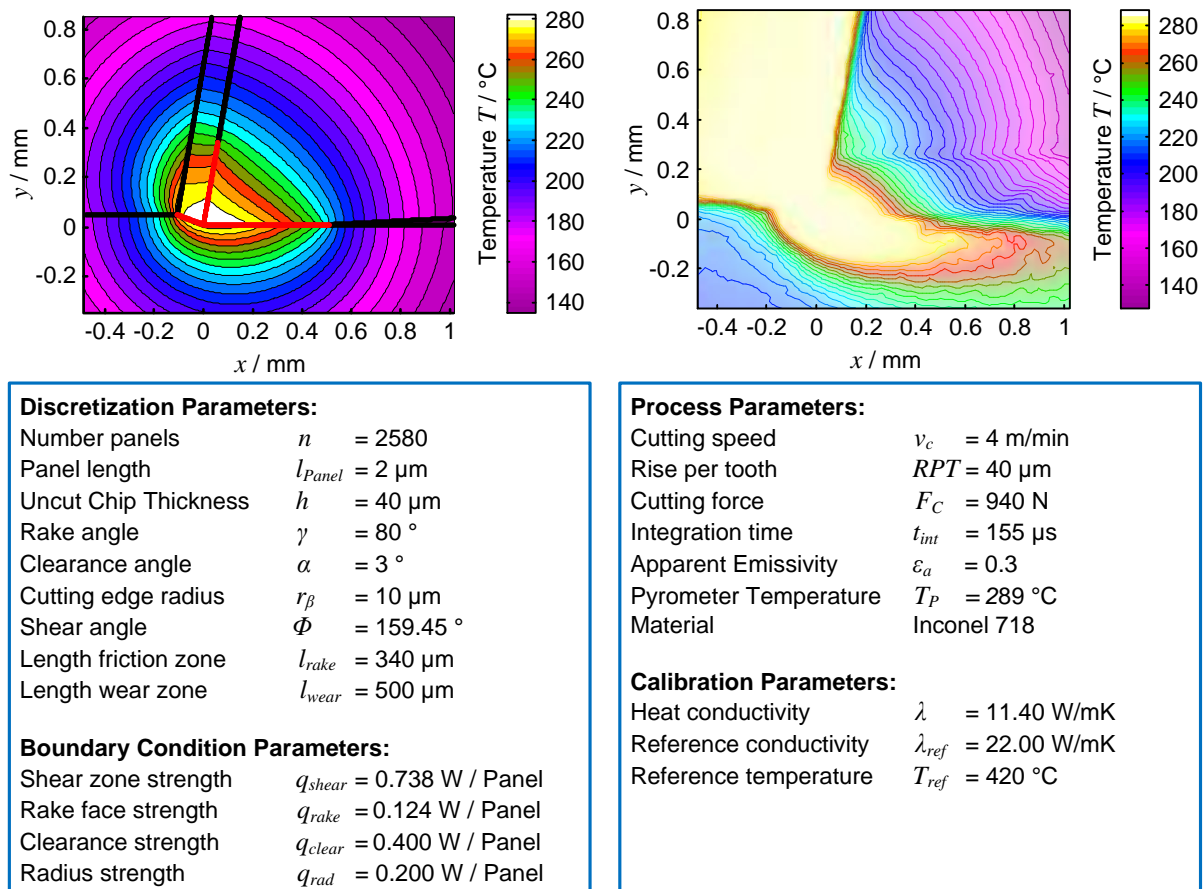


**Figure 6.22:** Comparison of the Influence of Rake Angle

*Vergleich des Einflusses des Spanwinkels*

This is due to the different rake angle and the appropriate force component. A different behavior of the panel method can be observed in the chip in the vicinity of the root point. While for the lower rake angle the maximum area of temperatures was found more inside the tool region, this area shifts toward the chip for the present case. This is most probable caused by the different choice of the source strengths of the panels on the rake face.

A case for the highest rise per tooth, which was investigated during the experiments, is shown in Figure 6.23. The shown infrared camera image was taken for a rake angle  $\gamma = 10^\circ$ , a cutting speed  $v_c = 4 \text{ m/min}$  and a rise per tooth  $RPT = 80 \mu\text{m}$ . While the temperature distribution in the tool yields the same characteristic than before, the temperature field in the work piece and near the shear zone show another behavior. The depth of influence in negative  $y$ -direction, i.e. inside the work piece is quite deep. However, the influence on positive  $x$ -direction, i.e. towards the cut work piece surface, appears relatively low. The absolute temperatures reach the same magnitude than the one yield for the higher cutting speed.

With the panel method this characteristic behavior was considered with a low value for the clearance face wear zone, while the measured contact length at the rake face was the highest measured during the experiments.

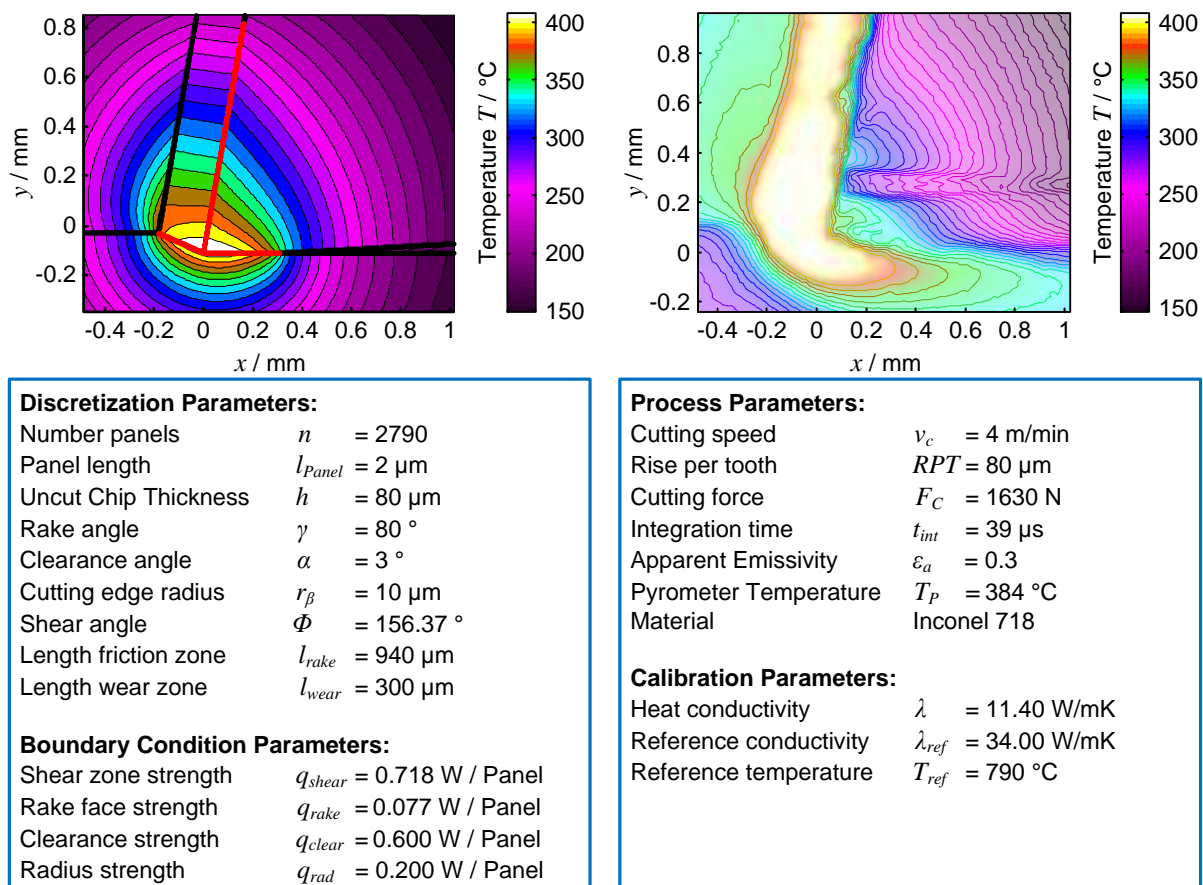


**Figure 6.23:** Comparison of the Influence of Increased Rise per Tooth  
*Vergleich des Einflusses erhöhtem Zahnsprunges*

Furthermore, the strengths of the panels on the rake face were chosen relatively low compared to those on the other panels. The high absolute temperatures yielded a reference temperature  $T_{ref} = 790^\circ\text{C}$ , which is again comparable to the cases with higher cutting speeds. Due the higher rise per tooth of the tool, the disturbance from the chamfer is significantly visible in the infrared camera image. Conclusion for the temperature field at the clearance face are therefore difficult.

The same applies for the tests conducted with the highest rake angle of the conducted trials. However, the infrared image shown in Figure 6.24 yields undisturbed isotherms in the tool above the chamfer. The image was taken for a rake angle  $\gamma = 15^\circ$ , a cutting speed  $v_c = 8 \text{ m/min}$  and a rise per tooth  $RPT = 40 \mu\text{m}$ . For this case, the lowest influence of the work piece was identified. The area of maximum temperatures is almost exclusively along the shear zone. The absolute temperature values are in a medium range within the frame of the measured temperatures during the broaching experiments.

With the panel method, this effect were considered with a relatively high value of the strengths for the panels on the shear zone. While the length of the section at the clearance face was comparable to the cases before, the friction zone length was determined to be relatively high.

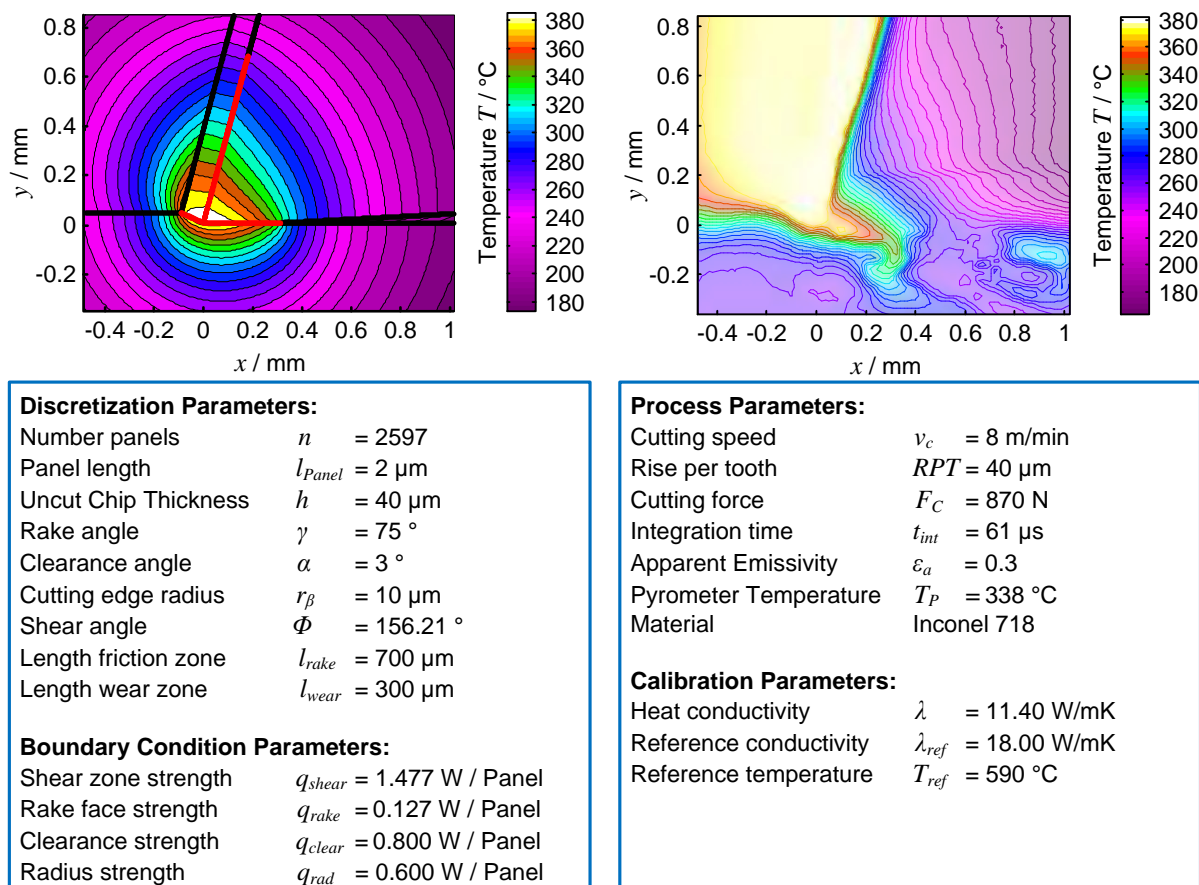


**Figure 6.24:** Comparison of the Influence of Higher Rake Angle

*Vergleich des Einflusses erhöhten Spanwinkels*

The absolute temperature values were considered with a reference temperature of  $T_{ref} = 590^\circ\text{C}$ . For the last case, the result from the panel method did not yield as good agreement with the infrared image as in the cases before. This might show the limitation of the method to moderate cutting speeds and rake angles. All other cases investigated were, however in good agreement with the reality.

## 6.4 Conclusions and Comparison of Both Approaches

### *Zwischenfazit und Vergleich der beiden Ansätze*

For the validation of both novel model approaches, cutting experiments on a fundamental test rig and a broaching machine were conducted. Materials with different machinability were tested. The temperature fields occurring during cutting, were measured with a combination of infrared camera and two-color pyrometer. Thereby, the measurement locations were chosen in a way that one spot of the measurement scene is covered from both measurement devices. By doing so, a calibration of emissivity over temperature was determined. The conducted experiments yielded the following results:

- In a first step, the validity of the assumed thermal boundary conditions was investigated. Therefore, so called mesh plots were generated, i.e. the three-dimensional plot of the temperature distribution over the two spatial dimensions. With the help of parallel and orthogonal horizon plots, providing the temperature function in a distinct plane, the characteristic regions in metal cutting were analyzed. The assumed adiabatic boundaries at the work piece and the clearance face were found in good agreement with the measurement. For the rake face and shear zone, the NEUMANN condition was found as suitable boundary condition. Furthermore, characteristic temperature distributions along the sources could be found.
- The validation of the elementary solution approach was conducted with the help of the results from the fundamental test rig. Emphasis was laid on cutting speed and work piece material. In general, the elementary solution approach is capable to represent the measured temperature fields. For increasing cutting speeds, a shift of the maximum temperature area from the root point to the rake face was observed. This behavior was modelled by means of the distribution and strength of the source solutions. While the qualitative behavior was found in good agreement, the absolute temperature values revealed partly significant deviations.
- For the panel method approach, the measurements of the cutting experiments from the broaching machine were used. For the tested parameter ranges, good qualitative and quantitative agreement was found, in particular in the area near the root point. It may be noted that for the panel method, only physical input data e.g. cutting force or contact length of chip and tool were used. The calibration which was, however, necessary can be considered as a global scaling factor. Using slight different values for the model parameters yield model plots with even more agreement to the measurements.

Summarized, both methods resulted in physical sensible predictions of the temperature fields for different materials and cutting parameters. The elementary solution approach can be considered as general feasibility study of the application of the potential theory. The panel method is a more systematic enhancement, which yielded also absolute temperatures in good agreement to the measurement.

# 7 Comparison to Other Modelling Approaches

## *Vergleich mit anderen Modellierungsansätzen*

While both presented methods for the potential theory are novel approaches for thermal modelling in metal cutting, conventional model approaches can be considered more mature. In particular, analytical models and FE simulation models yield acceptable results in terms of temperature prediction. The present chapter should give a classification of the developed potential theory methods in comparison. After a brief comparison of conventional approaches to both developed methods, a specific comparison with the Finite-Element Method is provided.

## 7.1 Comparison to Conventional Modelling Approaches

### *Vergleich mit konventionellen Modellenansätzen*

As outlined in the state of the art, analytical models inhere certain disadvantages, which prevent them to be more flexible. In particular the limited number of mathematical solutions in use makes analytical approaches suitable for only certain cases. Additionally to the limited number of mathematical solutions, a subsystem for each component is needed for most analytical approaches.

For the comparison with analytical models, a modified approach from GIERLINGS was applied [GIER15, pp. 51–78]. He recognized the limited validity of the original KOMANDURI AND Hou approach for the thermal behavior of broaching processes. In particular, the original approach does not allow a shift of the maximum temperature area towards the root point. This is due to the mathematical structure of the model. However, infrared camera measurements of the typical broaching processes revealed this area close to the root point, especially for worn tools. In the modified model, a third band heat source is introduced at the clearance face of the tool. The length of this source is chosen corresponding to the assumed or measured length of the clearance wear zone  $l_w$ . The other two band heat sources are chosen equivalent to rake angle  $\alpha$  and the shear angle, respectively the chip thickness. With the model, the cutting edge radius  $r_\beta$  can not be modelled. Furthermore, work piece and tool need to be modelled in two subsystems, a chip model is not provided for the modified approach. For the computation of temperature fields further parameters as heat partition ration are needed. Details for the parameterization can be found in [GIER15] and are not presented in detail here.

On the lower left-hand side of Figure 7.1 the model outcomes for this modified band heat source model is shown. For comparison, an infrared image for the described broaching case is shown on the upper left-hand side of the figure. As described, the area of maximum temperature can be found close to the root point. The work piece material was Inconel 718 and the experiments are corresponding to those presented in before. For the infrared camera measurements an emissivity of  $\varepsilon = 0.86$  was assumed due to the preparation of the tool with black color. The temperature field in

the work piece is stretched along the uncut work piece surface in an elliptic shape. The results from the modified model yields good agreement with the infrared camera image, in particular in the tool. The work piece temperature distribution appears concentric. Concerning absolute values, the temperatures are higher in comparison with the infrared camera measurements.

The appropriate values for the basic parameter which were used for all modelling approaches are given in Table 7.1. Besides the cutting parameters values for the cutting force, the passive force, chip thickness and lengths of friction zone and clearance face wear are given. All these parameters were measured during the process with the help of the infrared camera image. For the analysis the way of determination of this parameters at this point is not relevant. More interesting is, that for all modelling approaches the exactly the same parameter sets were used.

**Table 7.1:** Parameter Set for Comparison of Approaches

*Parametersatz für Vergleich der Ansätze*

Parameter	Units	Value
Rake Angle	$\gamma / {}^\circ$	10
Clearance Angle	$\alpha / {}^\circ$	3
Cutting Velocity	$v_c / \text{m/min}$	4
Cutting Edge Radius	$r_\beta / \text{mm}$	0.01
Uncut Chip Thickness	$h / \text{mm}$	0.04
Cutting Force	$F_C / \text{N}$	1139
Passive Force	$F_P / \text{N}$	878
Chip Thickness	$h' / \text{mm}$	0.112
Length of Friction Zone	$l_f / \text{mm}$	0.16
Length of Clearance Wear Zone	$l_w / \text{mm}$	0.17

The results of the panel method approach is presented in the upper right-hand side of the figure. For the temperature in the tool, the isotherms resulting, have a more stretched shape than with the band heat model. The area of maximum temperature is close to the root point with a slight shift along the rake face. In the chip, a parallel isotherm structure can be seen. The temperature influence zone at the work piece appears similar to the results from the band heat model. The absolute temperature value is also higher than measured with the infrared camera.

For comparison with the simulation approaches, a two-dimensional FE model (DEFORM) was created from PUTZ ET AL. [PUTZ15] was conducted. Only chip and work piece were simulated, a wear zone was not considered in the computation. The frictional contact was used with coefficient of  $\mu = 0.6$ . For the tool a heat transfer coefficient  $\alpha_{tool} = 45000 \text{ W/m}^2\text{K}$  was chosen. To consider the thermoplastic flow the JOHNSON-COOK law was applied. As shown on the figure, a non ideal chip formation according to the COCKCROFT-LATHAM criterion was approximated. The modelling results are shown in the lower right-hand side of the figure. As can be seen, the area of highest temperature appeared near the root point but shifted into the chip along the shear zone. The temperature distribution in the work piece appears similar to those

of the two latter approaches, however yielded a more complex shape. The absolute temperature values predicted from the FE simulation matches to the infrared camera measurements.

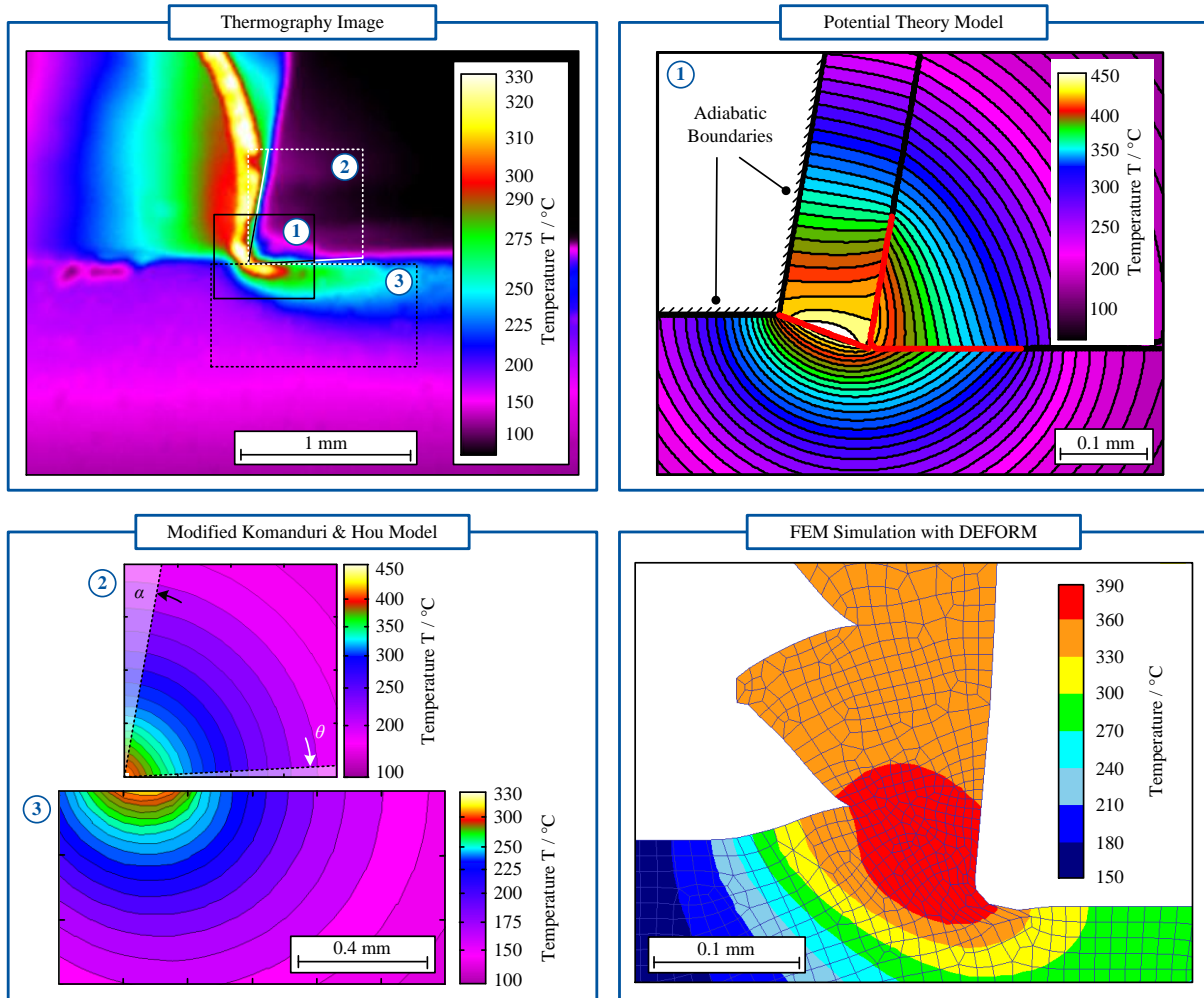


**Figure 7.1:** Comparison of Different Modelling Approaches according to [KLOC15]

*Vergleich verschiedener Modellierungsansätze [KLOC15]*

Summarized all modelling approaches yielded temperature distributions which are in suitable agreement with the experimental results. The modified band heat source model from GIERLINGS was in particular found to be in good accordance with the tool temperature distribution and can be considered as less computational effort. For geometrically more complex modelling (cutting edge radius), however, the model approach can not be used. The panel method is able to model chip, tool and work piece temperature in good agreement, however more computation effort (i.e. solving the linear equation system) is required. The most computation effort as well as different submodels are required for the FE simulation approach, however the predicted temperature distributions are in good agreement with the reality. Concluding from these results, the potential theory could be classified as a method approach in between the FE simulation and more simple (in terms of computation effort) analytical models. A further investigation of the validity and the limits of the panel method is provided in the following subchapter.

## 7.2 Comparison to the Finite Element Method

### Vergleich mit der Finite Elemente Methode

In general, the panel method can be considered as a geometrical discretization method, i.e. the characteristic geometrical boundaries (e.g. rake face) are approximated by means of nodes and panels. The partial differential equation, however, is not discretized, the elementary solutions in use are still solving this equation. In contrast to that, FE discretization methods approximate both, geometry and the differential equation. Different to the panel methodology, the boundaries and the space inside are discretized by means of nodes. For the FE method, the partial differential equation is replaced by the appropriate difference equation of second order, compare **Figure 7.2**.

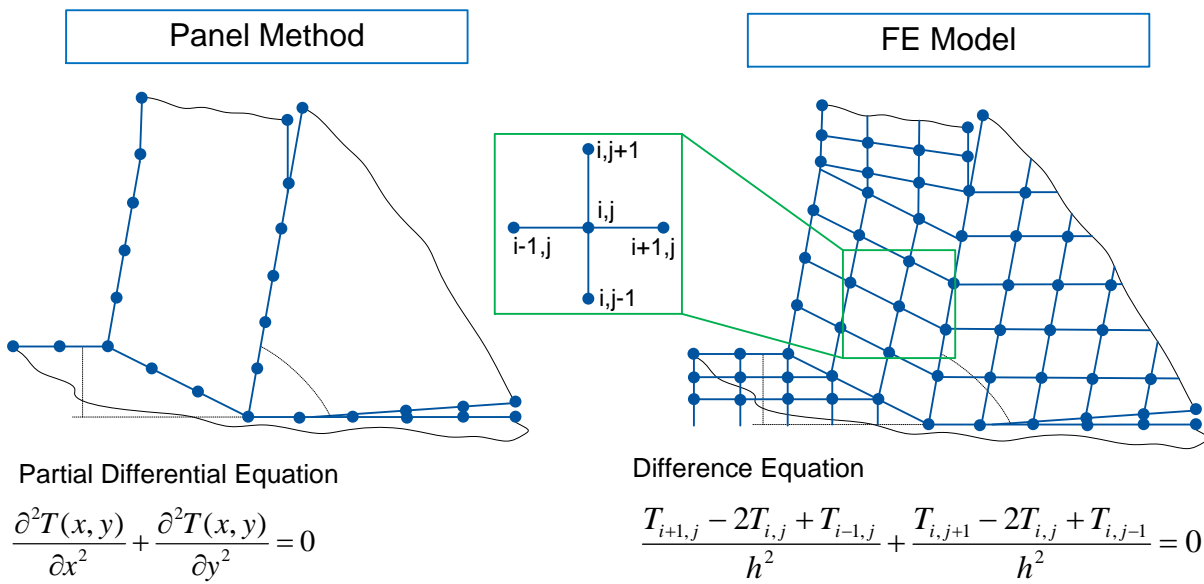


**Figure 7.2:** Discretization of Panel Method and FE Model  
*Diskretisierung der Panelmethode und des FE Modells*

As the FE modelling approach linearizes the partial differential equation before solving it, a consideration of force models, material models and friction models is possible. Furthermore, FE modelling can be applied for three-dimensional problems. At the current state, the FE modelling method can be considered as optimal when predicting complex geometries and coupled thermo-mechanical states.

For comparison of the developed panel method approach, comparisons with the results from an FE model were conducted. Furthermore, the model outcomes were validated by means of further cutting experiments. These experiments were again conducted on the broaching machine with the presented measurement devices and method. In contrast to the experiments before, the tool (uncoated cemented cut-off insert, WC H13A, rake angle  $\gamma = 6^\circ$ , clearance angle  $\alpha = 3^\circ$ , cutting edge radius  $r_\beta = 5 \mu\text{m}$ ) was fixed on the dynamometer and the work piece was moved against it. Details of the experimental setup are given from ABOURIDOUANE [ABOU15]. The presented FE model results are also taken from this work. For the investigation the C 45 E steel was used.

In Figure 7.3 the results for a cutting speed of  $v_c = 150$  m/min and an uncut chip thickness of  $h = 0.2$  mm are shown. On the upper left-hand side of the figure, the infrared camera image in the filled contour plot style is provided. The upper right-hand side shows the FE model. On the lower left-hand side the panel results using two heat sections at rake face and shear zone are presented, the lower right-hands side shows a modified panel model with a third heat section at the clearance face. The modification was necessary to adapt the results to the real results.

For both models, the same input parameters were used. The kinematic cutting parameters were thereby calculated with the OXLEY-MERCHANT model with the cutting parameters and the chip compression ratio  $\lambda_h$ , which was determined experimentally. For the shear flow stress a modified JOHNSON-COOK Model was applied.

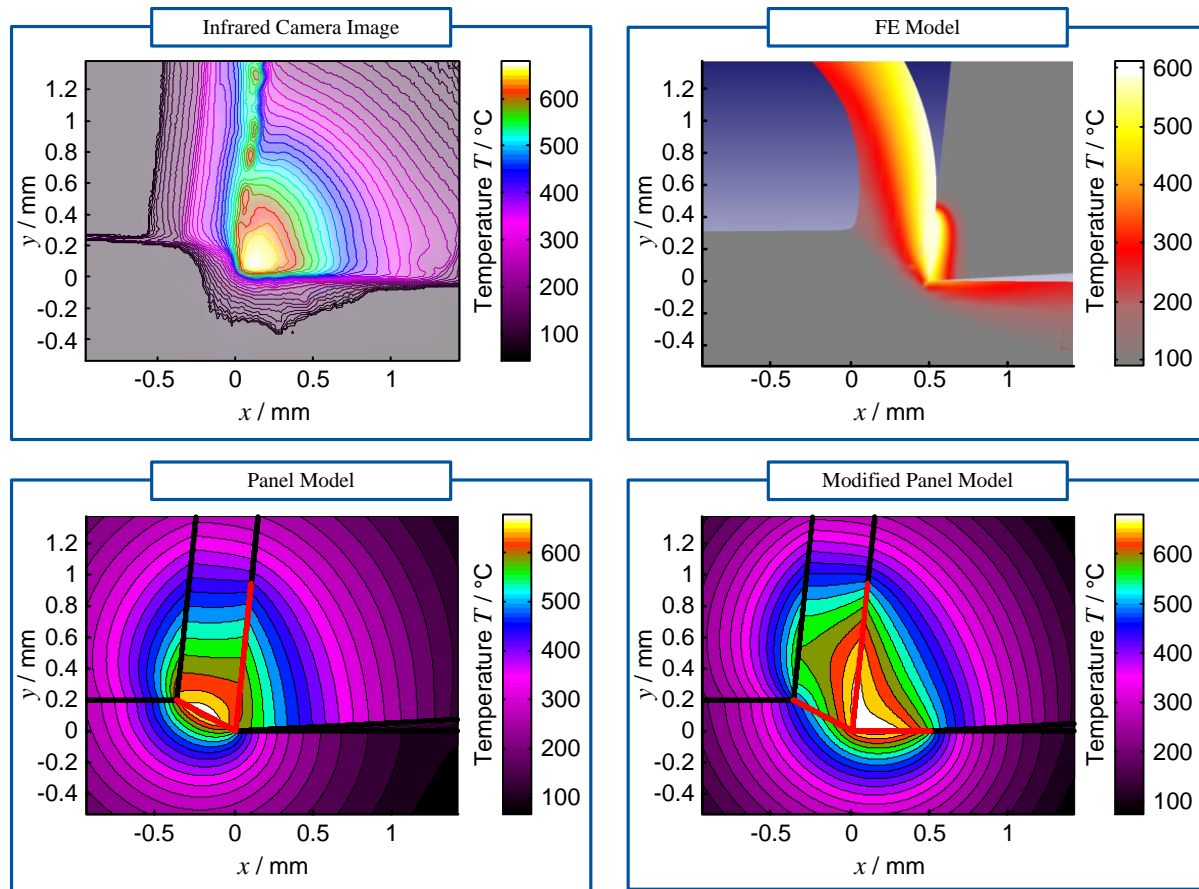


**Figure 7.3:** Comparison to FE Model ( $v_c = 150$  m/min,  $h = 0.2$  mm)

*Vergleich mit FE Modell ( $v_c = 150$  m/min,  $h = 0.2$  mm)*

The fraction of the plastic deformation energy concerted to heat was computed using the TAYLOR-QUINNEY Relation. For the friction a further optimized model was used. The DE simulation itself was conducted using a commercial software (DEFORM). Further details of the simulation can be found in [ABOU15].

When comparing the four temperature fields, the FE model and the modified panel method are found in good agreement with the infrared camera image. The maximum area of temperatures can be found in the tool, expanding in concentric isotherms. In the chip, parallel isotherms with maximum temperatures approaching the rake face

can be found. In contrast to the investigations before, for these experiments the measurements of the chip can be used as the chip thickness yields sufficiently high dimension ( $h' > 0.09 \text{ mm}$ ). When considering the not modified panel method model, the results are not found in good agreement with the infrared camera images. With the input parameters applied, the maximum area of temperatures is predicted around the shear zone and not inside the tool. The temperatures in the chip follow the known parallel characteristic.

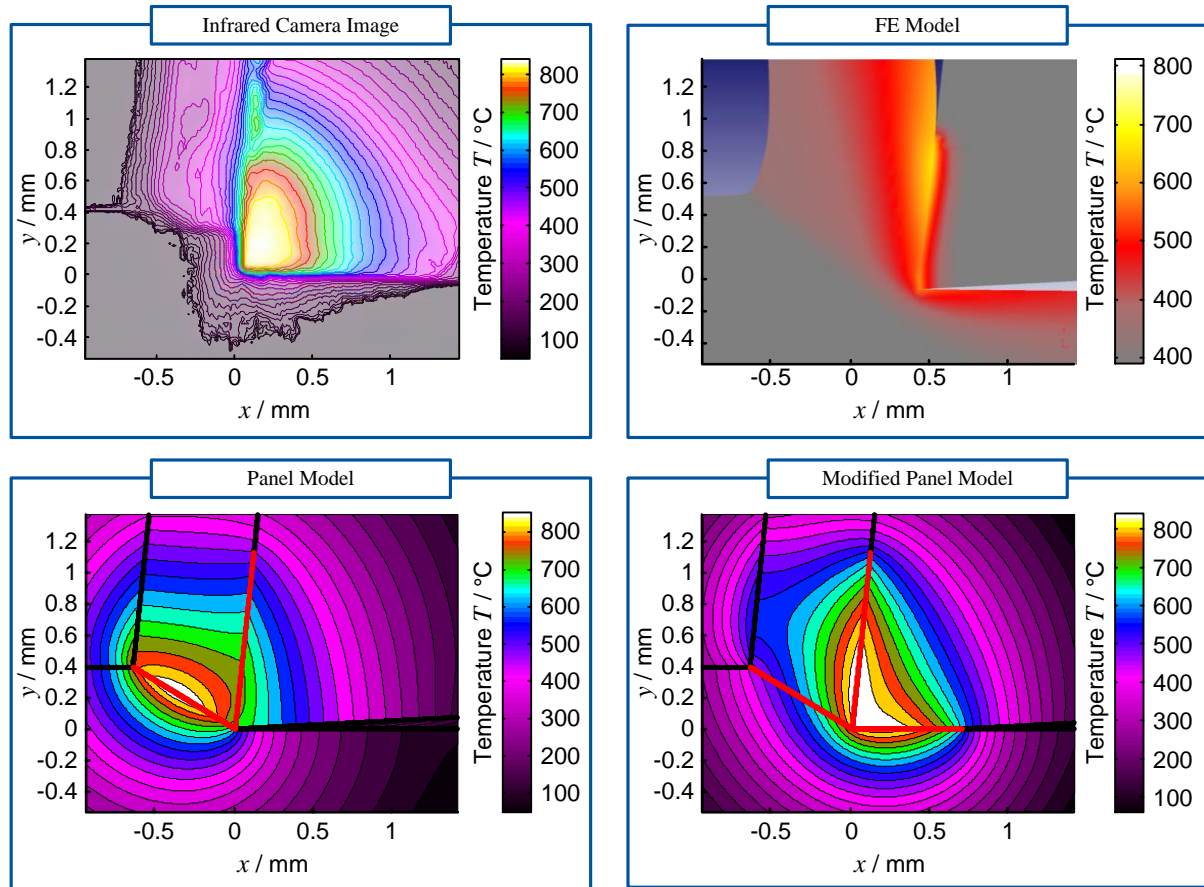


**Figure 7.4:** Comparison to FE Model ( $v_c = 150 \text{ m/min}$ ,  $h = 0.4 \text{ mm}$ )

*Vergleich mit FE Modell ( $v_c = 150 \text{ m/min}$ ,  $h = 0.4 \text{ mm}$ )*

This behavior can also be observed for an uncut chip thickness of  $h = 0.4 \text{ mm}$ . The appropriate results are shown in Figure 7.4. Again FE model and the modified panel model are in good agreement while the not modified panel model yields similar results as before.

For generating suitable results with the modified panel method, significant modifications had to be conducted. As in the approaches before, a third heat section at the clearance face was introduced, however in reality this zone is not apparent. The zone is used to generate the temperature field inside the tool, connecting the isotherms from rake face and clearance face. While the introduction of the clearance face zone and a cutting edge radius (which was also considered in the modified approach) seem sensible, the values of the boundary condition vector had to be modified significantly above the assumed values.

For the investigated case shown in Figure 7.5, e.g. the heat source strength per panel on the rake face was chosen to  $q_{rake} = 33.500 \text{ W/Panel}$ . The not modified approach assumes a value of  $q_{rake} = 3500 \text{ W/Panel}$ , calculated from the forces and the shear angle. An additional section at the clearance face with a length of  $l_{clear} = 0.9 \text{ mm}$  and a specific source strengths of  $q_{clear} = 40\,000 \text{ W/Panel}$ . Furthermore the calibration coefficient differs from  $\lambda_{ref} = 14$  for the not modified approach and  $\lambda_{ref} = 3.5$  for the modified approach.

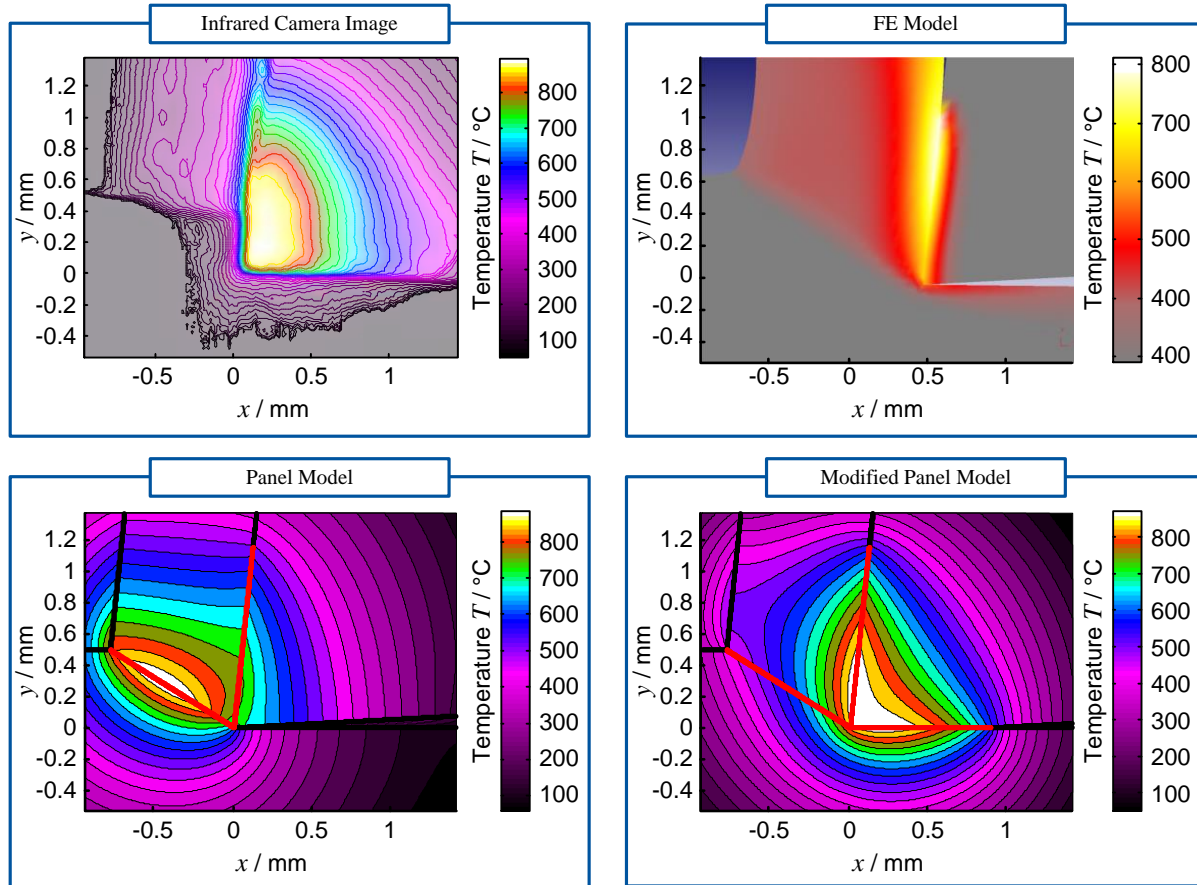


**Figure 7.5:** Comparison to FE Model ( $v_c = 150 \text{ m/min}$ ,  $h = 0.5 \text{ mm}$ )

*Vergleich mit FE Modell ( $v_c = 150 \text{ m/min}$ ,  $h = 0.5 \text{ mm}$ )*

While the numerical values need to be significantly changed, the deviations in the model were expected. The presented panel method approach based on sources does not include the influence of higher cutting speeds. For the relatively low cutting speeds and uncut chip thicknesses of the broaching process, the predicted temperature fields were found in good agreement. For the high cutting speeds and uncut chip thicknesses the presented method is limited. However, with the modification, temperature fields with average agreement can be found. For a further enhancement, the consideration of additional panels in the chip can be used, as proposed in Chapter 5.2.4. With consideration of these additional panels, the influence of the cutting speed, particularly in the chip could be modelled. At the present state, the source panel method, however, can be used with less modeling effort but suitable credibility for the modeling of temperature fields in metal cutting.

### 7.3 Intermediate Conclusions and Assessment

#### *Zwischenfazit und Bewertung*

The panel method approach uses a discretization of the cutting kinematics, however the mathematical functions applied are still solutions of the partial differential equation for heat conduction, i.e. no discretization of the partial differential equation is needed. Due to that, the panel method can be considered a modelling approach which combines the advantages of more simple analytic models and more complex discretization methods, i.e. FE simulation. An exemplary comparison between the panel method, a modified band heat source model and outcomes from FE simulation was conducted.

All model approach yielded results in good agreement to the measured infrared images. The band heat source model is only capable to predict temperatures in the tool and the work piece. Furthermore, only simple geometries can be provided. The FE simulation showed also good results for the tested cases, but requires more modelling effort and more complex submodels (i.e. material law, friction law). For low cutting speeds, the panel method was found as a good alternative, when considering the relatively low modelling effort. For higher cutting speeds, however, the actual panel method did not yield sufficient results when using physical sound input parameters for heat source lengths and forces. In principal, results in good agreement could be achieved by the panel method, however a further calibration was needed. This calibration did not correlate to the real physical input parameters.

The fact that the actual panel method approach, i.e. source panel approach, is limited to lower cutting speeds was expected. As described, an additional source at the chip could be used to model the convective heat transfer caused from the material flow. Overall, the results validated, that the potential theory can be a modelling alternative in between of simple analytical models and the FE simulation, as a compromise between accuracy and modelling efforts.

## 8 Summary and Outlook

The presented work introduces a novel approach for analytical thermal modelling of metal cutting processes. For the derivation of computational models, complex functions solving the partial differential equation of heat conduction were considered. The complex functions belong to a certain function class called potential functions. These class of functions already showed good results in other engineering fields e.g. fluid mechanics, where solutions of exactly the same partial differential equation are needed.

As a first step, a methodology based on the elementary solutions of the potential theory was developed. For derivation of thermal models, the steps: superposition, parameter study, calibration and correlation need to be conducted. The method was applied in this thesis mainly by using the source solutions of potential theory. By placing source solutions on lines representing shear zone and rake face suitable temperature fields were generated. The subsequent calibration and correlation led to computational models for temperature distribution and heat flow distribution in chip, tool and work piece. The successful use of the elementary solution approach can be considered as a feasibility study for the use of potential theory for thermal modeling in metal cutting. However, the derivation of distinct temperature models for metal cutting with this method is only suitable for certain cases and requires efforts in the parameter determination.

A more systematic method was presented in this thesis by application of the panel method. This method uses discretization of the cutting kinematics with the help of nodes and panels at characteristic boundaries. In this thesis, source panels were applied. For each panel the thermal boundary conditions, either adiabatic or preset heat flow value, need to be defined. The source strengths are subsequently determined in terms of a linear equation system. There is not a need for parameter studies or later correlation. Position and strength of each panel is determined solely by the boundary conditions and the geometries. The panel method can therefore be regarded as a systematic enhancement of the elementary solution approach.

Both model approaches were validated by means of cutting experiments. For this thesis, experiments on a fundamental test rig and a broaching machine were conducted. The temperature fields were measured with a combination of infrared camera and two-color pyrometer. By simultaneous measurement with both measurement devices at one spot of the measurement object, an emissivity calibration for each material was conducted. Both approaches were in general suitable for prediction of the measured temperature fields. The deviation of predicted and measured results were in a suitable range. Finally the methods were compared to conventional models, i.e. in particular the model of KOMANDURI AND Hou and to results from the FE simulation. While all approaches yield relevant results, the advantage of the use of potential theory is the modular consideration of geometry (e.g. cutting edge radius) with less computational effort than FE simulation.

Beyond the presented first approaches of using potential theory for modelling temperature fields in metal cutting, this work is only an initial contribution for an alternative approach for thermal modeling in metal cutting. The results from this thesis can be interpreted as a first step to verification of the research hypothesis: the use of potential functions is feasible for thermal modeling of metal cutting. Extending the findings from this thesis, the use of both presented methods should be researched in the future.

In the analysis of the elementary solution approach, only source, corner and parallel solution were investigated in detail. However, the combination of source and vortex solution yielded interesting results as briefly presented in this thesis. As described, the use of the elementary solution approach is strongly dependent on the application case, as calibration and correlation is a necessary part of the methodology. Further validation experiments could clarify if the presented computation model, and in particular the correlation of model and cutting parameters, are only valid for the presented case or have wider validity.

In terms of the panel method, only source panels were applied. The basic theory was also successfully extended to vortex flows, which found the basic for aerodynamic design of airfoils [ANDE01, pp. 177–418]. In general, also a combination of source, vortex and parallel solution could be applied. The parallel solution, assumed to correlate to the cutting speed did not lead to suitable results in the presented work. However, this conclusion is only true for the chosen approach and the parallel solution could be used additionally to the presented panel approach. For the thermal boundary conditions, only the orthogonal component of the heat flux was considered to derive the influence matrix. When using the panel method for aerodynamic modeling of flow around an airfoil, also a condition of the parallel component is used to solve the linear equation system. An equivalent condition to this renown KUTTA Condition could not be found during this thesis. However, it can not be excluded that such a condition also exists for metal cutting.

A numerical approach based on potential theory for three dimensional aerodynamic problems was described from KATZ [KATZ10, pp. 331–368]. As in reality most cutting processes need to be considered three dimensional (e.g. secondary cutting edge or three dimensional chip forming), an enhancement of the method should be applied. Furthermore the theory can be applied for periodic instationary problems, e.g. by the theory of small disturbances. The use of this transfer to instationary problems could be suitable for periodic cutting process, e.g. milling and drilling.

In general, the use of potential theory should be validated by means of further cutting processes. Further research in this field could lead to a modeling method in between the analytical-empirical and the FE simulation, as a compromise between precision and computational effort.

## Zusammenfassung und Ausblick

Die vorliegende Arbeit handelt von einem neuartigen Ansatz für die analytische thermische Modellierung von Zerspanprozessen. Für die Ableitung von Berechnungsmodellen wurden komplexe Funktionen, welche die Wärmeleitungs-differentialgleichung lösen, genutzt. Die komplexen Funktionen gehören zu einer bestimmten Funktionenklasse, den sogenannten Potenzialfunktionen. Diese Funktionenklasse zeigte bereits gute Ergebnisse in anderen Ingenieurwissenschaften, z. B. der Fluidmechanik, in denen Lösungen für exakt dieselbe Differenzialgleichung benötigt werden.

Als erster Schritt wurde eine Methode entwickelt, welche auf den Elementarlösungen der Potenzialtheorie basiert. Zur Herleitung thermischer Modelle, werden die Schritte: Superposition, Parameterstudie, Kalibrierung und Korrelation durchgeführt. Die Methode wurde in dieser Arbeit hauptsächlich mit der Quellenlösung der Potenzialtheorie angewandt. Durch Platzieren der Quellenlösungen auf Linien, welche Scherzone und Spanfläche repräsentieren, konnten geeignete Temperaturfelder erzeugt werden. Die anschließende Kalibrierung und Korrelation führte zu Berechnungsmodellen der Temperatur- und Wärmestromverteilung in Span, Werkzeug und Werkstück. Die erfolgreiche Anwendung des Ansatzes der Elementarfunktionen kann als eine Art Machbarkeitsstudie für den Gebrauch der Potenzialtheorie für die thermische Modellierung in der Zerspanung angesehen werden. Die Herleitung konkreter Temperaturmodelle erfordert jedoch hohen Aufwand speziell bei der Parameterbestimmung.

Eine systematischere Methode wurde in dieser Arbeit durch die Anwendung der Panelmethode gezeigt. Diese Methode nutzt eine Diskretisierung der kinematischen Eingriffsbedingungen durch Knoten und Panel an charakteristischen Grenzflächen. In dieser Arbeit wurden ausschließlich Quellenpanels verwendet. Für jedes Panel muss die zugehörige thermische Randbedingung, entweder adiabate Grenze oder Vorgabe eines Wärmestroms, definiert werden. Die Quellenstärken werden anschließend durch die Lösung eines Linearen Gleichungssystems ermittelt. Eine Parameterstudie oder Korrelation ist nicht mehr notwendig. Position und Stärke von jedem Panel werden ausschließlich durch Vorgabe der Randbedingungen und der Geometrie bestimmt. Die Panelmethode kann daher als systematische Erweiterung des Ansatzes der Elementarfunktionen angesehen werden.

Beide Modellierungsansätze wurden mit Zerspanversuchen validiert. Die gemessenen Temperaturfelder wurden mit einer Kombination aus Infrarotkamera und Zweifarbenpyrometer ermittelt. Durch simultane Messung mit beiden Messgeräten auf einem gemeinsamen Messfleck wurde eine Emissionsgrad Kalibrierung für alle Werkstoffe durchgeführt. Beide Ansätze zeigten gute Ergebnisse zur Vorhersage von Temperaturfeldern in der Zerspanung. Beide Ansätze wurden mit bestehenden Modellierungsansätzen, insbesondere dem KOMANDURI AND Hou Modell und der FE Simulation verglichen.

Hinausgehend über diese ersten Ansätze zum Gebrauch der Potenzialtheorie für die Modellierung von Temperaturfeldern in der Zerspanung, ist diese Arbeit nur ein erster Beitrag für einen alternativen Ansatz der thermischen Modellierung in der Zerspanung. Die Ergebnisse können als ein erster Schritt zu Verifikation der Forschungshypothese interpretiert werden: der Einsatz der Potenzialtheorie ist für die thermische Modellierung in der Zerspanung brauchbar. Über die Erkenntnisse dieser Arbeit hinausgehend sollten beide vorgestellten Methoden in Zukunft erforscht werden.

In der Analyse des Elementarfunktionenansatzes wurden nur Quellen-, Ecken- und Parallellösung im Detail untersucht. Allerdings resultierte auch die Kombination aus Quellen- und Wirbellösung, wie kurz in der Arbeit gezeigt, in interessanten Ergebnissen. Der Gebrauch des Elementarfunktionenansatzes ist, wie beschrieben, stark abhängig vom jeweiligen Anwendungsfall, Kalibrierung und Korrelation sind notwendiger Teil der Methodik. Weitere Validierungsexperimente könnten klären, ob das vorgestellte Berechnungsmodell, insbesondere die Korrelation von Modell- und Schnittparametern, nur für den untersuchten Fall oder für darüber hinausgehend gelten.

Bezüglich der Panelmethode wurden ebenfalls nur Quellenpanels angewandt. Die grundlegende Theorie wurde ebenfalls erfolgreich auf Wirbelpanels erweitert, was die Basis für die aerodynamische Auslegung von Profilen bildet [ANDE01, pp. 177–418]. Im Allgemeinen wären sogar Kombinationen aus Quellen-, Wirbel- und Parallellösung denkbar. Beim Einsatz der thermischen Randbedingungen wurde nur die orthogonale Komponente für die Ableitung der Beeinflussungsmatrix berücksichtigt. Beim Einsatz der Panelmethode für die aerodynamische Modellierung der Strömung um ein Profil werden ebenfalls Bedingungen für die Parallelkomponente genutzt um das lineare Gleichungssystem aufzustellen. Eine ähnliche Bedingung wie diese sogenannte KUTTA Bedingung konnte im Rahmen dieser Arbeit nicht gefunden werden, dies soll aber nicht bedeuten, dass eine solche Bedingung nicht existiert.

Einen numerischer, auf der Potenzialtheorie basierender Ansatz für dreidimensionale aerodynamische Fragestellung wurde von KATZ [KATZ10, pp. 331–368] beschrieben. Da in Realität die meisten Zerspanprozesse als dreidimensional betrachtet werden müssen ( z. B. Nebenschneideneingriff oder dreidimensionale Spanbildung) sollte eine Erweiterung der Methode durchgeführt werden. Weiterhin kann die Methode auf periodisch instationäre Problemstellungen erweitert werden, z. b. durch die Theorie kleiner Störungen. Die Übertragung auf solche instationären Fragestellungen könnte für periodische Zerspanprozesse, z. B. Bohren und Fräsen, von Interesse sein.

Im Allgemeinen sollte der Gebrauch der Potenzialtheorie für weitere Zerspanprozesse validiert werden. Weitere Forschung in diesem Gebiet könnte zu einer Modellierungsmethode zwischen analytisch-empirischen Modellen und der FE Simulation führen und einen Kompromiss zwischen Genauigkeit und Rechenaufwand darstellen.

# 9 Appendix

## Anhang

### 9.1 Definitions of Characteristic Thermal Values

#### *Definitionen charakteristischer thermischer Kennwerte*

For the characteristic thermal values, in particular for the heat, in this thesis a unified nomenclature is used. The indices and the choice of capital or small letter as abbreviation of the variable nomenclatures thereby give a direct description of the characteristic of the appropriate value. Capital letters, as a general convention for thermodynamic parameters, stand for values which are not specific values. Specific in this terms means: not related to the mass or an area or volume. Heat itself can be considered as a so-called extensive value, i.e. when dividing a given system in two subsystems, extensive values are also divided. Heat or more precise heat amount and heat flow are expressed as shown in Table 9.1.

**Table 9.1:** Heat and Heat Flow as Extensive Variable

#### *Wärme und Wärmestrom als extensive Größe*

Nomenclature	Description	Symbol	Unit
Heat Amount	Absolute amount of heat (energy)	$Q(t)$	[J] = [N·m]
Heat Flow	Heat amount per time	$\frac{\partial Q(t, x, y, z)}{\partial t} = \dot{Q}$	[J/s] = [W]

Small letters in Thermodynamics in contrast refer to specific values, i.e. if a system is divided in two systems, the specific value remains constant. The density of a material for instance is a specific variable. For thermal issues, the heat amount is related to the geometrical dimension, not the mass. The number of dashes relates to the dimension (line, area or volume) as shown in Table 9.2.

**Table 9.2:** Heat Flux as Specific Variable

#### *Wärmestromdichte als spezifische Größe*

Nomenclature	Description	Symbol	Unit
Heat Flux	Heat amount per time on a line	$\dot{q}'$	[W/m]
	Heat amount per time and area	$\dot{q}''$	[W/m <sup>2</sup> ]
	Heat amount per time and volume	$\dot{q}'''$	[W/m <sup>3</sup> ]

The used form is dependent on the intended use. While for the line heat source from the KOMANDURI AND Hou model mostly the heat on a line is addressed, the heat source strength in this thesis are mainly mentioned as heat flux related to an area.

For heat radiation, e.g. for the infrared camera, the characteristic heat values are given usually related to the volume. When referring to a volume, the term “*heat intensity*” is often used in literature. Sometimes a heat density is mentioned. This expression is physically not correct as it would refer to a heat amount per area. However, the heat amount is related to the time and not to the spatial dimension. The relation between the mentioned variables can be expressed using the general equation:

$$Q = \int_t \dot{Q} dt = \int_t \int_x \dot{q}' dx dt = \int_t \int_A \dot{q}'' dA dt = \int_t \int_V \dot{q}''' dV dt . \quad (9.1)$$

Another important thermal value results from the partial differential equation, which can be given as:

$$\frac{\partial^2 T}{\partial x^2} + \frac{\partial^2 T}{\partial y^2} + \frac{\partial^2 T}{\partial z^2} = \frac{\rho c}{\lambda} \frac{\partial T}{\partial t} \quad (9.2)$$

for constant heat conductivity  $\lambda$ . The coefficient of the instationary term on the right-hand side of the expression is defined as inverse of the temperature diffusivity  $a$ :

$$a = \frac{\rho c}{\lambda} . \quad (9.3)$$

It is obvious that different numerical values of this value change the partial differential equation and hence have an influence on all time related issued. When regarding the variables, this ratio, coming from the partial differential equation, can be interpreted as capacitive heat to heat conduction. The specific heat  $\rho c$  e.g. is high for stone material, while the heat conductivity is relatively low. In practice these materials will need long time to be heated up on an increased temperature. When reached this temperature, however, the temperature maintains relatively long, i.e. the cool down time is high. The same effect is occurring for high densities (or simply high masses) and low heat conductivities.

A dimensionless number closely connected to the temperature diffusivity is the PÉCLET Number:

$$Pe = \frac{v \cdot l}{a} = \frac{v}{\cancel{a/l}} = \frac{v}{v_{thermal}} . \quad (9.4)$$

The number is defined with the ratio of a local speed  $v$ , a characteristic length  $l$  and the temperature diffusivity  $a$ . When recombining these values as shown in Equation 9.4, the ration of  $a$  over  $l$  yields the dimension of a speed  $[m^2/s \cdot m^{-1}] = [m/s]$ . The PÉCLET Number can therefore be interpreted as the local speed of a moving body in relation to a “heat transparency” that is characteristic for the appropriate material. It becomes obvious that the characteristic length chosen plays a major role when interpreting this ratio. Many models in metal cutting consider this number, sometimes also referred to as Thermal Number  $N_{th}$  (when used with contact length as characteristic length instead of uncut chip thickness).

## 9.2 Detailed Mathematical Derivations

*Detaillierte mathematische Herleitungen*

### Derivation of PDE for Heat Conduction

In the following and alternative and more for Equation 2.8 is given. The appropriate sketch of the infinitesimal small control volume is given in Figure 2.5. Similar to Equation 2.7, the conversation of energy can be regarded for the control volume:

$$\frac{dU}{dt} + \dot{Q}_{\text{source}}'' = (\dot{Q}_{\text{out}}'' - \dot{Q}_{\text{in}}''). \quad (9.5)$$

The change of the internal energy is equal to the difference of heat flowing in and out of the control volume and heat sources inside of the volume. By using FOURIER'S Law, the incoming heat flow can be expresses as:

$$\dot{Q}_x'' = -\lambda \frac{\partial T}{\partial x} dydz. \quad (9.6)$$

As explained in the previous section, the heat flow is expresses as extensive variable as the infinitesimal area  $dxdz$  is multiplied to the specific heat flux. For the outgoing heat flow, a TAYLOR Series is assumed:

$$\dot{Q}_{x+dx}'' = \dot{Q}_x'' + \frac{\partial}{\partial x}(\dot{Q}_x'') dx = \dot{Q}_x'' + \frac{\partial}{\partial x}(-\lambda \frac{\partial T}{\partial x}) dxdydz. \quad (9.7)$$

Similar expressions can be found for the other directions. The change of the internal energy in the control volume can be given as:

$$\frac{dU}{dt} = \rho c \cdot dxdydz \cdot \frac{\partial T}{\partial t}. \quad (9.8)$$

For the specific heat capacity the term  $c$  is used instead of the correct term  $c_v$ , which describes the heat capacity for change of constant volume. For solid bodies  $c_v = c_p = c$ , where  $c_p$  is the capacity for constant pressure. For the internal heat sources (and sinks) again the expression:

$$\dot{Q}_{\text{source}}''' = \dot{q}_{\text{source}}''' \cdot dxdydz. \quad (9.9)$$

Again the three dashes indicate a specific value per volume. By putting Equations 9.7, 9.8 and 9.9 in Equation 9.5 yields:

$$\begin{aligned} \rho c \cdot dxdydz \cdot \frac{\partial T}{\partial t} &= \frac{\partial}{\partial x}(\lambda \frac{\partial T}{\partial x}) dxdydz + \frac{\partial}{\partial y}(\lambda \frac{\partial T}{\partial y}) dxdydz + \frac{\partial}{\partial z}(\lambda \frac{\partial T}{\partial z}) dxdydz \\ &+ \dot{q}_{\text{source}}''' \cdot dxdydz. \end{aligned} \quad (9.10)$$

Equation 9.7 was thereby rearranged and used for all three dimensions with a similar expression.

By eliminating the infinitesimal volume  $dxdydz$  the component form of Equation 2.8 is yielded:

$$\rho c \cdot \frac{\partial T}{\partial t} = \frac{\partial}{\partial x} (\lambda \frac{\partial T}{\partial x}) + \frac{\partial}{\partial y} (\lambda \frac{\partial T}{\partial y}) + \frac{\partial}{\partial z} (\lambda \frac{\partial T}{\partial z}) + \dot{q}_{source}''. \quad (9.11)$$

This form is the most general form of the PDE for instationary, three-dimensional cases with internal heat sources and sinks and varying heat conductivity  $\lambda$ . For constant heat conductivity, Equation 9.11 can be simplified:

$$\frac{1}{a} \cdot \frac{\partial T}{\partial t} = \frac{\partial^2 T}{\partial x^2} + \frac{\partial^2 T}{\partial y^2} + \frac{\partial^2 T}{\partial z^2} + \frac{\dot{q}_{source}''}{\lambda}. \quad (9.12)$$

Equation 9.12 is referred to as FOURIER's PDE, analytical solutions are not known, respectively are not in use at engineering applications. If the instationary part can be neglected the equation becomes:

$$\frac{\partial^2 T}{\partial x^2} + \frac{\partial^2 T}{\partial y^2} + \frac{\partial^2 T}{\partial z^2} + \frac{\dot{q}_{source}''}{\lambda} = 0. \quad (9.13)$$

This equation is often called POISSON's PDE, analytical solutions are only valid for special cases. If furthermore no heat sources and sinks are considered, the equation can finally be formulated as:

$$\frac{\partial^2 T}{\partial x^2} + \frac{\partial^2 T}{\partial y^2} + \frac{\partial^2 T}{\partial z^2} = 0. \quad (9.14)$$

This form is mostly in use, the analytical solutions used in this thesis refer to the two-dimensional case of this equation. As mentioned, this form is referred to as LAPLACE'S PDE. In mathematics, a special operator is defined as Laplace Operator:

$$\Delta T = \nabla^2 T = \frac{\partial^2 T}{\partial x^2} + \frac{\partial^2 T}{\partial y^2} + \frac{\partial^2 T}{\partial z^2}. \quad (9.15)$$

While the LAPLACE PDE does not consider heat sources inside the control volume, however, sources can be considered at the boundaries of the regarded control volumes. The sources itself are considered as mathematical singularities, the PDE is not defined at these places. This fact is the reason for the significant meaning of the thermal boundary conditions that are experimentally validated in the frame of this thesis.

The form of the PDE is the reason for the use of the potential theory only on closed areas, i.e. the panels in the panel method approach have only influence in one direction. The same fact is also true for the solution provided from KOMANDURI AND HOU. Their band heat source model can also be used only in closed areas, i.e. no heat sources inside the regarded area are allowed. However, a subsequent superposition can be conducted. Further solutions in metal cutting were applied for the instationary one-dimensional form of the PDE.

### Further Explanation of Cauchy-Riemann Condition

In Equation 2.19 the PDE for the CAUCHY RIEMANN Conditions is described. The conditions can be formulated as:

$$\frac{\partial \Phi}{\partial x} = \frac{\partial \Psi}{\partial y}, \quad \frac{\partial \Phi}{\partial y} = -\frac{\partial \Psi}{\partial x}. \quad (9.16)$$

In the following it will be shown, that each function  $F(z) = \Phi + i \cdot \Psi$  which fulfills Equation 9.16 is also a solution of the Laplace PDE and therefore a solution of the PDE for heat conduction. For the derivation, the following abbreviations are used:

$$\frac{\partial \Phi}{\partial x} = \Phi_x, \quad \frac{\partial^2 \Phi}{\partial x^2} = \Phi_{xx}, \quad (9.17)$$

The appropriate nomenclature is also used for the derivatives in  $y$  direction. Using these abbreviations on Equation 9.16 for the  $x$  derivative of the first equation and the  $y$  derivative of the second equation yields:

$$\Phi_{xx} = \Psi_{xy}, \quad \Phi_{yy} = -\Psi_{xy}. \quad (9.18)$$

A similar expression can be found for the function  $\Psi$  when generating the  $y$  derivative of the first equation and the  $x$  derivative of the second equation. The summation of the two derivatives of Equation 9.18 yields:

$$\Phi_{xx} + \Phi_{yy} = \Psi_{xy} - \Psi_{xy} = 0. \quad (9.19)$$

Again the same equation can be found for the function  $\Psi$ . For the proof that the function  $F(z)$  fulfills the Laplace PDE, the derivatives of  $F(z)$  are determined:

$$\begin{aligned} \frac{\partial^2 F(z)}{\partial x^2} + \frac{\partial^2 F(z)}{\partial y^2} &= \frac{\partial^2 [\Phi(x, y) + i \cdot \Psi(x, y)]}{\partial x^2} + \frac{\partial^2 [\Phi(x, y) + i \cdot \Psi(x, y)]}{\partial y^2} \\ &= \Phi_{xx} + i \cdot \Psi_{xx} + \Phi_{yy} + i \cdot \Psi_{yy} \\ &= (\Phi_{xx} + \Phi_{yy}) + i \cdot (\Psi_{xx} + \Psi_{yy}) \end{aligned} \quad (9.20)$$

Equation 9.20 becomes Zero when both, the real valued part and the imaginary part are equal to Zero. Putting Equation 9.19 as well as the appropriate equation for the derivatives of  $\Psi$  into Equation 9.20 finally yields:

$$\frac{\partial^2 F(z)}{\partial x^2} + \frac{\partial^2 F(z)}{\partial y^2} = 0. \quad (9.21)$$

Hence, each function  $F(z)$  is a solution of the heat conduction PDE if the CAUCHY RIEMANN Conditions are fulfilled. These functions are termed “*potential functions*”.

### Detailed Derivation of Temperature and Heat Flow Field

In Equation 4.22 the temperature field derived from the complex function is presented. In the following a more detailed derivation is provided. In general, the temperature function was defined as real-valued function of  $F(z)$ , the heat flow field as imaginary part of the function (compare Chapter 4.1).

As mentioned, there are two forms of describing the complex argument  $z$ , i.e. either in CARTESIAN coordinates or with polar coordinates. For the separation of the real-valued and the imaginary part for functions containing the logarithm function, usually the polar coordinates yield advantages. This is due to the nature of the logarithmic function:

$$\ln(x \cdot y) = \ln(x) + \ln(y) . \quad (9.22)$$

Furthermore, for a constant factor  $r$ , it can be stated:

$$\ln(x^r) = r \cdot \ln(x) . \quad (9.23)$$

Formulating the basic function 4.12 in polar coordinates yields:

$$F(z) = \sum_{n=1}^{40} \frac{a_{1n}}{2\pi} \ln(z - z_n) = \sum_{n=1}^{40} \frac{a_{1n}}{2\pi} \ln[(r - r_n) \cdot e^{\varphi - \varphi_n}] . \quad (9.24)$$

Using Equation 9.22 yields:

$$\sum_{n=1}^{40} \frac{a_{1n}}{2\pi} \ln[(r - r_n) \cdot e^{\varphi - \varphi_n}] = \sum_{n=1}^{40} \frac{a_{1n}}{2\pi} [\ln(r - r_n) + \ln(e^{i(\varphi - \varphi_n)})] . \quad (9.25)$$

Separating both terms and further use of Equation 9.23 yields:

$$F(z) = \sum_{n=1}^{40} \frac{a_{1n}}{2\pi} [\ln(r - r_n) + \ln(e^{i(\varphi - \varphi_n)})] = \sum_{n=1}^{40} \frac{a_{1n}}{2\pi} \cdot \ln(r - r_n) + i \cdot \sum_{n=1}^{40} \frac{a_{1n}}{2\pi} (\varphi - \varphi_n) . \quad (9.26)$$

For the replacement of the polar coordinates the expressions:

$$r = \sqrt{x^2 + y^2}, \varphi = \arctan\left(\frac{y}{x}\right) \quad (9.27)$$

can be used for the coordinate transformation to Cartesian coordinates. Using this equations yields for Equation 9.26:

$$\begin{aligned} F(z) &= T(x, y) + i \cdot H(x, y) \\ &= \sum_{n=1}^{40} \frac{a_{1n}}{2\pi} \cdot \ln[\sqrt{(x - x_n)^2 + (y - y_n)^2}] + i \cdot \sum_{n=1}^{40} \frac{a_{1n}}{2\pi} \arctan\left(\frac{y - y_n}{x - x_n}\right) . \end{aligned} \quad (9.28)$$

The real-valued part of the function is given in Equation 4.22 as temperature function, while the imaginary function is given in Equation 4.24. In some cases, the separation can also be conducted using other techniques, which was not of matter in this thesis.

### Detailed Derivation of Heat Flux from Complex Function

With the derivation of the temperature and heat flow field function, an expression for computation of the heat flux can be derived. The appropriate function based on the source solutions approach was presented in Equation 4.25. In the following the detailed derivation based on Equation 9.28 is presented.

Considering Fourier's Law and the Cauchy-Riemann Conditions, the heat flux can be derived by either the derivative of the heat flow field or the temperature function. Here, the derivative of the heat flow field function was chosen, however, the results are equal when choosing the temperature function. In Equation 4.25, the interesting derivative can be given to:

$$f'(x) = \frac{\partial}{\partial x} \arctan\left(\frac{y - y_n}{x - x_n}\right). \quad (9.29)$$

For yielding the final expression, initially the derivative of the "arctan" - function can be given to:

$$\frac{\partial}{\partial x} \arctan(x) = \frac{1}{1 + x^2}. \quad (9.30)$$

In Equation 9.29, the argument  $x$  is however given as a function. For the further derivation the expressions:

$$f[g(x)]' = f'[g(x)] \cdot g'(x), \quad (9.31)$$

for derivatives of functions and the expression:

$$f = \frac{g(x)}{h(x)}, f' = \frac{g'(x)h(x) - g(x)h'(x)}{h(x)^2}, \quad (9.32)$$

for the differentiation of ratios. Considering Equation 9.30, 9.31 and 9.32 for Equation 9.29 yields:

$$\begin{aligned} f'(x) &= \frac{\partial}{\partial x} \arctan\left(\frac{y - y_n}{x - x_n}\right) \\ &= \frac{1}{1 + \left(\frac{y - y_n}{x - x_n}\right)^2} \cdot \frac{\partial}{\partial x} \left(\frac{y - y_n}{x - x_n}\right) \\ &= \frac{1}{1 + \left(\frac{y - y_n}{x - x_n}\right)^2} \cdot \frac{0 - (y - y_n) \cdot 1}{(x - x_n)^2} \\ &= -\frac{y - y_n}{(x - x_n)^2 + (y - y_n)^2}. \end{aligned} \quad (9.33)$$

By putting Equation 9.33 in the expression in Equation 4.25 the final expression stated can be given. The negative sign of Equation 9.33 is eliminated.

### 9.3 Source Codes

#### *Quellcodes*

In the following, representative excerpts from the source code used for the modeling are provided. The code was programmed with MATLAB. For the first code provided, i.e the code for the generation of the panels on the characteristic sections, the length of the sections are determined and divided into panels with the same length. In the presented code a length of 1  $\mu\text{m}$  was chosen, generating a number of panels for the geometry shown in Figure 5.4 of 2000 panels. By doing so, a high accuracy of the computation was yielded.

**Source Code 1:**     Source Code for Generation of Panels

*Quellcode zur Erzeugung der Panelgeometrie*

```

panel_length = 1;
number_panels = sum(sections(:,5),1);
panels = zeros(number_panels,8);

for count = 1:(number_sections-2)
    if sections(count,5) ~=0
        panx = linspace(sections(count,1), sections(count,2),
                        sections(count,5)+1);
        pany = linspace(sections(count,3), sections(count,4),
                        sections(count,5)+1);
        panels(sections(count,6):sections(count,7),1) =
        panx(1:end-1);
        panels(sections(count,6):sections(count,7),2) =
        panx(2:end);
        panels(sections(count,6):sections(count,7),3) = pa-
        ny(1:end-1);
        panels(sections(count,6):sections(count,7),4) = pa-
        ny(2:end);
    end
end

for count = (number_sections-1):number_sections
    if sections(count,5) ~=0
        panels(sections(count,6),1) = point_D(1);
        panels(sections(count,6),3) = point_D(2);
        numpan=sections(count,5);
        deldeg = (alpha + pi/2)/numpan;
        for countn = 1:numpan-1
            panels(sections(count,6)+countn-1,2) =
                panels(sections(count,6),1) -
            r_c*sin(countn*deldeg);
            panels(sections(count,6)+countn-1,4) =
                panels(sections(count,6),3) + r_c*(1-
            cos(countn*deldeg));
            panels(sections(count,6)+countn,1) =
                panels(sections(count,6)+countn-1,2);
            panels(sections(count,6)+countn,3) =

```

```

    panels(sections(count,6)+countn-1,4);
end
panels(sections(count,7),2) = point_E(1);
panels(sections(count,7),4) = point_E(2);
end
end

panels(:,5) = (panels(:,1) + panels(:,2))/2;
panels(:,6) = (panels(:,3) + panels(:,4))/2;
panels(:,7) = atan2(panels(:,4)-panels(:,3), panels(:,2)-
panels(:,1));
panels(:,8) = sqrt((panels(:,4)-panels(:,3)).^2 +
(panels(:,2)-panels(:,1)).^2);

```

In the variable `panels` the coordinates for start, middle and end point, angle relative to the  $x$  axis and the length of the panels are stored inside a matrix. In this way, each individual panel is defined and addressable in the code.

After definition of the influence matrix, the boundary conditions are defined. The partition of sections which have influence in two directions is thereby generated by putting two panels upon each other. The appropriate panels are defined as transparent and let all heat flow through them, as explained in subchapter 5.2.2. An arbitrary partition of the heat into the areas is not permitted. The following code was used for computation of the boundary conditions vector and the solving of the linear equation system. The code is a modified version taken from [MORA03, pp. 118].

**Source Code 2:** Source Code for the Boundary Condition Vector

*Quellcode für den Randbedingungen Vektor*

```

A = zeros(number_panels,number_panels);

for counti = 1:number_panels
    for countj = 1:number_panels
        if counti == countj
            flog = 0;
            ftan = betaii(counti);
        else
            dxj = panels(counti,5)-panels(countj,1);
            dxjp = panels(counti,5)-panels(countj,2);
            dyj = panels(counti,6)-panels(countj,3);
            dyjp = panels(counti,6)-panels(countj,4);
            flog = log((dxjp^2+dyjp^2)/(dxj^2+dyj^2))/2;
            ftan = atan2((dyjp*dxj-dxjp*dyj),(dxjp*dxj+dyjp*dyj));
        end
        A(counti,countj) = (sin(panels(counti,7)-
panels(countj,7))*flog +
cos(panels(counti,7)-panels(countj,7))*ftan)/(2*pi);
    end
end

heatsources = zeros(number_panels,1);
adiabatic = zeros(number_panels,1);

```

```

heatgen = A*heatsources;

RHS = -heatgen.*adiabatic;

solution = A\RHS;

```

The variable `heatsources` contains the heat source strength of the distinct panels. Multiplied with the influence matrix the induced heat on each panel is yielded. This influence is written in the variable `heatgen`. The variable `adiabatic` contains the information about all panels considered to be adiabatic. With the boundary conditions vector the adiabatic panels need to be compensated yielding a induced heat strength of Zero. Therefore the variable `heatgen` is multiplied (vector multiplication) with the variable `adiabatic` and the values (with negative sign) are saved in the variable `RHS`. Finally the linear equation system is solved, the appropriate source strengths for each panel can be found in the variable `solution`.

After the derivation of the unknown source strengths, the potential function can be plotted. As MATLAB is working with matrix computation, a grid is defined in the two dimensional space. The grid dimensions are defined using the variable `spacing`, the window size corresponds to the chosen window size of the chosen cutting kinematics.

**Source Code 3:** Source Code for Generation of the Potential Function

*Quellcode zur Erzeugung der Potenzialfunktion*

```

spacing = 1;
[x,y] = meshgrid(window_xmin:spacing>window_xmax,
                  window_ymin:spacing>window_ymax);

Phi = 0;
Psi = 0;

for count = 1:number_panels
    Phi = Phi + (sources(count,3)+heatsources(count,1))/
        (2*pi)*log(sqrt((x-sources(count,1)).^2+(y-
    sources(count,2)).^2));
    Psi = Psi + (sources(count,3)+heatsources(count,1))/
        (2*pi)*atan2((y-sources(count,2)),(x-sources(count,1)));
end

```

With the variables `Phi` and `Psi` the real valued respectively imaginary functions are introduced. In these variables again a matrix is defined. This matrix contains the values for both functions at each location of the grid. These values are generated by the summation of all panels and the respective heat source strengths in the whole space.

After generating the potential function the temperature field can be plotted. The gradient of the potential function is generated with function `gradient` and the resulting heat source strengths (not calibrated) are saved in the variables `ux` and `uy`. These variables are matrix variables equal to the function `Phi` before. With the variables the

induced heat source strengths are known at each point of the grid. For the calibration they are subsequently multiplied with the heat conductivity (Inverse Method). The values for the heat conductivity are sometimes different to the real values, in the shown case the values are divided by 1000.

**Source Code 4:** Source Code for Generating of the Temperature Field

*Quellcode zur Erzeugung des Temperaturfeldes*

```

spacing = 1;
[ux, uy] = gradient(Phi,spacing);

lambda=ones(size(Phi));
lambda(:,:, :) = lambda_work;

m0 = round((point_O(2)-window_ymin)/spacing)+1;
n0 = round((point_O(1)-window_xmin)/spacing)+1;
T0 = 600;
TU = 295;

T=zeros(size(Phi));
T(m0,n0) = T0;

for m = m0+1 : m0+window_ymax.spacing
    T(m,n0) = T(m-1,n0) - uy(m,n0)*spacing/lambda(m,n0);
end

for m = m0+1 : m0+window_ymax.spacing
    for na = c_kt : n0+1 : n0+window_xmax.spacing
        T(m,n) = ((T(m-1,n) - uy(m,n)*spacing/lambda(m,n)) +
        (T(m,n-1) -
            ux(m,n)*spacing/lambda(m,n))/2;
    end
end

```

For the integral method the function `intgrad2` is applied. This function is the inverse operator of the function `gradient`. By using this function, the gradient variables `ux` and `uy` are integrated along the whole grid after they were multiplied with the heat conductivity `lambda`.

**Source Code 5:** Source Code for Calibration of the Temperature Field

*Quellcode zur Kalibrierung des Temperaturfeldes*

```

uxlambda = -ux./lambda;
uylambda = -uy./lambda;

Tinv = intgrad2(uxlambda,uylambda,spacing,spacing);
Tinv = Tinv + Tref;

```

After the integration the reference temperature `Tref` is added as static offset value to the whole field. The calibrated temperature field can then be plotted.

## 9.4 Result Tables from Cutting Experiments

*Ergebnistabellen der Zerspanversuche*

**Table 9.3:** Result Table from Broaching Experiments (Inconel 718)

*Ergebnistabelle der Räumversuche (Inconel 718)*

Rake Angle $\gamma / {}^\circ$	Rise per Tooth $RPT / \mu\text{m}$	Cutting Speed $v_c / \text{m/min}$	Cutting Force $F_c / \text{N}$	Normal Force $F_N / \text{N}$	Chip Thickness $h' / \mu\text{m}$	Contact Length $l_{rake} / \mu\text{m}$
5	40	4	1020	880	124	360
5	40	8	960	850	116	300
5	80	4	1820	1300	209	810
5	80	8	1660	1220	194	760
10	40	4	940	710	112	340
10	60	4	1260	890	153	600
10	80	4	1630	1040	194	940
15	40	4	860	580	100	540
15	40	8	860	600	98	730
15	80	4	1480	810	185	770
15	80	8	1360	820	166	760

**Table 9.4:** Result Table for Comparison to FE Method for C 45 E [ABOU15]

*Ergebnistabelle für den Vergleich zur FE Methode für C 45 E [ABOU15]*

Rake Angle $\gamma / {}^\circ$	Uncut Chip Thickness $RPT / \mu\text{m}$	Cutting Speed $v_c / \text{m/min}$	Cutting Force $F_c / \text{N}$	Normal Force $F_N / \text{N}$	Chip Thickness $h' / \mu\text{m}$	Contact Length $l_{rake} / \mu\text{m}$
6	200	150	1443	749	400	960
6	400	150	2524	924	700	1140
6	500	150	3092	1075	850	1170

## 10 References

### Literaturverzeichnis

- [ABOU15] Abouridouane, M. ; Klocke, F. ; Lung, D. ; Veselovac, D.: The Mechanics of Cutting: In-situ Measurement and Modelling. In: Procedia CIRP, 2015, pp. 246–251
- [ALJO12] Al Jourdi, A.: Adaption des Trockenbohrens über thermomechanische Modellierung zur Erhöhung der Fertigungsgenauigkeit. Berlin, TU Berlin. Dissertation. 2012
- [ANDE01] Anderson, J. D.: Fundamentals of aerodynamics. 3rd ed. Boston : McGraw-Hill, 2001 (McGraw-Hill series in aeronautical and aerospace engineering)
- [ARRA13] Arrazola, P. ; Özel, T. ; Umbrello, D. ; Davies, M. ; Jawahir, I.: Recent advances in modelling of metal machining processes. In: CIRP Annals - Manufacturing Technology 62, Vol. 2, 2013, pp. 695–718
- [ASME06] ASME: Guide for verification and validation in computational solid mechanics. New York : American Society of Mechanical Engineers, 2006
- [BICK51] Bickel, E. ; Widmer, M.: Die Temperaturen an der Werkzeugschneide. In: Industrielle Organisation Schweiz, Vol. 20, 1951, pp. 238–244
- [BIER13] Biermann, D. ; Kirschner, M. ; Pantke, K. ; Tillmann, W. ; Herper, J.: New coating systems for temperature monitoring in turning processes. In: Surface and Coatings Technology 215, 2013, pp. 376–380
- [BLOK38] Blok, H.: Theoretical study of temperature rise at surfaces of actual contact under oiliness lubricating conditions. In: Proceedings of General Discussion on Lubrication and Lubricants Institute of Mechanical Engineers London,, 1938, pp. 22–235
- [BRIN11] Brinksmeier, E. ; Gläbe, R. ; Klocke, F. ; Lucca, D.: Process Signatures – an Alternative Approach to Predicting Functional Workpiece Properties. In: Procedia Engineering, 2011, pp. 44–52
- [BUSC14] Busch, M.: Methodische Fräsprozessauslegung für die Bearbeitung hochwarmfester Werkstoffe. Aachen, RWTH Aachen. Dissertation. 23.01.2014
- [CARS59] Carslaw, H. S. ; Jaeger, J. C.: Conduction of heat in solids. 2nd ed. Oxford [Oxfordshire], New York : Clarendon Press; Oxford University Press, 1959

- [CHAO53] Chao, B. T. ; Trigger, K. J.: The significance of the thermal number in metal machining. In: *Transactions of ASME*, Vol. 75, 1953, pp. 109–120
- [CHAO55] Chao, B. T. ; Trigger, K. J.: Temperature Distribution at the Tool-Chip Interface in Metal Cutting. In: *Transactions of ASME*, Vol. 77, 1955, pp. 1107–1121
- [CHAO58] Chao, B. T. ; Trigger, K. J.: Temperature Distribution at Tool-Chip and Tool-Work Interface in Metal Cutting. In: *Transactions of ASME*, Vol. 80, 1958, pp. 311–329
- [CHIL78] Childs, T.: Some aspects of friction heating during metal cutting. In: *Wear* 50, Vol. 2, 1978, pp. 321–331
- [CHOU05] Chou, Y. K. ; Song, H.: Thermal modeling for white layer predictions in finish hard turning. In: *International Journal of Machine Tools and Manufacture* 45, 4-5, 2005, pp. 481–495
- [DAHM08] Dahmen, W. ; Reusken, A.: *Numerik für Ingenieure und Naturwissenschaftler*. Berlin, Heidelberg : Springer Berlin Heidelberg, 2008
- [DAVI07] Davies, M. A. ; Ueda, T. ; M'Saoubi, R. ; Mullany, B. ; Cooke, A. L.: On The Measurement of Temperature in Material Removal Processes. In: *CIRP Annals - Manufacturing Technology* 56, Vol. 2, 2007, pp. 581–604
- [DAWS84] Dawson, P. R. ; Malkin, S.: Inclined moving heat source model for calculating metal cutting temperatures. In: *Transactions of ASME*, Vol. 106, 1984, pp. 179–186
- [DENK10] Denkena, B. ; Schmidt, C. ; Krüger, M.: Experimental investigation and modeling of thermal and mechanical influences on shape deviations in machining structural parts. In: *International Journal of Machine Tools and Manufacture* 50, Vol. 11, 2010, pp. 1015–1021
- [FAHA13] Fahad, M. ; Mativenga, P. T. ; Sheikh, M. A.: On the contribution of primary deformation zone-generated chip temperature to heat partition in machining. In: *The International Journal of Advanced Manufacturing Technology* 68, 1-4, 2013, pp. 99–110
- [FANG02] Fang, N. ; Jawahir, I.: An Analytical Predictive Model and Experimental Validation for Machining with Grooved Tools Incorporating the Effects of Strains, Strain-rates, and Temperatures. In: *CIRP Annals - Manufacturing Technology* 51, Vol. 1, 2002, pp. 83–86
- [FLEI07] Fleischer, J. ; Pabst, R. ; Kelemen, S.: Heat flow simulation for dry machining of power train castings. In: *Annals of the CIRP* 1, Vol. 56, 2007, pp. 117–122
- [FOUR22] Fourier, J. B. J.: *Théorie analytique de la chaleur*, 1822

- [GIER15] Gierlings, S.: Model Based Temperature Monitoring for Broaching Safety-Critical Aero Engine Components. Aachen, RWTH Aachen. Dissertation. 2015
- [GOTT25] Gottwein, E.: Die Messung der Schneidentemperatur beim Abdrehen von Flusseisen 4, Vol. 23, 1925, pp. 1129–1135
- [GRZE06] Grzesik, W.: Determination of temperature distribution in the cutting zone using hybrid analytical-FEM technique. In: International Journal of Machine Tools and Manufacture 46, Vol. 6, 2006, pp. 651–658
- [HAHN51] Hahn, R. S.: On the temperature developed at the shear plane in the metal cutting process. In: Proceedings of First U.S. National Congress of Applied Mechanics, 1951, pp. 661–666
- [HESS67] Hess, J. L. ; Smith, A.: Calculation of potential flow about arbitrary bodies. In: Progress in Aerospace Sciences 8, 1967, pp. 1–138
- [HUAN05] Huang, Y. ; Liang, S. Y.: Cutting temperature modeling based on non-uniform heat intensityand partition ratio. In: Machining Science and Technology 9, Vol. 3, 2005, pp. 301–323
- [JAEG42] Jaeger, H. S.: Moving sources of heat and the temperature at sliding contacts. In: Proceedings Royal Society of New South Wales, Vol. 76, 1942, pp. 203–224
- [JIAN13] Jiang, F. ; Liu, Z. ; Wan, Y. ; Shi, Z.: Analytical modeling and experimental investigation of tool and workpiece temperatures for interrupted cutting 1045 steel by inverse heat conduction method. In: Journal of Materials Processing Technology 213, Vol. 6, 2013, pp. 887–894
- [KARA13] Karas, A. ; Bouzit, M.: Development of a thermal modell in the metal cutting process or prediction of temperature distributions at the tool-chip-workpiece interface. In: Journal of theoretical and applied mechanics 51, Vol. 3, 2013, pp. 553–567
- [KARP06a] Karpat, Y. ; Öznel, T.: Predictive Analytical and Thermal Modeling of Orthogonal Cutting Process—Part I: Predictions of Tool Forces, Stresses, and Temperature Distributions. In: Journal of Manufacturing Science and Engineering 128, Vol. 2, 2006, p. 435
- [KARP06b] Karpat, Y. ; Öznel, T.: Predictive Analytical and Thermal Modeling of Orthogonal Cutting Process—Part II: Effect of Tool Flank Wear on Tool Forces, Stresses, and Temperature Distributions. In: Journal of Manufacturing Science and Engineering 128, Vol. 2, 2006, p. 445

- [KATZ10] Katz, J. ; Plotkin, A.: Low-Speed Aerodynamics. 2. Aufl. Cambridge : Cambridge Univ. Press, 2010
- [KERR12] Kerrigan, K. ; Thil, J. ; Hewison, R. ; O'Donnell, G. E.: An Integrated Telemetric Thermocouple Sensor for Process Monitoring of CFRP Milling Operations. In: Procedia CIRP 1, 2012, pp. 449–454
- [KIM11] Kim, C.-K.: An analytical solution to heat conduction with a moving heat source. In: Journal of Mechanical Science and Technology 25, Vol. 4, 2011, pp. 895–899
- [KLOC07] Klocke, F. ; König, W.: Fertigungsverfahren 1 : Drehen, Fräsen, Bohren. 8. Aufl. Berlin : Springer, 2007
- [KLOC13] Klocke, F.; Gierlings, S.; Brockmann, M.; Veselovac, D.: Thermal Investigations for Finishing Conditions in Broaching Nickel-Based Turbine Components for Aero Engines, IMC 30, Dublin, 2013
- [KLOC15] Klocke, F. ; Brockmann, M. ; Gierlings, S. ; Veselovac, D. ; Kever, D. ; Roidl, B. ; Schmidt, G. ; Semmler, U.: Analytical Modelling Methods for Temperature Fields in Metal Cutting Based on Panel Method of Fluid Mechanics. In: Procedia CIRP, 2015, pp. 352–356
- [KOMA00] Komanduri, R. ; Hou, Z. B.: Thermal modeling of the metal cutting process : Part I - Temperature rise distribution due to shear plane heat source. In: International Journal of Mechanical Sciences 42, Vol. 9, 2000, pp. 1715–1752
- [KOMA01a] Komanduri, R. ; Hou, Z. B.: Thermal modeling of the metal cutting process : Part II: temperature rise distribution due to frictional heat source at the tool-chip interface. In: International Journal of Mechanical Sciences 43, Vol. 1, 2001, pp. 57–88
- [KOMA01b] Komanduri, R. ; Hou, Z. B.: Thermal modeling of the metal cutting process : Part III: temperature rise distribution due to the combined effects of shear plane heat source and the tool-chip interface frictional heat source. In: International Journal of Mechanical Sciences 43, Vol. 1, 2001, pp. 89–107
- [KUMA12] Kumar, L. D. ; Ajay, V.: Modelling of Temperature Profile in Metal Cutting Process. In: International Journal of Innovative Research and Development 1, Vol. 8, 2012, pp. 216–277
- [LECO12] Le Coz, G. ; Marinescu, M. ; Devillez, A. ; Dudzinski, D. ; Velnom, L.: Measuring temperature of rotating cutting tools: Application to MQL drilling and dry milling of aerospace alloys. In: Applied Thermal Engineering 36, 2012, pp. 434–441
- [LEON54] Leone, W. C.: Distribution of shear-zone heat in metal cutting. In: Transactions of ASME, Vol. 76, 1954, pp. 121–125

- [LIEN11] Lienhard, J. H.: A heat transfer textbook. 4th ed. Mineola, N.Y. : Dover Publications, 2011
- [LIN13] Lin, S. ; Peng, F. ; Wen, J. ; Liu, Y. ; Yan, R.: An investigation of workpiece temperature variation in end milling considering flank rubbing effect. In: International Journal of Machine Tools and Manufacture 73, 2013, pp. 71–86
- [LING02] Ling, F. F. ; Lai, W. M. ; Lucca, D. A.: Fundamentals of Surface Mechanics. New York, NY : Springer New York, 2002
- [LIU02] Liu, X. ; Wen, D. ; Li, Z. ; Xiao, L. ; Yan, F.: Cutting temperature and tool wear of hard turning hardened bearing steel. In: Journal of Materials Processing Technology 129, 1-3, 2002, pp. 200–206
- [LOEW54] Loewen, E. G. ; Shaw, M. C.: On the analysis of cutting-tool temperatures, Vol. 71, 1954, pp. 217–231
- [LUCH12] Luchesi, V. M. ; Coelho, R. T.: An inverse method to estimate the moving heat source in machining process. In: Applied Thermal Engineering 45-46, 2012, pp. 64–78
- [MERC45] Merchant, M. E.: Mechanics of the Metal Cutting Process. I. Orthogonal Cutting and a Type 2 Chip. In: Journal of Applied Physics 16, Vol. 5, 1945, p. 267
- [MORA03] Moran, J.: An introduction to theoretical and computational aerodynamics. Mineola, N.Y. : Dover Publications, 2003
- [MOUF04] Moufki, A. ; Devillez, A. ; Dudzinski, D. ; Molinari, A.: Thermomechanical modelling of oblique cutting and experimental validation. In: International Journal of Machine Tools and Manufacture 44, Vol. 9, 2004, pp. 971–989
- [MOUF98] Moufki, A. ; Molinari, A. ; Dudzinski, D.: Modelling of orthogonal cutting with a temperature dependent friction law. In: Journal of the Mechanics and Physics of Solids 46, Vol. 10, 1998, pp. 2103–2138
- [MÜLL04] Müller, B.: Thermische Analyse des Zerspanens metallischer Werkstoffe bei hohen Schnittgeschwindigkeiten. Aachen, RWTH Aachen. Dissertation. 2004
- [NAKA56] Nakayama, K.: Temperature rise of workpiece during metal cutting. In: Journal of the Japan Society of Precision Engineering, Vol. 22, 1956, pp. 269–273
- [NEUG11] Neugebauer, R. ; Bouzakis, K.-D. ; Denkena, B. ; Klocke, F. ; Sterzing, A. ; Tekkaya, A. E. ; Wertheim, R.: Velocity effects in metal forming and machining processes. In: CIRP Annals - Manufacturing Technology 60, Vol. 2, 2011, pp. 627–650

- [ORTL09] Ortlieb, C. P. ; Dresky, C. v. ; Gasser, I. ; Günzel, S.: Mathematische Modellierung. Wiesbaden : Vieweg+Teubner Verlag / GWV Fachverlage GmbH Wiesbaden, 2009
- [PIIS48] Piispanen, V.: Theory of formation of metal chips. In: Journal of Applied Physics, Vol. 19, 1948, pp. 876–881
- [PUTZ15] Putz, M. ; Schmidt, G. ; Semmler, U. ; Dix, M. ; Bräunig, M. ; Brockmann, M. ; Gierlings, S.: Heat Flux in Cutting: Importance, Simulation and Validation. In: Procedia CIRP, 2015, pp. 334–339
- [RADU94] Radulescu, R. ; Kapoor, S. G.: An Analytical Model for Prediction of Tool Temperature Fields during Continuous and Interrupted Cutting. In: Journal of Engineering for Industry 116, Vol. 2, 1994, p. 135
- [RAPI54] Rapier, A. C.: A theoretical investigation of the temperature distribution in the metal cutting process. In: British Journal Applied Physics, Vol. 5, 1954, pp. 400–405
- [RICH06] Richardson, D. J. ; Keavey, M. A. ; Dailami, F.: Modelling of cutting induced workpiece temperatures for dry milling. In: International Journal of Machine Tools and Manufacture 46, Vol. 10, 2006, pp. 1139–1145
- [ROSE46] Rosenthal, D.: The theory of moving sources of heat and its application to metal treatments. In: Transactions of ASME, Vol. 68, 1946, pp. 849–866
- [SATO13] Sato, M. ; Aoki, T. ; Tanaka, H. ; Takeda, S.: Variation of temperature at the bottom surface of a hole during drilling and its effect on tool wear. In: International Journal of Machine Tools and Manufacture 68, 2013, pp. 40–47
- [SCHL79] Schlesinger, S.: Terminology for model credibility. In: Simulation 32, Vol. 3, 1979, pp. 103–104
- [SCHW07] Schwer, L. E.: Guide for verification and validation in computational solid mechanics, 2007
- [SCHW33] Schwerd, F.: Über die Bestimmung des Temperaturfeldes beim Spanablauf. In: Zeitschrift des Vereins deutscher Ingenieure, Vol. 77, 1933, pp. 211–216
- [SHAW05] Shaw, M. C.: Metal cutting principles. 2nd ed. New York : Oxford University Press, 2005 (Oxford series on advanced manufacturing)
- [STEP92] Stephenson, D. A. ; Ali, A.: Tool Temperatures in Interrupted Metal Cutting. In: Journal of Manufacturing Science and Engineering 114, Vol. 2, 1992, p. 127

- [STEP97] Stephenson, D. A. ; Jen, T.-C. ; Lavine, A. S.: Cutting Tool Temperatures in Contour Turning: Transient Analysis and Experimental Verification. In: *Journal of Manufacturing Science and Engineering* 119, 4A, 1997, p. 494
- [SUHA10] Suhail, A. H. ; Ismail, N. ; Wong, S. V. ; Abdul Jalil, N. A.: Optimization of cutting parameters based on surface roughness and assistance of workpiece surface Temperature in Turning Process. In: *American Journal of Engineering and Applied Sciences* 3, Vol. 1, 2010, pp. 102–108
- [SUTT07] Sutter, G. ; Ranc, N.: Temperature fields in a chip during high-speed orthogonal cutting—An experimental investigation. In: *International Journal of Machine Tools and Manufacture* 47, Vol. 10, 2007, pp. 1507–1517
- [TAY93] Tay, A.: A review of methods of calculating machining temperature. In: *Journal of Materials Processing Technology* 36, Vol. 3, 1993, pp. 225–257
- [TAY80] Tay, A. ; Farmer, L. ; Oxley, P.: A numerical method for calculating temperature distributions in metal working processes. In: *International Journal of Mechanical Sciences* 22, Vol. 1, 1980, pp. 41–57
- [TAYL07] Taylor, F. W.: On the art of cutting metals. In: *Transactions of ASME*, Vol. 28, 1907, pp. 31–248
- [THAC04] Thacker, B. H. ; Doebling, S. W. ; Hemez, F. M. ; Anderson, M. C. ; Pepin, J. E. ; Rodriguez, E. A.: Concepts of model verification and validation. In: Report Los Alamos National Laboratories, LA-14167-MS, 2004
- [THAK15] Thakare, A. ; Nordgren, A.: Experimental Study and Modeling of Steady State Temperature Distributions in Coated Cemented Carbide Tools in Turning. In: *Procedia CIRP*, 2015, pp. 234–239
- [THOM98] Thompson Count Rumford, B.: An inquiry concerning the source of heat which is excited by friction. In: *Philosophical Transactions of the Royal Society of London*, Vol. 18, 1798, pp. 278–287
- [TOUN02] Tounsi, N. ; Vincenti, J. ; Otho, A. ; Elbestawi, M. A.: From the basic mechanics of orthogonal metal cutting toward the identification of the constitutive equation. In: *International Journal of Machine Tools and Manufacture* 42, Vol. 12, 2002, pp. 1373–1383
- [TRIG51] Trigger, K. J. ; Chao, B. T.: Trigger Chao - An Analytical Evaluation of Metal-Cutting Temperatures. In: *Transactions of ASME*, Vol. 73, 1951, pp. 57–68

- [TRUC08] Truckenbrodt, E.: Fluidmechanik. Berlin, Heidelberg : Springer Berlin Heidelberg, 2008
- [VENU86] Venuvinod, P. K. ; Lau, W. S.: Estimation of rake face temperatures in free oblique cutting. In: International Journal Machine Tool Design and Research, Vol. 26, 1986, pp. 1–14
- [WANI05] Wanigarathne, P. C. ; Kardekar, A. D. ; Dillon, O. W. ; Poulachon, G. ; Jawahir, I. S.: Progressive tool-wear in machining with coated grooved tools and its correlation with cutting temperature. In: Wear 259, 7-12, 2005, pp. 1215–1224
- [WEIN55] Weiner, J. H.: Shear-Plane Temperature Distribution in Orthogonal Cutting. In: Transactions of ASME, Vol. 77, 1955, pp. 1331–1341
- [WERS11] Werschmoeller, D. ; Ehmann, K. ; Li, X.: Tool Embedded Thin Film Microsensors for Monitoring Thermal Phenomena at Tool-Workpiece Interface During Machining. In: Journal of Manufacturing Science and Engineering 133, Vol. 2, 2011, pp. 71–78
- [YOUN94] Young, H. T. ; Chou, T. L.: Modelling of tool/chip interface temperature distribution in metal cutting. In: International Journal of Mechanical Sciences 36, Vol. 10, 1994, pp. 931–943
- [ZHAN08] Zhang, S. ; Liu, Z.: An analytical model for transient temperature distributions in coated carbide cutting tools. In: International Communications in Heat and Mass Transfer 35, Vol. 10, 2008, pp. 1311–1315
- [ZHAN09] Zhang, S. ; Liu, Z.: A new approach to cutting temperature prediction considering the diffusion layer in coated tools. In: International Journal of Machine Tools and Manufacture 49, 7-8, 2009, pp. 619–624
- [ZHOU13] Zhou, F. ; Wang, X. ; Hu, Y. ; Ling, L.: Modeling temperature of non-equidistant primary shear zone in metal cutting. In: International Journal of Thermal Sciences 73, 2013, pp. 38–45